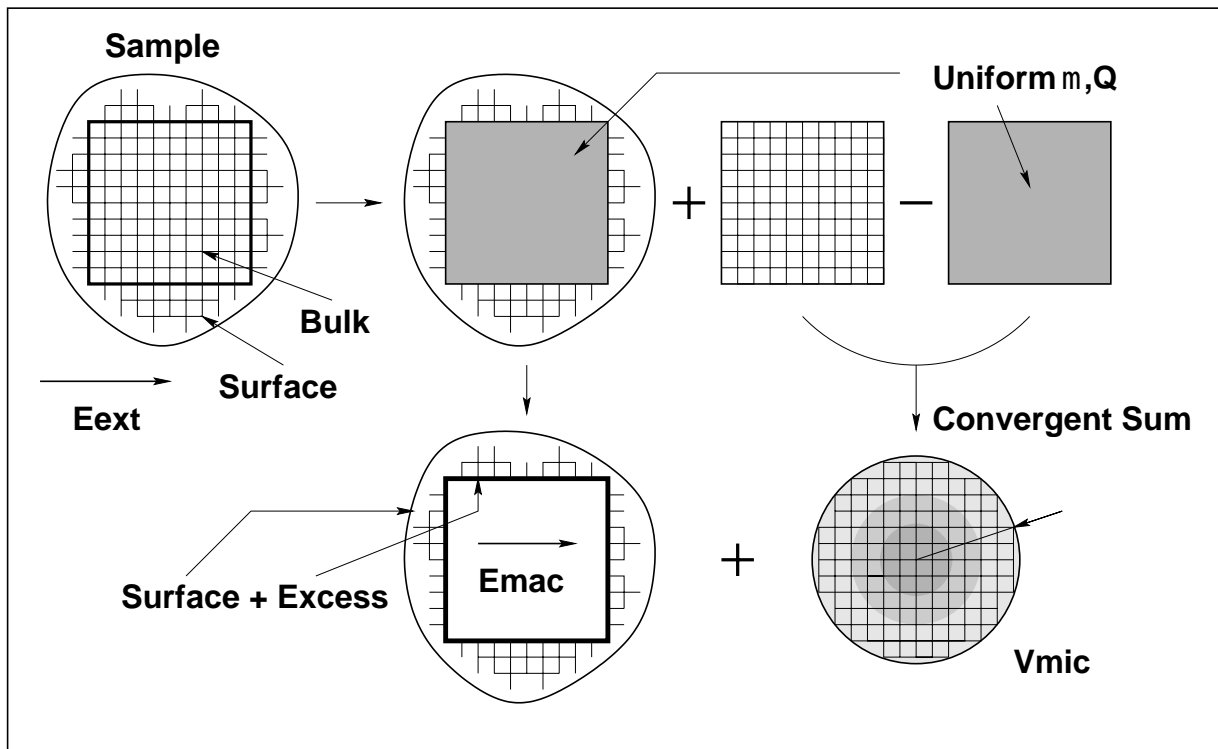


Time-Dependent Density Functional Theory for Periodic Systems



Freddie Kootstra

Time-Dependent Density Functional Theory for Periodic Systems

Freddie Kootstra

Time-Dependent Density Functional Theory for Periodic Systems

Front cover: The construction of the macroscopic electric field \mathbf{E}_{mac} and the microscopic Coulomb potential v_{mic} for a dielectric sample in an external field (Chapter 4).

The work described in this thesis was performed in the Theoretical Chemistry Group of the Materials Science Centre at the *Rijksuniversiteit* Groningen, Nijenborgh 4, 9747 AG Groningen, The Netherlands.

Freddie Kootstra,

Time-Dependent Density Functional Theory for Periodic Systems,

Proefschrift *Rijksuniversiteit* Groningen, The Netherlands.

Druk: PrintPartners Ipskamp B.V., Enschede, The Netherlands.

© F. Kootstra, 2001

RIJKSUNIVERSITEIT GRONINGEN

Time-Dependent Density Functional Theory for Periodic Systems

PROEFSCHRIFT

ter verkrijging van het doctoraat in de
Wiskunde en Natuurwetenschappen
aan de Rijksuniversiteit Groningen
op gezag van de
Rector Magnificus, dr. D.F.J. Bosscher,
in het openbaar te verdedigen op
vrijdag 30 november 2001
om 16.00 uur

door

Freddie Kootstra

geboren op 29 mei 1974
te Hengelo (o)

Promotor:

prof. dr. J.G. Snijders

Referent:

dr. ir. P.L. de Boeij

Beoordelingscommissie:

prof. dr. E.J. Baerends

prof. dr. K. Duppen

prof. dr. J. Knoester

voor Jurjen, Gezina en Saskia

voor Jenny

Contents

1	General Introduction	1
1.1	Introduction	1
1.2	Outline of this thesis	5
2	Introduction to (TD)DFT	9
2.1	The (first) Hohenberg-Kohn theorem	9
2.2	The (second) Hohenberg-Kohn theorem	11
2.3	The Kohn-Sham equations	12
2.4	The time-dependent Hohenberg-Kohn-Sham formalism	13
3	Polarization of a dielectric medium	17
3.1	Electric Polarization	17
3.2	Clausius-Mossotti Relation	19
3.3	Polarization in Extended Systems	22
4	A TDDFT approach for periodic systems	23
	F. Kootstra, P. L. de Boeij, and J. G. Snijders, " <i>Efficient real-space approach to time-dependent density functional theory for the dielectric response of nonmetallic crystals</i> ", J. Chem. Phys. 112 , 6517-6531 (2000).	
4.1	Abstract	23
4.2	Introduction	23
4.3	Theory	25
4.4	Implementation	34
4.5	Results and Discussion	39
4.6	Conclusions	41
4.7	Appendix A: Screened Potential	44
4.8	Appendix B: Quadrature for Response Kernels	46
4.9	Appendix C: Symmetry Adapted Fitfunctions	47
5	Application of the TDDFT approach to crystals	51
	F. Kootstra, P. L. de Boeij, and J. G. Snijders, " <i>Application of time-dependent density-functional theory to the dielectric function of various nonmetallic crystals</i> ", Phys. Rev. B 62 , 7071-7083 (2000).	

5.1	Abstract	51
5.2	Introduction	51
5.3	Method	52
5.4	Dielectric Constants	55
5.4.1	Sodium chloride structure	56
5.4.2	Fluoride structure	56
5.4.3	Wurtzite structure	59
5.4.4	Diamond structure	60
5.4.5	Zinc-blende structure	62
5.5	Dielectric Functions	62
5.6	Conclusions	65
6	Relativistic effects in TDDFT calculations	71
	F. Kootstra, P. L. de Boeij, H. Aissa, and J. G. Snijders, " <i>Relativistic effects on the optical response of InSb by time-dependent density-functional theory</i> ", J. Chem. Phys. 114 , 1860-1865 (2001).	
	P. L. de Boeij, F. Kootstra, and J. G. Snijders, " <i>Relativistic effects in the optical response of HgSe by time-dependent density-functional theory</i> ", Int. J. Quantum Chem. accepted.	
6.1	Abstract	71
6.2	Introduction	72
6.3	Theory	73
6.4	Method and Implementation	74
6.5	Results for Indium Antimonide	75
6.5.1	Band structure	75
6.5.2	Static dielectric constant	76
6.5.3	Dielectric function	77
6.6	Results for Mercury Selenide	79
6.6.1	Bandstructure, static dielectric constant and the dielectric function	79
6.7	Conclusions	82
6.8	Appendix: Small-Frequency Response	83
7	A polarization dependent functional	87
	P. L. de Boeij, F. Kootstra, J. A. Berger, R. van Leeuwen, and J. G. Snijders, " <i>Current density functional theory for optical spectra, a polarization functional</i> ", J. Chem. Phys. 115 , 1995-1999 (2001).	
7.1	Abstract	87
7.2	Introduction	87
7.3	Theory	88
7.4	Calculations	90
7.5	Results	91
7.5.1	Silicon	91
7.5.2	Diamond	93

7.5.3	Gallium phosphide	94
7.5.4	Gallium arsenide	95
7.5.5	Zinc sulfide	96
7.6	Conclusions	96
8	Excitons in crystalline insulators, described by TDDFT	97
	F. Kootstra, P. L. de Boeij, and J. G. Snijders, J. Chem. Phys. to be submitted.	
8.1	Abstract	97
8.2	Introduction	97
8.3	Theory	98
	8.3.1 Green's function approach	98
	8.3.2 TDDFT approach	102
8.4	Calculations on insulators	104
	8.4.1 Calcium fluoride	104
	8.4.2 α -Quartz	107
	8.4.3 Gallium nitride	110
8.5	Conclusions	113
9	Infinite conjugated polymeric chains	115
	F. Kootstra, P. L. de Boeij, R. van Leeuwen, and J. G. Snijders, to be submitted.	
9.1	Abstract	115
9.2	Introduction	115
9.3	DFT versus other calculation methods	117
9.4	Extrapolation procedures	118
9.5	Theory	119
9.6	Basis sets and parameters in the calculations	121
9.7	Results	121
	9.7.1 The model system polyhydrogen	121
	9.7.2 Other polymeric chains	124
9.8	Conclusions	127
9.9	Appendix: Periodic implementation	127
	9.9.1 Quadrature for the response kernels	127
	9.9.2 Integrations in the IBZ	128
	9.9.3 Crystals, surfaces, and polymers	129
	Summary	131
	Samenvatting	135
	Bibliography	139
	List of publications	149
	Dankwoord	151

Curriculum vitae

153

Chapter 1

General Introduction

1.1 Introduction

All materials we are surrounded by are built from atoms. Atoms are enormously small particles, which themselves are built from a positively charged nucleus surrounded by negatively charged electrons. The electrons are attracted by the nucleus, and move with high speed in specific shells (also called orbitals) around the nucleus. This is understood by first looking at Coulomb's law,

$$\frac{q_1 q_2}{r_{12}^2} \propto F. \quad (1.1)$$

It tells us that the force exerted on the electron by the nucleus is inversely proportional to the square of the distance between the electron and the nucleus. Electrons which are closer to the nucleus are, according to Coulomb's law, stronger bound, and thus have a lower potential energy. However the velocity of the electrons is much higher near the nucleus, and thus these electrons have a higher kinetic energy. That the electrons do not fall onto the nucleus comes from the fact that the potential energy loss and kinetic energy gain for the electron approaching the nucleus are balanced at a certain distance. In this way stable orbitals are formed. In general, the closer the electrons are to the nucleus, the lower the energy of the orbital in which the electrons are moving. It is a purely quantum mechanical effect that such orbitals can contain at maximum two electrons, with opposite spins according to the Pauli principle. The atoms can therefore be characterised by the energy levels of the orbitals in which the electrons are located. This is called the electronic structure of the atom.

In solids, the atoms are closely packed and arranged in an orderly way thereby forming a regular lattice. The atoms are so closely packed that the outer shells of neighbouring atoms start to overlap (See Fig. 1.1). The atomic picture of the electronic structure breaks down and a new picture emerges, in which the electrons are no longer attached to a single nucleus. In metals for instance, the electrons can 'jump' from one atom to another, and can more or less move freely through the solid. The electronic structure of a solid can, however, still be deduced from the constituent atoms. The energy levels of the atomic orbitals combine into so-called energy bands, as can be seen in Fig. 1.1 for a metal. The highest

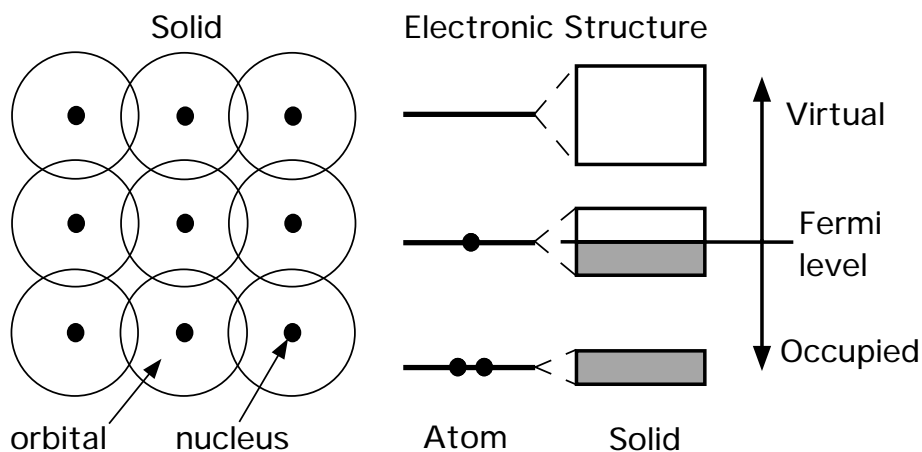


Figure 1.1: Schematical view of a solid, the overlapping orbitals of neighbouring atoms [left], and the electronic band structure [right].

energy level which is filled by electrons is called the Fermi level, which hence marks the separation between occupied and virtual states (See Fig. 1.1). Many properties of solids are determined by the behaviour of the electrons in the bands that have energies close to the Fermi level. Depending on the occupation of the energy bands a solid is called a metal, a semiconductor, or an insulator (See Fig. 1.2).

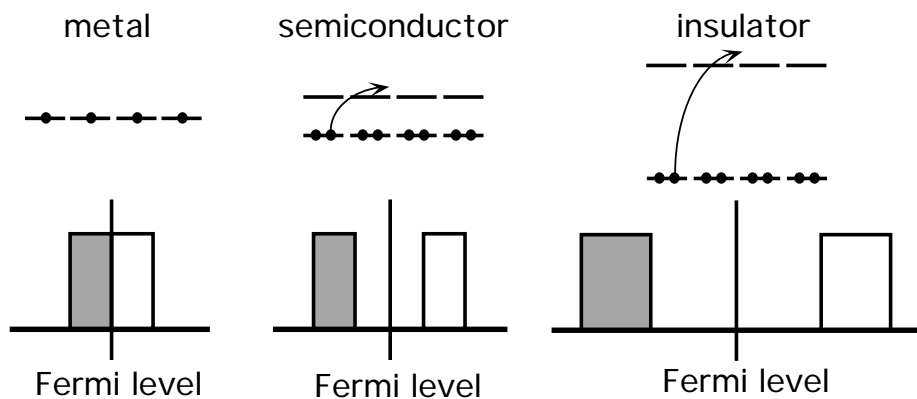


Figure 1.2: Schematical view of the occupation of the energy bands in a solid around the Fermi level for a metal [left], semiconductor [middle], and insulator [right]. The gray bands have lower energies and are hence occupied (filled), whereas the white bands have higher energies and are unoccupied (empty).

In metals the Fermi level is somewhere inside an energy band, which implies that it takes just a very small amount of energy to promote an electron to a higher energy level within

the same band. This characterises a metal and implies that the electrons can 'jump' freely from one atom to another, delocalising them over the complete metal. If the Fermi level is somewhere between a completely occupied (valence) band and an unoccupied (conduction) band, it takes a finite amount of energy to promote an electron from the valence band to the conduction band. One can show that in the latter case the electrons are more or less localised i.e., they can not easily 'jump' from one atom to the next. If the energy difference between the valence and the conduction band is big, the solid is called an insulator, and when it is small the solid is called a semiconductor.

As was already mentioned before, many properties of solids are determined by the dynamics of the electrons at the Fermi level. A prototypical example is the response of a solid to an electromagnetic field. Such an external field provides the solids with the energy needed to promote an electron to a higher energy level or band. The promoted electron leaves an empty level behind, which is often referred to as a 'hole'. Both the excited electron and the 'hole' are free to move. Therefore, the response of a solid to such an external field consists of the formation of electron-hole pairs, which respond to the electric field and cause electrical currents to flow in the solid. These induced currents give rise to an induced field, which tends to oppose, i.e., screen, the externally applied field. The perturbing field is effectively reduced inside the solid. In metals the electrons are able to flow over very large distances, as we already described before, they are able to completely screen the externally applied electric field to which the solid is exposed. However, at optical frequencies the screening can only be partial due to the inertia of the electrons. In insulators this screening is also restricted since in these materials the electronic charge can not flow over such large distances. The charge density then merely changes by, what is called polarization of the solid.

Many physical properties of many-particle systems have been under constant investigation during the past century. In general the description of the interacting many-particle systems is too complicated and approximations need to be made. By now several approximate methods are available to model the interacting many-particle systems. In the Born-Oppenheimer approximation the motion of the electrons is separated from the motion of the nuclei, which is much slower. This reduces the problem to the motion of the electrons only, with the nuclei at fixed positions. In principle, the motion of the electrons is described by the electronic wavefunction $\Psi_{\text{el}}(\mathbf{r}_1, \mathbf{r}_2, \dots, \mathbf{r}_n, t)$, which is the solution of the time-dependent Schrödinger equation

$$\hat{H}(t)\Psi_{\text{el}}(\mathbf{r}_1, \mathbf{r}_2, \dots, \mathbf{r}_n, t) = i\frac{\partial}{\partial t}\Psi_{\text{el}}(\mathbf{r}_1, \mathbf{r}_2, \dots, \mathbf{r}_n, t) , \quad (1.2)$$

in which \hat{H} is the many-particle Hamiltonian. Many approaches in quantum chemistry try to find this - very complicated - electronic wavefunction $\Psi_{\text{el}}(\mathbf{r}_1, \mathbf{r}_2, \dots, \mathbf{r}_n, t)$. As a first approximation one could model the Hamiltonian in Eq. 1.2, by replacing all the interactions between the particles by some effective mean field. Still the computational effort for evaluating the electronic wavefunction in several of such approximations is very high. However, there exist a set of theorems (the Hohenberg-Kohn theorems), which state that such an approach can actually be exact, at least for the stationary state of the system,

and, as turned out, much lower computational costs. The strong and attractive point of these theorems, called density functional theory (DFT), comes from the fact that it is not necessary to calculate the electronic wavefunction $\Psi_{\text{el}}(\mathbf{r}_1, \mathbf{r}_2, \dots, \mathbf{r}_n, t)$ for a full description of the system, but it is sufficient to look at the electron density $\rho(\mathbf{r})$. In the Kohn-Sham approach to DFT, one models the interacting many-particle system in terms of an effective non-interacting particle system (also called Kohn-Sham system). The external field is hereby replaced by an effective external field, which incorporates the interparticle interactions in an average way. The effective potential has to be modelled in such a way that the density of the Kohn-Sham system $\rho_{\text{ks}}(\mathbf{r})$ reproduces exactly the density of the real interacting many-particle system $\rho_{\text{real}}(\mathbf{r})$. Further, for the effective potential in such a Kohn-Sham system, it can be shown that it is completely determined by the electron density of the true interacting many-particle system.

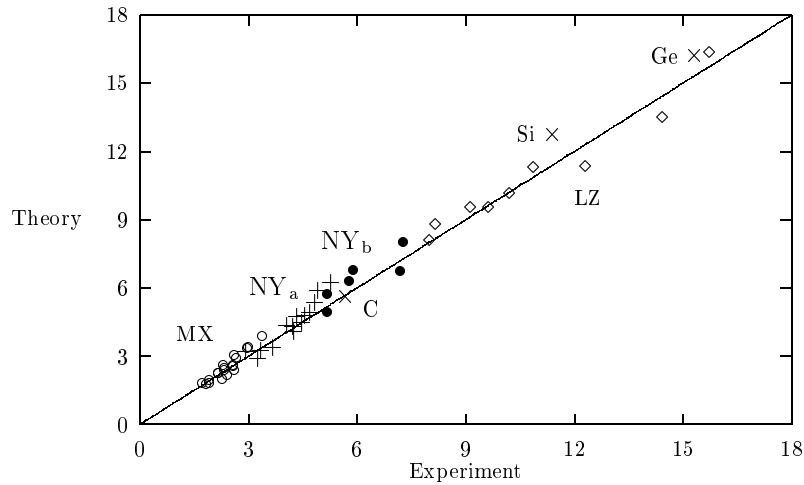


Figure 1.3: Theoretical versus experimental dielectric constant for various elementary and binary crystals. The sodium chloride crystals (\circ) of the I-VI type MX (M=Li, Na, K, Rb, Cs; X=F, Cl, Br, I) and (+) of the II-VI type NY_a (N=Mg, Ca, Sr, Ba; Y=O, S, Se, Te). The crystals in the diamond structure (\times) (C, Si, Ge) and in the zincblende structure (\diamond) for the III-V type LZ (L=Al, Ga, In; Z=P, As, Sb) and (\bullet) for the II-VI type NY_b (N=Zn, Cd; Y=S, Se, Te).

In the time-dependent version of DFT, one not only needs to consider the effective scalar potential, but also the effective vector potential of the non-interacting many-particle system. Both these potentials have to be modelled in such a way that the density and current density of the Kohn-Sham system, $\delta\rho_{\text{ks}}(\mathbf{r}, t)$ and $\delta\mathbf{j}_{\text{ks}}(\mathbf{r}, t)$, reproduce the exact density and current density of the real interacting many-particle system, $\delta\rho_{\text{real}}(\mathbf{r}, t)$ and $\delta\mathbf{j}_{\text{real}}(\mathbf{r}, t)$.

In this thesis we describe the macroscopic optical properties of solids, by looking at the dynamics of the moving electrons as a response to an externally applied perturbing field. We have successfully applied time-dependent density functional theory to calculate such properties, as can be seen in Fig. 1.3. In Fig. 1.3 we compiled the theoretical (TDDFT)

versus experimental results for the dielectric constant ϵ_∞ for various elementary and binary crystals.

1.2 Outline of this thesis

In this thesis we describe *time-dependent density functional theory for periodic systems*. We hereby aim to describe if, and in which way, the theoretical concepts of time-dependent density functional theory (TDDFT) can be applied to systems with periodicity in multiple dimensions (polymers, surfaces and solids). Throughout the thesis we give the development of a computer implementation to test these theoretical ideas and concepts.

In the **chapter 2**, a brief summary of the theoretical concepts of time-dependent density functional theory is given. We describe density functional theory (DFT), which was first introduced in 1965 by Hohenberg and Kohn [2] (section 2.1 and 2.2). The practical implementation of DFT was given one year later by Kohn and Sham [3], and resulted into a self-consistent scheme (section 2.3). The time-dependent version of DFT, was not given before the 1980s by Runge and Gross [4] (section 2.4).

In **chapter 3**, we address the problem of what is exactly the definition of polarization in a dielectric medium. Together with the question of how to define properly and uniquely polarization in such dielectric media. Therefore, in this chapter, polarization in a dielectricum is introduced as the dynamic response of the system to an externaly applied electric field. (section 3.1). The dynamic response of the system consists of electric currents flowing through the system. Thereby an electromagnetic field is generated, which tends to oppose this external field and effectively reduces the perturbing field inside the dielectricum. In section 3.2 we show that if the system can be decomposed into an assembly of localised elements which are all charge neutral and independently polarizable, the macroscopic polarization can be considered in a simple discrete dipole model. For such a discrete dipole model the Clausius-Mossotti relation is valid. In section 3.3 the proper definition for polarization in an extended system is considered. The polarization as it was used in a discrete dipole model is, in general, ill-defined because it depends on the particular choice of partitioning the system into the seperate elements. There is no unique way to do this partitioning. The definition for polarization in terms of the induced current provides a simple way to avoid this problem. Therefore, it provides a unique definition for polarization in extended systems. The induced current which flows through the interior of the system is also directly related to the intrinsic charge that piles up at the surface of the system. Thus it is not necessary to consider the surface of the system explicitly, and, in addition to the above, this makes the definition for the polarization in terms of the induced current more attractive.

In **chapter 4** we show how time-dependent density functional theory becomes feasible in a real-space description for the calculation of the static and frequency-dependent dielectric function $\epsilon(\omega)$ of nonmetallic crystals. A combination of a lattice-periodic *microscopic* scalar potential with a uniform *macroscopic* electric field as perturbation in a periodic structure calculation is used (section 4.3). The induced density and microscopic potential

can be obtained self-consistently for fixed macroscopic field by using linear response theory in which Coulomb interactions and exchange-correlation effects are included. An iterative scheme, in which the density and the potential are updated in every cycle, is used (section 4.4). The explicit evaluation of Kohn-Sham response kernels is avoided and their singular behavior as function of the frequency is treated analytically (section 4.8). Coulomb integrals are evaluated efficiently using auxiliary fitfunctions (section 4.9) and a screening technique is applied for the lattice sums (section 4.7). The dielectric functions $\epsilon(\omega)$ for diamond, silicon, and gallium arsenide, within the adiabatic local density approximation, are obtained from the induced current (section 4.5). In particular in the low-frequency range no adjustment of the local density approximation band gap seems to be necessary to get good agreement for the static dielectric function ϵ_∞ with experiment.

In **chapter 5** the results, of the TDDFT method as introduced in chapter 4, for a wide range of nonmetallic crystals are given for the dielectric constant ϵ_∞ (at optical frequencies). The crystals have the sodium chloride, the fluoride, the wurtzite, the diamond, and the zinc-blende lattice structure (section 5.4). The frequency-dependent dielectric function $\epsilon(\omega)$ for the crystals in the diamond and zincblende lattice structure are also presented (sections 5.5). The calculated results are compared with experimental data and other theoretical investigations. For the dielectric constants ϵ_∞ and the dielectric functions $\epsilon(\omega)$ the results are in good agreement with the experimental values. The average deviation is 4-5% from experiment for the group IV and III-V compounds in the wurtzite, zincblende and diamond lattice structure, 8-9% for the II-VI and I-VII compounds in the zinc-blende and sodium chloride lattice structure, and up to 14% deviation for the fluoride lattice structure. The spectral features of the dielectric functions $\epsilon(\omega)$ appear in the calculations at somewhat too low energies compared to experiment.

In **chapter 6** the effects of including relativistic effects in time-dependent density functional theory for the optical response properties of nonmetallic crystals are investigated. The dominant scalar relativistic effects have been included using the zeroth-order regular approximation (ZORA) in the ground-state DFT calculations, as well as in the time-dependent response calculations (section 6.3). It is derived that this theory can also be applied to indium antimonide (InSb) and mercury selenide (HgSe) in the zinc-blende structure, notwithstanding the fact that they turn into semimetals when scalar relativistic effects are included (section 6.8). Results are given for the band structure, the static dielectric constant ϵ_∞ and the dielectric function $\epsilon(\omega)$ of InSb (section 6.5) and HgSe (section 6.6), for the various levels on which relativity can be included, i.e., nonrelativistic, only in the ground-state, or also in the response calculation. With the inclusion of scalar relativistic effects, the band structure of InSb and HgSe become semimetallic within the local density approximation and we find a deviation of 5% from experiment for the static dielectric constant of InSb. Also the dielectric functions are improved and the spectra are now in good agreement with experiment.

In **chapter 7** a new approach is proposed to calculate optical spectra, which for the first time uses a polarization dependent functional within current density functional theory, as proposed by Vignale and Kohn [108] (section 7.3). This polarization dependent functional includes exchange-correlation contributions in the effective macroscopic electric

field. The functional is tested and used to calculate the optical absorption spectrum of the semiconductors: silicon, diamond, gallium phosphide, gallium arsenide and zinc sulfide (section 7.5). In all cases a better agreement with experiment is obtained than before.

In **chapter 8** we demonstrate that time-dependent density-functional theory, within the adiabatic local density approximation, describes the excitonic effects for the insulators CaF_2 , SiO_2 , and GaN correctly. Results for the electronic band structure, the density of states and the optical spectra (ϵ_2) are reported for these wide band gap insulators (section 8.4). The optical spectra calculated by TDDFT are compared directly with experimental measurements, and with the ϵ_2 's as calculated by a Green's function approach (DFT/GW/BSE). In DFT/GW/BSE, these excitons are explicitly taken into account by evaluating the two-body Green's function G_2 . The features in the optical absorption spectra, that are attributed to excitonic effects according to the DFT/GW/BSE results, are also found in the TDDFT calculations. This contradicts the common assumption that TDDFT is not able to describe these excitonic effects properly.

In **chapter 9** the linear optical polarizability of several infinite conjugated polymers is examined within the time-dependent density functional theory approach, by making use of the periodicity in these systems. The polymeric chains examined were the model system polyhydrogen (H), polyacetylene (PA), polydiacetylene (PDA), polybutatriene (PBT), polythiophene (PT), polysilane (PSi) and polymethineimine (PMI). The results for the longitudinal polarizability, i.e., along the polymeric backbone α_{zz} , were highly overestimated by TDDFT in comparison with the more traditional calculation methods (like e.g., Hartree-Fock and coupled cluster) for all the considered polymeric chains. The overestimation is most likely due to the incorrect description of the macroscopic exchange-correlation (xc) electric field contribution by the LDA and GGA approximation for the xc-functional. An estimate for this macroscopic exchange-correlation contribution $E_{xc,mac}$, is given for the polymeric chains considered.

Chapter 2

Introduction to (TD)DFT

Over the last 35 years Density Functional Theory (DFT) has become one of the standard methods for calculations in several branches of physics and chemistry. Among all the other methods to electronic structure calculations, like e.g. Configuration Interaction (CI), Coupled Cluster (CC) and Møller-Plesset (MP) Perturbation Theory [1], the rather special place of DFT becomes directly clear from the fundamentals, as it was first formulated in 1964 by Hohenberg and Kohn [2].

2.1 The (first) Hohenberg-Kohn theorem

Every observable quantity of a stationary quantum mechanical system is determined by the ground-state density alone.

In other words, the aim of DFT is not to obtain a good approximation to the ground state wave-function of the system, but rather to find the energy of the system as a functional of the density, without any reference to the wavefunction. This proof, that all observables of a many electron system are unique functionals of the electron density, provides the theoretical basis for DFT.

Consider a nonrelativistic N -electron system in the Born-Oppenheimer approximation. The Hamiltonian \hat{H} in the Schrödinger Equation (SE)

$$\hat{H}\Psi(\mathbf{x}_1, \mathbf{x}_2, \dots) = E\Psi(\mathbf{x}_1, \mathbf{x}_2, \dots) , \quad (2.1)$$

consists of the kinetic energy \hat{T} , the nuclear-electron interaction \hat{V} , and the electron-electron interaction \hat{V}_{ee} . Further in Eq. 2.1, the \mathbf{x}_i denotes the space \mathbf{r}_i and spin σ_i variables of the electrons.

Therefore the Hamiltonian is given by

$$\hat{H} = \hat{T} + \hat{V} + \hat{V}_{ee} , \quad (2.2)$$

where

$$\hat{T} = \sum_{i=1}^N \left(-\frac{\nabla_i^2}{2} \right), \quad (2.3)$$

$$\hat{V} = \sum_{i=1}^N v(\mathbf{r}_i) = - \sum_{i=1}^N \sum_{\alpha} \frac{Z_{\alpha}}{r_{i\alpha}}, \quad (2.4)$$

$$\hat{V}_{ee} = \sum_{i < j}^N \frac{1}{r_{ij}}. \quad (2.5)$$

In the Hohenberg-Kohn (HK) theorem the one-to-one mapping between the electron density ρ :

$$\rho(\mathbf{r}_1) = \sum_{\sigma_1=\uparrow\downarrow} N \int |\Psi(\mathbf{x}_1, \mathbf{x}_2, \dots, \mathbf{x}_N)|^2 d\mathbf{x}_2 \dots d\mathbf{x}_N, \quad (2.6)$$

and the external potential \hat{V} is proved.

The mapping

$$\hat{V} \xrightarrow{\text{Eq. 2.1}} \Psi \xrightarrow{\text{Eq. 2.6}} \rho, \quad (2.7)$$

is rather simple and straightforward.

Each \hat{V} connects to a wavefunction Ψ by solving the SE (Eq. 2.1), and the corresponding density ρ can be found by integrating the square of the wavefunction (Eq. 2.6).

The proof of the mapping in the other direction (that ρ determines \hat{V})

$$\hat{V} \xleftarrow{(i)} \Psi \xleftarrow{(ii)} \rho, \quad (2.8)$$

is done in two steps.

(i) if \hat{V} and \hat{V}' differ by more than a constant C , they will not lead to the same wavefunction Ψ .

(ii) if the ground state Ψ of \hat{H} and Ψ' of \hat{H}' are different, they cannot lead to the same density ρ .

For a *nondegenerate* ground state it follows (i)

$$(\hat{T} + \hat{V}_{ee} + \hat{V})|\Psi\rangle = E_{gs}|\Psi\rangle, \quad (2.9)$$

$$(\hat{T} + \hat{V}_{ee} + \hat{V}')|\Psi'\rangle = E'_{gs}|\Psi'\rangle. \quad (2.10)$$

Now we assume that $\Psi = \Psi'$, and one gets

$$(\hat{V} - \hat{V}')|\Psi\rangle = (E_{gs} - E'_{gs})|\Psi\rangle, \quad (2.11)$$

which immediately leads to $\hat{V} = \hat{V}' + C$, in contradiction with the assumption made in (i).

Using the variational theorem, in the case for (ii) one proves that if $\Psi \neq \Psi'$ this implies that $\rho(\mathbf{r}) \neq \rho'(\mathbf{r})$.

$$\begin{aligned} E_{gs} = \langle \Psi | \hat{H} | \Psi \rangle &< \langle \Psi' | \hat{H} | \Psi' \rangle = \langle \Psi' | \hat{H}' + \hat{V} - \hat{V}' | \Psi' \rangle \\ &= E'_{gs} + \int \rho'(\mathbf{r}) [v(\mathbf{r}) - v'(\mathbf{r})] d\mathbf{r} . \end{aligned} \quad (2.12)$$

And similarly

$$\begin{aligned} E'_{gs} = \langle \Psi' | \hat{H}' | \Psi' \rangle &< \langle \Psi | \hat{H}' | \Psi \rangle = \langle \Psi | \hat{H} + \hat{V}' - \hat{V} | \Psi \rangle \\ &= E_{gs} + \int \rho(\mathbf{r}) [v'(\mathbf{r}) - v(\mathbf{r})] d\mathbf{r} . \end{aligned} \quad (2.13)$$

Assuming that $\rho(\mathbf{r}) = \rho'(\mathbf{r})$, the combination of the equations 2.12 and 2.13 leads to the following contradiction

$$E_{gs} + E'_{gs} < E_{gs} + E'_{gs} . \quad (2.14)$$

Therefore the maps between \hat{V} , Ψ , and ρ are bijective (one-to-one).

$$\hat{V} \longleftrightarrow \Psi \longleftrightarrow \rho , \quad (2.15)$$

and as a consequence of the bijective map $\Psi \longleftrightarrow \rho$, every observable O of the system is a unique functional of the density

$$\langle \Psi[\rho] | \hat{O} | \Psi[\rho] \rangle = O[\rho] . \quad (2.16)$$

2.2 The (second) Hohenberg-Kohn theorem

The exact ground-state density of a system in a particular external potential can be found by minimization of the energy functional.

As a direct consequence of Eq. 2.15, the map $\rho \longrightarrow \hat{V}$ indicates that ρ determines the external potential and thus the entire Hamiltonian. Therefore, in addition, the (first) HK theorem tells us that for the energy functional of a system in a particular external potential v_0

$$E_{v_0}[\rho] = \langle \Psi[\rho] | \hat{T} + \hat{V}_{ee} + \hat{V}_0 | \Psi[\rho] \rangle , \quad (2.17)$$

the exact ground-state density can be found by minimization of $E_{v_0}[\rho]$

$$E_0 = \min_{\rho} E_{v_0}[\rho] . \quad (2.18)$$

The part of the energy functional, $F_{\text{HK}}[\rho]$, which does not involve the external potential is a *universal* density functional

$$E_{\text{HK}}[\rho] = E_{v_0}[\rho] = F_{\text{HK}}[\rho] + \int v_0(\mathbf{r})\rho_0(\mathbf{r}) d\mathbf{r} , \quad (2.19)$$

$$F_{\text{HK}}[\rho] = \langle \Psi[\rho] | \hat{T} + \hat{V}_{ee} | \Psi[\rho] \rangle . \quad (2.20)$$

Unfortunately the Hohenberg-Kohn theorem does not provide us with a practical scheme for doing calculations. It does not tell us how to perform the map $\rho \rightarrow \Psi$ in practice, and only defines formally what F_{HK} is. This practical scheme was given, a little later, in 1965 by Kohn and Sham [3].

2.3 The Kohn-Sham equations

The ground-state density of the interacting particle system can be calculated as the ground-state density of an auxiliary non-interacting system.

In other words, the central assumption in the Kohn-Sham (KS) scheme is that, for each interacting electron system with external potential $v_0(\mathbf{r})$, a local potential $v_{s,0}(\mathbf{r})$ (the Kohn-Sham potential) exists such that the density $\rho_s(\mathbf{r})$ of the non-interacting system equals the density ρ of the interacting system.

Consequently, if this is true, this KS potential $v_{s,0}(\mathbf{r})$ must, according to the (first) HK theorem ($v_s(\mathbf{r}) \leftrightarrow \Psi_s(\mathbf{r}) \leftrightarrow \rho_s(\mathbf{r})$) be unique, in the sense that it is a unique functional of the density $v_s[\rho](\mathbf{r})$.

The SE for such a system of non-interacting electrons ($\hat{V}_{ee} = 0$), which move in an external potential $\hat{V}_{s,0}$ reads

$$\left(-\frac{\nabla^2}{2} + v_{s,0}(\mathbf{r}) \right) \phi_i(\mathbf{r}) = \epsilon_i \phi_i(\mathbf{r}) . \quad (2.21)$$

And the density of such a system is determined by the N lowest energy orbitals

$$\rho_s(\mathbf{r}) = \sum_{i=1}^N |\phi_i(\mathbf{r})|^2 . \quad (2.22)$$

The kinetic energy of this non-interacting KS system is given by

$$T_s[\rho] = \sum_{i=1}^N \langle \phi_i | -\frac{\nabla^2}{2} | \phi_i \rangle . \quad (2.23)$$

In order to arrive at a useful expression for the KS potential $v_{s,0}(\mathbf{r})$, we write the total energy expression for the interacting system in the following way

$$E[\rho] = T_s[\rho] + \int v_0(\mathbf{r})\rho(\mathbf{r}) \, d\mathbf{r} + \frac{1}{2} \int \int \frac{\rho(\mathbf{r})\rho(\mathbf{r}')}{|\mathbf{r} - \mathbf{r}'|} \, d\mathbf{r}d\mathbf{r}' + E_{\text{xc}}[\rho] , \quad (2.24)$$

hereby introducing an xc energy functional $E_{\text{xc}}[\rho]$ which looks like

$$E_{\text{xc}}[\rho] = F_{\text{HK}}[\rho] - T_s[\rho] - \frac{1}{2} \int \int \frac{\rho(\mathbf{r})\rho(\mathbf{r}')}{|\mathbf{r} - \mathbf{r}'|} \, d\mathbf{r}d\mathbf{r}' . \quad (2.25)$$

The HK theorem ensures that the energy functional $E[\rho]$ is stationary for small variations $\delta\rho(\mathbf{r})$ around the exact density $\rho_0(\mathbf{r})$

$$\frac{\delta E[\rho]}{\delta\rho(\mathbf{r})}\Big|_{\rho=\rho_0} = 0 , \quad (2.26)$$

this leads to

$$\frac{\delta F_{\text{HK}}[\rho]}{\delta\rho(\mathbf{r})}\Big|_{\rho=\rho_0} = -v_0(\mathbf{r}) . \quad (2.27)$$

Similarly for the non-interacting system we can find

$$\frac{\delta T_s[\rho]}{\delta\rho(\mathbf{r})}\Big|_{\rho=\rho_0} = -v_{s,0}(\mathbf{r}) . \quad (2.28)$$

Differentiating now Eq. 2.25 to $\rho(\mathbf{r})$ yields

$$v_{s,0}(\mathbf{r}) = v_0(\mathbf{r}) + \int \frac{\rho(\mathbf{r}')}{|\mathbf{r} - \mathbf{r}'|} d\mathbf{r}' + \frac{\delta E_{\text{xc}}}{\delta\rho(\mathbf{r})} , \quad (2.29)$$

which is often shortly denoted as

$$v_{s,0}(\mathbf{r}) = v_0(\mathbf{r}) + v_{\text{H}}(\mathbf{r}) + v_{\text{xc}}(\mathbf{r}) . \quad (2.30)$$

And hence with Eq. 2.21 we find

$$\left[-\frac{\nabla^2}{2} + v_0(\mathbf{r}) + \int \frac{\rho(\mathbf{r}')}{|\mathbf{r} - \mathbf{r}'|} d\mathbf{r}' + \frac{\delta E_{\text{xc}}}{\delta\rho(\mathbf{r})} \right] \phi_i(\mathbf{r}) = \epsilon_i \phi_i(\mathbf{r}) . \quad (2.31)$$

Thus the exchange-correlation potential is given by

$$v_{\text{xc}}(\mathbf{r}) = \frac{\delta E_{\text{xc}}}{\delta\rho(\mathbf{r})} . \quad (2.32)$$

Since the KS potential depends on the density, the Eqs. 2.29 and 2.31 have to be solved self-consistently. And therefore, once an approximation for the E_{xc} has been made, the KS equations provide a way for calculating the density $\rho(\mathbf{r})$, and from that e.g. the energy of the system.

2.4 The time-dependent Hohenberg-Kohn-Sham formalism

The derivation for the time-dependent KS equations is, compared to the static case, severely more complicated, and it was first formulated in 1984 by Runge and Gross [4]. Runge and Gross derived the density functional formalism, comparable to the ground state DFT formalism of Hohenberg, Kohn and Sham [2, 3], for arbitrary time-dependent systems. For

recent reviews on time-dependent density functional theory, see Gross [5] and van Leeuwen [6].

Given the initial state at t_0 , the single particle potential $v(\mathbf{r}, t)$ leading to a given density $\rho(\mathbf{r}, t)$ is uniquely determined, so that the map $v(\mathbf{r}, t) \rightarrow \rho(\mathbf{r}, t)$ is invertible.

As a consequence of the bijective map $v(\mathbf{r}, t) \longleftrightarrow \rho(\mathbf{r}, t)$, every observable $O(t)$ is a unique functional of, and can be calculated from, the density $\rho(\mathbf{r}, t)$. In Eq. 2.33, ρ_t denotes ρ at time t .

$$O[\rho_t](t) = \langle \Phi[\rho_t](t) | \hat{O}(t) | \Phi[\rho_t](t) \rangle . \quad (2.33)$$

In a general time-dependent situation such a proof starts from the time-dependent Schrödinger Equation (SE):

$$i \frac{\partial}{\partial t} \Psi(t) = \hat{H}(t) \Psi(t) , \quad (2.34)$$

in which the Hamiltonian $\hat{H}(t) = \hat{T} + \hat{W} + \hat{V}(t)$, consists of a kinetic part \hat{T} , some particle-particle interaction \hat{W} , and the single-particle potential $\hat{V}(t)$.

If the time-dependent SE (Eq. 2.34) is solved for a *fixed* initial state Ψ_0 and several potentials $v(\mathbf{r}, t)$, we obtain the map $v(\mathbf{r}, t) \rightarrow \Psi(t)$. From the wavefunction we get the density by $\rho(\mathbf{r}, t) = \langle \Psi(t) | \hat{\rho}(\mathbf{r}) | \Psi(t) \rangle$, which defines the map $\Psi(t) \rightarrow \rho(\mathbf{r}, t)$, and in which the density operator $\hat{\rho}(\mathbf{r})$ is given by

$$\hat{\rho}(\mathbf{r}) = \sum_{k=1}^N \delta(\mathbf{r} - \mathbf{r}_k) . \quad (2.35)$$

In order now to prove that there exists a time-dependent version of the HK theorem, one has to show that the map $v(\mathbf{r}, t) \rightarrow \Psi(t) \rightarrow \rho(\mathbf{r}, t)$ is invertible up to a purely time-dependent function $\alpha(t)$ in the potential, which appears in the wave functions as a phase factor: $\Psi(t) = e^{-i\alpha(t)} \Phi[\rho](t)$, and under the requirement that the potential is expandable in a Taylor series around $t = t_0$. Despite this phase factor which appears in the wave functions, the expectation value of any observable can still be regarded as a functional of the density alone, because the ambiguity of the phase cancels out in Eq. 2.33.

The proof is fully given in Ref. [4] and a short outline is given here. If two potentials $v(\mathbf{r}, t)$ and $v'(\mathbf{r}, t)$ differ by more than a purely time-dependent function $\alpha(t)$, there must exist some nonnegative integer k for which

$$\frac{\partial^k}{\partial t^k} [v(\mathbf{r}, t) - v'(\mathbf{r}, t)]|_{t=t_0} \neq \text{const. in } \mathbf{r} \quad (2.36)$$

The thing to prove now is that the densities $\rho(\mathbf{r}, t)$ and $\rho'(\mathbf{r}, t)$, which correspond to the potentials $v(\mathbf{r}, t)$ and $v'(\mathbf{r}, t)$ are different, if Eq. 2.36 is fulfilled for $k \geq 0$.

Since we start from the *fixed* initial state wave function Ψ_0 it should be noted that the particle $\rho(\mathbf{r}, t)$, and also current $j(\mathbf{r}, t)$ densities are of course identical at the initial time t_0 , and start therefore to differ infinitesimally later than t_0 .

This proof consists of two steps:

a. The time evolution of the current density is given by the equation of motion

$$i \frac{\partial \mathbf{j}(\mathbf{r}, t)}{\partial t} = \langle \Phi(t) | [\hat{\mathbf{j}}(\mathbf{r}), \hat{H}(t)] | \Phi(t) \rangle , \quad (2.37)$$

where the current operator $\hat{\mathbf{j}}(\mathbf{r})$ is given by

$$\hat{\mathbf{j}}(\mathbf{r}) = \frac{1}{2i} \sum_{k=1}^N (\nabla_{\mathbf{r}_k} \delta(\mathbf{r} - \mathbf{r}_k) + \delta(\mathbf{r} - \mathbf{r}_k) \nabla_{\mathbf{r}_k}) . \quad (2.38)$$

Since $\Phi(t)$ and $\Phi'(t)$ evolve from the same initial state Φ_0 , Eq. 2.37 gives

$$\begin{aligned} i \frac{\partial}{\partial t} [\mathbf{j}(\mathbf{r}, t) - \mathbf{j}'(\mathbf{r}, t)]|_{t=t_0} &= \langle \Phi_0 | [\hat{\mathbf{j}}(\mathbf{r}), \hat{H}(t_0) - \hat{H}'(t_0)] | \Phi_0 \rangle \\ &= i \rho(\mathbf{r}, t_0) \nabla [v(\mathbf{r}, t_0) - v'(\mathbf{r}, t_0)] . \end{aligned} \quad (2.39)$$

Working out the commutator in Eq. 2.39 (for $k = 0$ and $k > 0$ in Eq. 2.36) shows after some 'straightforward' algebra that $\mathbf{j}(\mathbf{r}, t)$ and $\mathbf{j}'(\mathbf{r}, t)$ will become different infinitesimally later than t_0 .

b. To arrive at the corresponding densities, the continuity equation is used

$$\frac{\partial \rho(\mathbf{r}, t)}{\partial t} = -\nabla \cdot \mathbf{j}(\mathbf{r}, t) , \quad (2.40)$$

in which the result of a. has to be inserted to finally find that also $\rho(\mathbf{r}, t)$ and $\rho'(\mathbf{r}, t)$ will become different infinitesimally later than t_0 .

Based on the Runge and Gross theorem, we can construct a time-dependent KS scheme.

The time-dependent density $\rho(\mathbf{r}, t)$ of the interacting particle system can be calculated as the density $\rho_s(\mathbf{r}, t)$ of an auxiliary non-interacting (KS) system with the local potential $v_s(\mathbf{r}, t)$.

Thus the exact time-dependent density of the interacting system can be computed from

$$\rho(\mathbf{r}, t) = \rho_s(\mathbf{r}, t) = \sum_{i=1}^N |\phi_i(\mathbf{r}, t)|^2 , \quad (2.41)$$

where the time-dependent KS orbitals are obtained by solving the time-dependent SE of the non-interacting particle system

$$i \frac{\partial}{\partial t} \phi_j(\mathbf{r}, t) = \left(-\frac{\nabla^2}{2} + v_s[\rho_t](\mathbf{r}, t) \right) \phi_j(\mathbf{r}, t) , \quad (2.42)$$

in which the single-particle KS potential is given by

$$v_s[\rho_t](\mathbf{r}, t) = v(\mathbf{r}, t) + \int \frac{\rho(\mathbf{r}', t)}{|\mathbf{r} - \mathbf{r}'|} d\mathbf{r}' + v_{xc}(\mathbf{r}, t) , \quad (2.43)$$

and Eqn. 2.43 formally defines the exchange-correlation potential $v_{xc}(\mathbf{r}, t)$.

In the limit of an external potential $v(\mathbf{r}, t)$, which varies slowly in time, the local density approximation (LDA) is used to calculate this exchange-correlation potential $v_{xc}(\mathbf{r}, t)$. Just like LDA in the case of time-independent DFT, it works well beyond its domain of justification. Therefore $v_{xc}(\mathbf{r}, t)$ is approximated by the same exchange-correlation potential as in time-independent DFT, but now using the time-dependent density at a particular time t , rather than the time-independent density.

Thus, evaluated with the density at a particular time t , the exchange-correlation potential is approximated by

$$v_{xc}[\rho_t](\mathbf{r}, t) = \frac{\partial E_{xc}[\rho_t]}{\partial \rho_t(\mathbf{r})} , \quad (2.44)$$

and it should be noted that, in this approximation, all retardation effects are neglected, and an instantaneous reaction of the self-consistent field to changes in ρ is assumed.

Chapter 3

Polarization of a dielectric medium

In this chapter we introduce the concept of polarization in dielectric media¹. We will treat the induced polarization as a dynamical response of the system to an externally applied electric field. In this thesis we will only consider nonmetallic systems that do not possess a static polarization. This excludes for instance ferroelectrics, which do possess a finite polarization in the ground state due to a symmetry-breaking lattice deformation.

3.1 Electric Polarization

When a solid is placed in an externally applied electric field, the medium will adapt to this perturbation by dynamically changing the positions of the nuclei and the electrons. We will only consider time-varying fields of optical frequencies. At such high frequencies the motion of the nuclei is not only effectively independent of the motion of the electrons, but also far from resonance. Therefore we can assume the lattice to be rigid.

The reaction of the system to the external field consists of electric currents flowing through the system. These currents generate electromagnetic fields by themselves, and thus the motion of all constituent particles in the system is coupled. The response of the system should therefore be considered as a collective phenomenon. The electrical currents now determine in what way the externally applied electric field is screened. The induced field resulting from these induced currents tends to oppose the externally applied field, effectively reducing the perturbing field inside the solid. In metals the moving electrons are able to flow over very large distances, so they are able to completely screen any *static* (externally applied) electric field to which the system is exposed. For fields varying in time, however, this screening can only be partial due to the inertia of the electrons. In insulators this screening is also restricted since in these materials the electronic charge is bound to the nuclei and can not flow over such large distances. The charge density then merely changes by *polarization* of the dielectricum.

¹Excellent background reading material on the polarization of a dielectric medium can be found in Ashcroft and Mermin [7], Kittel [8], Born and Wolf [9] and Jackson [10].

We define the induced polarization $\mathbf{P}(\mathbf{r}, t)$ as the time-integral of the induced current,

$$\mathbf{P}(\mathbf{r}, t) = - \int_{t_0}^t \delta \mathbf{j}(\mathbf{r}, t') dt' . \quad (3.1)$$

This completely defines the polarization as a microscopic quantity up to an (irrelevant) constant function of \mathbf{r} , being the polarization of the initial state $\mathbf{P}(\mathbf{r}, t_0)$. Now by evaluating the divergence of this $\mathbf{P}(\mathbf{r}, t)$, we immediately get

$$\nabla \cdot \mathbf{P}(\mathbf{r}, t) = - \int_{t_0}^t \nabla \cdot \delta \mathbf{j}(\mathbf{r}, t') dt' = \int_{t_0}^t \frac{\partial \rho(\mathbf{r}, t')}{\partial t'} dt' = \delta \rho(\mathbf{r}, t) - \delta \rho(\mathbf{r}, t_0) , \quad (3.2)$$

in which the induced density at t_0 , $\delta \rho(\mathbf{r}, t_0)$ is zero by definition. In the second step we have inserted the continuity equation,

$$\frac{\partial}{\partial t} \rho(\mathbf{r}, t) + \nabla \cdot \mathbf{j}(\mathbf{r}, t) = 0 . \quad (3.3)$$

On the other hand we get that the time-derivative of $\mathbf{P}(\mathbf{r}, t)$ is equal to the induced current density,

$$\frac{d}{dt} \mathbf{P}(\mathbf{r}, t) = -\delta \mathbf{j}(\mathbf{r}, t) . \quad (3.4)$$

From the Eqs. 3.2 and 3.4, we immediately see that the polarization $\mathbf{P}(\mathbf{r}, t)$, uniquely determines both the induced density and the current density. As such, the polarization is just an auxilliary quantity, which does not contain any new information.

The above definition for the polarization is very appealing since it is exactly this polarization that is used in the macroscopic Maxwell equations. It is zero outside the dielectricum, where no currents can exist. Moreover, it will turn out that the polarization, as defined in this way, is also very well suited as a basis to define the induced *macroscopic* polarization. The latter quantity is easily accessible in experiments. We obtain the (induced) macroscopic polarization as the average value of $\mathbf{P}(\mathbf{r}, t)$ by,

$$\mathbf{P}_{mac}(\mathbf{r}, t) = \frac{1}{|\Omega_{\mathbf{r}}|} \int_{\Omega_{\mathbf{r}}} \mathbf{P}(\mathbf{r}', t) d\mathbf{r}' = - \frac{1}{|\Omega_{\mathbf{r}}|} \int_{t_0}^t \int_{\Omega_{\mathbf{r}}} \delta \mathbf{j}(\mathbf{r}', t') d\mathbf{r}' dt' , \quad (3.5)$$

where $\Omega_{\mathbf{r}}$ is a small region surrounding the point \mathbf{r} . The diameter d of this region should be large compared to the lattice parameter a , but small compared to the wavelength of the perturbing field λ , thus $\lambda \gg d \gg a$.

In this thesis we want to know the induced polarization $\mathbf{P}(\mathbf{r}, t)$ that occurs as the first-order response of a dielectric medium to an externally applied electric field. We will not treat effects that go beyond linear response. The strength of the induced current, and hence the polarization, depends *not only* on the external electric field *but also* on the contributions from the induced sources in the dielectric medium itself. Therefore it is better to describe the polarization as a response of the system, not just to the externally applied electric field, but in addition also to the induced field. This induced field is the result of the induced

density and current density. We can write the induced polarization as linear response to these fields, according to

$$\mathbf{P}(\mathbf{r}, t) = \int \int_{t_0}^t \chi(\mathbf{r}, t; \mathbf{r}', t') \cdot (\mathbf{E}_{ext}(\mathbf{r}', t') + \mathbf{E}_{ind}(\mathbf{r}', t')) dt' d\mathbf{r}' . \quad (3.6)$$

The response kernel $\chi(\mathbf{r}, t; \mathbf{r}', t')$ is a material property. This response kernel is a function of \mathbf{r} and \mathbf{r}' , which is in general nonlocal, but has a short range behaviour, i.e., it decays sufficiently fast as a function of $|\mathbf{r} - \mathbf{r}'|$, and it is causal, i.e., χ vanishes for $t' > t$, which is already made explicit in the time-integral. Furthermore, χ does not depend on the absolute value of t and t' , but just on the time-lapse $(t - t')$.

Before we proceed, we define the macroscopic electric field $\mathbf{E}_{mac}(\mathbf{r}, t)$, in analogy with the macroscopic polarization, as the average of the external plus the induced field,

$$\mathbf{E}_{mac}(\mathbf{r}, t) = \frac{1}{|\Omega_{\mathbf{r}}|} \int_{\Omega_{\mathbf{r}}} (\mathbf{E}_{ext}(\mathbf{r}', t) + \mathbf{E}_{ind}(\mathbf{r}', t)) d\mathbf{r}' . \quad (3.7)$$

All contributions to the perturbing field that are due to remote sources, i.e., external sources and remote induced sources, are contained in this macroscopic field. The microscopic part of the perturbing field, which is due to the local structure of the induced sources, is averaged out. This microscopic part has to be proportional to the macroscopic component due to the short range of the response kernel. We can now give the macroscopic polarization as response to the macroscopic field, which is also known as the constitutive equation,

$$\mathbf{P}_{mac}(\mathbf{r}, t) = \int_{t_0}^t \chi_e(\mathbf{r}, t - t') \cdot \mathbf{E}_{mac}(\mathbf{r}, t') dt' . \quad (3.8)$$

For homogeneous systems the $\chi_e(\mathbf{r}, t - t')$ is independent of the position \mathbf{r} . Eq. 3.8 then defines the material property $\chi_e(t - t')$ called the electric susceptibility, from which the macroscopic dielectric function $\epsilon(t - t')$ is derived,

$$\epsilon(t - t') = 1 + 4\pi\chi_e(t - t') . \quad (3.9)$$

3.2 Clausius-Mossotti Relation

The relation of the macroscopic polarization to the macroscopic field in a system is often considered in a simple discrete dipole model. Thereby, the system is decomposed into an assembly of localised elements. If the constituent elements are all charge neutral and independently polarizable entities, there is no fundamental problem to derive such a relation. For simplicity we will assume the system to be homogeneous and isotropic, which implies that we can consider the system as a regular (cubic) array of identical dipoles. For each element we can obtain the dipole moment from the polarization \mathbf{P} along the following lines. Conventionally the dipole moment of such an entity can be obtained as the first moment of the induced density,

$$\boldsymbol{\mu}(t) = - \int_V \mathbf{r} \delta\rho(\mathbf{r}, t) d\mathbf{r} . \quad (3.10)$$

We will now show that this dipole moment is equivalent to the integrated polarization defined in Eq. 3.1. Consider therefore the variation in time of a Cartesian component of this dipole moment

$$\frac{\partial}{\partial t} \mu_x(t) = - \int_V x \left(\frac{\partial}{\partial t} \delta \rho(\mathbf{r}, t) \right) d\mathbf{r} . \quad (3.11)$$

Inserting the continuity relation (Eq. 3.3) gives

$$\frac{\partial}{\partial t} \mu_x(t) = \int_V x (\nabla \cdot \delta \mathbf{j}(\mathbf{r}, t)) d\mathbf{r} . \quad (3.12)$$

We can now integrate by parts, and use Gauss' theorem, to arrive at

$$\begin{aligned} \frac{\partial}{\partial t} \mu_x(t) &= \int_V (\nabla \cdot (x \delta \mathbf{j}(\mathbf{r}, t)) - (\nabla x) \cdot \delta \mathbf{j}(\mathbf{r}, t)) d\mathbf{r} \\ &= \int_S x \delta \mathbf{j}(\mathbf{r}, t) \cdot \mathbf{n} ds - \int_V \delta j_x(\mathbf{r}, t) d\mathbf{r} . \end{aligned} \quad (3.13)$$

If the current crossing the surface is zero, then the surface integral in Eq. 3.13 vanishes. This is ensured by the assumption of independently polarizable elements. Therefore the change in the dipole moment becomes directly related to the current flowing in the interior of each element, and we can conclude that the induced dipole moment is given by

$$\boldsymbol{\mu}(t) = - \int_{t_0}^t \int_V \delta \mathbf{j}(\mathbf{r}, t') d\mathbf{r} dt' = \int_V \mathbf{P}(\mathbf{r}, t) d\mathbf{r} . \quad (3.14)$$

We can now relate the macroscopic polarization $\mathbf{P}_{mac}(t)$ to $\boldsymbol{\mu}(t)$ by using Eq. 3.5,

$$\mathbf{P}_{mac}(t) = \frac{\boldsymbol{\mu}(t)}{V} . \quad (3.15)$$

In the sequel we will only consider the static case. The dipole moment $\boldsymbol{\mu}$, is related to the *local* electric field \mathbf{E}_{loc} (i.e., the local perturbing field acting on each element), by the polarizability α of the element,

$$\boldsymbol{\mu} = \alpha \cdot \mathbf{E}_{loc} . \quad (3.16)$$

The local electric field in such an element of the system can be decomposed into a number of contributions, for which the *general* expression is given by

$$\mathbf{E}_{loc} = \mathbf{E}_{ext} + \mathbf{E}_{ind}^{mac} - \mathbf{E}_{near}^{cont} + \mathbf{E}_{near}^{discr} . \quad (3.17)$$

The various contributions to \mathbf{E}_{loc} are depicted in Fig. 3.1. In this figure, \mathbf{E}_{ext} is the field produced by fixed charges external to the system. \mathbf{E}_{ind}^{mac} is conventionally called the depolarization field, i.e., the field of a uniformly polarized medium, or equivalently the field due to the surface charge density $\hat{\mathbf{n}} \cdot \mathbf{P}$, on the boundary of the system, which in the interior of the system tends to oppose the external applied field. We create a cavity in the system by subtracting the contribution of a uniformly polarized sphere. The corresponding field, \mathbf{E}_{near}^{cont} , is called the Lorentz cavity field, which is the field from this sphere that can

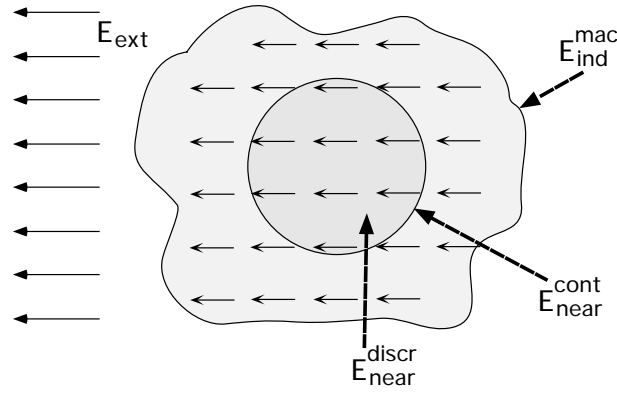


Figure 3.1: Contributions to the local electric field \mathbf{E}_{loc} in an element of the system. It is the sum of the externally applied electric field \mathbf{E}_{ext} , and the field due to all the other elements $\mathbf{E}_{ind}^{mac} - \mathbf{E}_{near}^{cont} + \mathbf{E}_{near}^{discr}$ of the system.

be described by a polarization charge on the inside of the spherical cavity cut out of the system, with the reference element in the center. Finally the contribution $\mathbf{E}_{near}^{discr}$ is the field produced by the elements inside this cavity.

We can now use the Lorentz relation for the local field in an element of the system,

$$\mathbf{E}_{loc} = \mathbf{E}_{ext} + \mathbf{E}_{ind}^{mac} + \frac{4\pi}{3}\mathbf{P}_{mac} , \quad (3.18)$$

in which we have used that the field inside a uniformly polarized sphere is given by $\mathbf{E}_{near}^{cont} = -4\pi\mathbf{P}_{mac}/3$, and that the contribution of the discrete elements in the cavity vanishes on symmetry grounds [7, 8], $\mathbf{E}_{near}^{discr} = 0$. By combining the Eqs. 3.15, 3.16, and 3.18, we can solve for the polarization \mathbf{P}_{mac}

$$\mathbf{P}_{mac} = \frac{\alpha}{V} \left(\mathbf{E}_{ext} + \mathbf{E}_{ind}^{mac} + \frac{4\pi}{3}\mathbf{P}_{mac} \right) = \frac{\alpha}{V} \left(\mathbf{E}_{mac} + \frac{4\pi}{3}\mathbf{P}_{mac} \right) , \quad (3.19)$$

in this equation we have identified: $\mathbf{E}_{mac} = \mathbf{E}_{ext} + \mathbf{E}_{ind}^{mac}$. Simple algebraic manipulations reveal that $\mathbf{P}_{mac} = \chi_e \mathbf{E}_{mac}$, in which χ is given by

$$\chi_e = \frac{\alpha/V}{1 - 4\pi\alpha/3V} . \quad (3.20)$$

Now by using the definition $\epsilon = 1 + 4\pi\chi_e$, and rearranging Eq. 3.20, we obtain the Clausius-Mossotti relation.

$$\frac{\epsilon - 1}{\epsilon + 2} = \frac{4\pi\alpha}{3V} . \quad (3.21)$$

We have now related the property of the system to the response properties of the constituent elements.

3.3 Polarization in Extended Systems

In the previous section we have shown that for a simple discrete dipole model one can derive an expression for the collective response of the total system to a macroscopic field, by only using the intrinsic properties of the constituent elements. The approximations used in that derivation break down as soon as the elements can no longer be considered as independent. In general this is the case, since electrons do not belong to the individual elements of the system. The electron density should be regarded as a continuous function of the position. There is no way to uniquely partition the system into separate elements and derive the polarization from the dipole moments of the elements. The dipole moment of the density is not a good measure for the polarization because currents can flow across the borders of the elements. From Eq. 3.13, it is clear that the dipole moment in Eq. 3.10 and the polarization as derived from the current density in Eq. 3.1, become different as soon as such currents exist. The polarization in terms of the dipole moment of the elements is ill-defined because it depends on the particular choice how to partition the system. However, the definition in terms of the induced current provides a simple way to obtain a well-defined polarization, which is model independent in the sense that it does not depend on the particular choice for the subdivision of the system into the various elements. Only in the above mentioned extreme Clausius-Mossotti case, in which the system consists of well-separated, independently polarizable, and charge neutral entities, the two definitions become equivalent.

There is a second, more subtle argument which makes the definition of the polarization in terms of the induced current more attractive, if we want to consider extended systems. The intrinsic charge that piles up at the surface is directly related to the current flowing through the interior of the system, and therefore it is not necessary to consider the surface of the system explicitly. The polarization is defined as being locally dependent on the induced current and has a unique value at every position in the system. The induced dipole moment is connected to a volume element of the system and is in general not model independent. More over its value depends on the induced density in a very nonlocal way. If we consider the dipole moment of the complete sample, the two alternative descriptions, based either on the dipole strength of the charge distribution of the system, including the surface, or on the total integrated current, are equivalent (Eq. 3.14), owing to the continuity equation. In the following chapter we will treat the extended system in the thermodynamic limit of infinite system size. In this limit the system is modeled using periodic boundary conditions and consequently the knowledge of the surface is lost in the process. The charge and current distributions then become disconnected and carry quite distinct pieces of information, though the variations of these distributions remain connected by the continuity equation. In periodic systems, polarization is therefore a property of the current and not of the charge density.

Chapter 4

A TDDFT approach for periodic systems

F. Kootstra, P. L. de Boeij and J. G. Snijders, "*Efficient real-space approach to time-dependent density functional theory for the dielectric response of nonmetallic crystals*", J. Chem. Phys. **112**, 6517-6531 (2000).

4.1 Abstract

Time-dependent density functional theory has been used to calculate the static and frequency-dependent dielectric function $\epsilon(\omega)$ of nonmetallic crystals. We show that a real-space description becomes feasible for crystals by using a combination of a lattice-periodic (microscopic) scalar potential with a uniform (macroscopic) electric field as perturbation in a periodic structure calculation. The induced density and microscopic potential can be obtained self-consistently for fixed macroscopic field by using linear response theory in which Coulomb interactions and exchange-correlation effects are included. We use an iterative scheme, in which density and potential are updated in every cycle. The explicit evaluation of Kohn-Sham response kernels is avoided and their singular behavior as function of the frequency is treated analytically. Coulomb integrals are evaluated efficiently using auxiliary fitfunctions and we apply a screening technique for the lattice sums. The dielectric function can then be obtained from the induced current. We obtained $\epsilon(\omega)$ for C, Si, and GaAs within the adiabatic local density approximation in good agreement with experiment. In particular in the low-frequency range no adjustment of the local density approximation (LDA) band gap seems to be necessary.

4.2 Introduction

In the early 1960's Hohenberg and Kohn [2] formulated the fundamental theorems of density functional theory (DFT) for the description of the ground state of an interacting-electron system in an external potential. This theory proved to be very practical after Kohn and

Sham [3] incorporated it in a one-electron self-consistent field calculation scheme (SCF). This method has nowadays become one of the standard tools for the first-principle calculation of the properties of solids [11], and also for atoms and molecules [12, 13, 14]. The accuracy of the results obtained with these methods is very good for a wide variety of ground state properties of solids, atoms, and molecules. Amongst the exceptions the most prominent is the large deviation for the energy gap and the dielectric constant in semiconductors and insulators. The value for the dielectric constant obtained within the local density approximation (LDA) is usually much larger (more than 10%) [15, 16] than the experimental data. A similar overestimation has been found for the static polarizabilities of atoms [17]. However, inclusion of the correct asymptotic behavior of the exchange-correlation potential [18] greatly improves the results for the atomic polarizabilities [19]. This correction, which is due to the contribution of the outer region, seems to be less important for molecules [19], so we should not expect large deviations for the LDA results in solids either. In solids the discrepancy for the dielectric constant is often attributed to the mismatch between the Kohn-Sham energy gap and the gap as observed in optical spectra. LDA typically underestimates the gap by 30%-50%. Attempts to improve these results by improving the quality of the various approximations for the exchange-correlation functional have had limited success. The inclusion of gradient corrections to the LDA reduces the error only slightly [20, 21]. The error in the Kohn-Sham energy gap can be attributed to a discontinuity in the DFT exchange-correlation potential [22, 23] and it is commonly believed that the gap has to be corrected by a rigid shift of the virtual states in order to get good results for the quasiparticle energies and dielectric constant [16, 24, 25, 26]. There is however no formal justification within DFT for this so-called scissors operator [21]. In some materials, one has to use a different shift in order to match the excitation spectrum than to get a correct dielectric constant [26]. Gonze, Ghosez and Godby [27] have indicated that this scissors-operator is an approximate way to deal with the special role of macroscopic polarization in these infinite systems. They made the remark that the original assumptions of Hohenberg and Kohn, are no longer valid in these systems, and that in principle the density must be supplemented with the macroscopic polarization in order to describe these systems completely. The time-dependent extension of DFT, (TDDFT) rigorously proven in the 1980's by Runge and Gross [4], gave some new impetus to this field of research. Whereas ordinary DFT was formulated originally only for the nondegenerate ground state. Runge and Gross showed that the validity of the theorems could be extended to cover systems in time-dependent scalar potentials as well. The application of this theory to atoms and molecules proved to be very successful, e.g., the calculated response properties and excitation energies were greatly improved [19, 28, 29, 30]. Ghosh and Dhara [31, 32] showed that TDDFT also applies to systems which are being subjected to general time-dependent electromagnetic fields, in which case both the density and the current density are needed to fully describe the system. We will follow their description and derive an expression for the macroscopic polarization from the current density. Most implementations of TDDFT for solids use pseudopotentials in combination with a plane-wave basis [15, 16, 24]. This combination facilitates the description for the induced properties, like density and induced fields in Fourier space [33, 34]. Self-consistency is achieved in a method which needs the

construction of various response kernels as large matrix representations on this plane-wave basis, and for which one usually has to invert these matrices [15, 35]. High accuracy can only be achieved at the expense of huge computation costs. We will show that a real-space description is possible, and we present a self-consistent field method, which is comparable in efficiency to ordinary ground-state calculations. This computational scheme is similar to the density-functional perturbation scheme of Baroni *et al.* [36]. We extended the full-potential linear combination of atomic orbitals (LCAO) implementation (ADF-BAND [37, 38]) for our response calculations, in which we achieve the same spatial resolution for the induced density as for the ground-state density. Coulomb interaction (local-field effects) and exchange-correlation effects have been fully included in this calculation scheme. The outline of this article is as follows. First we give the derivation of the real-space description for crystalline systems. We make use of a separation into microscopic and macroscopic components for the potentials and fields, and we describe how they can be used in the time-dependent Kohn-Sham scheme. Then the main aspects of the implementation are given. We show how symmetry can be used to reduce the computational effort, and we explain the self-consistency procedure. Finally we demonstrate the method for the crystals of C, Si, and GaAs, and discuss the results.

4.3 Theory

The theory of the dielectric properties of solids describes the linear response of crystals to externally applied electric fields. One of the central problems in this theory is how to model real systems that are large but nevertheless finite using idealized periodic crystals of infinite extent. One can only make this connection by considering the proper asymptotic limit of finite systems to infinite size. In this section we show that it is important to identify macroscopic and microscopic contributions to the electric field and polarization. For the finite system we have to do this in such a way that surface and sample-shape dependent contributions can be separated from the bulk-intrinsic parts. Before we formulate our microscopic treatment, let us recall the definitions for the macroscopic electric field $\mathbf{E}_{mac}(\mathbf{r}, t)$ and the macroscopic polarization $\mathbf{P}_{mac}(\mathbf{r}, t)$. Without losing generality we can consider the time-dependence to be harmonic with frequency ω . One commonly defines the macroscopic field at a point \mathbf{r} inside the bulk as the average field that a test charge would experience in a region $\Omega_{\mathbf{r}}$ surrounding the point \mathbf{r} . This region must have a size d that is small compared to the wavelength $\lambda = 2\pi c/\omega$, but it nevertheless has to contain a large number of bulk unit cells; i.e., for $\lambda \gg d \gg a$, where a is the lattice parameter, we can define

$$\mathbf{E}_{mac}(\mathbf{r}, t) = \frac{1}{|\Omega_{\mathbf{r}}|} \int_{\Omega_{\mathbf{r}}} (\mathbf{E}_{ext}(\mathbf{r}', t) + \mathbf{E}_{ind}(\mathbf{r}', t)) d\mathbf{r}'. \quad (4.1)$$

This macroscopic field contains the externally applied electric field plus the macroscopic part of the induced field. This induced field is the result of the reaction of the system to the external field.

Similarly the induced macroscopic polarization can be defined as the time-integral of the

average induced current flowing in this region $\Omega_{\mathbf{r}}$,

$$\mathbf{P}_{mac}(\mathbf{r}, t) = -\frac{1}{|\Omega_{\mathbf{r}}|} \int^t \int_{\Omega_{\mathbf{r}}} \delta \mathbf{j}(\mathbf{r}', t') d\mathbf{r}' dt', \quad (4.2)$$

where $\delta \mathbf{j}(\mathbf{r}, t)$ is the induced current density. Note that the definition for the macroscopic polarization of Eq. (4.2) is valid in all systems. It only becomes equivalent to the more common notion of ‘an induced average dipole moment per unit volume,’ i.e., to $-\int_{\Omega_{\mathbf{r}}} \mathbf{r}' \delta \rho(\mathbf{r}', t) d\mathbf{r}' / |\Omega_{\mathbf{r}}|$ when this property is properly defined. This is only the case in systems where we can define the volume $\Omega_{\mathbf{r}}$ such that no currents flow across its boundary. Inside the bulk the macroscopic polarization is related to the macroscopic electric field rather than to the externally applied field, via what is called the constitutive equation

$$\mathbf{P}_{mac}(\mathbf{r}, t) = \int^t \chi_e(t - t') \cdot \mathbf{E}_{mac}(\mathbf{r}, t') dt'. \quad (4.3)$$

This equation defines the material property $\chi_e(\tau)$ called the electric susceptibility, from which the macroscopic dielectric function $\epsilon(\tau)$ is derived,

$$\epsilon(\tau) = 1 + 4\pi\chi_e(\tau). \quad (4.4)$$

In general $\chi_e(\tau)$ and $\epsilon(\tau)$ are tensors, which, however, simplify to scalars in isotropic systems.

In order to be able to derive these material properties, we have to give a microscopic account of the macroscopic contributions to the electric field and polarization for an arbitrary but fixed region $\mathcal{B}_{\mathbf{r}}$ inside the bulk. We therefore identify in the interior of the sample a large number of identical but otherwise arbitrary bulk unit cells, each having the same volume $|V|$. The cells which comprise the region $\mathcal{B}_{\mathbf{r}}$ will be enumerated using the indices i and are denoted by V_i .

Within the long-wavelength limit we can assume that in these cells both the induced charge and current distribution become lattice periodic. Hence the macroscopic field component becomes uniform throughout $\mathcal{B}_{\mathbf{r}}$. Under these conditions all relevant properties become lattice periodic and we can model the response of the region $\mathcal{B}_{\mathbf{r}}$ by using a model system with periodic boundary conditions.

However, we cannot obtain the electric field by simply evaluating the contributions of the lattice-periodic sources. Only the microscopic part can be obtained using the periodic lattice, since the macroscopic component depends also on the external field and the sample shape, which are no longer properly defined in the periodic - hence infinite - model system. Instead we can consider the uniform macroscopic field for the periodic model system to be fixed. We will now construct the microscopic and macroscopic (scalar and vector) potentials which are due to the induced sources, and we will show that they lead to microscopic and macroscopic fields, respectively.

For any finite region Ω we can define the scalar potential $\delta v(\mathbf{r}, t)$ of the induced density $\delta \rho(\mathbf{r}, t) = \rho(\mathbf{r}, t) - \rho_0(\mathbf{r})$. The action is instantaneous within the Coulomb gauge, so the

potential follows from [we will use atomic units ($e = \hbar = m = 1$) throughout this article]

$$\delta v(\mathbf{r}, t) = \int_{\Omega} \frac{\delta \rho(\mathbf{r}', t)}{|\mathbf{r} - \mathbf{r}'|} d\mathbf{r}'. \quad (4.5)$$

It is well-established that this potential is not properly defined in the limit of $|\Omega|$ to infinite size. In the periodic model system this ambiguity arises due to the divergent and conditionally convergent lattice sum contributions of the monopole, dipole, and quadrupole moments of the density in the cells V_i .

We can, however, define the microscopic component of this Coulomb potential by removing these conditionally convergent contributions. Therefore we construct for each unit cell V_i a uniform monopole, dipole and quadrupole density, and we subtract their contributions $\delta v_i(\mathbf{r}, t)$ from the bare Coulomb potential of Eq. (4.5) according to

$$\delta v_{mic}(\mathbf{r}, t) = \sum_i \left(\int_{V_i} \frac{\delta \rho(\mathbf{r}', t)}{|\mathbf{r} - \mathbf{r}'|} d\mathbf{r}' - \delta v_i(\mathbf{r}, t) \right). \quad (4.6)$$

The summation is over all cells V_i in the region $\mathcal{B}_{\mathbf{r}}$. The potential $\delta v_i(\mathbf{r}, t)$ is defined as

$$\delta v_i(\mathbf{r}, t) = \int_{V_i} \sum_{n=0}^2 \frac{1}{n!} \delta \mu_{i,j_1 \dots j_n}^{(n)}(t) \cdot \frac{\partial}{\partial r'_{j_1}} \dots \frac{\partial}{\partial r'_{j_n}} \frac{1}{|\mathbf{r} - \mathbf{r}'|} d\mathbf{r}'. \quad (4.7)$$

In this expression we have implied a summation over all Cartesian components j_1 through j_n of the uniform multipole density of rank n , which are denoted by $\delta \mu_i^{(n)}(t)$. These uniform densities have to be constructed carefully in order to ensure that the conditionally convergent terms of Eq. (4.5) are exactly canceled in Eq. (4.6). Their value can be obtained for each cell V_i by requiring that all three lowest-order terms in the multipole expansion of the contribution of this cell to the microscopic potential of Eq. (4.6) must vanish. The expansion can be taken with respect to an arbitrary origin \mathbf{R}_i inside V_i . The monopole density has to vanish in the periodic system due to the condition of charge neutrality. One can easily check that the uniform dipole and quadrupole densities can then be obtained from the average dipole and quadrupole moments of the unit cells. If we choose to represent these moments with respect to the geometric centres, i.e., with respect to $\mathbf{R}_i = (1/|V|) \int_{V_i} \mathbf{r}' d\mathbf{r}'$, we obtain for this particular choice

$$\delta \mu_i^{(n)}(t) = \frac{1}{|V|} \int_{V_i} \delta \rho(\mathbf{r}', t) (\mathbf{r}' - \mathbf{R}_i)^n d\mathbf{r}', \quad (4.8)$$

where on the right-hand side the n^{th} tensor product is meant. Due to the periodicity these multipole densities are identical for each cell, so we can drop the index i in the sequel. By removing the conditionally convergent terms in this way, the series of Eq. (4.6) becomes nicely convergent. If we choose $\mathcal{B}_{\mathbf{r}}$ finite but nevertheless sufficiently large, so that convergence is reached within $\mathcal{B}_{\mathbf{r}}$, we have established a proper definition for the microscopic potential for both periodic and finite systems.

On the other hand, the macroscopic potential can only be defined for the true, finite system.

It forms the remainder of the bare Coulomb potential after the microscopic part has been removed. The terms $\delta v_i(\mathbf{r}, t)$ (which were not included in the microscopic contribution of region $\mathcal{B}_{\mathbf{r}}$) have to be included in the macroscopic part of the potential

$$\delta v_{mac}(\mathbf{r}, t) = \int' \frac{\delta \rho(\mathbf{r}', t)}{|\mathbf{r} - \mathbf{r}'|} d\mathbf{r}' + \sum_i \delta v_i(\mathbf{r}, t). \quad (4.9)$$

Here the integration domain in the first term on the right-hand side is the whole (finite) system, however, with the exclusion of the region $\mathcal{B}_{\mathbf{r}}$. This is indicated by the prime on the integral sign. The contribution of $\mathcal{B}_{\mathbf{r}}$ is given by the potential of the uniform multipole densities. Note that the resulting macroscopic potential comprises all surface and sample-shape dependent contributions, but excludes the microscopic contributions from the region $\mathcal{B}_{\mathbf{r}}$.

The uniform dipole and quadrupole sources in the region $\mathcal{B}_{\mathbf{r}}$ can equally well be represented using surface excess monopole and dipole layers at the boundary of $\mathcal{B}_{\mathbf{r}}$. Being remote, these can only lead to smooth, i.e. macroscopic fields at \mathbf{r} . A similar analysis holds for a uniform density in $\mathcal{B}_{\mathbf{r}}$. Although this density has to vanish in the periodic model system, a macroscopic density fluctuation on a wavelength scale can exist in the finite system, but it also can lead to only macroscopic fields. The microscopic potential, on the other hand, is lattice periodic, and can only lead to microscopic fields.

The nice result of this separation into microscopic and macroscopic contributions is that we are now able to evaluate the microscopic component of the Coulomb potential using the periodic model system. The construction is visualized in Fig. 4.1. The summation of Eq. (4.6) is nicely convergent, since remote cells do not contribute. For its evaluation we can make use of a screening technique. Therefore, we introduce an envelope function which weighs the contributions of the individual cells such that it leaves nearby cells unchanged, but removes remote cells explicitly. This can be achieved using a spherically symmetric function $h_c(r)$ which is a smooth function of just the distance of the origin of the cells to the coordinate at which to evaluate the potential. This function is characterized by some cutoff radius c for the screening. The limiting case, where this cutoff radius is infinite automatically yields the correct (unscreened) value,

$$\delta v_{mic}(\mathbf{r}, t) = \lim_{c \rightarrow \infty} \sum_i h_c(|\mathbf{r} - \mathbf{R}_i|) \left(\int_{V_i} \frac{\delta \rho(\mathbf{r}', t)}{|\mathbf{r} - \mathbf{r}'|} d\mathbf{r}' - \delta v_i(\mathbf{r}, t) \right). \quad (4.10)$$

We can separate the two contributions into two separately converging series. The screened potential of the periodic density can be evaluated efficiently, whereas the screened uniform multipole densities lead to a mere (time-dependent) uniform contribution (see Chapter 4.7 Appendix A). The latter contribution can always be chosen to vanish by a suitable gauge transformation. We obtain

$$\delta v_{mic}(\mathbf{r}, t) = \lim_{c \rightarrow \infty} \left(\sum_i h_c(|\mathbf{r} - \mathbf{R}_i|) \int_{V_i} \frac{\delta \rho(\mathbf{r}', t)}{|\mathbf{r} - \mathbf{r}'|} d\mathbf{r}' \right). \quad (4.11)$$

In practice the convergence can be quite fast for suitably chosen screening functions such that the numerical evaluation of it can be very efficient.

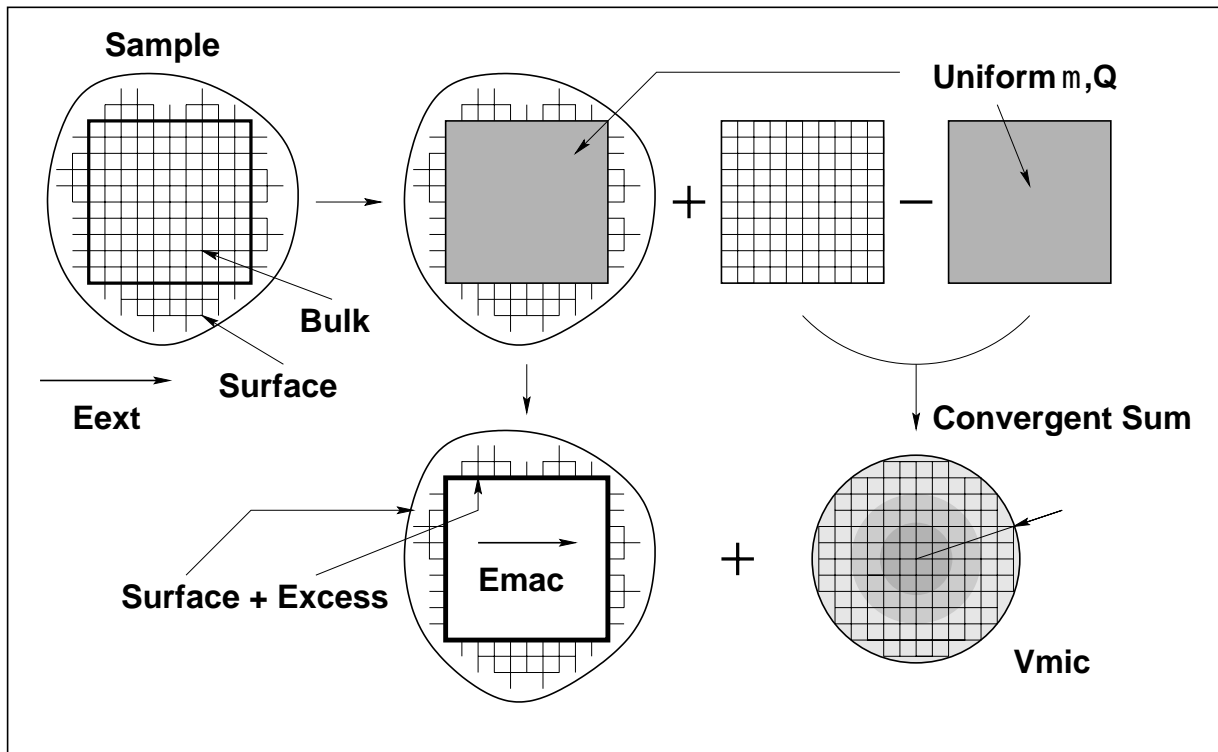


Figure 4.1: The construction of the macroscopic electric field \mathbf{E}_{mac} and the microscopic Coulomb potential v_{mic} for a dielectric sample in an external field. The bulk region $\mathcal{B}_{\mathbf{r}}$ is removed from the sample and replaced by a uniformly polarized medium. The difference between the true bulk and this substitute leads to a microscopic potential. The field produced inside the uniform medium is equivalent to the field produced by additional excess surface charges. In combination with the surface region this yields the macroscopic field.

The time-dependent induced density is not the only source of the electromagnetic fields. In large systems, the induced current density also contributes considerably. Therefore, we also have to consider the induced vector potential $\delta\mathbf{A}(\mathbf{r}, t)$ which is defined within the Coulomb gauge according to

$$\delta\mathbf{A}(\mathbf{r}, t) = \frac{1}{c} \int \frac{\delta\mathbf{j}_T(\mathbf{r}', t - |\mathbf{r} - \mathbf{r}'|/c)}{|\mathbf{r} - \mathbf{r}'|} d\mathbf{r}'. \quad (4.12)$$

Here $\delta\mathbf{j}_T(\mathbf{r}, t)$ is the induced transverse current density. This vector potential accounts, apart from the properly retarded contribution of the total induced current, also for the retardation effects which have not been included in the instantaneous Coulomb potential [39]. We can safely neglect the effect of retardation in the microscopic part of the scalar potential which is due to the nearby surrounding only, but we cannot do this for the macroscopic part. This part also contains contributions from remote regions. As we did for

the density and the Coulomb potential, we have to distinguish microscopic and macroscopic contributions of the induced current density to this vector potential. We can safely ignore the microscopic part, because its electric field contribution is already a factor ω^2/c^2 in order smaller than that of the microscopic Coulomb potential. We will only have to retain the macroscopic part. This part is sample-shape dependent just like the macroscopic scalar potential.

We obtain the total macroscopic field from

$$\mathbf{E}_{mac}(\mathbf{r}, t) = \mathbf{E}_{ext}(\mathbf{r}, t) - \frac{1}{c} \frac{\partial}{\partial t} \delta \mathbf{A}_{mac}(\mathbf{r}, t) + \nabla \delta v_{mac}(\mathbf{r}, t). \quad (4.13)$$

Here all macroscopic retardation effects are properly accounted for. The microscopic contribution to the field is completely described using the instantaneous microscopic Coulomb potential. This potential is lattice periodic and can therefore not contain any components that represent a macroscopic electric field. The field $\mathbf{E}_{mac}(\mathbf{r}, t)$ of Eq. (4.13) is therefore indeed the macroscopic field of Eq. (4.1).

We can now define a new gauge which we will call the microscopic Coulomb gauge. In this gauge the new scalar potential $\Phi'(\mathbf{r}, t)$ is given by the instantaneous microscopic potential $\delta v_{mic}(\mathbf{r}, t)$ of Eq. (4.11), while the associated vector potential $\mathbf{A}'(\mathbf{r}, t)$ is fully retarded and completely specified by the macroscopic electric field $\mathbf{E}_{mac}(\mathbf{r}, t)$ of Eq. (4.13)

$$\Phi'(\mathbf{r}, t) = -\delta v_{mic}(\mathbf{r}, t) \quad (4.14)$$

$$\mathbf{A}'(\mathbf{r}, t) = -c \int^t \mathbf{E}_{mac}(\mathbf{r}, t') dt'. \quad (4.15)$$

In the definition of these potentials we have neglected the microscopic retardation and microscopic magnetic effects. This is consistent with the neglect of the Breit corrections [40] in ground-state calculations.

The problems posed by the sample-shape dependence of the macroscopic field are circumvented by prescribing the total macroscopic electric field in the bulk as being uniform. We explicitly leave the surface region and sample shape undefined. We then only have to obtain the microscopic Coulomb potential of the periodic system in order to completely describe the fields in the bulk region. The main conclusion of this analysis is that in the long-wavelength limit it suffices to know the induced lattice-periodic density and the induced macroscopic current density in the bulk for a given uniform macroscopic electric field in order to obtain the bulk-intrinsic induced microscopic potential and macroscopic polarization.

We can now treat the dynamic linear response of a crystal to a fixed macroscopic field, within the idealized periodic boundary approximation. We use the perturbation approach to time-dependent density functional theory (TDDFT), in which both scalar and vector potentials are used to describe the perturbation. In its most general form this theory states that all observable quantities are functionals of both the time-dependent particle density $\rho(\mathbf{r}, t)$ and the current density $\mathbf{j}(\mathbf{r}, t)$. Ghosh and Dhara [32] have shown that this time-dependent density and current density can be constructed using a generalization of the

effective one-electron scheme of Kohn and Sham [3]. In this scheme the single-particle wave functions $\psi_n(\mathbf{r}, t)$ are solutions of the following time-dependent Schrödinger-type equation,

$$i\frac{\partial}{\partial t}\psi_n(\mathbf{r}, t) = \left(\frac{1}{2} \left| -i\nabla + \frac{1}{c}\mathbf{A}_{eff}(\mathbf{r}, t) \right|^2 + v_{eff}(\mathbf{r}, t) \right) \psi_n(\mathbf{r}, t) \quad (4.16)$$

for suitably chosen initial conditions. The particles move in time-dependent effective potentials $\{v_{eff}(\mathbf{r}, t), \mathbf{A}_{eff}(\mathbf{r}, t)\}$, which are uniquely determined (apart from an arbitrary gauge transform) by the exact time-dependent density and current density. These exact time-dependent densities follow from the solutions $\psi_n(\mathbf{r}, t)$ via

$$\rho(\mathbf{r}, t) = \sum_{n=1}^N |\psi_n(\mathbf{r}, t)|^2, \quad (4.17)$$

and

$$\mathbf{j}(\mathbf{r}, t) = \sum_{n=1}^N \Re \{ -i\psi_n^*(\mathbf{r}, t)\nabla\psi_n(\mathbf{r}, t) \} - \frac{1}{c}\rho(\mathbf{r}, t)\mathbf{A}_{eff}(\mathbf{r}, t). \quad (4.18)$$

The first and second term on the right-hand side of Eq. (4.18) are the paramagnetic and diamagnetic currents respectively. The initial ground-state configuration is obtained by occupying only those one-electron states, which have evolved from the N solutions that are lowest in energy for the stationary state.

The effective potentials are the result of the externally applied potentials supplemented by internal contributions of the density and current density. These internal contributions comprise the classical potentials due the density and current density, in addition to contributions that account for the exchange and correlation effects. These exchange-correlation contributions are universal functionals of the density and current density. Like in the original Kohn-Sham scheme, these effective potentials have to be obtained self-consistently.

As we argued above, we choose to work in the microscopic Coulomb gauge, also for the effective potentials. We then have to split the exchange-correlation contributions into microscopic and macroscopic components. We will assume that the microscopic component of the exchange-correlation scalar potential is a functional of the periodic density alone, so that the effective microscopic scalar potential takes the following form:

$$v_{eff}(\mathbf{r}, t) = v_{mic}(\mathbf{r}, t) + v_{xc,mic}[\rho](\mathbf{r}, t). \quad (4.19)$$

For the microscopic xc potential we will use the same functional dependence on the periodic density as in the ground state calculation, which is known as the adiabatic approximation. Again we will neglect any microscopic component of the effective vector potential. Moreover, all macroscopic components of the exchange-correlation contribution, which could give rise to a macroscopic exchange-correlation electric field,

$$\mathbf{E}_{xc,mac}(\mathbf{r}, t) = -\frac{1}{c}\frac{\partial}{\partial t}\mathbf{A}_{xc,mac}(\mathbf{r}, t) + \nabla v_{xc,mac}(\mathbf{r}, t), \quad (4.20)$$

will not be taken into account in the sequel. The effective vector potential becomes entirely defined by the macroscopic electric field via Eq. (4.15),

$$\mathbf{A}_{eff}(\mathbf{r}, t) = \mathbf{A}'(\mathbf{r}, t) = -c \int^t \mathbf{E}_{mac}(\mathbf{r}, t') dt'. \quad (4.21)$$

With both effective potentials $v_{eff}(\mathbf{r}, t)$ and $\mathbf{A}_{eff}(\mathbf{r}, t)$ now properly defined, this completes the time-dependent self-consistency scheme.

For the calculation of linear response properties we only need to treat the time-dependent components of the density, current density, and potentials as first-order perturbations. First we obtain the ground-state density $\rho_0(\mathbf{r})$ and the ground state effective scalar potential $v_{eff,0}(\mathbf{r})$ of this generalized Kohn-Sham problem. In the absence of any time-dependent macroscopic field this is an ordinary ground-state calculation. We then define the perturbation of the ground-state density by $\delta\rho(\mathbf{r}, t) = \rho(\mathbf{r}, t) - \rho_0(\mathbf{r})$. The change in the effective scalar potential $\delta v_{eff}(\mathbf{r}, t) = v_{eff}(\mathbf{r}, t) - v_{eff,0}(\mathbf{r})$ comprises two contributions,

$$\delta v_{eff}(\mathbf{r}, t) = \delta v_{mic}(\mathbf{r}, t) + \delta v_{xc}[\rho](\mathbf{r}, t). \quad (4.22)$$

The classical part of this potential, i.e., the induced microscopic scalar potential $\delta v_{mic}(\mathbf{r}, t)$, follows directly from Eq. (4.11). The first-order correction to the exchange-correlation potential, $\delta v_{xc}[\rho](\mathbf{r}, t)$, is formally defined using the (universal) exchange-correlation kernel $f_{xc}(\mathbf{r}, t; \mathbf{r}', t')$,

$$\delta v_{xc}[\rho](\mathbf{r}, t) = \int^t \int f_{xc}[\rho_0](\mathbf{r}, t; \mathbf{r}', t') \delta\rho(\mathbf{r}', t') d\mathbf{r}' dt'. \quad (4.23)$$

This kernel is the functional derivative of the time-dependent $v_{xc}[\rho](\mathbf{r}, t)$ with respect to the time-dependent density $\rho(\mathbf{r}', t')$. In this article we apply the adiabatic local-density approximation (ALDA) for the exchange-correlation kernel,

$$\begin{aligned} f_{xc}^{ALDA}[\rho_0](\mathbf{r}, \mathbf{r}', t - t') &= \delta(t - t') \frac{\partial v_{xc}^{LDA}[\rho_0](\mathbf{r})}{\partial \rho_0(\mathbf{r}')} \\ &= \delta(t - t') \delta(\mathbf{r} - \mathbf{r}') \left. \frac{d^2 (\rho \epsilon_{xc}^{hom}(\rho))}{d\rho^2} \right|_{\rho=\rho_0(\mathbf{r})}, \end{aligned} \quad (4.24)$$

where the exchange-correlation energy density $\epsilon_{xc}^{hom}(\rho)$ of the homogeneous electron gas is modeled using the Vosko-Wilk-Nussair [41] parameterization.

The induced density has to be obtained self-consistently. We do this in an iterative way, in which the macroscopic field $\mathbf{E}_{mac}(t)$ is kept fixed while the induced effective potential $\delta v_{eff}(\mathbf{r}, t)$ is updated in each cycle using the perturbed density of the previous cycle. This procedure is repeated until it converged sufficiently.

The perturbation of the ground state which is due to the presence of the fixed uniform electric field and the induced scalar potential is governed by the perturbation Hamiltonian $\delta \hat{h}_{eff}$, which is given by

$$\delta \hat{h}_{eff}(\mathbf{E}_{mac}, \mathbf{r}, t) = - \int^t \hat{\mathbf{j}} \cdot \mathbf{E}_{mac}(t') dt' + \delta v_{eff}(\mathbf{r}, t). \quad (4.25)$$

Here only terms linear in the field have been retained. This perturbation is no longer a simple multiplicative operator like in ordinary TDDFT, since the macroscopic field couples to the (paramagnetic) current operator. This operator is defined as $\hat{\mathbf{j}} = -i(\nabla - \nabla^\dagger)/2$, where the dagger indicates that terms to the left have to be differentiated. It is more convenient to go to the frequency domain to obtain an expression for the perturbed density. Using linear response theory, we get the induced density in first order,

$$\delta\rho(\mathbf{r}, \omega) = \int \left(\frac{i}{\omega} \chi_{\rho\mathbf{j}}(\mathbf{r}, \mathbf{r}', \omega) \cdot \mathbf{E}_{mac}(\omega) + \chi_{\rho\rho}(\mathbf{r}, \mathbf{r}', \omega) \delta v_{eff}(\mathbf{r}', \omega) \right) d\mathbf{r}', \quad (4.26)$$

where the Kohn-Sham response functions $\chi_{\rho\rho}, \chi_{\rho\mathbf{j}}(\mathbf{r}, \mathbf{r}', \omega)$ are properties of the ground state. For periodic systems the ground-state solutions are characterized by Bloch functions $\psi_{n\mathbf{k}}$ having energies $\epsilon_{n\mathbf{k}}$. They are counted by their integer band index n and continuous Bloch vector \mathbf{k} which is restricted to the first Brillouin zone V_{BZ} . The various response kernels $\chi_{ab}(\mathbf{r}, \mathbf{r}', \omega)$ can be obtained from the following expression:

$$\chi_{ab}(\mathbf{r}, \mathbf{r}', \omega) = \frac{1}{V_{BZ}} \sum_{n, n'} \int_{V_{BZ}} (f_{n\mathbf{k}} - f_{n'\mathbf{k}}) \frac{(\psi_{n\mathbf{k}}^*(\mathbf{r}) \hat{a} \psi_{n'\mathbf{k}}(\mathbf{r})) (\psi_{n'\mathbf{k}}^*(\mathbf{r}') \hat{b} \psi_{n\mathbf{k}}(\mathbf{r}'))}{\epsilon_{n\mathbf{k}} - \epsilon_{n'\mathbf{k}} + \omega + i\eta} d\mathbf{k}, \quad (4.27)$$

by substituting either $\hat{\rho} = 1$ or $\hat{\mathbf{j}} = -i(\nabla - \nabla^\dagger)/2$ for the operators \hat{a} and \hat{b} . Here $f_{n\mathbf{k}}$ are the occupation numbers of the Bloch functions in the ground-state configuration. The positive infinitesimal η results from the adiabatic onset of the perturbation. Note that, since the perturbations are all lattice periodic, we only have to include those contributions in the response kernel that conserve the Bloch vector \mathbf{k} .

The induced current density can be obtained as soon as self-consistency is established. Correct up to first order we obtain an expression similar to Eq. (9.15),

$$\delta\mathbf{j}(\mathbf{r}, \omega) = \int \left(\frac{i}{\omega} (\chi_{\mathbf{j}\mathbf{j}}(\mathbf{r}, \mathbf{r}', \omega) + \rho_0(\mathbf{r})\delta(\mathbf{r} - \mathbf{r}')) \cdot \mathbf{E}_{mac}(\omega) + \chi_{\mathbf{j}\rho}(\mathbf{r}, \mathbf{r}', \omega) \delta v_{eff}(\mathbf{r}', \omega) \right) d\mathbf{r}', \quad (4.28)$$

where it is important to note that the macroscopic field also contributes in first order via the diamagnetic contribution to the current, $\mathbf{j}_d(\mathbf{r}, \omega) = i\rho_0(\mathbf{r})\mathbf{E}_{mac}(\omega)/\omega$. This contribution can be related to the static Kohn-Sham current-current response function, $\chi_{\mathbf{j}\mathbf{j}}(\mathbf{r}, \mathbf{r}', 0)$ using the conductivity sum rule

$$[\chi_{\mathbf{j}\mathbf{j}}(\mathbf{r}, \mathbf{r}', 0)]_{ij} + \rho_0(\mathbf{r})\delta_{ij}\delta(\mathbf{r} - \mathbf{r}') = 0. \quad (4.29)$$

Note also that

$$\chi_{\mathbf{j}\rho}(\mathbf{r}, \mathbf{r}', 0) = \mathbf{0}. \quad (4.30)$$

The induced current density is lattice-periodic, so that the macroscopic polarization is uniform and can be obtained from either Eq. (4.2) or (4.3) in their fourier representations,

$$\mathbf{P}_{mac}(\omega) = \chi_e(\omega) \cdot \mathbf{E}_{mac}(\omega) = \frac{i}{V\omega} \int_V \delta\mathbf{j}(\mathbf{r}, \omega) d\mathbf{r}. \quad (4.31)$$

During the SCF cycles we can set the macroscopic field to $\mathbf{E}_{mac}(\omega) = -i\omega \mathbf{e}_j$, i.e., to a field linear in ω and directed along a unit vector \mathbf{e}_j and thus avoid the singularities at $\omega = 0$ in Eq. (9.15) and Eq. (4.28). Note that $\mathbf{E}_{mac}(\omega) = \mathbf{E}_{mac}^*(-\omega)$, so that this choice represents a real-valued electric field. This particular choice is equivalent to choosing a frequency-independent value for the vector potential, $\mathbf{A}'(\omega) = \mathbf{e}_j$. The diamagnetic contribution to the total induced current density of Eq. (4.28) then becomes frequency-independent, and, by using the special values for the static Kohn-Sham response functions of Eq. (4.29) and (4.30), we obtain

$$\delta\mathbf{j}(\mathbf{r}, \omega) = \delta\mathbf{j}_p(\mathbf{r}, \omega) + \delta\mathbf{j}_d(\mathbf{r}, \omega) = \delta\mathbf{j}_p(\mathbf{r}, \omega) + \delta\mathbf{j}_d(\mathbf{r}, 0) = \delta\mathbf{j}_p(\mathbf{r}, \omega) - \delta\mathbf{j}_p(\mathbf{r}, 0). \quad (4.32)$$

The Cartesian components of the susceptibility then follow from Eq. (4.31)

$$[\chi_e(\omega)]_{ij} = \left\{ -\frac{1}{V\omega^2} \int_V [\delta\mathbf{j}_p(\mathbf{r}, \omega) - \delta\mathbf{j}_p(\mathbf{r}, 0)]_i d\mathbf{r} \right\} \Big|_{\mathbf{E}_{mac}(\omega) = -i\omega \mathbf{e}_j}. \quad (4.33)$$

There is a definite numerical advantage in rewriting the expression in this way. The diamagnetic and paramagnetic parts are treated on equal footing, hence a proper behaviour for the static limit $\omega \rightarrow 0$ is established.

4.4 Implementation

In this section we describe the main aspects of the implementation of the previously outlined method for TDDFT in crystalline systems. We will first discuss the role of symmetry in reducing the amount of computational effort. This has some important implications for the way the response calculations have been implemented.

The set of inhomogeneous linear transformations $\{\hat{\alpha}|\mathbf{t}_\alpha\}\mathbf{r} = \alpha \cdot \mathbf{r} + \mathbf{t}_\alpha$ that leave the crystal invariant constitutes the space group \mathcal{G} of the crystal. Here α is a 3×3 rotation matrix, and \mathbf{t}_α a translation vector. The rotation parts $\hat{\alpha}$ separately form a finite group of order n_G , which is referred to as the point group G of the crystal. For clarity we will not consider the consequences of time-reversal symmetry here, and we will limit the discussion to the space-group elements only.

For a given macroscopic perturbing field $\mathbf{E}(\omega)$ of frequency ω we get an induced density at position \mathbf{r} given by $\delta\rho(\mathbf{E}, \mathbf{r}, \omega)$. Here we have included the field as a parameter for notational convenience. Due to linearity we can treat the response to the Cartesian components of the field separately, and we get

$$\delta\rho(\mathbf{E}, \mathbf{r}, \omega) = \delta\rho\left(\sum_i E_i \mathbf{e}_i, \mathbf{r}, \omega\right) = \sum_i E_i \delta\rho(\mathbf{e}_i, \mathbf{r}, \omega). \quad (4.34)$$

The \mathbf{e}_i are unit vectors in each of the three Cartesian directions. We can now define a vector field $\delta\boldsymbol{\rho}(\mathbf{r}, \omega)$ by specifying its i^{th} Cartesian component as the response to an electric field $\mathbf{E}(\omega) = -i\omega \mathbf{e}_i$, in the following way

$$\delta\boldsymbol{\rho}(\mathbf{r}, \omega) = \sum_i \delta\rho(-i\omega \mathbf{e}_i, \mathbf{r}, \omega) \mathbf{e}_i. \quad (4.35)$$

For arbitrary given field $\mathbf{E}(\omega)$ the induced density then follows from Eq. (4.34)

$$\delta\rho(\mathbf{E}, \mathbf{r}, \omega) = \frac{i}{\omega} \delta\boldsymbol{\rho}(\mathbf{r}, \omega) \cdot \mathbf{E}(\omega). \quad (4.36)$$

Under the application of a general rotation-translation $\{\hat{\alpha}|\mathbf{t}_\alpha\}$ this vector field transforms by definition as

$$\{\hat{\alpha}|\mathbf{t}_\alpha\} \delta\boldsymbol{\rho}(\mathbf{r}, \omega) = \alpha \cdot \delta\boldsymbol{\rho}(\{\hat{\alpha}|\mathbf{t}_\alpha\}^{-1}\mathbf{r}, \omega). \quad (4.37)$$

By subsequently substituting the definition of $\delta\boldsymbol{\rho}(\mathbf{r}, \omega)$ of Eq. (4.35) and by applying the linearity property of Eq. (4.34) we obtain

$$\begin{aligned} \{\hat{\alpha}|\mathbf{t}_\alpha\} \delta\boldsymbol{\rho}(\mathbf{r}, \omega) &= \sum_{ij} \alpha_{ji} \delta\rho(-i\omega \mathbf{e}_i, \{\hat{\alpha}|\mathbf{t}_\alpha\}^{-1}\mathbf{r}, \omega) \mathbf{e}_j \\ &= \sum_j \delta\rho(-i\omega \sum_i \alpha_{ji} \mathbf{e}_i, \{\hat{\alpha}|\mathbf{t}_\alpha\}^{-1}\mathbf{r}, \omega) \mathbf{e}_j \\ &= \sum_j \delta\rho(-i\omega \alpha^{-1} \cdot \mathbf{e}_j, \{\hat{\alpha}|\mathbf{t}_\alpha\}^{-1}\mathbf{r}, \omega) \mathbf{e}_j. \end{aligned} \quad (4.38)$$

If $\{\hat{\alpha}|\mathbf{t}_\alpha\}$ is a symmetry operation of the crystal, then a rotated electric field $\alpha^{-1} \cdot \mathbf{e}_j$ gives the same response at the rotated point $\{\hat{\alpha}|\mathbf{t}_\alpha\}^{-1}\mathbf{r}$ as the original field \mathbf{e}_j did at the original point \mathbf{r} . Hence we have

$$\begin{aligned} \{\hat{\alpha}|\mathbf{t}_\alpha\} \delta\boldsymbol{\rho}(\mathbf{r}, \omega) &= \sum_j \delta\rho(-i\omega \alpha^{-1} \cdot \mathbf{e}_j, \{\hat{\alpha}|\mathbf{t}_\alpha\}^{-1}\mathbf{r}, \omega) \mathbf{e}_j \\ &= \sum_j \delta\rho(-i\omega \mathbf{e}_j, \mathbf{r}, \omega) \mathbf{e}_j \\ &= \delta\boldsymbol{\rho}(\mathbf{r}, \omega), \end{aligned} \quad (4.39)$$

which proves that $\delta\boldsymbol{\rho}(\mathbf{r}, \omega)$ transforms as a fully symmetric vector field under the operations of the crystal space group.

A similar analysis holds for the induced effective potential $\delta v_{eff}(\mathbf{E}, \mathbf{r}, \omega)$, and we can introduce the vector field $\delta\mathbf{v}_{eff}(\mathbf{r}, \omega)$ accordingly, by an equation similar to Eq. (4.35),

$$\delta\mathbf{v}_{eff}(\mathbf{r}, \omega) = \sum_i \delta v_{eff}(-i\omega \mathbf{e}_i, \mathbf{r}, \omega) \mathbf{e}_i, \quad (4.40)$$

such that we have

$$\delta v_{eff}(\mathbf{E}, \mathbf{r}, \omega) = \frac{i}{\omega} \delta\mathbf{v}_{eff}(\mathbf{r}, \omega) \cdot \mathbf{E}(\omega). \quad (4.41)$$

Note that, due to the totally-symmetric vector transformation property, we will have to evaluate these induced vector fields only for the irreducible wedge of the Wigner-Seitz cell. We can now inspect that our formulas for the induced density indeed reflect these symmetry properties. By inserting the expression for the Kohn-Sham response kernels from Eq. (4.27) into the expression for the induced density from Eq. (9.15), we obtain

$$\delta\rho(\mathbf{E}, \mathbf{r}, \omega) = \frac{1}{V_{BZ}} \sum_{n,n'} \int_{BZ} \psi_{n\mathbf{k}}^*(\mathbf{r}) \psi_{n'\mathbf{k}}(\mathbf{r}) \frac{(f_{n\mathbf{k}} - f_{n'\mathbf{k}}) M_{n'n\mathbf{k}}(\mathbf{E}, \omega)}{(\epsilon_{n\mathbf{k}} - \epsilon_{n'\mathbf{k}}) + \omega + i\eta} d\mathbf{k}, \quad (4.42)$$

where the matrix elements $M_{n'\mathbf{k}}$ are defined by

$$M_{n'\mathbf{k}}(\mathbf{E}, \omega) = \int \psi_{n'\mathbf{k}}^*(\mathbf{r}') \left(\frac{i}{\omega} \hat{\mathbf{j}} \cdot \mathbf{E}(\omega) + \delta v_{eff}(\mathbf{r}', \omega) \right) \psi_{n\mathbf{k}}(\mathbf{r}') d\mathbf{r}'. \quad (4.43)$$

It immediately becomes clear that we do not have to evaluate and store the Kohn-Sham response kernels explicitly. Instead, we can obtain the induced density directly for any given perturbation, by evaluating these matrix elements separately.

The transformation properties of the Bloch functions enable us to limit the integration to the irreducible wedge of the Brillouin zone only. Since we do not consider the consequences of time-reversal symmetry here, the irreducible part is taken with respect to the crystal point group only. In a general \mathbf{k} -point we have the following transformation relation for any element $\{\hat{\alpha}|\mathbf{t}_\alpha\}$ of the space group:

$$\psi_{n\alpha\cdot\mathbf{k}}(\mathbf{r}) = \exp(i\phi_{n\mathbf{k}}(\{\hat{\alpha}|\mathbf{t}_\alpha\})) \psi_{n\mathbf{k}}(\{\hat{\alpha}|\mathbf{t}_\alpha\}^{-1}\mathbf{r}). \quad (4.44)$$

Here $\phi_{n\mathbf{k}}(\{\hat{\alpha}|\mathbf{t}_\alpha\})$ is a real-valued function of \mathbf{k} which depends on the particular band index and operator. Since $\psi_{n\mathbf{k}}(\mathbf{r})$ always occurs in Eq. (4.42) in combination with its complex conjugate via $M_{n'\mathbf{k}}(\mathbf{E}, \omega)$, this phase factor is irrelevant for our calculations. The occupation numbers $f_{n\mathbf{k}}$ are obtained in the ground-state configuration and are therefore functions of just the Kohn-Sham energy $\epsilon_{n\mathbf{k}}$. Since the energy transforms as $\epsilon_{n\alpha\cdot\mathbf{k}} = \epsilon_{n\mathbf{k}}$, we also have $f_{n\alpha\cdot\mathbf{k}} = f_{n\mathbf{k}}$. Hence both $f_{n\mathbf{k}}$ and $\epsilon_{n\mathbf{k}}$ are fully symmetric under the operations of the point group.

We can split the summation over the band indices n, n' into two parts, which involve only combinations of occupied with virtual states. Furthermore, we split the integration domain into equivalent wedges, which are related through the n_G operators $\hat{\alpha}$ of the point group. We obtain

$$\delta\rho(\mathbf{E}, \mathbf{r}, \omega) = \frac{1}{n_G V_{IBZ}} \sum_{\hat{\alpha} \in G} \sum_i^{occ} \sum_a^{virt} \int_{IBZ} \psi_{i\alpha\cdot\mathbf{k}}^*(\mathbf{r}) \psi_{a\alpha\cdot\mathbf{k}}(\mathbf{r}) \frac{(f_{i\mathbf{k}} - f_{a\mathbf{k}}) M_{ai\alpha\cdot\mathbf{k}}(\mathbf{E}, \omega)}{(\epsilon_{i\mathbf{k}} - \epsilon_{a\mathbf{k}}) + \omega + i\eta} d\mathbf{k} + c.c.(-\omega). \quad (4.45)$$

The second part is the complex conjugate of the first part in which we have to replace ω by $-\omega$. This simple relation between the two parts is due to the fact that both $\mathbf{E}(t)$ and $v_{eff}(\mathbf{r}, t)$ have to be real-valued, such that $M_{i\mathbf{k}}(\mathbf{E}, \omega) = M_{ai\mathbf{k}}^*(\mathbf{E}^*, -\omega)$. Using the transformation rules of Eq. (4.44) for the wave functions $\psi_{n\alpha\cdot\mathbf{k}}(\mathbf{r})$, we can interchange the action of the symmetry operators between the reciprocal and real space. For the matrix elements we then get the following result:

$$M_{ai\alpha\cdot\mathbf{k}}(\mathbf{E}, \omega) = \int \psi_{a\mathbf{k}}^*(\{\hat{\alpha}|\mathbf{t}_\alpha\}^{-1}\mathbf{r}') \left(\frac{i}{\omega} \hat{\mathbf{j}} \cdot \mathbf{E}(\omega) + \delta v_{eff}(\mathbf{r}', \omega) \right) \psi_{i\mathbf{k}}(\{\hat{\alpha}|\mathbf{t}_\alpha\}^{-1}\mathbf{r}') d\mathbf{r}', \quad (4.46)$$

where we have dropped the phase factor of the transformation rule, as was argued above. By substituting $\mathbf{r}'' = \{\hat{\alpha}|\mathbf{t}_\alpha\}^{-1}\mathbf{r}'$ and by making use of the vector transformation properties of both the current operator $\hat{\mathbf{j}}$ and the potential vector $\delta\mathbf{v}_{eff}(\mathbf{r}', \omega)$ we obtain

$$M_{ai\alpha\cdot\mathbf{k}}(\mathbf{E}, \omega) = \frac{i}{\omega} (\alpha \cdot \mathbf{M}_{ai\mathbf{k}}(\omega)) \cdot \mathbf{E}(\omega), \quad (4.47)$$

with the vector $\mathbf{M}_{aik}(\omega)$ being given by

$$\mathbf{M}_{aik}(\omega) = \int \psi_{ak}^*(\mathbf{r}'') \left(\hat{\mathbf{j}} + \delta \mathbf{v}_{eff}(\mathbf{r}'', \omega) \right) \psi_{ik}(\mathbf{r}'') d\mathbf{r}''. \quad (4.48)$$

Substituting this result in Eq. (4.45) and applying again the transformation rule Eq. (4.44) yields the final result for the induced density. This density is fully specified by the vector density $\delta \boldsymbol{\rho}(\mathbf{r}, \omega)$, which can be obtained as the totally-symmetric component of the auxiliary vector field $\delta \tilde{\boldsymbol{\rho}}(\mathbf{r}, \omega)$ following

$$\delta \boldsymbol{\rho}(\mathbf{r}, \omega) = \frac{1}{n_G} \sum_{\hat{\alpha} \in G} \{ \hat{\alpha} | \mathbf{t}_\alpha \} \delta \tilde{\boldsymbol{\rho}}(\mathbf{r}, \omega) + c.c.(-\omega), \quad (4.49)$$

where we have defined $\delta \tilde{\boldsymbol{\rho}}(\mathbf{r}, \omega)$ as

$$\delta \tilde{\boldsymbol{\rho}}(\mathbf{r}, \omega) = \frac{1}{V_{IBZ}} \sum_i^{occ} \sum_a^{virt} \int_{IBZ} \psi_{ik}^*(\mathbf{r}) \psi_{ak}(\mathbf{r}) \frac{(f_{ik} - f_{ak}) \mathbf{M}_{aik}(\omega)}{(\epsilon_{ik} - \epsilon_{ak}) + \omega + i\eta} d\mathbf{k}. \quad (4.50)$$

The integrations over the irreducible wedge of the Brillouin zone are evaluated numerically, by including the energy denominator into the integration weights of the quadrature

$$\frac{1}{V_{IBZ}} \int_{IBZ} \frac{(f_{ik} - f_{ak})}{(\epsilon_{ik} - \epsilon_{ak}) + \omega + i\eta} g(\mathbf{k}) d\mathbf{k} = \sum_{\mathbf{k}_j} w_{iak_j}(\omega) g(\mathbf{k}_j). \quad (4.51)$$

This way, the singular denominator can be handled analytically. The way these weights are obtained is the subject of Chapter 4.8 Appendix B.

The induced density can now be used to evaluate the exchange-correlation potential using Eq. (4.23), which reduces in the ALDA approximation to the following simple relation:

$$\delta \mathbf{v}_{xc}(\mathbf{r}, \omega) = f_{xc}^{ALDA}[\rho_0](\mathbf{r}) \delta \boldsymbol{\rho}(\mathbf{r}, \omega). \quad (4.52)$$

The evaluation of the screened Coulomb potential becomes tractable by using auxiliary fitfunctions in a procedure similar to the one which was used in the ground-state calculation [37]. These fitfunctions have to be constructed in such a way that they reflect the symmetry transformation properties of the induced density. We therefore construct a set of real-valued vector functions $\{\mathbf{f}_i\}$, which transform as totally-symmetric vector fields

$$\mathbf{f}_i(\mathbf{r}) = \{ \hat{\alpha} | \mathbf{t}_\alpha \} \mathbf{f}_i(\mathbf{r}) = \alpha \cdot \mathbf{f}_i(\{ \hat{\alpha} | \mathbf{t}_\alpha \}^{-1} \mathbf{r}), \quad (4.53)$$

and for which the screened Coulomb integrals can be evaluated analytically. Thus we obtain for each function $\mathbf{f}_i(\mathbf{r})$ a potential function $\mathbf{g}_i(\mathbf{r})$ using Eq. (4.11),

$$\mathbf{g}_i(\mathbf{r}) = \lim_{c \rightarrow \infty} \sum_j h_c(|\mathbf{r} - \mathbf{R}_j|) \int_{V_j} \frac{\mathbf{f}_i(\mathbf{r}')}{|\mathbf{r} - \mathbf{r}'|} d\mathbf{r}'. \quad (4.54)$$

The first-order density change $\delta \boldsymbol{\rho}(\mathbf{r}, \omega)$ can then be represented on this basis of vector functions, using frequency dependent coefficients $c_i(\omega)$

$$\delta \boldsymbol{\rho}(\mathbf{r}, \omega) = \sum_i c_i(\omega) \mathbf{f}_i(\mathbf{r}). \quad (4.55)$$

The coefficients $c_i(\omega)$ are fitted under the constraint that the net charge vanishes, which can be achieved automatically if none of the fitfunctions contains charge. This constraint is necessary to ensure that the microscopic potential actually exists. We obtain

$$\delta\mathbf{v}_{eff}(\mathbf{r}, \omega) = \sum_i c_i(\omega) \mathbf{g}_i(\mathbf{r}) + \delta\mathbf{v}_{xc}(\mathbf{r}, \omega). \quad (4.56)$$

The way in which these fitfunctions can be constructed and the implementation of the constraint are the subject of Chapter 4.9 Appendix C.

The self-consistent field scheme is now complete. Given a start-up value for the induced effective potential [e.g., $\delta\mathbf{v}_{eff}(\mathbf{r}, \omega) = \mathbf{0}$ for the uncoupled case], we can obtain the matrix elements for the perturbation from Eq. (4.48), and, with them, the induced density from Eq. (4.50) and Eq. (4.49). Using the fitting procedure, we obtain the new Coulomb contribution to the effective potential, and, from the density itself, the exchange-correlation contribution Eq. (4.52) and Eq. (4.56). This completes the first cycle of the SCF scheme, and we iterate until convergence is reached. As convergence criterion we use the maximum change in the fitting coefficients for subsequent cycles, which must become negligible in order to reach convergence. The efficiency of this SCF procedure is increased by using the DIIS method (direct inversion of the iterative space) of Pulay [42]. The efficiency can be improved even further by using the converged result of a nearby frequency as start-up value for the calculation at the frequency at hand. Typically, convergence is reached in a few cycles.

With the converged results for the induced density and potential we can use the matrix elements of the SCF perturbation of Eq. (4.48) again to obtain the induced current density. We will only need to consider the paramagnetic part for the evaluation of the susceptibility. Similar to the definitions of the totally-symmetric density vector and potential vector, we define a tensor $\delta\mathcal{J}_p(\mathbf{r}, \omega)$, by

$$\delta\mathcal{J}_p(\mathbf{r}, \omega) = \sum_i \delta\mathbf{j}_p(-i\omega \mathbf{e}_i, \mathbf{r}, \omega) \otimes \mathbf{e}_i, \quad (4.57)$$

so that we can obtain the induced paramagnetic current density from

$$\delta\mathbf{j}_p(\mathbf{E}, \mathbf{r}, \omega) = \frac{i}{\omega} \delta\mathcal{J}_p(\mathbf{r}, \omega) \cdot \mathbf{E}(\omega). \quad (4.58)$$

In an analogous way as was proven for vector quantities, one easily verifies that this tensor transforms as a totally-symmetric tensor field,

$$\delta\mathcal{J}_p(\mathbf{r}, \omega) = \{\hat{\alpha}|\mathbf{t}_\alpha\} \delta\mathcal{J}_p(\mathbf{r}, \omega) = \alpha \cdot \delta\mathcal{J}_p(\{\hat{\alpha}|\mathbf{t}_\alpha\}^{-1}\mathbf{r}, \omega) \cdot \alpha^{-1}. \quad (4.59)$$

The paramagnetic current density is obtained as the totally-symmetric part of the auxiliary tensor function $\delta\tilde{\mathcal{J}}_p(\mathbf{r}, \omega)$, via

$$\delta\mathcal{J}_p(\mathbf{r}, \omega) = \frac{1}{n_G} \sum_{\hat{\alpha} \in G} \{\hat{\alpha}|\mathbf{t}_\alpha\} \delta\tilde{\mathcal{J}}_p(\mathbf{r}, \omega) + c.c.(-\omega), \quad (4.60)$$

in which we have defined $\delta\tilde{\mathcal{J}}_p(\mathbf{r}, \omega)$ as

$$\delta\tilde{\mathcal{J}}_p(\mathbf{r}, \omega) = \frac{-i}{2V_{IBZ}} \sum_i^{occ} \sum_a^{virt} \int_{IBZ} (\psi_{i\mathbf{k}}^*(\mathbf{r}) \nabla \psi_{a\mathbf{k}}(\mathbf{r}) - \nabla \psi_{i\mathbf{k}}^*(\mathbf{r}) \psi_{a\mathbf{k}}(\mathbf{r})) \frac{(f_{i\mathbf{k}} - f_{a\mathbf{k}}) \mathbf{M}_{ai\mathbf{k}}(\omega)}{(\epsilon_{i\mathbf{k}} - \epsilon_{a\mathbf{k}}) + \omega + i\eta} d\mathbf{k}. \quad (4.61)$$

The susceptibility then follows from Eq. (4.33) as

$$\chi_e(\omega) = \frac{-1}{\omega^2 V} \int_V (\delta\mathcal{J}_p(\mathbf{r}, \omega) - \delta\mathcal{J}_p(\mathbf{r}, 0)) d\mathbf{r}. \quad (4.62)$$

4.5 Results and Discussion

We have performed some calculations to test this method for calculating the dielectric properties of crystals. Therefore, we obtained the static and frequency-dependent dielectric function for the isotropic crystals of diamond (C), silicon (Si), and gallium arsenide (GaAs). The first two have the diamond, and the third the zinc-blend lattice type. All calculations were performed within the ADF-BAND (Refs. [37, 38]) program. We made use of frozen cores and a hybrid valence basis set consisting of the numerical solutions of a free-atom Herman-Skillman (HS) program [43], in combination with Slater-type one-center functions (STO). The spatial resolution of this basis is equivalent to a triple-zeta STO basis that is augmented with two polarization functions. This valence basis was orthogonalized to the core states. The free-atom effective potential was provided by the same HS program. For the evaluation of the Coulomb integrals we used a single auxiliary basis of STO functions to represent the deformation density in the ground-state calculation and the induced density in the response calculation.

All matrix elements were evaluated numerically using an efficient and accurate quadrature scheme [37, 44]. The numerical integration scheme for the \mathbf{k} -space integrals was varied and used from 5 to 175 symmetry-unique sample points in the irreducible wedge of the Brillouin zone. All results shown here were obtained using the Vosko-Wilk-Nusair parametrization of the LDA exchange-correlation potential, which was also used to derive the ALDA exchange-correlation kernel.

First we obtained the static value for the dielectric function for diamond, and we investigated the convergence behavior as a function of the \mathbf{k} -space sampling. In Fig. 4.2 we show the results for diamond in the low-frequency range, which were obtained using various \mathbf{k} -space sampling densities, together with the experimental data as obtained from Ref. [45]. The highest sampling density with 175 points gave identical results as the calculation using 111 points. This graph clearly shows that the results depend strongly on the accuracy of the numerical integration in \mathbf{k} -space. Whereas in general most methods typically yield an overestimation for the static value of about 10%, we find for diamond an underestimation of about 5% for our most accurate result. In Table 4.1 we summarize our results for the static values for C, Si, and GaAs, which were obtained using the \mathbf{k} -space sampling of 111 points, and we compare them with other theoretical and experimental values. Our results are in good agreement with the experimental data, and are comparable to other calculations.

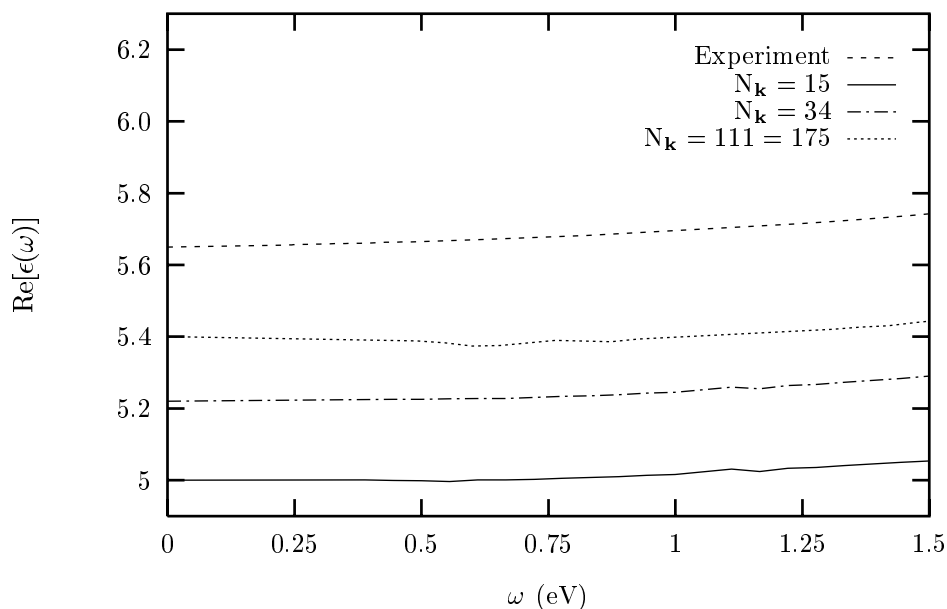


Figure 4.2: The dielectric function for diamond in the low frequency range, obtained for various \mathbf{k} -space samplings. The experimental data is taken from [46].

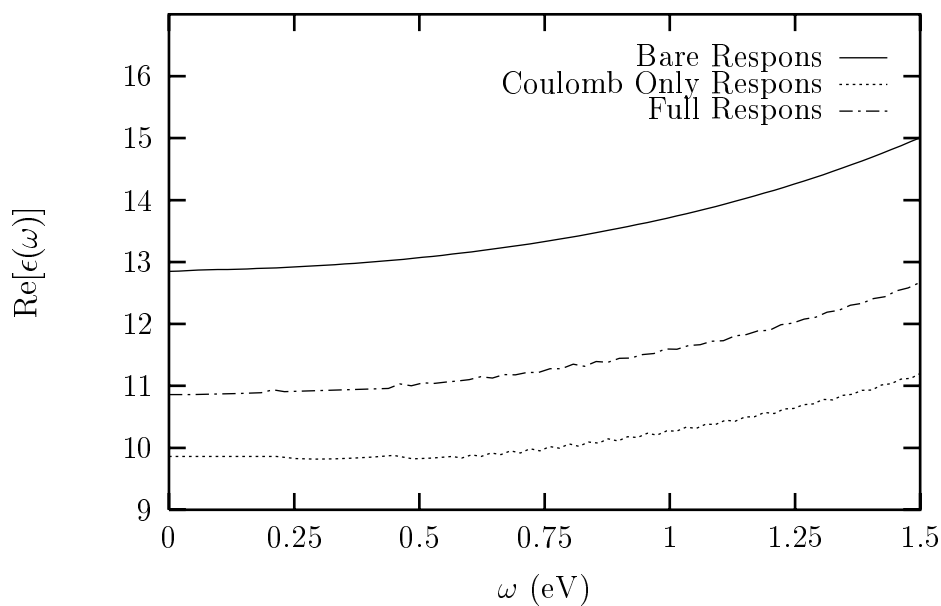


Figure 4.3: The various contributions to the dielectric function of Si in the low-frequency range.

We have also investigated the Coulomb and exchange-correlation contributions to the self-consistent potential. In Fig. 4.3 we plot the results for Si in the low-frequency range, which were obtained using a \mathbf{k} -space sampling of 34 points. The uncoupled result is obtained by setting $\delta\mathbf{v}_{eff}(\mathbf{r},\omega) = \mathbf{0}$, which yields the bare response of the Kohn-Sham system. The coupled results have been obtained with and without inclusion of the exchange-correlation contribution. By including only the Coulomb contribution in the SCF procedure, the static value drops by about 25% relative to the bare response, from 12.9 to 9.9. Similar shifts, though smaller in magnitude, have been obtained in the dielectric matrix methods [15, 16, 24, 35]. Including the exchange-correlation contribution in the coupled response raises the value again, relative to the Coulomb-only value by 10%, to 10.9. We can conclude that both the Coulomb interaction and exchange-correlation effects contribute considerably to the dielectric response, and that they are in the order of about 10%-15%. We find no major qualitative changes in the frequency dependence of the dielectric function, due to the coupling.

In Figs. 4.4 and 4.5 we show the real and imaginary parts of the frequency-dependent dielectric function for the three materials C, Si, and GaAs, and we compare them with the experimental data as obtained from Refs. [45, 46]. All results have been obtained by including the Coulomb interaction and exchange-correlation effects in the SCF procedure. We verified numerically that the real and imaginary parts form Kramers-Kronig pairs. The overall correspondence with experiment is quite good, in particular for the low frequency ranges. The sharp features in the spectra are reasonably well reproduced, and can be attributed to the van Hove-type singularities in the joint-density of states, as obtained from the Kohn-Sham band structure. They appear at energies which are uniformly shifted downwards with respect to the experiments by, respectively, about 1.0, 0.5, and 0.4 eV for C, Si, and GaAs. The calculated absorption edges coincide with the vertical Kohn-Sham energy gap of, respectively, 5.6, 2.6, and 1.0 eV.

4.6 Conclusions

We have successfully applied time-dependent density functional theory to the dielectric response of nonmetallic crystalline systems. We used a perturbation approach to the time-dependent self-consistent field scheme, for which we derived a real-space description. This could only be achieved by combining a self-consistent lattice-periodic scalar potential with a uniform electric field. This field could be identified as the macroscopic electric field. In this description, exchange-correlation contributions and the microscopic Coulomb interactions were included in the self-consistent effective scalar potential. The macroscopic polarization and the electric susceptibility can then be obtained from the induced current density.

This method was implemented in a full-potential LCAO program. The coupled response can then be obtained with an efficiency that can be compared to ordinary DFT ground-state calculations. This high efficiency was achieved by using the space-group symmetry of the crystals, which led to the use of fully symmetric vector functions for the representation of the induced density and the SCF potential. The evaluation of Coulomb integrals was

Table 4.1: Static dielectric constants for diamond (C), silicon (Si), and gallium arsenide (GaAs).

Solid	Experiment	This Work	Other Theory	Method ^{a,b,c,d}
C	5.67 ^e	5.4	5.90 ^f	DM,PP,PW,XC
			5.20-5.86 ^g	DM,PP,PW,QP
			5.5 ^h	DM,PP,LCGO,QP
			4.34 ⁱ	UR,FP,LCAO
			5.7 ^j	UR,EP,LCAO
			12.4-12.9 ^l	DFPT,PP,PW,XC
Si	11.4 ^k	11.6	12.7 ^m	DFPT,PP,PW,XC
			13.6 ⁿ	DFPT,PP,PW,XC
			12.05 ^o	DM,FP,LMTO,QP
			12.7 ^p	DM,PP,PW,XC
			12.9 ^q	DM,PP,PW,XC
			11.2 ^r	DM,PP,PW,QP
			12.8 ^h	DM,PP,LCGO,QP
			9.03 ⁱ	UR,FP,LCAO
			11.7 ^s	UR,PP,LCGO,QP
			12.0 ^j	UR,EP,LCAO
			GaAs	10.8 ^t
10.83 ^o	DM,FP,LMTO,QP			
10.2 ^u	DM,PP,PW,QP			
13.1 ^h	DM,PP,LCGO,QP			
11.21 ⁱ	UR,FP,LCAO			
10.9 ^s	UR,PP,LCGO,QP			
10.9 ^j	UR,EP,LCAO			

^aDFPT: Density Function Perturbation Theory, DM: Dielectric Matrix, UR: Uncoupled Response.

^bFP: Full Potential, PP: Pseudopotential, EP: Empirical Potential.

^cPW: Plane Wave, LMTO: Linearized Muffin-Tin Orbitals, LCAO: Linear Combination of Atomic Orbitals, LCGO: Linear Combination of Gaussian Orbitals.

^dXC: Exchange-Correlation Effects, QP: Quasi-Particle Energy Shift.

^eRef. [49] ^fRef. [35] ^gRef. [26] ^hRef. [50] ⁱRef. [51] ^jRef. [52] ^kRef. [53] ^lRef. [21] ^mRef. [36] ⁿRef. [54]

^oRef. [55] ^pRef. [15] ^qRef. [35] ^rRef. [16] ^sRef. [56] ^tRef. [57] ^uRef. [58]

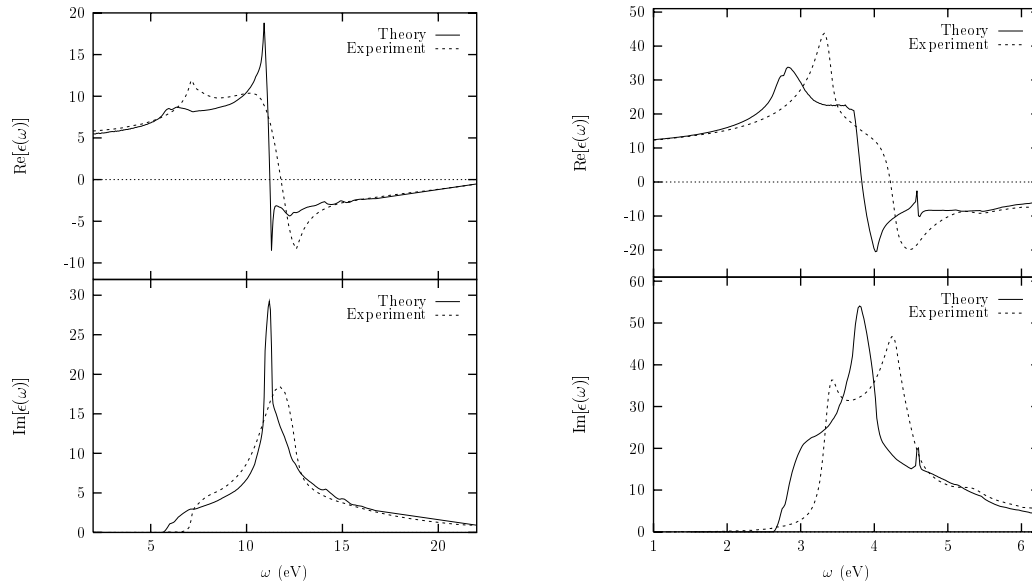


Figure 4.4: Plots of the real and imaginary part of the calculated dielectric function of diamond (C) [left] and silicon (Si) [right] in comparison with the experimental data (Refs. [45] and [46]).

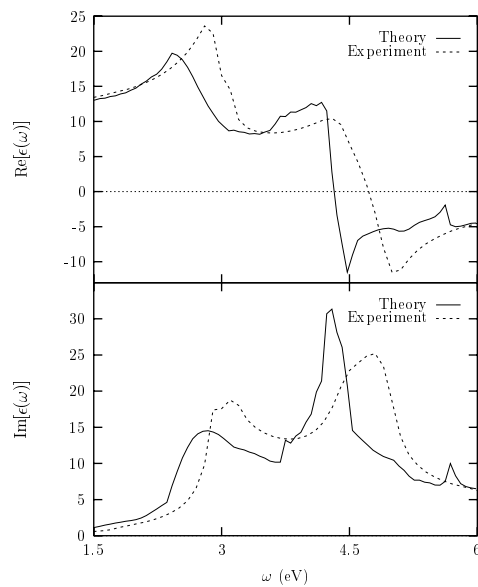


Figure 4.5: Plots of the real and imaginary part of the calculated dielectric function of gallium arsenide (GaAs) in comparison with the experimental data (Ref. [46]).

facilitated by using an auxiliary basis of vector functions to represent the density. This basis was constructed in such a way that the Coulomb integrals could be evaluated analytically. The lattice sums could be evaluated efficiently using a screening technique. The expensive, direct evaluation of the Kohn-Sham response kernels was avoided, and the singular integrals which appear in these kernels could be treated analytically.

We applied this method to obtain the dielectric function for the crystals of C, Si, and GaAs. The results show that Coulomb and exchange-correlation effects each contribute up to about 10%-15% of the coupled response. We obtained the static value and low-frequency range for the dielectric functions in good agreement with experiment. The frequency dependent response reveals that spectral features appear at energies which coincide with the van Hove-type singularities in the bare Kohn-Sham response. The absorption edges can be found at the direct energy gap of the Kohn-Sham ground state band structure. The spectral features seem to be uniformly shifted downwards in energy by several tenths of an electron volt. However, a modification of the Kohn-Sham band structure by rigidly shifting the energies of the virtual states, (the scissors operator) seems not to be justified here. Such a procedure would affect the good agreement for the static value and low frequency range, even though it would correct the positions of the spectral features.

4.7 Appendix A: Screened Potential

An essential part of the screening technique is that the screened contribution of the uniform multipoles to the microscopic potential is uniform, i.e., not depending on the particular coordinate \mathbf{r} at which the potential is evaluated. The screened instantaneous Coulomb potential $\delta v(\mathbf{r}, t)$ of the uniform moments $\delta\mu^{(n)}(t)$ as needed in Eq. (4.11) is given by Eq. (4.7),

$$\delta v(\mathbf{r}, t) = \lim_{c \rightarrow \infty} \sum_i h_c(|\mathbf{r} - \mathbf{R}_i|) \int_{V_i} \sum_{n=0}^2 \frac{1}{n!} \delta\mu_{j_1 \dots j_n}^{(n)}(t) \cdot \frac{\partial^n}{\partial r'_{j_1} \dots \partial r'_{j_n}} \frac{1}{|\mathbf{r} - \mathbf{r}'|} d\mathbf{r}', \quad (4.63)$$

where a summation over all Cartesian components j_1 through j_n of the multipoles of rank n was implied. For notational convenience we will introduce the shorthand notation $\delta\mu^{(n)} \cdot \nabla'^n$ for this contraction. This potential can only be finite if $\delta\mu^{(0)}(t) = 0$, i.e., if the uniform density vanishes identically. In the sequel we will only consider such cases.

As a first step, we will make the scale parameter c of the envelope function $h_c(|\mathbf{r}|)$ explicit. Let us therefore introduce the new scaled relative coordinates $\mathbf{x} = (\mathbf{r} - \mathbf{r}')/c$ and define also a much denser lattice (with an \mathbf{r} -dependent origin) by setting $\mathbf{X}_i = (\mathbf{r} - \mathbf{R}_i)/c$. The integration domains, i.e., the unit cells V_i map under this transformation to the \mathbf{r} -dependent $V_{i,\mathbf{r}}$. These $V_{i,\mathbf{r}}$ are the unit cells of the lattice defined by the \mathbf{X}_i . We will make a particular choice for the shape of the envelope function by setting $h_c(r) = h_1(r/c)$ for all c . For increasing c this envelope then only grows in size, but its shape remains the same. Application of this coordinate substitution yields the following expression

$$\delta v(\mathbf{r}, t) = \lim_{c \rightarrow \infty} \sum_i h_1(|\mathbf{X}_i|) \int_{V_{i,\mathbf{r}}} \left(\sum_{n=1}^2 \frac{(-c)^{2-n}}{n!} \delta\mu^{(n)}(t) \cdot \nabla^n \frac{1}{|\mathbf{x}|} \right) d\mathbf{x}. \quad (4.64)$$

The singularity at $\mathbf{x} = \mathbf{0}$ is integrable for $n \leq 2$. This formula reveals that the contribution of a multipole of rank n to the integrand scales like c^{2-n} . Somewhat hidden, though, is the c -dependence of the integration domain. However, naively replacing the summation and integration in the following way,

$$\lim_{c \rightarrow \infty} \sum_i h_1(|\mathbf{X}_i|) \int_{V_{i,\mathbf{r}}} g(\mathbf{x}) d\mathbf{x} = \int h_1(|\mathbf{x}|) g(\mathbf{x}) d\mathbf{x}, \quad (4.65)$$

can only be justified for finite integrands $g(\mathbf{x})$. We will have to show that the corrugation, which is due to the evaluation of the envelope function at \mathbf{r} -dependent discrete lattice points \mathbf{X}_i on one hand, and to the integration over the \mathbf{r} -dependent domains $V_{i,\mathbf{r}}$ on the other, vanishes in the limit. Let us include the \mathbf{x} -dependent part of the envelope in the integrand by using the following Taylor expansion around $\mathbf{x} \in V_{i,\mathbf{r}}$

$$h_1(|\mathbf{X}_i|) = \sum_{m=0}^{\infty} \frac{1}{m!} (\mathbf{X}_i - \mathbf{x})^m \cdot \nabla^m h_1(|\mathbf{x}|). \quad (4.66)$$

The order of the general term in this Taylor series scales like $\mathcal{O}(|\mathbf{x} - \mathbf{X}_i|^m) = \mathcal{O}(c^{-m})$. Substitution gives

$$\delta v(\mathbf{r}, t) = \lim_{c \rightarrow \infty} \sum_{n=1}^2 \sum_{m=0}^{\infty} \frac{(-c)^{2-n-m}}{n!m!} \left(\sum_i \int_{V_{i,\mathbf{r}}} c^m (\mathbf{x} - \mathbf{X}_i)^m \cdot \nabla^m h_1(|\mathbf{x}|) \times \delta \mu^{(n)}(t) \cdot \nabla^n \frac{1}{|\mathbf{x}|} d\mathbf{x} \right). \quad (4.67)$$

We will now show that the factor between brackets has a finite value for $c \rightarrow \infty$, so that all terms with $n + m > 2$ vanish identically. Since the spacing of the lattice points \mathbf{X}_i and the size of $V_{i,\mathbf{r}}$ will decrease for increasing c , the factor $c^m (\mathbf{x} - \mathbf{X}_i)^m$ will become an increasingly rapid fluctuating part of the integrand. It has the shape of a saw-tooth function with fixed extreme values. In the limit, only the average value of this fluctuating term is relevant, which can be separated from the rest according to

$$\begin{aligned} & \lim_{c \rightarrow \infty} \sum_i \int_{V_{i,\mathbf{r}}} c^m (\mathbf{x} - \mathbf{X}_i)^m \cdot \nabla^m h_1(|\mathbf{x}|) \times \delta \mu^{(n)}(t) \cdot \nabla^n \frac{1}{|\mathbf{x}|} d\mathbf{x} \\ &= \frac{1}{V_i} \int_{V_i} (\mathbf{r}' - \mathbf{R}_i)^m d\mathbf{r}' \cdot \int \nabla^m h_1(|\mathbf{x}|) \times \delta \mu^{(n)}(t) \cdot \nabla^n \frac{1}{|\mathbf{x}|} d\mathbf{x}. \end{aligned} \quad (4.68)$$

For $m = 0$ this separation is trivial and already valid for arbitrary - finite - c . Here the first integral is over any one of the identical cells V_i . The second integral is over all space, and its value is finite for all m (and not depending on the particular coordinate \mathbf{r}), if we require all m^{th} derivatives of the envelope to be regular in the origin and to fall off sufficiently fast for $|\mathbf{x}| \rightarrow \infty$. These demands can be met, by choosing e.g. $h_1(x) = [1 + \exp(\beta[x - 1/x])]^{-1}$; $\beta > 0$, yielding a step-like function around $x = 1$ with step width $1/\beta$, and a tail that falls off exponentially. Since it obeys the symmetry rule $h_1(x) = 1 - h_1(1/x)$ with $h_1(0) = 1$; $h_1(\infty) = 0$, it has the proper behaviour at $x = 0$ and $x = \infty$.

As argued above we have shown that all terms in Eq. (4.67) with $n + m > 2$ vanish in

the limit. The terms with $n = 0$ do not contribute since $\delta\mu^{(0)}(t) = 0$, whereas the term with $n = 1, m = 0$ can be dropped (already for finite c) since the second integral in the right hand side of Eq. (4.68) vanishes on symmetry grounds. All remaining terms have $m = 2 - n$, for which we obtain

$$\int \nabla^{2-n} h_1(|\mathbf{x}|) \otimes \nabla^n \frac{1}{|\mathbf{x}|} d\mathbf{x} = -(-1)^n \frac{4\pi}{3} 1 \quad (n = 0, 1, 2). \quad (4.69)$$

This result is not depending on the particular shape of the spherically symmetric screening function if it has the proper asymptotic behavior. These terms can merely lead to a uniform finite potential

$$\delta v(t) = \frac{4\pi}{3} \left(\delta\mu^{(1)}(t) \cdot \frac{1}{V} \int_V (\mathbf{r} - \mathbf{R}) d\mathbf{r} - \frac{1}{2} \text{Tr}(\delta\mu^{(2)}(t)) \right). \quad (4.70)$$

In conclusion, we get a uniform contribution $\delta v(t)$ to the microscopic potential due to the uniform multipoles if the unit cell is charge-neutral $\delta\mu^{(0)} = 0$. This contribution has a value which does not depend on the particular shape of the spherically symmetric screening function.

4.8 Appendix B: Quadrature for Response Kernels

The response integrals of Eq. (4.50) and Eq. (4.61) involve integrations over the irreducible wedge of the Brillouin zone, in which the denominator can become singular. A good way to treat these singularities is to use a Lehmann-Taut tetrahedron scheme [47], in which the energy-dispersion relation of the denominator $\epsilon(\mathbf{k}) = \epsilon_{a\mathbf{k}} - \epsilon_{i\mathbf{k}}$ is parametrized for each combination of i and a . We can separate the energy dependent part from the rest according to

$$I_{ia}(\omega) = \frac{1}{V_{IBZ}} \int_{V_{IBZ}} \frac{(f_{i\mathbf{k}} - f_{a\mathbf{k}})g(\mathbf{k})}{\omega - (\epsilon_{a\mathbf{k}} - \epsilon_{i\mathbf{k}}) + i\eta} d\mathbf{k} = \int_{\epsilon_0}^{\epsilon_1} \frac{g_{ia}(\epsilon)}{\omega - \epsilon + i\eta} d\epsilon, \quad (4.71)$$

where ϵ_0 and ϵ_1 are the minimum and maximum value of $\epsilon(\mathbf{k})$ occurring in V_{IBZ} . Since in non-metallic systems the bands are either completely occupied or completely virtual, we can make the simplification $f_{i\mathbf{k}} - f_{a\mathbf{k}} = 2$ and we get

$$g_{ia}(\epsilon) = \frac{2}{V_{IBZ}} \int_{V_{IBZ}} g(\mathbf{k}) \delta(\epsilon - (\epsilon_{a\mathbf{k}} - \epsilon_{i\mathbf{k}})) d\mathbf{k}. \quad (4.72)$$

For this integration accurate quadrature schemes exist (e.g., Ref. [48]) which give us the weights $\tilde{w}_{ia\mathbf{k}_j}(\epsilon)$, such that

$$g_{ia}(\epsilon) = \sum_j \tilde{w}_{ia\mathbf{k}_j}(\epsilon) g(\mathbf{k}_j). \quad (4.73)$$

In the linear tetrahedron scheme these weights are piecewise cubic polynomials in ϵ . For the quadrature of Eq. (4.51) we can write

$$I_{ia}(\omega) = \sum_j w_{ia\mathbf{k}_j}(\omega) g(\mathbf{k}_j). \quad (4.74)$$

We only have to integrate the weights $\tilde{w}_{iak_j}(\epsilon)$ in the following way to obtain the new weights $w_{iak_j}(\omega)$ as functions of ω ,

$$w_{iak_j}(\omega) = \int_{\epsilon_0}^{\epsilon_1} \frac{\tilde{w}_{iak_j}(\epsilon)}{\omega - \epsilon + i\eta} d\epsilon = \mathcal{P} \int_{\epsilon_0}^{\epsilon_1} \frac{\tilde{w}_{iak_j}(\epsilon)}{\omega - \epsilon} d\epsilon + i\pi \tilde{w}_{iak_j}(\omega). \quad (4.75)$$

The real and imaginary parts of this weight can thus be obtained separately using the Cauchy principle value and residual parts.

4.9 Appendix C: Symmetry Adapted Fitfunctions

For the efficient evaluation of the microscopic Coulomb potential we have to construct a basis of vector functions, which are orthogonal in the following sense:

$$\int \mathbf{f}_i(\mathbf{r}) \cdot \mathbf{f}_j(\mathbf{r}) d\mathbf{r} = \delta_{ij}, \quad (4.76)$$

and which transform as totally-symmetric vector fields according to

$$\mathbf{f}_i(\mathbf{r}) = \{\hat{\alpha}|\mathbf{t}_\alpha\}\mathbf{f}_i(\mathbf{r}) = \alpha \cdot \mathbf{f}_i(\{\hat{\alpha}|\mathbf{t}_\alpha\}^{-1}\mathbf{r}). \quad (4.77)$$

We can construct these fitfunctions as totally-symmetric Bloch sums of one-center functions $f_{nlm}(r)$,

$$f_{nlm}(\mathbf{r}) = r^{n+l-1} \exp(-\zeta r) Z_{lm}(\hat{\mathbf{r}}). \quad (4.78)$$

The $Z_{lm}(\hat{\mathbf{r}})$ are the real-valued spherical harmonics. In the actual fitset more than one value is used for the parameter ζ for each combination of n , l , and m . The Coulomb integrals of these one-center functions can be evaluated analytically using the following expansion of $1/|\mathbf{r} - \mathbf{r}'|$ in these spherical harmonics,

$$\frac{1}{|\mathbf{r} - \mathbf{r}'|} = \sum_{lm} \frac{4\pi}{2l+1} \frac{r_{<}^l}{r_{>}^{l+1}} Z_{lm}(\hat{\mathbf{r}}) Z_{lm}(\hat{\mathbf{r}}'), \quad (4.79)$$

where the $r_{<}$ and $r_{>}$ refer to the smaller and larger values, respectively, of the two radii r and r' . Using the orthogonality of the Z_{lm} functions we obtain

$$g_{nlm}(\mathbf{r}) = \int \frac{f_{nlm}(\mathbf{r}')}{|\mathbf{r} - \mathbf{r}'|} d\mathbf{r}' = \frac{4\pi}{2l+1} Z_{lm}(\hat{\mathbf{r}}) \int_0^\infty \frac{r_{<}^l}{r_{>}^{l+1}} r'^{m+l+1} \exp(-\zeta r') dr'. \quad (4.80)$$

This is again a one-center function of the same l and m value, but with a different radial dependence. The remaining integration over the radial coordinate r' can be evaluated easily. We can now construct the totally-symmetric Bloch sums of the fitfunctions $f_{nlm}(\mathbf{r})$ according to

$$\mathbf{f}_i(\mathbf{r}) = \sum_{\{\hat{\alpha}|\mathbf{t}_\alpha\} \in \mathcal{G}} \{\hat{\alpha}|\mathbf{t}_\alpha\} f_{nlm}(\mathbf{r} - \mathbf{a}) \mathbf{e}_\mu. \quad (4.81)$$

The vectors \mathbf{a} are the coordinates of the atoms in the irreducible wedge of the Wigner-Seitz cell, and \mathbf{e}_μ is a unit vector in either one of the Cartesian directions μ . For notational convenience we introduced the compound index $i = \{nlm, \mathbf{a}, \mu\}$. Due to the operations $\{\hat{\alpha}|\mathbf{t}_\alpha\}$ of the crystal space group \mathcal{G} this series develops into a linear combination of one-center functions with the same n and l values at equivalent atoms. The potential functions are constructed simultaneously, by using the screened Bloch sums of the one-center potential functions,

$$\mathbf{g}_i(\mathbf{r}) = \sum_{\{\hat{\alpha}|\mathbf{t}_\alpha\} \in \mathcal{G}} \{\hat{\alpha}|\mathbf{t}_\alpha\} h_c(|\mathbf{r} - \mathbf{a}|) g_{nlm}(\mathbf{r} - \mathbf{a}) \mathbf{e}_\mu. \quad (4.82)$$

This set of functions is then orthogonalized by diagonalizing the (real and symmetric) overlap matrix of the vector fitfunctions $S_{ij} = \int \mathbf{f}_i(\mathbf{r}) \cdot \mathbf{f}_j \, d\mathbf{r}$, i.e., by rewriting S in $S = ODO^T$ with O the orthogonal transformation matrix, and D a diagonal matrix. We only keep those elements j for which the diagonal elements d_j are larger than some threshold, and we obtain the orthogonalized set of fitfunctions $\mathbf{f}'_j(\mathbf{r}) = d_j^{-1/2} \sum_i O_{ij} \mathbf{f}_i(\mathbf{r})$ and simultaneously we transform the potential functions accordingly to $\mathbf{g}'_j(\mathbf{r}) = d_j^{-1/2} \sum_i O_{ij} \mathbf{g}_i(\mathbf{r})$.

The microscopic potential can only be defined for a neutral unit cell. Therefore, we have to do a constrained fit which automatically conserves charge. Using Eq. (4.55) we get

$$0 = \int \delta\rho(\mathbf{r}, \omega) \, d\mathbf{r} = \int \sum_i c_i(\omega) \mathbf{f}'_i(\mathbf{r}) \, d\mathbf{r} = \sum_i c_i(\omega) \int \mathbf{f}'_i(\mathbf{r}) \, d\mathbf{r} = \sum_i c_i(\omega) \mathbf{n}_i, \quad (4.83)$$

in which the vectors \mathbf{n}_i^μ are the charge content of the fitfunctions

$$\mathbf{n}_i = \int \mathbf{f}'_i(\mathbf{r}) \, d\mathbf{r}. \quad (4.84)$$

This constraint results in three linear relations between the coefficients $c_i(\omega)$, one for each Cartesian component of the \mathbf{n}_i . We can minimize the fit error and implement the constraint by using the Lagrange multiplier technique. The set of Euler-Lagrange equations becomes

$$\frac{\partial}{\partial c_j} \left[\int \left| \delta\rho(\mathbf{r}, \omega) - \sum_i c_i(\omega) \mathbf{f}'_i(\mathbf{r}) \right|^2 \, d\mathbf{r} + \boldsymbol{\lambda}(\omega) \cdot \sum_i c_i(\omega) \mathbf{n}_i \right] = 0, \quad (4.85)$$

which gives

$$-2v_j(\omega) + 2c_j(\omega) + \boldsymbol{\lambda}(\omega) \cdot \mathbf{n}_j = 0, \quad (4.86)$$

where the $v_j(\omega)$ are obtained as the unconstrained fit coefficients

$$v_j(\omega) = \int \delta\rho(\mathbf{r}, \omega) \cdot \mathbf{f}'_j(\mathbf{r}) \, d\mathbf{r}. \quad (4.87)$$

Multiplying by \mathbf{n}_j , and summing over the indices j again, gives, after application of the constraint $\sum_j c_j(\omega) \mathbf{n}_j = 0$, the following equation:

$$\left(\sum_j \mathbf{n}_j \otimes \mathbf{n}_j \right) \cdot \boldsymbol{\lambda}(\omega) = 2 \sum_j v_j(\omega) \mathbf{n}_j, \quad (4.88)$$

which can be solved for $\boldsymbol{\lambda}(\omega)$ by inverting the 3×3 matrix $A = \sum_j \mathbf{n}_j \otimes \mathbf{n}_j$. The coefficients $c_i(\omega)$ then follow from this solution as

$$c_i(\omega) = v_i(\omega) - \frac{1}{2} \boldsymbol{\lambda}(\omega) \cdot \mathbf{n}_i. \quad (4.89)$$

It is worthwhile to investigate if this constraint can be implemented during the construction of the fitfunctions, i.e., by making new linear combinations of them. The fitted density is obtained from Eq. (4.55) again, and, with the use of the expressions for the expansion coefficients Eq. (4.89) and the solution for the multipliers Eq. (4.88), it takes the form

$$\delta \boldsymbol{\rho}(\mathbf{r}, \omega) = \sum_i (v_i(\omega) - \frac{1}{2} \boldsymbol{\lambda}(\omega) \cdot \mathbf{n}_i) \mathbf{f}'_i(\mathbf{r}) = \sum_{ij} \mathbf{f}'_i(\mathbf{r}) (\delta_{ij} - \mathbf{n}_i \cdot A^{-1} \cdot \mathbf{n}_j) v_j(\omega). \quad (4.90)$$

Substitution of the expression (4.87) for $v_j(\omega)$ yields

$$\delta \boldsymbol{\rho}(\mathbf{r}, \omega) = \int \sum_{ij} \mathbf{f}'_i(\mathbf{r}) (\delta_{ij} - \mathbf{n}_i \cdot A^{-1} \cdot \mathbf{n}_j) \mathbf{f}'_j(\mathbf{r}') \cdot \delta \boldsymbol{\rho}(\mathbf{r}', \omega) d\mathbf{r}'. \quad (4.91)$$

It directly becomes clear that by diagonalizing the real and symmetric matrix B , which is defined by its components $B_{ij} = \delta_{ij} - \mathbf{n}_i \cdot A^{-1} \cdot \mathbf{n}_j$, we get a new set of orthogonal fitfunctions. Note that B is idempotent, i.e., $B^2 = B$, so that it can only have eigenvalues equal to 1 or 0. With $B = O D O^T$ the reduced set of functions is then obtained by defining $\mathbf{f}''_i(\mathbf{r}) = d_i^{1/2} \sum_j O_{ji} \mathbf{f}'_j(\mathbf{r})$. In exactly the same way the corresponding potential functions are transformed. The density can then be fitted as

$$\delta \boldsymbol{\rho}(\mathbf{r}, \omega) = \sum_i c'_i(\omega) \mathbf{f}''_i(\mathbf{r}), \quad (4.92)$$

where the fitcoefficients $c'_i(\omega)$ can be found as in an unconstrained fit from the relation

$$c'_i(\omega) = \int \delta \boldsymbol{\rho}(\mathbf{r}, \omega) \cdot \mathbf{f}''_i(\mathbf{r}) d\mathbf{r}. \quad (4.93)$$

Chapter 5

Application of the TDDFT approach to crystals

F. Kootstra, P. L. de Boeij, and J. G. Snijders, "*Application of time-dependent density-functional theory to the dielectric function of various nonmetallic crystals*", Phys. Rev. B **62**, 7071-7083 (2000).

5.1 Abstract

The dielectric function of a range of nonmetallic crystals of various lattice types is studied by means of a real-space and full-potential time-dependent density-functional method within the adiabatic local-density approximation. Results for the dielectric constant ϵ_∞ (at optical frequencies) are given for crystals in the sodium chloride, the fluoride, the wurtzite, the diamond, and the zinc-blende lattice structure. The frequency-dependent dielectric function $\epsilon(\omega)$ for the crystals in the diamond and zincblende lattice structure are also presented. We compare our calculated results with experimental data and other theoretical investigations. Our results for the dielectric constants ϵ_∞ and the dielectric functions $\epsilon(\omega)$ are in good agreement with the experimental values. The accuracy of the results is comparable to the one which is commonly found for time-dependent density-functional theory calculations on molecular systems. On average we find a deviation of 4-5% from experiment for the group IV and III-V compounds in the wurtzite, zincblende and diamond lattice structure, 8-9% for the II-VI and I-VII compounds in the zinc-blende and sodium chloride lattice structure, and up to 14% deviation for the fluoride lattice structure. The spectral features of the dielectric functions $\epsilon(\omega)$ appear in the calculations at somewhat too low energies compared to experiment.

5.2 Introduction

After the introduction of the density-functional theory (DFT) (Refs. [2] and [3] in the 60's, there have been numerous calculations on solids, predominantly in the local-density

approximation (LDA). The accuracy of the results for many ground-state properties were very good, typically within a few percent of the experimental values. Therefore DFT has now become one of the standard methods in the field. Notable exceptions, however, are the dielectric constants of crystals, which are generally believed to be overestimated substantially by DFT-LDA. This failure is remarkable and in clear contrast with the success of DFT calculations on molecular systems [19, 30, 59] for which polarizabilities of molecules can be obtained typically to within 5% of the experimental values. The reason for the overestimation of the dielectric constants by DFT-LDA is often attributed to the underestimation of the band gap by LDA. There have been several attempts, within DFT, to go beyond LDA [35, 60, 61, 62], but all with limited success as far as the dielectric function is concerned. In the 1980s Runge and Gross [4] gave a sound basis for the time-dependent version of DFT (TDDFT). Nowadays TDDFT has been used successfully in atomic and molecular systems [30] and a lot of experience has been built up in this area. Most of the present DFT implementations for solids use pseudopotentials in combination with a plane-wave basis [15, 16, 24]. In this paper we present the results of our real-space approach [63] to TDDFT, which is a full-potential linear combination of atomic orbitals (LCAO) implementation. The calculated dielectric response functions for several crystals of various lattice types, are compared with other theoretical investigations [15, 16, 21, 26, 35, 36, 50, 51, 52, 54, 55, 56, 58, 64, 65, 66, 67, 68, 69, 70] and with experimental data [7, 45, 46, 49, 51, 53, 57, 73, 74, 75, 76, 77, 78, 79, 80, 81, 82, 83, 84, 85, 86, 87, 88, 89, 90]. The different crystals, which we have studied, have the sodium chloride structure (MX with $M = \text{Li, Na, K, Rb, Cs}$; $X = \text{F, Cl, Br, I}$, and NY with $N = \text{Mg, Ca, Sr, Ba}$; $Y = \text{O, S, Se, Te}$) the fluoride structure (MF_2 with $M = \text{Ca, Sr, Cd, Ba}$), the wurtzite structure ($\text{BeO, BN, SiC, AlN, GaN, InN, ZnO, ZnS, CdS, CdSe}$) the diamond structure (C, Si, Ge), or the zinc-blende structure (MX with $M = \text{Al, Ga, In}$; $X = \text{P, As, Sb}$, and NY with $N = \text{Zn, Cd}$; $Y = \text{S, Se, Te}$). The outline of this paper is as follows. First we give a brief review of our (TD)DFT method and implementation [37, 38, 63]. Then, in the next section, we present our results for the dielectric constants and functions, and compare them with other theoretical calculations and (available) experimental data. Finally, in the last section, we draw the conclusions.

5.3 Method

Our real-space approach to time-dependent density-functional theory for crystals, is based on the Amsterdam density functional band-structure (ADF-BAND) (Refs. [37] and [38]) implementation for ground-state DFT. The Kohn-Sham equation [2, 3] reads

$$H \psi_{n\mathbf{k}}(\mathbf{r}) = [T + V_C(\mathbf{r}) + V_{XC}(\mathbf{r})] \psi_{n\mathbf{k}}(\mathbf{r}) = \epsilon_{n\mathbf{k}} \psi_{n\mathbf{k}}(\mathbf{r}) , \quad (5.1)$$

in which T is the kinetic energy operator, V_C the Coulomb potential due to the nuclear charges and the self-consistent electron density and V_{XC} is the exchange-correlation potential for which we used the LDA approximation in the Vosko-Wilk-Nusair parameterization [41]. The one-electron states $\psi_{n\mathbf{k}}(\mathbf{r})$ are expressed on a basis of Bloch functions $\varphi_{i\alpha\mathbf{k}}(\mathbf{r})$.

At a particular \mathbf{k} point in the Brillouin zone (BZ) the basis functions $\varphi_{i\alpha\mathbf{k}}(\mathbf{r})$ are obtained by constructing the Bloch combinations of the atomic one-centered functions χ_i according to

$$\varphi_{i\alpha\mathbf{k}}(\mathbf{r}) = \sum_{\mathbf{R}} e^{i\mathbf{k}\cdot\mathbf{R}} \chi_i(\mathbf{r} - \mathbf{R} - \mathbf{s}_\alpha) . \quad (5.2)$$

Here χ_i can be a numerical atomic orbital (NAO) or a Slater-type exponential function (STO) which are centered on atom α at position \mathbf{s}_α in the crystal unit cell. The summation runs over all lattice points \mathbf{R} . The NAO's are obtained from the fully numerical Herman-Skillman (HS) program [43], which solves the density-functional equations for the spherically symmetric atoms. This basis of NAO's is extended by STO's to a $3Z2P$ basis (triple zeta basis, augmented with two polarization functions). It is possible to use the frozen core approximation for the innermost atomic states. All matrix elements that involve these functions are evaluated using an accurate numerical integration scheme [37, 91] which uses Gauss quadrature formulas. The Coulomb potentials V_α which are due to the spherically symmetric atomic densities ρ_α are provided by the HS program. The crystal Coulomb potential is then given by

$$V_C(\mathbf{r}) = \sum_{\alpha} V_\alpha(\mathbf{r}) + \int \frac{\rho_{\text{def}}(\mathbf{r}')}{|\mathbf{r} - \mathbf{r}'|} d\mathbf{r}' , \quad (5.3)$$

in which the deformation density ρ_{def} is defined as the difference between the crystal charge distribution and the superposition of atomic densities. The deformation density is obtained by summing over products of basis functions, which makes the direct evaluation of the second term in Eq. (5.3) laborious. The problem is solved by the use of a fitting procedure [12], in which the density is expanded on a basis of fit functions

$$\rho_{\text{def}}(\mathbf{r}) \approx \sum_i c_i f_i(\mathbf{r}) . \quad (5.4)$$

Here the fitfunctions f_i are the totally symmetric Bloch combinations of the atomic Slater-type exponential functions $r^{n-1}e^{-\alpha r} Z_{lm}(\Omega)$, where $Z_{lm}(\Omega)$ are the real-valued spherical harmonics. The corresponding Coulomb potentials f_i^C of these fit functions can easily be evaluated analytically

$$f_i^C(\mathbf{r}) = \int \frac{f_i(\mathbf{r}')}{|\mathbf{r} - \mathbf{r}'|} d\mathbf{r}' . \quad (5.5)$$

The Coulomb integrals can now be constructed according to

$$V_C(\mathbf{r}) \approx \sum_{\alpha} V_\alpha(\mathbf{r}) + \sum_i c_i f_i^C(\mathbf{r}) . \quad (5.6)$$

The fit coefficients c_i are determined by a least-squares solution of Eq. (5.4), where the total amount of deformation charge is constrained to vanish. The integrals over the BZ are evaluated by using a quadratic tetrahedron method [48].

In the time-dependent extension [63] we employ a lattice periodic (microscopic) effective scalar potential $v_{\text{eff}}(\mathbf{r}, t)$, in combination with a uniform (macroscopic) electric field

$\mathbf{E}_{mac}(\mathbf{r}, t)$. This macroscopic electric field can be represented by a uniform vector potential $\mathbf{A}(\mathbf{r}, t)$. In this scheme the time-dependent Kohn-Sham equation reads

$$i\frac{\partial}{\partial t}\psi_n(\mathbf{r}, t) = \left(\frac{1}{2} \left| -i\nabla + \frac{1}{c}\mathbf{A}_{eff}(\mathbf{r}, t) \right|^2 + v_{eff}(\mathbf{r}, t) \right) \psi_n(\mathbf{r}, t), \quad (5.7)$$

so the particles move in time-dependent effective potentials $\{v_{eff}(\mathbf{r}, t), \mathbf{A}_{eff}(\mathbf{r}, t)\}$ which comprise the externally applied potentials, and the Coulomb and exchange-correlation contributions of the perturbed density and current distributions. For the exchange-correlation contribution to the scalar potential we used the adiabatic local-density approximation (ALDA). We neglected such a contribution to the vector potential. The TDDFT equations are solved in an iterative scheme, in which the macroscopic electric field is kept fixed and the microscopic potential is updated in each cycle, until self-consistency is established. The first-order density change $\delta\rho(\mathbf{r}, \omega)$ (Fourier transformed) is obtained from the first-order potential change $\delta v_{eff}(\mathbf{r}', \omega)$ according to

$$\delta\rho(\mathbf{r}, \omega) = \int \left(\frac{i}{\omega} \chi_{\rho j}(\mathbf{r}, \mathbf{r}', \omega) \cdot \mathbf{E}_{mac}(\omega) + \chi_{\rho\rho}(\mathbf{r}, \mathbf{r}', \omega) \delta v_{eff}(\mathbf{r}', \omega) \right) d\mathbf{r}', \quad (5.8)$$

where the various response kernels $\chi_{ab}(\mathbf{r}, \mathbf{r}', \omega)$ can be obtained from the following expression:

$$\chi_{ab}(\mathbf{r}, \mathbf{r}', \omega) = \frac{1}{V_{BZ}} \sum_{n, n'} \int_{V_{BZ}} (f_{n\mathbf{k}} - f_{n'\mathbf{k}}) \frac{[\psi_{n\mathbf{k}}^*(\mathbf{r}) \hat{a} \psi_{n'\mathbf{k}}(\mathbf{r})][\psi_{n'\mathbf{k}}^*(\mathbf{r}') \hat{b} \psi_{n\mathbf{k}}(\mathbf{r}')] }{\epsilon_{n\mathbf{k}} - \epsilon_{n'\mathbf{k}} + \omega + i\eta} d\mathbf{k}, \quad (5.9)$$

by substituting either $\hat{\rho} = 1$ or $\hat{\mathbf{j}} = -i(\vec{\nabla} - \vec{\nabla}')/2$ (the arrows indicate whether the left or right side should be differentiated) for the operators \hat{a} and \hat{b} . Here $f_{n\mathbf{k}}$ is the occupation number and $\epsilon_{n\mathbf{k}}$ the energy eigenvalue of the Bloch orbital $\psi_{n\mathbf{k}}$ of the ground state. They are labeled by the band index n and wave vector \mathbf{k} . The integrations over the Bloch vector \mathbf{k} in Eq. (5.9) can be restricted to the irreducible part of the Brillouin zone (IBZ) due to the transformation properties of the Bloch functions, and they are evaluated numerically using the following quadrature (see Appendix B of Ref. [63]):

$$\frac{1}{V_{IBZ}} \int_{IBZ} \frac{(f_{n\mathbf{k}} - f_{n'\mathbf{k}})}{\epsilon_{n\mathbf{k}} - \epsilon_{n'\mathbf{k}} + \omega + i\eta} g(\mathbf{k}) d\mathbf{k} = \sum_{\mathbf{k}_j} w_{nn'\mathbf{k}_j}(\omega) g(\mathbf{k}_j). \quad (5.10)$$

The singular behavior of the denominator can thus be handled analytically, and is incorporated in the ω -dependent integration weights $w_{nn'\mathbf{k}_j}(\omega)$. Using a fitting procedure similar to the one used in the ground-state calculation, we can obtain the potential change δv_{eff} as a function of the density change $\delta\rho$. The induced macroscopic polarization \mathbf{P}_{mac} is defined as the time integral of the average induced current density $\delta\mathbf{j}$,

$$\mathbf{P}_{mac}(\mathbf{r}, t) = -\frac{1}{V} \int_V \int_V^t \delta\mathbf{j}(\mathbf{r}', t') d\mathbf{r}' dt'. \quad (5.11)$$

The Cartesian components of the electric susceptibility can then be obtained, as soon as self-consistency in the density change $\delta\rho$ is achieved. From $\mathbf{P}_{mac}(\omega) = \chi_e(\omega) \cdot \mathbf{E}_{mac}(\omega)$ it follows that

$$[\chi_e(\omega)]_{ij} = \left\{ -\frac{1}{V\omega^2} \int_V [\delta\mathbf{j}_p(\mathbf{r}, \omega) - \delta\mathbf{j}_p(\mathbf{r}, 0)]_i d\mathbf{r} \right\} \Big|_{\mathbf{E}_{mac}(\omega) = -i\omega \mathbf{e}_j}, \quad (5.12)$$

in which the macroscopic field $\mathbf{E}_{mac}(\omega)$ is directed along the unit vector \mathbf{e}_j and the induced paramagnetic current $\delta\mathbf{j}_p(\mathbf{r}, \omega)$ is given by

$$\delta\mathbf{j}_p(\mathbf{r}, \omega) = \int \left(\frac{i}{\omega} \chi_{ij}(\mathbf{r}, \mathbf{r}', \omega) \cdot \mathbf{E}_{mac}(\omega) + \chi_{j\rho}(\mathbf{r}, \mathbf{r}', \omega) \delta v_{eff}(\mathbf{r}', \omega) \right) d\mathbf{r}'. \quad (5.13)$$

5.4 Dielectric Constants

The dielectric constants were calculated for a wide variety of nonmetallic crystals to test the accuracy of our implementation [63] and to benchmark the performance of our calculation method. The crystals for which we calculated the dielectric constants ϵ_∞ can be ordered into five groups according to their lattice structures. They have either the sodium chloride, the fluoride, the wurtzite, the diamond, or the zinc-blende lattice structure. For all lattice structures we compared our result for ϵ_∞ with those found by a wide variety of other theoretical approaches [15, 16, 21, 26, 35, 36, 50, 51, 52, 54, 55, 56, 58, 64, 65, 66, 67, 68, 69, 70] This comparison is made to demonstrate the accuracy of our method, and to show the importance of the inclusion of both Coulomb and exchange-correlation contributions in response calculations. We can classify the other approaches according to the way they treat these contributions. If one calculates the χ_0 response directly from the ground-state solutions, without inclusion of any Coulomb or exchange-correlation contributions in the response part, we classify them as uncoupled response (UR). Other approaches include the Coulomb interaction (and possibly also exchange-correlation contributions), but involve the inversion of a large dielectric matrix (DM). Usually these methods use plane waves in combination with pseudopotentials, and they include the macroscopic contributions to the field in the Coulomb term, for which they need a special treatment of the long wavelength limit. The density-functional perturbation theory (DFPT) (Ref. [21]) closely resembles our method [63] in the way the response calculation is performed. DFPT only treats static perturbations, whereas we consider time-dependent perturbations. Where we use a LCAO basis in a full-potential method, the DFPT implementation uses pseudopotentials and plane waves. Furthermore, DFPT uses a plane-wave expansion of the density to solve the Poisson equation and to separate microscopic and macroscopic contributions, where we use an expansion in Slater-type fit functions, which treat the cusps correctly, in combination with a screening technique. In the present work the time-dependent polarization is directly related to the current density through Eq. (5.11), which is consistent with the use of the polarization current $d\mathbf{P}/dt$ in the macroscopic Maxwell equations. It is exactly this polarization that is measured in experiment. The static susceptibility can be obtained in a gauge invariant way from the paramagnetic current [Eq. (5.12)]. This way we establish

a proper behavior for the static limit ($\omega \rightarrow 0$). Note that in this limit the resulting expressions become identical to those used in the static DFPT method. However, we do not need to transform dipole matrix elements into the velocity form.

5.4.1 Sodium chloride structure

The sodium chloride lattice structure calculations were done by using a $3Z2P$ NAO/STO basis (basis V in the BAND program), which consists of a triple zeta basis augmented with two polarization functions. For integration in the reciprocal space, it turned out to be sufficient for these materials to use 15 symmetry unique \mathbf{k} points in the IBZ. We found that the Kohn-Sham energy gap in the LDA approximation underestimates the optical-absorption energies by about 40%, as is well known [64, 65]. In Table 5.1 and 5.2 we list the lattice constants for the investigated crystals, our results for the dielectric constant (ϵ_∞) together with the experimental values [73], and the relative errors. We have also included the theoretical results of Ching *et al.* [64], who use full-potential (FP) wave functions but UR, and of Li *et al.* [65], who use an empirical potential (EP) in a linearized augmented-plane-wave (LAPW) method. The results for ϵ_∞ in our work are obtained without shifting the virtual energy bands, which is known as the scissors operator Δ or quasiparticle (QP) energy shift. It can be seen that our results for ϵ_∞ show an average deviation from experiment of about 8%. The results of Ching *et al.* [64] (UR, FP) were considerably less accurate. Their use of a QP shift does not systematically improve their results for ϵ_∞ , as can be seen in Table 5.1 and 5.2. Other calculations by Li *et al.* [65] (LAPW, EP) found for the alkali halides MX ($M=\text{Na, K}$; $X=\text{F, Cl, Br, I}$) results for ϵ_∞ which deviate, without the use of a QP shift, up to 15% from experiment. A QP shift made their results even worse, up to 33% deviation from experiment. Without using a QP shift, we get ϵ_∞ values for these alkali halides which are more accurate compared to those found by the other methods [64, 65].

5.4.2 Fluoride structure

Using the same $3Z2P$ NAO/STO basis and \mathbf{k} space integration accuracy as for the sodium chloride structures, we calculated the dielectric constants ϵ_∞ of four fluoride crystals (CaF_2 , SrF_2 , CdF_2 , and BaF_2). In these compounds LDA underestimates the Kohn-Sham energy gap, compared to the optical-absorption energy, around 30%. Our results for the dielectric constants are listed in Table 5.3 together with the experimental values of Refs. [73], [83] and [84], and relative errors compared to these experimental values. We have also included other theoretical results [64, 70]. The results for the dielectric constants found by Ching *et al.* [64] (UR, FP) deviate, without the use of a QP shift, up to 47% from experimental data of Lines [73]. When using a QP shift this deviation increased up to 55% (for CdF_2 even more than 100%). The experimental value for CaF_2 shows a large variation, from 2.04 found by Lines [73] to 1.50 found by Barth *et al.* [83] and Stephan *et al.* [84]. The calculated ϵ_∞ value for CaF_2 by Gan *et al.* [70], who uses a FP method, varies from 2.02 (UR) (which agrees with the experiment by Lines [73]) to 1.80, when allowing for self

Table 5.1: Optical dielectric constants for crystals in the sodium chloride lattice structure

Solid	a (Å) ^a	This work	Experiment	Error (%)	Other theory	Method ^{b,c,d,e}
LiF	4.017	2.01	1.92 ^f	5	3.60 ^a	UR,FP,OLCAO,QP
			1.96 ^g	3	4.09 ^a	UR,FP,OLCAO
LiCl	5.129	2.97	2.68 ^f	11	3.07 ^h	DM,PP,PW,LF,XC
					2.17 ^a	UR,FP,OLCAO,QP
					3.50 ^a	UR,FP,OLCAO
LiBr	5.507	3.42	3.00 ^f	14	3.03 ^a	UR,FP,OLCAO,QP
					5.64 ^a	UR,FP,OLCAO
LiI	6.000	3.90	3.40 ^f	15	2.30 ^a	UR,FP,OLCAO,QP
					3.61 ^a	UR,FP,OLCAO
NaF	4.620	1.87	1.74 ^f	7	1.74 ^a	UR,FP,OLCAO,QP
					2.66 ^a	UR,FP,OLCAO
					1.670 ⁱ	TDPT,EP,LAPW
NaCl	5.630	2.66	2.33 ^f	14	1.317 ⁱ	TDPT,EP,LAPW,QP
					1.88 ^a	UR,FP,OLCAO,QP
					3.48 ^a	UR,FP,OLCAO
					2.529 ⁱ	TDPT,EP,LAPW
					1.819 ⁱ	TDPT,EP,LAPW,QP
NaBr	5.937	2.58	2.60 ^f	1	1.91 ^a	UR,FP,OLCAO,QP
					3.05 ^a	UR,FP,OLCAO
					2.762 ⁱ	TDPT,EP,LAPW
					2.194 ⁱ	TDPT,EP,LAPW,QP
NaI	6.473	3.39	2.98 ^f	14	2.49 ^a	UR,FP,OLCAO,QP
					2.76 ^a	UR,FP,OLCAO
					3.394 ⁱ	TDPT,EP,LAPW
					2.353 ⁱ	TDPT,EP,LAPW,QP
KF	5.347	1.82	1.84 ^f	1	1.39 ^a	UR,FP,OLCAO,QP
					2.15 ^a	UR,FP,OLCAO
					1.588 ⁱ	TDPT,EP,LAPW
					1.230 ⁱ	TDPT,EP,LAPW,QP
KCl	6.290	2.31	2.17 ^f	6	2.43 ^a	UR,FP,OLCAO,QP
					2.87 ^a	UR,FP,OLCAO
					2.268 ⁱ	TDPT,EP,LAPW
					1.493 ⁱ	TDPT,EP,LAPW,QP
KBr	6.600	2.51	2.35 ^f	7	2.17 ^a	UR,FP,OLCAO,QP
					2.62 ^a	UR,FP,OLCAO
					2.680 ⁱ	TDPT,EP,LAPW
KI	7.066	3.08	2.63 ^f	17	1.779 ⁱ	TDPT,EP,LAPW,QP
					2.18 ^a	UR,FP,OLCAO,QP
					2.81 ^a	UR,FP,OLCAO
					2.842 ⁱ	TDPT,EP,LAPW
					1.867 ⁱ	TDPT,EP,LAPW,QP

a,b,c,d,e,f,g,h,i See Table 5.2

Table 5.2: Continued Table 5.1

Solid	a (Å) ^a	This work	Experiment	Error (%)	Other theory	Method ^{b,c,d,e}
RbF	5.640	1.87	1.93 ^f	3	1.10 ^a 1.14 ^a	UR,FP,OLCAO,QP UR,FP,OLCAO
RbCl	6.581	2.28	2.17 ^f	5	1.38 ^a 1.43 ^a	UR,FP,OLCAO,QP UR,FP,OLCAO
RbBr	6.854	2.43	2.34 ^f	4	1.77 ^a 2.00 ^a	UR,FP,OLCAO,QP UR,FP,OLCAO
RbI	7.342	2.65	2.59 ^f	2	1.37 ^a 1.50 ^a	UR,FP,OLCAO,QP UR,FP,OLCAO
CsF	6.010	1.84				
CsCl	7.140	2.04	2.30 ^f	11		
CsBr	7.420	2.21	2.43 ^f	9		
CsI	7.900	2.40	2.63 ^f	9		
MgO	4.210	3.20	2.95 ^f	8	3.10 ^a 4.28 ^a	UR,FP,OLCAO,QP UR,FP,OLCAO
MgS	5.203	5.37	4.84 ^f	11	4.52 ^a 5.12 ^a	UR,FP,OLCAO,QP UR,FP,OLCAO
MgSe	5.460	6.25	5.28 ^f	18		
CaO	4.810	2.90	3.27 ^f	11	1.66 ^a 3.22 ^a	UR,FP,OLCAO,QP UR,FP,OLCAO
CaS	5.690	4.30	4.24 ^f	1	3.01 ^a 4.47 ^a	UR,FP,OLCAO,QP UR,FP,OLCAO
CaSe	5.920	4.81	4.58 ^f	5		
SrO	5.160	3.26	3.35 ^f	3	1.90 ^a 3.04 ^a	UR,FP,OLCAO,QP UR,FP,OLCAO
SrS	6.020	4.37	4.09 ^f	7	2.78 ^a 3.68 ^a	UR,FP,OLCAO,QP UR,FP,OLCAO
SrSe	6.240	4.77	4.33 ^f	10		
SrTe	6.480	5.88	4.91 ^f	19		
BaO	5.520	3.36	3.68 ^f	9	2.90 ^a 4.01 ^a	UR,FP,OLCAO,QP UR,FP,OLCAO
BaS	6.380	4.07	4.26 ^f	4		
BaSe	6.600	4.50	4.48 ^f	1		
BaTe	6.980	4.94	4.71 ^f	5		

^aRef. [64]^bTDPT: time-dependent perturbation theory; DM: dielectric matrix; UR: uncoupled response.^cFP: full potential; PP: pseudopotential; EP: empirical potential.^dPW: plane wave; LAPW: linearized augmented plane wave; OLCAO: orthogonalized linear combination of atomic orbitals.^eXC: exchange-correlation effects; QP: quasiparticle energy shift; LF: local field effects.^fRef. [73] ^gRef. [45] ^hRef. [35] ⁱRef. [65]

Table 5.3: Optical dielectric constants for crystals in the fluoride lattice structure

Solid	a (Å) ^a	This work	Experiment	Error (%)	Other theory	Method ^{b,c,d,e}
CaF ₂	5.460	1.78	2.04 ^f	13	1.49 ^a	UR,FP,OLCAO,QP
			1.50 ^g	19	2.02 ^a	UR,FP,OLCAO
			1.50 ^h	19	2.02 ⁱ	UR,FP,OLCAO
					1.80 ⁱ	UR,FP,OLCAO,SIC
SrF ₂	5.800	1.89	2.06 ^f	8	1.49 ⁱ	UR,FP,OLCAO,QP
					1.12 ^a	UR,FP,OLCAO,QP
CdF ₂	5.388	2.48	3.14 ^f	21	1.23 ^a	UR,FP,OLCAO
					6.90 ^a	UR,FP,OLCAO,QP
BaF ₂	6.200	1.97	2.15 ^f	8	8.00 ^a	UR,FP,OLCAO
					1.07 ^a	UR,FP,OLCAO,QP
					1.12 ^a	UR,FP,OLCAO

^aRef. [64]^bUR: uncoupled response.^cFP: full potential.^dOLCAO: orthogonalized linear combination of atomic orbitals^eQP: quasiparticle energy shift; SIC: self-interaction correction.^fRef. [73] ^gRef. [83] ^hRef. [84] ⁱRef. [70]

interacting corrections (SIC), and to 1.49, when using a QP shift (which agrees with the experiment by Barth *et al.* [83] and Stephan *et al.* [84]). Our results for the dielectric constants ϵ_∞ , obtained without the use of a QP shift, show an average deviation of about 14% from experiment, and they are the best values up to date, but we do not achieve the same accuracy as for the other lattice structures. In the case of CaF₂ our result for ϵ_∞ is in between the two experimental ones [73, 83].

5.4.3 Wurtzite structure

As an example of anisotropic crystals, we studied several crystals of the wurtzite structure. For these calculations the same $3Z2P$ NAO/STO basis and \mathbf{k} space integration accuracy was used as for the sodium chloride structures. The wurtzite structure is very similar to the zinc-blende structure (see later) and only differs in the stacking of the layers along the [111] direction. Therefore many crystals like SiC, ZnS, CdS, etc. exist in both forms. Ideally the c/a ratio equals $\sqrt{8/3}$ and the internal parameter $u = 3/8$. In Table 5.4 we summarize the geometrical parameters, the calculated isotropic average values for the dielectric constant $\bar{\epsilon}_\infty$ and the anisotropy $\Delta\epsilon_\infty$ in this dielectric constant, together with the experimental values for $\bar{\epsilon}_\infty$ [85, 86, 87, 88, 89], and relative errors compared to these experimental values. We have also included other theoretical results (UR) for $\bar{\epsilon}_\infty$ and $\Delta\epsilon_\infty$ found by Xu *et al.* [66] (FP), Chen *et al.* [67] (PP), Christensen *et al.* [68] (LMTO-ASA), and Wang *et al.* [69] (PP). The isotropic average values for the dielectric constant is defined as $\bar{\epsilon}_\infty = \frac{1}{3}(\epsilon_{xx} + \epsilon_{yy} + \epsilon_{zz})$ and the anisotropy as $\Delta\epsilon_\infty = \epsilon_{zz} - \frac{1}{2}(\epsilon_{xx} + \epsilon_{yy})$. Our results for $\bar{\epsilon}_\infty$

showed substantial differences from the theoretical results found by others [66, 67, 68, 69], and an average deviation of about 5% from the experimental values [85, 86, 87, 88, 89], which is a substantial improvement over the other theoretical methods.

Table 5.4: Optical dielectric constant and anisotropy for crystals in the wurtzite lattice structure

Crystal	Lattice ^a (Å)			This work		Exp. Err.		Other theory		Method d,e,f,g	
	a	c	u	$\bar{\epsilon}_\infty$ ^b	$\Delta\epsilon_\infty$ ^c	$\bar{\epsilon}_\infty$	%	$\bar{\epsilon}_\infty$	$\Delta\epsilon_\infty$		
BeO	2.698	4.380	0.378	2.92	0.05			2.76	0.02 ^a	UR,FP,LCAO	
BN	2.536	4.199	0.375	4.17	0.38			4.07	0.25 ^a	UR,FP,LCAO	
								4.57	0.18 ^h	UR,PP,PW,LF	
								4.14	0.13 ⁱ	UR,ASA,LMTO	
SiC	3.076	5.048	0.375	6.93	0.75			8.09	1.17 ^a	UR,FP,LCAO	
AlN	3.110	4.980	0.382	4.56	-0.01		4.84 ^j	6	4.27	1.19 ^a	UR,FP,LCAO
								3	4.51	0.28 ^h	UR,PP,PW,LF
									3.86	0.14 ⁱ	UR,ASA,LMTO
GaN	3.190	5.189	0.375	5.31	0.30		5.2 ^l	2	9.53	2.44 ^a	UR,FP,LCAO
								7	5.56	0.06 ^h	UR,PP,PW,LF
									4.68	0.09 ⁱ	UR,ASA,LMTO
InN	3.533	5.692	0.375	8.78	-1.13	8.4 ^o	5	7.39	1.01 ^a	UR,FP,LCAO	
									7.16	0.33 ⁱ	UR,ASA,LMTO
									8.62	0.86 ^a	UR,FP,LCAO
ZnO	3.249	5.207	0.375	4.26	-0.03			6.81	1.58 ^a	UR,FP,LCAO	
ZnS	3.811	6.234	0.375	5.71	0.30			5.07	-0.03 ^a	UR,FP,LCAO	
CdS	4.137	6.714	0.375	5.22	0.30			4.94	-0.03 ^a	UR,FP,LCAO	
CdSe	4.299	7.015	0.375	6.11	0.21						

^aRef. [66]

$$\text{b} \bar{\epsilon}_\infty = \frac{1}{3}(\epsilon_{xx} + \epsilon_{yy} + \epsilon_{zz})$$

$$\text{c} \Delta\epsilon_\infty = \epsilon_{zz} - \frac{1}{2}(\epsilon_{xx} + \epsilon_{yy})$$

^dUR: uncoupled response.

^eFP: full potential; PP: pseudopotential; ASA: atomic-sphere approximation.

^fPW: plane wave; LMTO: linearized muffin-tin orbitals; LCAO: linear combination of atomic orbitals.

^gLF: local-field effects.

^hRef. [67] ⁱRef. [68] ^jRef. [85] ^kRef. [86] ^lRef. [87] ^mRef. [88] ⁿRef. [69] ^oRef. [89]

5.4.4 Diamond structure

The calculations for the diamond structures were performed by using 175 symmetry unique \mathbf{k} points in the IBZ for the (numerical) integrations in the reciprocal space, and using the standard $3Z2P$ NAO/STO basis. In Table 5.5 we list for carbon (C), silicon (Si), and germanium (Ge) the lattice constants, the calculated dielectric constants ϵ_∞ of this work together with the experimental values [7, 49, 53, 74, 75], and relative errors compared to

these experimental values. Other theoretical results of Refs. [15, 16, 21, 26, 35, 36, 50, 51, 52, 54, 55, 56] are also included. Our results for ϵ_∞ show an average deviation of about 5% from the experimental values [7], and compared to other theoretical investigations, it can be seen from Table 5.5 that our results are again of better quality.

Table 5.5: Optical dielectric constants for crystals in the diamond lattice structure

Solid	a (\AA) ^a	This work	Exp.	Error (%)	Other theory	Method ^{b,c,d,e}
C	3.57	5.62	5.7 ^a	1	5.90 ^f	DM,PP,PW,LF,XC
			5.7 ^g	1	4.34 ^h	UR,FP,LCAO
			5.67 ⁱ	1	5.20 - 5.86 ^j	DM,PP,PW,LF,QP
					5.5 ^k	DM,PP,LCGO,LF,QP
					5.7 ^l	UR,EP,LCAO
Si	5.43	12.78	12.0 ^a	7	12.9 ^f	DM,PP,PW,LF,XC
			11.4 ^m	12	9.03 ^h	UR,FP,LCAO
					12.7 ⁿ	DM,PP,PW,LF,XC
					11.2 ^o	DM,PP,PW,LF,QP
					12.4 - 12.9 ^p	DFPT,PP,PW,LF,XC
					12.7 ^q	DFPT,PP,PW,LF,XC
					12.05 ^r	DM,FP,LMTO,LF,QP
					12.8 ^k	DM,PP,LCGO,LF,QP
					11.7 ^s	UR,PP,LCGO,QP
					12.0 ^l	UR,EP,LCAO
					13.6 ^t	DFPT,PP,PW,LF,XC
Ge	5.66	16.22	16.0 ^a	1	20.7 ^f	DM,PP,PW,LF,XC
			15.3 ^m	6	12.31 ^h	UR,FP,LCAO
			15.3 ^u	6	16.5 ^o	DM,PP,PW,LF,QP
					15.58 ^r	DM,FP,LMTO,LF,QP
					21.8 ^k	DM,PP,LCGO,LF,QP
					16.0 ^s	UR,PP,LCGO,QP
					16.0 ^l	UR,EP,LCAO
					18.7 ^t	DFPT,PP,PW,LF,XC

^aRef. [7]

^bDFPT: density-function perturbation theory; DM: dielectric matrix; UR: uncoupled response.

^cFP: full potential; PP: pseudopotential; EP: empirical potential.

^dPW: plane wave; LMTO: linearized muffin-tin orbitals; LCAO: linear combination of atomic orbitals; LCGO: linear combination of Gaussian orbitals.

^eXC: exchange-correlation effects; QP: quasiparticle energy shift; LF: local-field effects.

^fRef. [35] ^gRef. [74] ^hRef. [51] ⁱRef. [49] ^jRef. [26] ^kRef. [50] ^lRef. [52] ^mRef. [53] ⁿRef. [15] ^oRef. [16]

^pRef. [21] ^qRef. [36] ^rRef. [55] ^sRef. [56] ^tRef. [54] ^uRef. [75]

5.4.5 Zinc-blende structure

The zinc-blende structures we studied can be grouped into the III-V (AlP, AlAs, AlSb, GaP, GaAs, GaSb, InP, InAs, InSb) and the II-VI (ZnS, ZnSe, ZnTe, CdS, CdSe, CdTe) compounds. These calculations were done using the same $3Z2P$ NAO/STO basis and \mathbf{k} space integration accuracy as for the diamond structures.

III-V compounds

The calculated dielectric constants for these compounds are collected in Table 5.6, together with the lattice constants, the experimental values for ϵ_∞ [57, 75, 76, 77, 78], the errors compared to these experimental values, and other theoretical results [36, 50, 51, 52, 54, 55, 56, 58]. We find that our results for ϵ_∞ are closer to experiment than those found by others [51, 52, 54], with the exception of InSb, for which we find an underestimation of about 40%. At the same time we find a considerable overestimation of the experimental band gap for this small-gap semiconductor, as can be seen in Table 5.8. In this calculation we have included the $4d$ atomic states in the valence basis, as these give rise to shallow core states, which can affect the position of the valence-band maximum [71, 72]. The overestimation of the band gap is in clear contrast with the general trend observed in LDA-DFT band-structure calculations, i.e., that the band gap tends to be underestimated in semiconductors. However, inclusion of scalar relativistic corrections stabilizes the s -like conduction-band minimum considerably. In the LDA this causes the gap even to vanish, thus incorrectly predicting the InSb crystal to be a semimetal, as was found in full-potential scalar relativistic LAPW calculations [72], and as we have checked in our ground-state calculations. We are not yet able to include these scalar relativistic corrections in the time-dependent calculations. Nevertheless, with the exception of the InSb crystal, we find an average deviation of about 4% from experiment for the III-V compounds.

II-VI compounds

Our results for the calculated dielectric constants ϵ_∞ are collected in Table 5.7, together with experimental values [78, 79, 80, 81, 82] and other theoretical investigations [51, 56]. We find that our results for ϵ_∞ show an average deviation of about 9% from experiment, and are comparable to those found by Huang *et al.* [51] (UR, FP) and Wang *et al.* [56] (UR, PP), except for the Te compounds, where our results are substantially better.

5.5 Dielectric Functions

The dielectric functions $\epsilon(\omega)$ for all zinc-blende structures (which reduces to the diamond structure in case of group IV elementary solids) were calculated using the same $3Z2P$ NAO/STO basis and \mathbf{k} space integration accuracy as mentioned before for calculating the dielectric constants of the diamond and zinc-blende structures. We report the dielectric

Table 5.6: Optical dielectric constants for crystals in the III-V zinc-blende lattice structure

Solid	a (Å) ^a	This work	Exp.	Error (%)	Other theory	Method ^{b,c,d,e}
AlP	5.45	8.16	8.0 ^f	2	5.63 ^g	UR,FP,LCAO
AlAs	5.62	8.83	8.16 ^h	8	6.81 ^g 9.2 ⁱ	UR,FP,LCAO DFPT,PP,PW,LF,XC
AlSb	6.13	10.22	10.2 ^j	1	7.21 ^g 12.2 ⁱ	UR,FP,LCAO DFPT,PP,PW,LF,XC
GaP	5.45	9.59	9.1 ^k	5	9.29 ^g 9.4 ^l 9.1 ^m	UR,FP,LCAO UR,PP,LCGO,QP UR,EP,LCAO
GaAs	5.65	11.33	10.9 ^j 10.8 ⁿ	4 5	11.21 ^g 12.3 ^o 10.83 ^p 13.1 ^q 10.9 ^l 10.9 ^m 12.3 ⁱ 10.2 ^r	UR,FP,LCAO DFPT,PP,PW,LF,XC DM,FP,LMTO,LF,QP DM,PP,LCGO,LF,QP UR,PP,LCGO,QP UR,EP,LCAO DFPT,PP,PW,LF,XC DM,PP,PW,LF,QP
GaSb	6.12	13.54	14.4 ^j	6	11.42 ^g 14.4 ^m 18.1 ⁱ	UR,FP,LCAO UR,EP,LCAO DFPT,PP,PW,LF,XC
InP	5.87	9.60	9.6 ^j	0	7.92 ^g 9.6 ^m	UR,FP,LCAO UR,EP,LCAO
InAs	6.04	11.40	12.3 ^j	7	10.02 ^g 12.3 ^m	UR,FP,LCAO UR,EP,LCAO
InSb	6.48	9.15	15.7 ^j	42	13.51 ^g 15.7 ^m	UR,FP,LCAO UR,EP,LCAO

^aRef. [7]^bDFPT: density-function perturbation theory; DM: dielectric matrix; UR: uncoupled response.^cFP: full potential; PP: pseudopotential; EP: empirical potential.^dPW: plane wave; LMTO: linearized muffin-tin orbitals; LCAO: linear combination of atomic orbitals; LCGO: linear combination of Gaussian orbitals.^eXC: exchange-correlation effects; QP: quasiparticle energy Shift; LF: local-field effects.^fRef. [75] ^gRef. [51] ^hRef. [76] ⁱRef. [54] ^jRef. [77] ^kRef. [78] ^lRef. [56] ^mRef. [52] ⁿRef. [57] ^oRef. [36]^pRef. [55] ^qRef. [50] ^rRef. [58]

Table 5.7: Optical dielectric constants for crystals in the II-VI zinc-blende lattice structure

Solid	a (Å) ^a	This work	Exp.	Error (%)	Other theory	Method ^{b,c,d,e}
ZnS	5.41	5.71	5.2 ^f	10	5.63 ^g	UR,FP,LCAO
					5.50 ^h	UR,PP,LCGO,QP
ZnSe	5.67	6.74	5.9 ⁱ	14	5.56 ^g	UR,FP,LCAO
					6.60 ^h	UR,PP,LCGO,QP
ZnTe	6.09	7.99	7.3 ^j	9	5.24 ^g	UR,FP,LCAO
CdS	5.82	4.89	5.2 ^k	6	5.05 ^g	UR,FP,LCAO
CdSe	6.08	6.26	5.8 ⁱ	8	5.68 ^g	UR,FP,LCAO
CdTe	6.48	6.70	7.2 ^j	7	9.02 ^g	UR,FP,LCAO

^aRef. [7]^bUR: uncoupled response.^cFP: full potential; PP: pseudopotential.^dLCAO: linear combination of atomic orbitals; LCGO: linear combination of Gaussian orbitals.^eQP: quasiparticle energy shift.^fRef. [79] ^gRef. [51] ^hRef. [56] ⁱRef. [80] ^jRef. [81] ^kRef. [82]

functions $\epsilon(\omega)$ for a selected range of compounds, for which experimental data was available. The calculated dielectric functions for the remaining compounds are available on request. When comparing our calculated dielectric functions with the experiment ones, we found all features uniformly shifted to lower energies. Therefore, in order to facilitate the comparison with experiment, we shifted the calculated results for the dielectric functions to higher energies, in such a way that the zero crossings in the calculated $\text{Re}[\epsilon(\omega)]$ coincided with the experimental zero crossings. The values for the applied shifts to the calculated dielectric functions are compared in Table 5.8 with the LDA and the experimental band gap (E_g) [92].

As can be seen from Table 5.8, there is no direct relation between the applied shifts and the error in the LDA band gap for these compounds. The calculated (shifted) dielectric functions $\epsilon(\omega)$ for C, Si, and Ge are depicted in Figs. 5.1 and 5.2, together with the experimental data of Palik [45] and Aspnes *et al.* [46].

These spectra are in very good agreement with the experimental spectra, there are, however, features that need improvement. The E_2 peak [93] for C, Si, and Ge (high-energy peak in $\text{Im}[\epsilon(\omega)]$) is too sharp, and its magnitude is overestimated compared to experiment. Looking at the E_1 peak in Si and Ge (low-energy peak in $\text{Im}[\epsilon(\omega)]$), we see that it is underestimated in amplitude and appears as a shoulder, which can be ascribed to a failure in the description of excitonic effects (screened Coulomb attraction between electron and hole). The sharp structures which were found in the calculated spectra at energies higher than the E_2 peak, were much less pronounced in experiment.

The calculated (shifted) dielectric functions $\epsilon(\omega)$ for the Ga and In series are depicted in Figs. 5.2-5.5, together with the experimental data of Aspnes *et al.* [46]. The $\epsilon(\omega)$ for the Zn series and CdTe are depicted in Figs. 5.5-5.7, together with the experimental data of Freelouf [90]. The experimental data of Freelouf [90] for the imaginary parts of the

Table 5.8: The calculated LDA band gaps and the experimental values, in comparison with the applied energy shifts to the dielectric functions for the crystals in Figs. 5.1-5.7. All values are given in electron volts (eV).

Solid	$E_g(\text{Experiment})^a$	$E_g(\text{LDA})$	Δ^b	Applied shift
C	5.47	4.14	1.33	0.60
Si	1.11	0.55	0.56	0.40
Ge	0.67	0.39	0.28	0.30
GaP	2.24	1.50	0.74	0.50
GaAs	1.35	1.02	0.33	0.45
GaSb	0.67	0.79	-0.12	0.30
InP	1.27	1.00	0.27	0.40
InAs	0.36	0.47	-0.11	0.35
InSb	0.17	0.99	-0.82	0.15
ZnS	3.54	2.06	1.48	0.90
ZnSe	2.58	1.52	1.06	1.05
ZnTe	2.26	1.99	0.27	0.70
CdTe	1.44	1.70	-0.26	0.65

^aRef. [92]

^b $\Delta = E_g(\text{experiment}) - E_g(\text{LDA})$

dielectric functions $\epsilon(\omega)$ have been obtained by digitizing the data in their plots. The real parts have been obtained as the Kramers-Kronig transform of these imaginary parts. The result of applying a shift to our calculated dielectric functions for these compounds is that we find an overall agreement between our spectra and the experimental spectra which is quite good. However, when looking in more detail, we find that the E_2 peaks coincide with experiment, but are (also in these compounds) too sharp and their magnitudes are still overestimated compared to experiment. Looking at the E_1 peaks, we see that they are underestimated in amplitude and in general too close to the E_2 peak. Further, the calculated E_1 peaks do not reproduce the experimental double peak structure for the As, Sb, Se, and Te compounds. The sharp structures in the calculated dielectric functions at energies higher than the E_2 peak are less pronounced in experiment.

5.6 Conclusions

The dielectric function of a large range of nonmetallic crystals, of various lattice types, is calculated by using an efficient, accurate, and rapidly converging real-space implementation of time-dependent density-functional theory. In this method we employ a lattice periodic (microscopic) effective scalar potential in combination with a uniform (macroscopic) electric field. Our results for the dielectric constants ϵ_∞ (at optical frequencies) were obtained without the use of a scissors operator. They are in good agreement with experiment and in general more accurate than those found by others. The accuracy of our calculated ϵ_∞

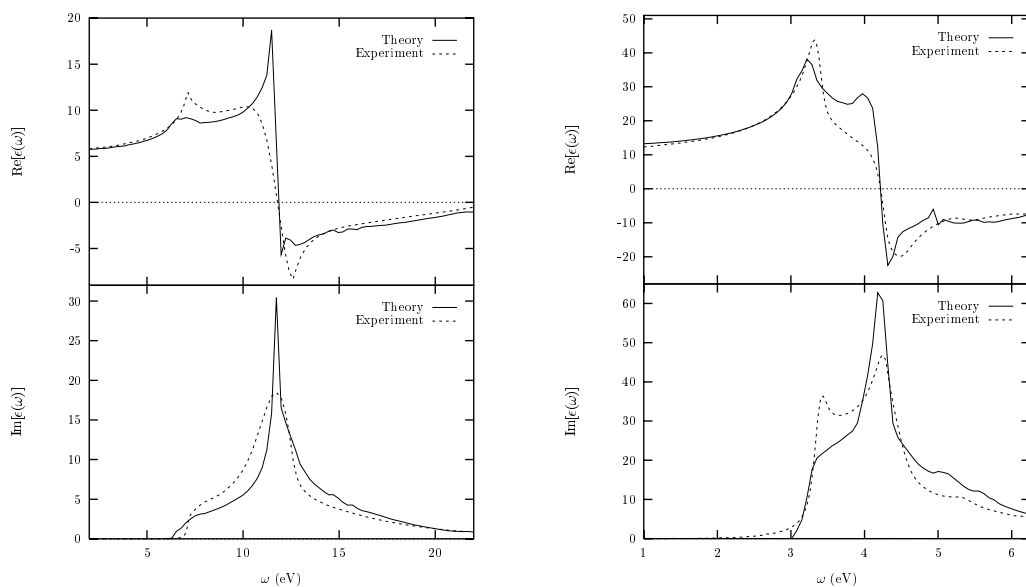


Figure 5.1: Plots of the real and imaginary part of the calculated dielectric function of diamond (C) [left] and silicon (Si) [right] in comparison with the experimental data (Refs. [45] and [46]).

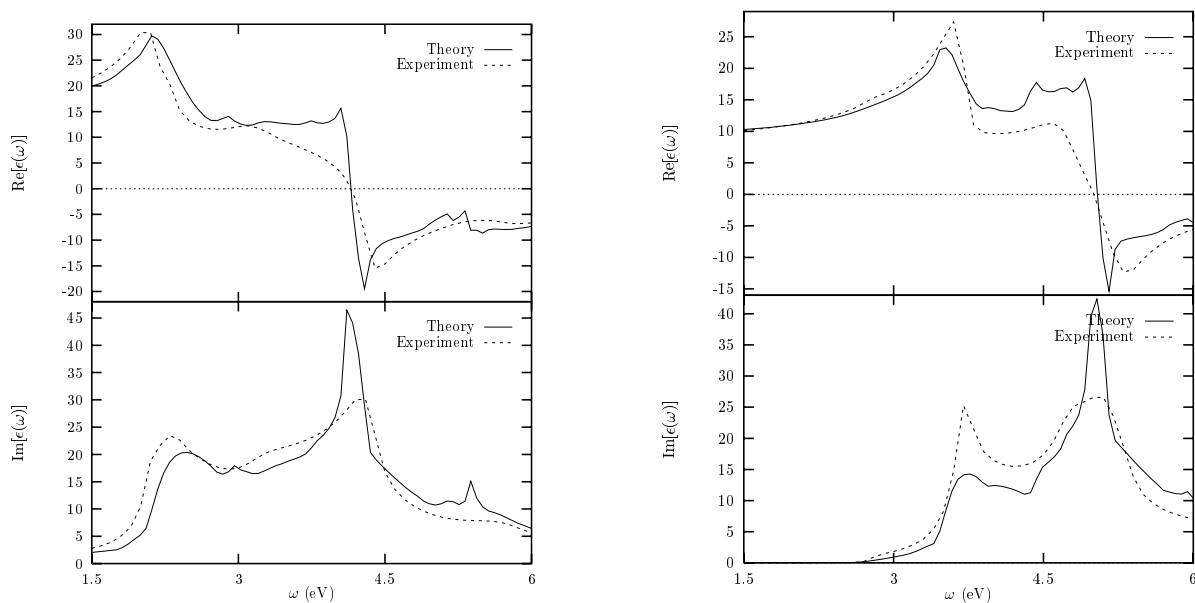


Figure 5.2: Plots of the real and imaginary part of the calculated dielectric function of germanium (Ge) [left] and gallium phosphide (GaP) [right] in comparison with the experimental data (Ref. [46]).

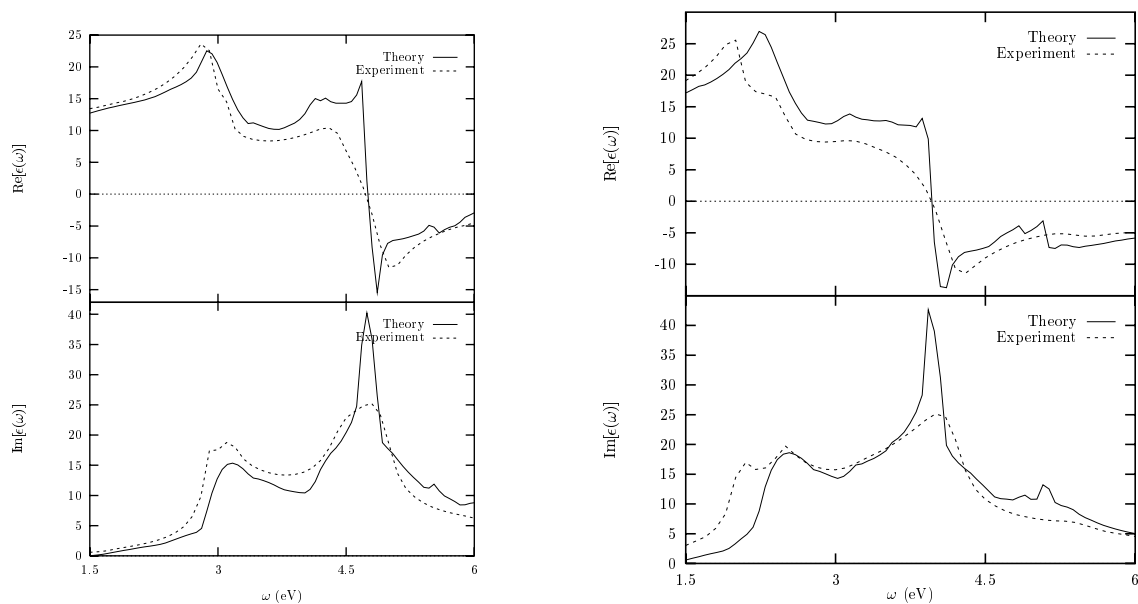


Figure 5.3: Plots of the real and imaginary part of the calculated dielectric function of gallium arsenide (GaAs) [left] and gallium antimonide (GaSb) [right] in comparison with the experimental data (Ref. [46]).

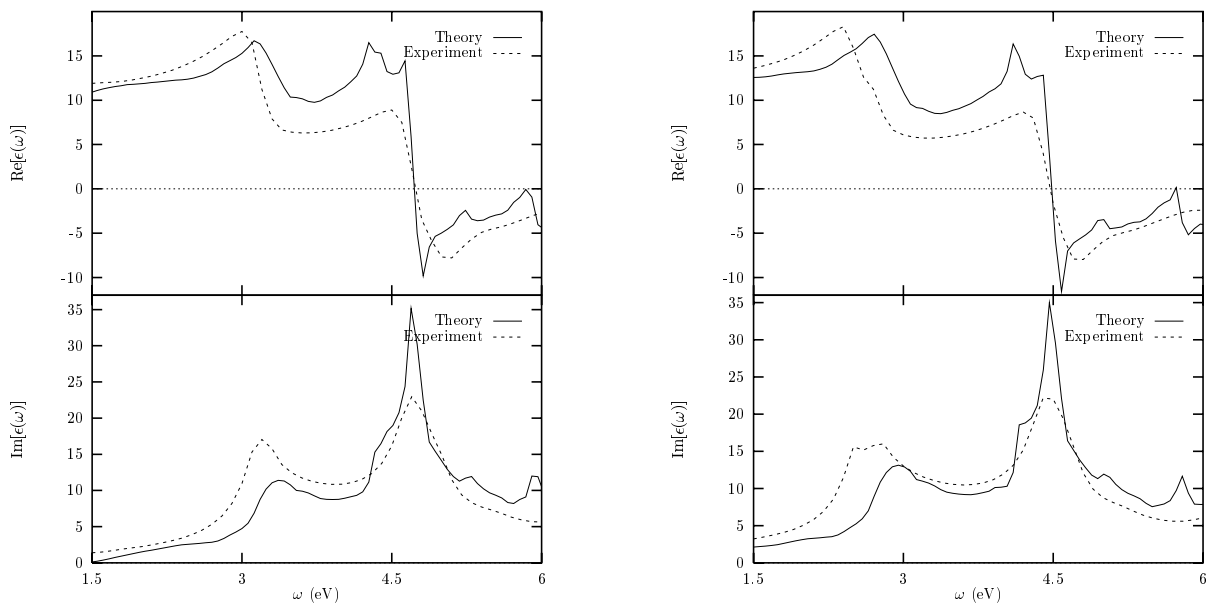


Figure 5.4: Plots of the real and imaginary part of the calculated dielectric function of indium phosphide (InP) [left] and indium arsenide (InAs) [right] in comparison with the experimental data (Ref. [46]).

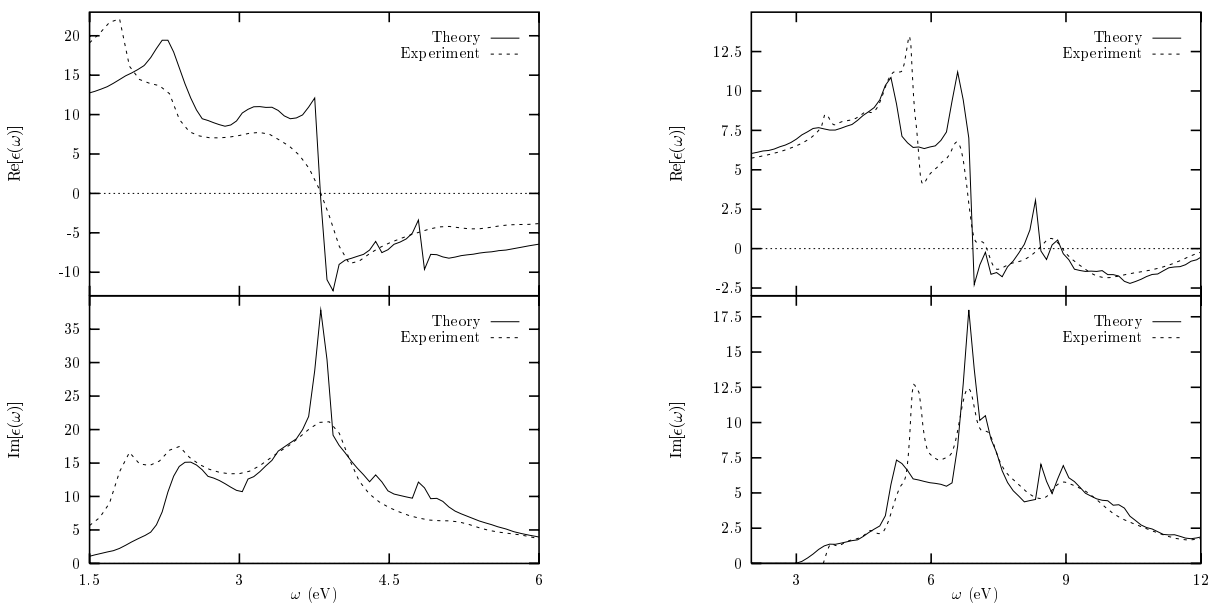


Figure 5.5: Plots of the real and imaginary part of the calculated dielectric function of indium antimonide (InSb) [left] and zinc sulfide (ZnS) [right] in comparison with the experimental data (Refs. [46] and [90]).

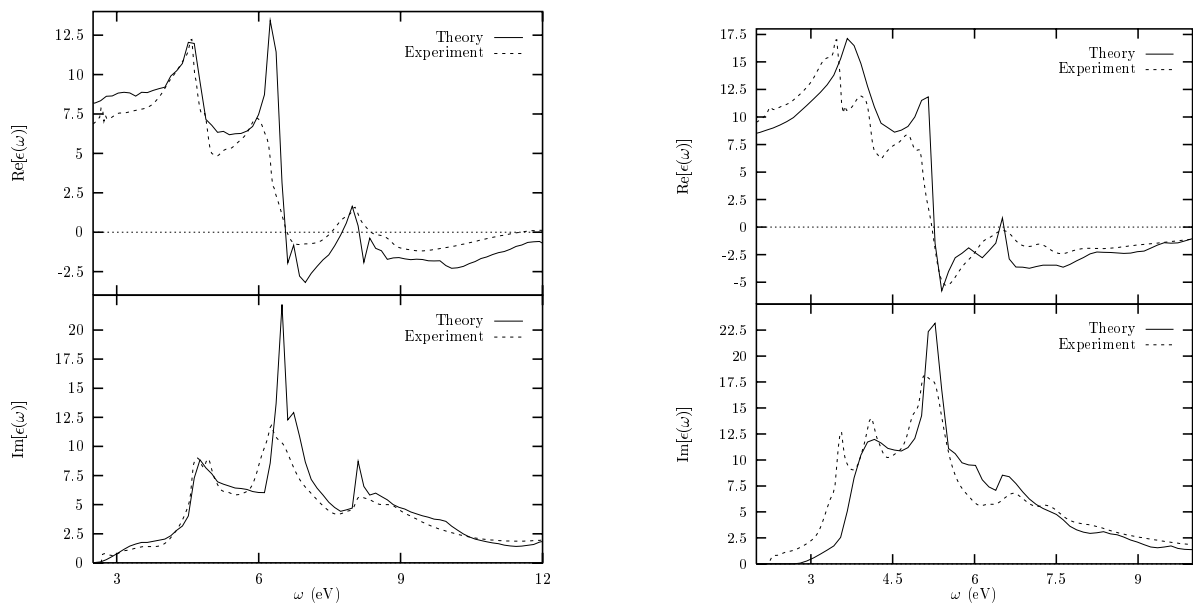


Figure 5.6: Plots of the real and imaginary part of the calculated dielectric function of zinc selenide (ZnSe) [left] and zinc telluride (ZnTe) [right] in comparison with the experimental data (Ref. [90]).

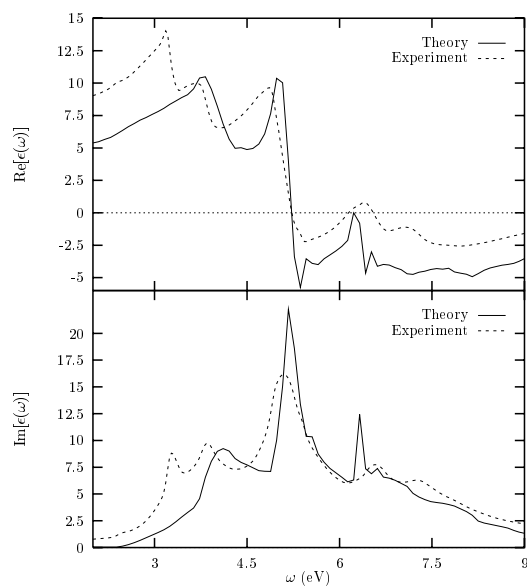


Figure 5.7: Plots of the real and imaginary part of the calculated dielectric function of cadmium telluride (CdTe) in comparison with the experimental data (Ref. [90]).

values for crystals is comparable with the TDDFT results for polarizabilities in molecular systems. On average we find a deviation of 4-5% from experiment for the group IV and III-V compounds in the wurtzite, zinc-blende, and diamond lattice structure, 8-9% for the II-VI and I-VII compounds in the zinc-blende and sodium chloride lattice structure, and up to 14% deviation for the fluoride lattice structure. Therefore we observe a trend that the accuracy of the results is reduced in the strongly ionic compounds. The calculated dielectric functions $\epsilon(\omega)$ reproduce the experimental spectral features quite accurately, although there is a more or less uniform shift necessary between the experimental and theoretical spectra.

Chapter 6

Relativistic effects in TDDFT calculations

F. Kootstra, P. L. de Boeij, H. Aissa, and J. G. Snijders, "Relativistic effects on the optical response of InSb by time-dependent density-functional theory", J. Chem. Phys. **114**, 1860-1865 (2001).

P. L. de Boeij, F. Kootstra, and J. G. Snijders, "Relativistic effects in the optical response of HgSe by time-dependent density-functional theory", Int. J. Quant. Chem. accepted.

6.1 Abstract

We show how relativistic effects can be included in the time-dependent density-functional theory (DFT) for the optical response properties of nonmetallic crystals. The dominant scalar relativistic effects have been included using the zeroth-order regular approximation (ZORA) in the ground-state DFT calculations, as well as in the time-dependent response calculations. We show that this theory can also be applied to indium antimonide and mercury selenide in the zinc-blende structure, notwithstanding the fact that they turn into semimetals when scalar relativistic effects are included. Results are given for the band structure, the static dielectric constant ϵ_∞ and the dielectric function $\epsilon(\omega)$, for the various levels on which relativity can be included, i.e., nonrelativistic, only in the ground-state, or also in the response calculation. Comparisons of our calculated results are made with experiment and other theoretical investigations. With the inclusion of scalar relativistic effects, the band structure of InSb and HgSe become semimetallic within the local density approximation and we find a deviation of 5% from experiment for the static dielectric constant of InSb. Also the dielectric functions are improved and the spectra are in good agreement with experiment, although the spectral features are shifted to somewhat lower energies compared to experiment.

6.2 Introduction

In a recent paper [94] we found that time-dependent density-functional theory (TDDFT) [63] in the adiabatic local density approximation (ALDA) works very well for a large range of nonmetallic crystals, for which we achieved, on average, an accuracy of about 5% compared with experiment. A clear exception, however, was found for InSb in the zinc-blende structure ($a=6.48 \text{ \AA}$), for which the predicted static dielectric constant was underestimated by about 40% compared with experiment [77]. Simultaneously we found a considerable overestimation of the experimental bandgap, 0.99 eV DFT-LDA, in comparison with experimental bandgaps of 0.17 eV [92] ($T=300 \text{ K}$) and 0.23 eV [7] ($T=0 \text{ K}$) for this small-gap semiconductor. This overestimation of the bandgap is in clear contrast with the general trend which is observed in LDA band structure calculations, i.e., that the bandgaps are generally underestimated by about 50%. The inclusion of scalar relativistic effects within the zeroth-order regular approximation in our full-potential ground-state DFT-LDA band structure calculation causes the lowest s -like conduction band to be stabilized considerably more than the upper p -like valence bands. The band order is changed in the centre of the Brillouin Zone (BZ), which results in a vanishing bandgap, and consequently the incorrect prediction of the InSb crystal being a semimetal. A similar result was found in the fully relativistic linear-muffin-tin-orbital method (LMTO) of Cardona *et al.* [71] and in the full-potential scalar relativistic linear augmented plane-wave (FLAPW) calculation of Guo *et al.* [72]. Recently, the nature of the material HgSe was also debated, whether it is a small-gap semiconductor or a semimetal in the zinc-blende structure. Experimentally, as determined using photoemission spectroscopy [103], there seemed to be no evidence of a bulk-like conduction band that either crosses or touches the valence-band maximum, hence favoring it to be a small-gap (0.42 eV) semiconductor. On the other hand, conductivity, optical and magneto-optical measurements, compiled in Ref. [104], favored an inverted bandstructure with zero fundamental gap, and thus a semimetallic nature. The seemingly contradicting experimental results have been brought into accordance with an *ab-initio* quasiparticle bandstructure calculation [105]. This GW calculation (like the DFT-LDA calculation on which it was based) predicts an inverted semimetallic bandstructure. The experimentally observed very low photoemission intensity just above the valence band maximum could be attributed to the enhanced dispersion, and hence very light effective mass and low density of states, of the lowest conduction band. We investigate the effects on the optical response properties of InSb and HgSe after including scalar relativistic ZORA in the ground-state DFT, as well as in the time-dependent response calculations. The outline of this paper is as follows. First we show the way in which scalar relativistic ZORA is incorporated in the present TDDFT calculations, and validate the use of the TDDFT equations in this special case of semimetals. This is followed by a section about the method and implementation. Then, in the next sections, we present the results for the band structure, the dielectric constant and function for InSb and HgSe, and compare these with experimental data. Finally, in the last section, we draw the conclusions.

6.3 Theory

Scalar relativistic (SR) effects can be included in the ground-state DFT calculation as described by van Lenthe *et al.* in Refs. [95] and [96] and Philipson *et al.* in Ref. [97], by replacing the kinetic-energy operator by the ZORA term

$$T_{\text{ZORA}}^{\text{SR}} = p \cdot \frac{c^2}{2c^2 - v_{\text{eff}}(\mathbf{r})} p, \quad (6.1)$$

in which $p = -i\nabla$, c the velocity of light, and $v_{\text{eff}}(\mathbf{r})$ the self-consistent effective potential. This results in a semi-metallic band structure for InSb and HgSe, the bottom s -like conduction band is lowered in energy, below the top p -like valence band in the centre of the BZ. The Fermi energy coincides with the three degenerate energy bands of p -character at Γ . Two of these are completely occupied and one is unoccupied, hence there is no Kohn-Sham bandgap. However, the Fermi-surface reduces to a point (Γ), and more importantly, the density of states vanishes at the Fermi energy. In this special case we expect no intraband contributions so we can use our TDDFT formulas [94] as before. The susceptibility of this isotropic material follows as one-third of the trace of the susceptibility tensor according to [63]

$$\chi_e(\omega) = \frac{1}{3} \sum_i \left\{ \frac{-1}{\omega^2 V} [\delta \mathbf{J}_p(\omega) - \delta \mathbf{J}_p(0)]_i \Big|_{\mathbf{E} = -i\omega \mathbf{e}_i} \right\}, \quad (6.2)$$

in which the macroscopic paramagnetic current $\delta \mathbf{J}_p(\omega)$ that is induced by a macroscopic electric field $\mathbf{E}(\omega)$ is obtained from

$$\delta \mathbf{J}_p(\omega) = \int \int \left(\frac{i}{\omega} \chi_{\mathbf{jj}}(\mathbf{r}, \mathbf{r}', \omega) \cdot \mathbf{E}_{\text{mac}}(\omega) + \chi_{\mathbf{j}\rho}(\mathbf{r}, \mathbf{r}', \omega) \delta v_{\text{eff}}(\mathbf{r}', \omega) \right) d\mathbf{r}' d\mathbf{r}. \quad (6.3)$$

Here the induced effective potential $\delta v_{\text{eff}}(\mathbf{r}', \omega)$ is lattice periodic and comprises the induced microscopic part of the Coulomb and exchange-correlation contributions. It is a functional of the induced density and in linear response it can be given in the adiabatic approximation by

$$\delta v_{\text{eff}}(\mathbf{r}, \omega) = \int \frac{\partial v_{\text{eff}}[\rho](\mathbf{r})}{\partial \rho(\mathbf{r}')} \delta \rho(\mathbf{r}', \omega) d\mathbf{r}', \quad (6.4)$$

where the ground-state expression is used for the functional dependence of the $v_{\text{eff}}[\rho](\mathbf{r})$. The induced density is obtained by solving the following equation self-consistently:

$$\delta \rho(\mathbf{r}, \omega) = \int \left(\frac{i}{\omega} \chi_{\rho\mathbf{j}}(\mathbf{r}, \mathbf{r}', \omega) \cdot \mathbf{E}_{\text{mac}}(\omega) + \chi_{\rho\rho}(\mathbf{r}, \mathbf{r}', \omega) \delta v_{\text{eff}}(\mathbf{r}', \omega) \right) d\mathbf{r}'. \quad (6.5)$$

In these equations the various response kernels follow from the expression:

$$\chi_{ab}(\mathbf{r}, \mathbf{r}', \omega) = \frac{V}{4\pi^3} \sum_{i,a} \int \frac{(\psi_{i\mathbf{k}}^*(\mathbf{r}) \hat{a} \psi_{a\mathbf{k}}(\mathbf{r})) (\psi_{a\mathbf{k}}^*(\mathbf{r}') \hat{b} \psi_{i\mathbf{k}}(\mathbf{r}'))}{\epsilon_{i\mathbf{k}} - \epsilon_{a\mathbf{k}} + \omega + i\eta} d\mathbf{k} + c.c.(-\omega), \quad (6.6)$$

in which i runs over all occupied and a over all virtual band indices. The operator \hat{a} and \hat{b} are either the density or the current operator. The acronym $c.c.(-\omega)$ denotes the complex

conjugate expression at negative frequency. The Bloch functions $\psi_{n\mathbf{k}}(\mathbf{r})$ are the solutions of the ground-state ZORA equation with eigenvalues $\epsilon_{n\mathbf{k}}$

$$\left[-\nabla \cdot \frac{c^2}{2c^2 - v_{eff}(\mathbf{r})} \nabla + v_{eff}(\mathbf{r}) \right] \psi_{n\mathbf{k}}(\mathbf{r}) = \epsilon_{n\mathbf{k}} \psi_{n\mathbf{k}}(\mathbf{r}). \quad (6.7)$$

The four appearing kernels are obtained by substituting for \hat{a} and \hat{b} either $\hat{\rho} = 1$ or the relativistic velocity operator $\hat{\mathbf{j}}$, which is given by,

$$\hat{\mathbf{j}} = -i[\mathbf{r}, \hat{\mathcal{H}}_{ZORA}] = -i \frac{c^2}{2c^2 - v_{eff}(\mathbf{r})} \nabla + h.a., \quad (6.8)$$

where *h.a.* is the hermitian adjoint expression. As can be seen by inspecting Eqs. (6.3) and (6.5), the factors involving the operator $\hat{\mathbf{j}}$ are always integrated, so that only the values of the matrix elements matter. The absence of an energy gap, and the quadratic dispersion of the valence and conduction bands make it necessary to investigate the small-frequency behaviour of the response kernels. In Chapter 6.8 Appendix, we show that all off-diagonal matrix elements are of the order $\mathcal{O}(|\mathbf{k}|^2)$, thus falling-off sufficiently fast to smooth any singular behaviour near $\omega = 0$, such that the electrical susceptibility has the asymptotic behavior $\chi_e(\omega) \approx \chi_e(0) + \mathcal{O}(\sqrt{\omega})$.

6.4 Method and Implementation

The ground-state DFT calculations are performed by using the Amsterdam Density Functional BAND-structure program (ADF-BAND) [37, 38]. The general characteristics of this implementation are described in Ref. [94] and more specific details can be found, e.g., about the accurate numerical integration scheme, for evaluating matrix elements between basisfunctions which are either numerical atomic orbitals (NAO) or Slater type exponential functions (STO) in Refs. [37] and [91], the density fitting procedure, for evaluating the Coulomb potential, in Ref. [12], and the quadratic tetrahedron method, for evaluating the integrals over the BZ, in Ref. [48]. In the time-dependent extension [63] on this DFT implementation we employ a lattice periodic (microscopic) effective scalar potential, in combination with a uniform (macroscopic) transverse electric field $\mathbf{E}_{mac}(\mathbf{r}, t)$. For solving the TDDFT equations, an iterative scheme is used, with a fixed macroscopic electric field and in which the microscopic potential is updated in each cycle, until self-consistency in the first order density change $[\delta\rho(\mathbf{r}, \omega)]$ is established. The evaluation of the integrals over the irreducible Brillouin zone (IBZ) in the Kohn-Sham response kernels, $\chi_{ab}(\mathbf{r}, \mathbf{r}', \omega)$ (which show up in the first order density change) are done numerically with integration weights as described in Ref. [94], so singularities in the response kernels, at resonance frequencies, are handled analytically. Finally, after establishing self-consistency in the density change, we obtain the electric susceptibility $\chi_e(\omega)$ and thus the dielectric function $\epsilon(\omega)$ from the (paramagnetic) induced current $\delta\mathbf{j}_p(\mathbf{r}, \omega)$, hereby using the conductivity sumrule. Results for the dielectric function of various nonmetallic crystals using this TDDFT implementation can be found in Ref. [94].

6.5 Results for Indium Antimonide

6.5.1 Band structure

In Fig. 6.1 we show the band structure of InSb, with and without the inclusion of scalar relativistic effects in the ground-state DFT calculation.

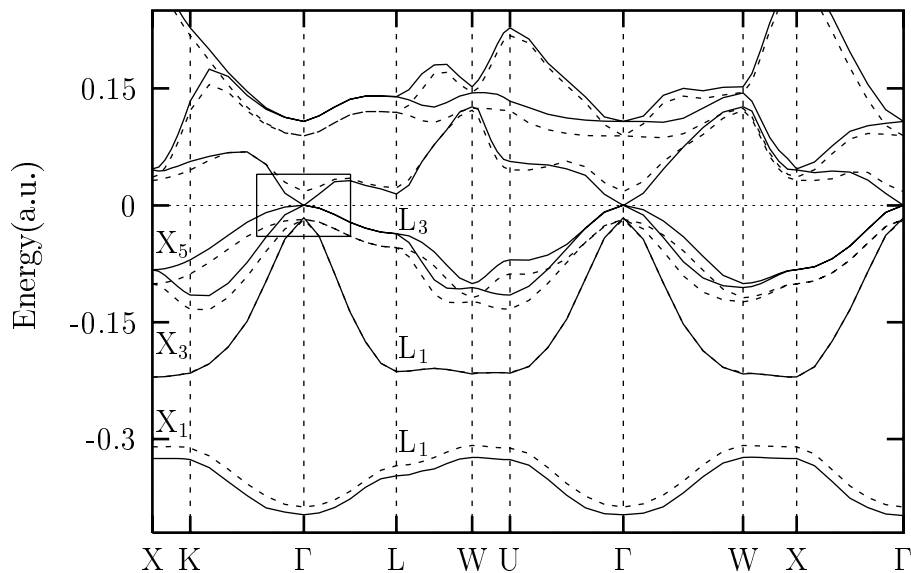


Figure 6.1: Band structure of indium antimonide (InSb), the solid line is the scalar relativistic (SR), and the dashed line is the nonrelativistic (NR) ground-state calculation.

In order to facilitate the comparison between the two band structure calculations we made the Fermi energy levels coincide. The calculations were done by using a 3Z2P NAO/STO basis (basis V in the BAND program), which is a triple zeta basis augmented with two polarization functions and frozen core. In the calculations, the $4d$ atomic states of In and Sb were included in the valence basis. These states give rise to shallow core bands, which can affect the position of the valence band maximum [71, 72]. As can be seen from the band structure in Fig. 6.1 and the blowup of the band structure around the center (Γ) of the BZ in Fig. 6.2, the inclusion of scalar relativistic effects stabilizes the lowest s -like conduction band considerably more than the highest valence bands [98, 99]. Consequently the conduction band is lowered in energy below the top valence bands, and this causes an avoided crossing between the s -like conduction band and one of the valence bands. These bands change in character from s -like to p -like near Γ and vice versa, as indicated in Fig. 6.2. The ordering of the energy bands is changed and the bandgap vanishes at the Γ point. Thus LDA-ZORA predicts InSb to be a semimetal, as was also found in Ref. [100] and in the full-potential scalar relativistic LAPW calculations of Ref. [72]. The inclusion of spin-orbit coupling in the relativistic calculation will only cause a splitting of the top p -like valence bands into an occupied $p_{1/2}$ band and a half occupied $p_{3/2}$

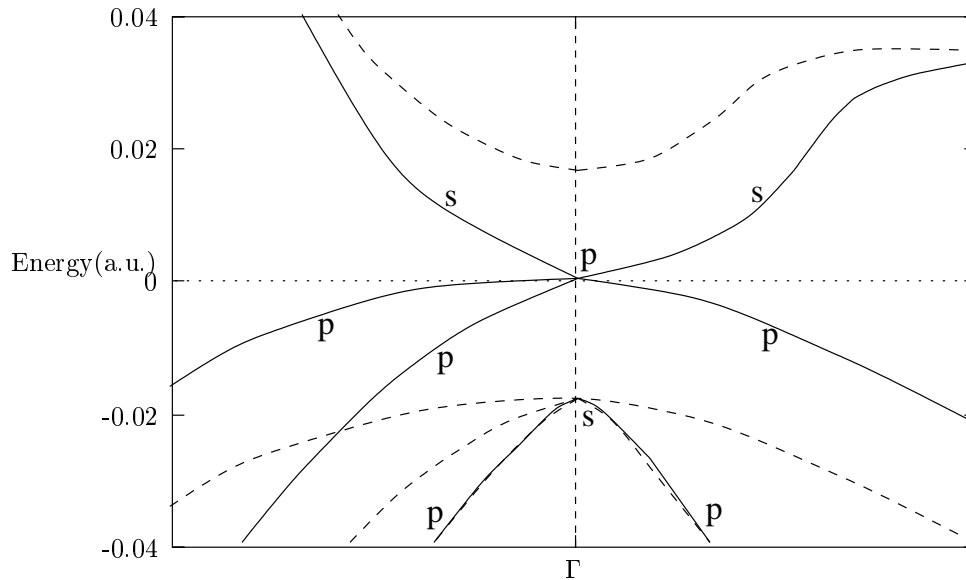


Figure 6.2: Blowup of the band structure around the centre (Γ) of the Brillouin zone, as indicated in Fig. 6.1. The solid line is the SR and the dashed line is the NR ground-state calculation.

band, thereby leaving InSb to be a semimetal, as was confirmed by earlier fully relativistic LMTO calculations in Ref. [71]. Experimentally InSb is found to be a semiconductor with a narrow bandgap of 0.23 eV [7]. In our SR band structure we find the generally accepted trend for DFT-LDA band structure calculations, that the bandgaps are normally underestimated for semiconductors, and in the case of InSb predicting this crystal even to be a semimetal. Nevertheless the scalar relativistic calculated band structure is in good agreement with experiment [101], e.g. comparing the valence band width of 10.8 eV in our SR band structure with experiment [101] of 11.2 eV [ultraviolet photoemission spectroscopy (UPS)] and 11.7 eV [x-ray photoemission spectroscopy (XPS)]. The valence band energies for L_3 , X_3 , and X_1 [see Fig. 6.1] are -1.0, -6.0, and -8.8 eV, respectively, which is also in good agreement with the UPS experimental values of -1.1, -6.5, and -9.0 eV respectively.

6.5.2 Static dielectric constant

In Table 6.1 we give the values for the calculated static dielectric constant (ϵ_∞) for InSb with and without including scalar relativistic effects in the ground-state and also the time-dependent DFT calculation.

For the integration in reciprocal space we used several accuracies, in which we varied the number of \mathbf{k} -points in the irreducible part of the Brillouin zone (IBZ). The improvement upon the static value for the dielectric constant with the inclusion of SR effects in the ground-state DFT calculation is very clear from Table 6.1. Looking at the relative errors compared to the experimental value ($\epsilon_\infty = 15.7$) of Ref. [77], it can be seen that the error is 42% in the non-relativistic calculation, and 8% when scalar relativistic effects were

Table 6.1: Static dielectric constant of InSb including non/scalar relativistic (NR/SR) effects in the ground-state/time-dependent DFT calculation, and error compared to the experimental value of 15.7 [77].

k -space / # k -points	NR/NR	Error (%)	SR/NR	Error (%)	SR/SR	Error (%)
3/15	11.91	24	18.13	15	18.12	15
4/34	11.22	29	16.63	6	16.61	6
5/65	9.15	42	16.91	8	16.42	5

included in the ground-state calculation. From Table 6.1 it can be seen that for the value of ϵ_∞ the inclusion of SR effects in the ground-state DFT calculation is most significant, and that the improvement becomes even more evident when SR effects are also included in the response calculation. Now, after including SR effects for InSb, we find the same accuracy for ϵ_∞ , about 5% deviation from experiment, as we found earlier for the III-V compounds in the zinc-blende structure of Ref. [94]. Other theoretical calculations for the ϵ_∞ of InSb by Huang *et al.* [51] were less accurate, their value of 13.51 underestimates experiment [77] by 14%. This nonrelativistic value was obtained from an uncoupled response calculation in which the χ_0 response is directly calculated from the ground-state DFT solutions, and therefore, this value does not include the Coulomb or exchange-correlation contributions.

6.5.3 Dielectric function

In Fig. 6.3 we show the dielectric function $\epsilon(\omega)$ of InSb, with and without the inclusion of scalar relativistic effects in the ground-state DFT calculation, in comparison with the experimental data of Ref. [46].

The result for $\epsilon(\omega)$ with SR effects also included in the response calculation did not deviate by more than a few percent from the one in which SR effects were only included in the ground-state calculation. The calculated spectra for $\epsilon(\omega)$ were shifted to higher energies in order to facilitate the comparison with experiment in such a way that the zero crossings in the calculated $\text{Re}[\epsilon(\omega)]$ coincided with the experimental zero crossings. The shifts needed to accomplish this were 0.15 eV for the NR and 0.3 eV for the SR spectra. LDA calculated the bandgaps to be 0.99 and $\simeq 0$ eV in the NR and SR case, respectively, and these values should be compared to the experimental gap of 0.23 eV [7]. Therefore, we find, in agreement with earlier findings [94], that there is no direct relation between the necessary shifts of the spectra, and the error in the calculated LDA bandgaps. The improvement upon the calculated (shifted) dielectric function $\epsilon(\omega)$ after the inclusion of scalar relativistic effects in the ground-state DFT calculation is clear from Fig. 6.3. The overall agreement of the $\epsilon(\omega)$ with the inclusion of SR effects and experiment [46] is very good, even though there are still some features to be improved. E.g., the position of the E_2 peak [93] (high-energy peak in $\text{Im}[\epsilon(\omega)]$) coincides with experiment, but it is too sharp and the magnitude is overestimated compared to experiment. Although we do find the right magnitude for the E_1 peak (low-energy peak in $\text{Im}[\epsilon(\omega)]$), the double peak structure found in experiment is not reproduced.

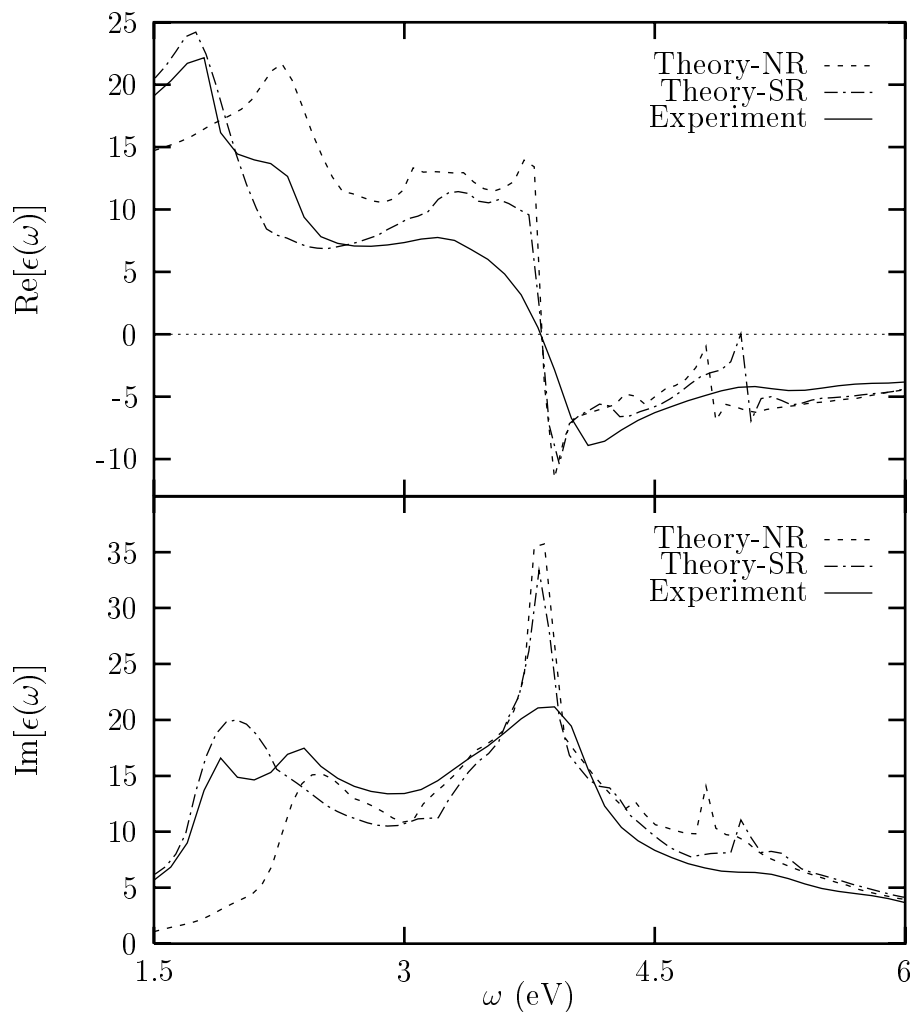


Figure 6.3: Plots of the real and imaginary part of the calculated dielectric function of InSb including non/scalar relativistic (NR/SR) effects in the ground-state/time-dependent DFT calculation, in comparison with the experimental data [46]. The calculated spectra are shifted 0.15 eV NR, and 0.3 eV in the SR case.

6.6 Results for Mercury Selenide

The optical response calculations on HgSe were performed using the full-potential ADF-BAND package [37, 38]. For both the ground state and the response calculations we used the free-atom core and valence orbitals, which were supplemented with Slater-type functions to form a triple-zeta valence basis. The free atom orbitals were obtained numerically using a Herman-Skillman type program [43] employing the same ZORA approximation in the relativistic case. We kept the deepest core levels frozen and orthogonalized the valence basis to these cores, but the shallow $5d$ quasi-core states of Hg were included in the valence set. This basis was then further augmented using a double-zeta polarization set. All matrix elements were evaluated numerically with a relative accuracy of $1e-3$. For the numerical evaluation of \mathbf{k} -space integrals, 175 symmetry-unique points were used to sample the irreducible wedge of the Brillouin zone. As lattice parameter of the HgSe zinc-blende structure we used $a = 6.08 \text{ \AA}$.

6.6.1 Bandstructure, static dielectric constant and the dielectric function

The experimental optical data compiled in Ref. [104] have been used to derive the low frequency behavior for the dielectric function of HgSe. The room temperature refractive index data, which show a large scatter, were used in the frequency range above 0.2 eV to fit a quadratic polynomial in a least squares procedure (Fig. 6.5). In this range both the temperature dependence and the intraband contributions due to impurity carriers are small [104]. This refractive index measurements together with the absorption coefficients obtained at 5K [104], provided the data to derive the experimental dielectric function in the infrared frequency range from 0.2 to 0.55 eV. We thus find an extrapolated value of 11.7 for the dielectric constant ϵ_∞ . For the optical and ultraviolet frequencies we used ellipsometric data [106] in the range from 1.75 to 5.35 eV.

In Fig. 6.4 we have depicted the energy dispersion of the highest valence and lowest conduction bands of HgSe. These bandstructures are shown for the two cases where we either included or excluded the relativistic effects. We can clearly see that the small direct gap at the center of the Brillouin zone Γ is reduced, and even inverted, upon inclusion of the scalar relativistic effects. The s -like ($6s$ Hg) states at the conduction band minimum are stabilized with respect to the p -like ($4p$ Se) states at the valence band maximum mainly due to the relativistic mass-velocity effect near the nucleus of Hg. This inversion of the typical band order [71] of zinc-blende type semiconductors results in an avoided crossing, even at high symmetry directions, since the s -like band hybridizes with one of these p -like bands into Γ_{6v} . This results in an inverted gap of about -1.16 eV, which overestimates the experimental value of -0.45 eV by about 0.8 eV [104]. A further inclusion of spin-orbit coupling will split the p -like Se bands into an occupied $p_{\frac{1}{2}}$ band (Γ_{7v}) about 0.3 eV [105] below a half-occupied $p_{\frac{3}{2}}$ degenerate pair of bands (Γ_{8cv}), hence preserving the semimetallic nature of the bandstructure.

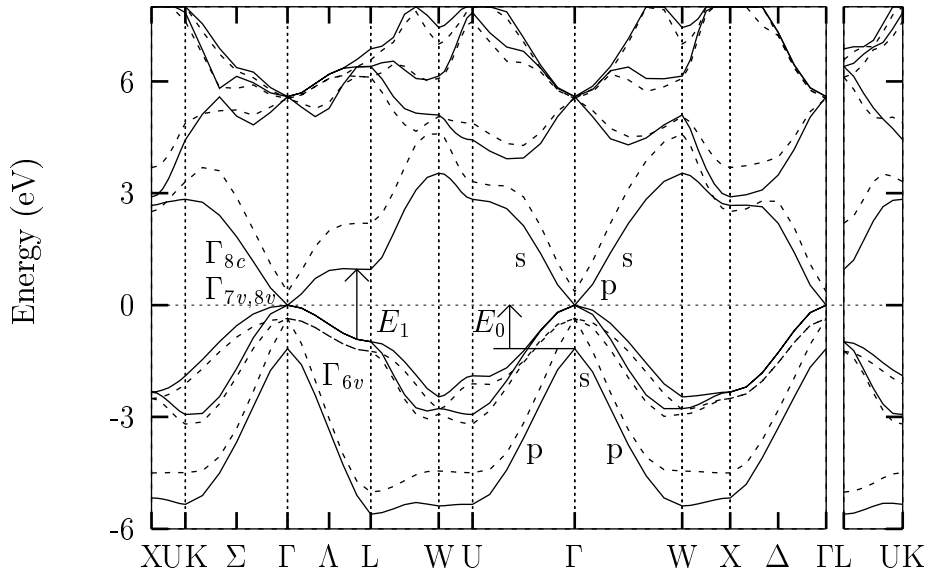


Figure 6.4: The inverted band structure of HgSe. The solid line is the result with scalar relativistic effects included. The dashed line is the nonrelativistic ground-state calculation. Critical points E_0 and E_1 and the band character (s or p) are indicated near the zone center Γ .

This splitting will cause the Γ_{8cv} bands to be raised by about 0.1 eV (and the Γ_{7v} band to be lowered by about 0.2 eV), thus further increasing the inverted LDA gap to about -1.26 eV. This is in good agreement with the relativistic pseudopotential/LDA result (-1.27 eV) of Rohlfiing and Louie [105], in which spin-orbit splitting was included. They found that quasiparticle (QP) corrections (within the GW approximation) mainly affect the s -like states, moving them upward rigidly by about 0.8 eV, thus reducing the gap $\Gamma_{6v} - \Gamma_{8cv}$ to about -0.51 eV. In the experimental optical spectra of HgSe, shown in Fig. 6.5, this inverted gap appears as the critical point labelled E_0 at about 0.5 eV [104]. However, the absorption edge visible in the experiment at about 0.3 eV is most likely due to the transition between the bands connecting to Γ_{8v} and Γ_{8c} , which is symmetry forbidden at Γ , but becomes allowed outside this point since there Γ_{8c} changes character rapidly from p - to s -like. Simultaneous with the changing of Γ_{8c} the band connecting to Γ_{6v} changes from s - to p -character, while the bands connecting to Γ_{8v} and Γ_{7v} remain of p -character. The quasiparticle shift of the s -like states will bring the s - and p -like bands closer together at Γ which will further enhance the steepness of the transition in character. This will allow for optical transitions of lower frequency, with a steeper edge in the absorption spectrum. The gap of about 1.95 eV between the nearly parallel top valence and lowest conduction band along the line Λ and at the point L at the zone boundary gives rise to the critical point E_1 . This gap is again increased by about 0.80 eV when QP corrections are included. The top valence states $\Lambda_{4,5}$ along this line Λ will split by about 0.8 eV upon inclusion of spin-orbit coupling [71], but the bottom conduction band Λ_6 will not. This will give rise to a doublet structure in the dielectric function [104], which is however not clearly resolved

experimentally at room temperature [106].

The TDDFT result for the dielectric function, depicted in Fig. 6.5, shows a drastic change with the inclusion of the scalar relativistic corrections. We observe an almost fourfold increase in the absorption in the range from 1 to 3 eV, with a prominent E_1 -feature just above 2.2 eV. The experimental E_1 -peak appears around 3 eV. This shift is consistent with the underestimation of the energy gap along the line Λ in our ground state DFT-LDA calculation. Due to the Kramers-Kronig relation, the too low position of this peak will give rise to a too high calculated value for the dielectric constant $\epsilon_\infty = 14.4$, vs. 11.7 experimentally.

It is clear that with the removal of the energy gap, also the absorption onset has disappeared, although we do not reproduce the steep increase at the absorption edge $\Gamma_{8v} \rightarrow \Gamma_{8c}$. The E_0 critical point shows up as a knee in the calculation at around 1.25 eV (experimentally 0.45 eV), where again the relative shift of about 0.8 eV is in agreement with the overestimation of the $\Gamma_{6v} - \Gamma_{8c}$ gap in the ground-state calculation.

These findings are quite similar to the results we obtained previously for the InSb crystal [102]. For comparison, the relativistic and non-relativistic bandstructures of InSb are shown in Fig. 6.1. Here again the order of the energy bands is inverted at the point Γ within the local density approximation upon inclusion of relativistic effects. The interchanged s - and p -like character of the upper valence bands and the lowest conduction band switches back to the usual ordering just outside the zone center, along the same lines as in the analyses given above for HgSe. The inverted bandgap is much smaller than in HgSe, in InSb it is -0.42 eV, whereas in HgSe it is -1.26 eV. Experimentally, however, InSb is not found to be a semimetal but a narrow-gap semiconductor, with a direct gap of 0.23 eV [7]. A QP-correction of 0.65 eV for the s -like band, similar to the rigid 0.8 eV energy shift for the s -like band in HgSe would revert the LDA-band ordering in InSb again, resulting in a semiconducting bandstructure. In our LDA calculation for InSb, unlike the dispersion of the HgSe bands, both the lowest conduction band and the band connecting to Γ_{6v} have very strong dispersions, which hence corresponds to very low densities of states. We can therefore expect a very small contribution to the absorption at the E_0 critical point. We get a good overall agreement in the low energy range, with a value of 16.4 for ϵ_∞ (15.7 experimentally [77]), which can be inferred by comparing the calculated dielectric function with the available experimental data [46] as depicted in Fig. 6.3. To facilitate the comparison, the calculated spectra have been shifted 0.30 eV to higher energy in the relativistic case and 0.15 eV for the nonrelativistic case. These shifts have been determined, such that the frequencies at which the respective real parts become negative coincide, effectively fixing the position of the very sharp E_2 at the experimental value. We do not reproduce the double peak feature at the critical point E_1 which requires inclusion of spin-orbit effects in the calculation. The spin-orbit splitting of the upper valence bands along the line Λ varies from about 0.8 eV at Γ [71, 107] to about 0.5 eV at the zone boundary L [71]. This results in the experimentally clearly resolved doublet structure at about 2 and 2.5 eV.

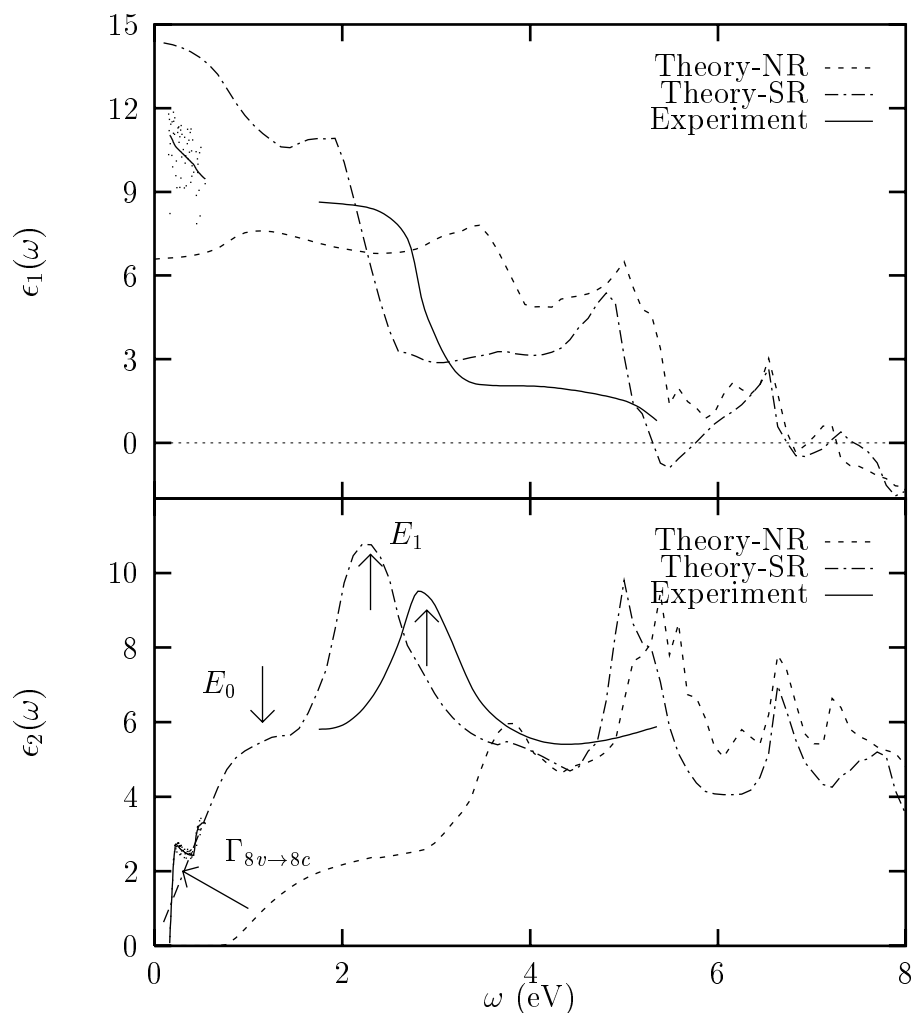


Figure 6.5: Plots of the real (top) and imaginary part (bottom) of the calculated dielectric function of HgSe with (SR, dash-dotted line) or without (NR, dotted line) including scalar relativistic effects. The experimental data have been compiled from the Refs. [104] and [106] (dots and solid line, for discussion see text).

6.7 Conclusions

We show how to include scalar relativistic effect within the zeroth-order regular approximation in time-dependent density-functional theory for the optical response properties of nonmetallic crystals. These TDDFT equations can also be applied to calculate the optical response properties of semimetals, because they do not show any singular behavior even though the Kohn-Sham bandgap vanishes. The band structure of InSb and HgSe show a considerable stabilization of the s -like conduction band minimum with the inclusion of SR effects in the ground-state DFT calculation. LDA predicts the bandgap in the Γ point even to vanish, and therefore predicting them to be a semimetals. The relative error in the static

value of the dielectric constant for InSb becomes 5% compared to experiment when SR effects are included in the ground-state DFT calculation as well as in the time-dependent response calculation. The same accuracy as was found earlier with our TDDFT implementation for the III-V compounds in the zinc-blende structure. The dielectric functions for InSb and HgSe, with inclusion of SR effects are clearly improved over the NR ones, and are quite good compared to experiment, although the spectral features are still somewhat shifted to too low energies compared to experiment.

6.8 Appendix: Small-Frequency Response

As we argued before, it is instructive to investigate the \mathbf{k} -dependence of the off-diagonal $\hat{\mathbf{j}}$ -matrix elements for the critical bands and region around Γ . Therefore, let us consider the following $\mathbf{k} \cdot \mathbf{p}$ analytic continuation of the Bloch, respectively, eigenfunctions near a special \mathbf{k} -point. The Bloch theorem allows for the following expansion:

$$\psi_{n\mathbf{k}+\mathbf{h}}(\mathbf{r}) = \exp(i\mathbf{h} \cdot \mathbf{r}) \sum_s c_{n\mathbf{k}}^s(\mathbf{h}) \phi_{s\mathbf{k}}(\mathbf{r}), \quad (6.9)$$

where the particular choice of eigenfunctions $\phi_{s\mathbf{k}}(\mathbf{r})$ constitutes a complete orthogonal basis at \mathbf{k} . In order to establish the orthogonality also for the $\psi_{n\mathbf{k}+\mathbf{h}}(\mathbf{r})$ functions the expansion coefficients have to satisfy

$$\sum_s c_{n\mathbf{k}}^{s*}(\mathbf{h}) c_{m\mathbf{k}}^s(\mathbf{h}) = \delta_{nm}. \quad (6.10)$$

These coefficients can be found by substituting the expansion in the scalar relativistic Kohn-Sham equation and by calculating the inner products with respect to $\exp(i\mathbf{h} \cdot \mathbf{r}) \psi_{s\mathbf{k}}(\mathbf{r})$. This yields the set of equations

$$\sum_t \left[\mathbf{h} \cdot \langle \phi_{s\mathbf{k}} | \hat{\mathbf{j}} | \phi_{t\mathbf{k}} \rangle + \left(\gamma_{s\mathbf{k}} h^2 - \epsilon_{n\mathbf{k}+\mathbf{h}} + \epsilon_{s\mathbf{k}} \right) \delta_{st} \right] c_{n\mathbf{k}}^t(\mathbf{h}) = 0, \quad (6.11)$$

in which the factor $\gamma_{s\mathbf{k}} = \langle \phi_{s\mathbf{k}} | \gamma(\mathbf{r}) | \phi_{s\mathbf{k}} \rangle$, where we introduced the shorthand notation $\gamma(\mathbf{r}) = c^2 / (2c^2 - v_{eff}(\mathbf{r}))$. In the limit of $h \rightarrow 0$ the expression reduces to the simple relation $(\epsilon_{s\mathbf{k}} - \epsilon_{n\mathbf{k}}) c_{n\mathbf{k}}^s(\mathbf{0}) = 0$. Thus the coefficients $c_{n\mathbf{k}}^s(\mathbf{h})$ have to vanish asymptotically unless $\epsilon_{s\mathbf{k}} = \epsilon_{n\mathbf{k}}$ and hence they constitute an ordinary unitary transformation that mixes merely degenerate states. Using these relations we can now evaluate the analytic continuation of the (vertical) $\hat{\mathbf{j}}$ -matrix elements near \mathbf{k} . First consider

$$\langle \psi_{n\mathbf{k}+\mathbf{h}} | -i\gamma(\mathbf{r}) \nabla | \psi_{m\mathbf{k}+\mathbf{h}} \rangle = \sum_{s,t} c_{n\mathbf{k}}^{s*}(\mathbf{h}) \langle \phi_{s\mathbf{k}} | \gamma(\mathbf{r}) (\mathbf{h} - i\nabla) | \phi_{t\mathbf{k}} \rangle c_{m\mathbf{k}}^t(\mathbf{h}). \quad (6.12)$$

The current matrices follow directly by adding the hermitian adjoint to this expression. Note that $\gamma(\mathbf{r}) = c^2 / (2c^2 - v_{eff}(\mathbf{r}))$ involves only the fully symmetric ground-state potential. The orthogonality of degenerate $\phi_{s\mathbf{k}}(\mathbf{r})$ eigenfunctions is due to symmetry, which is not affected by this totally symmetric factor. The orthogonality involving nondegenerate states with $\epsilon_{s\mathbf{k}} \neq \epsilon_{n\mathbf{k}}$ can be affected, but here the expansion coefficients behave asymptotically

as $c_{n\mathbf{k}}^s(\mathbf{h}) \propto h$, i.e., they vanish in zeroth order as argued above. Since the factor $\gamma_{s\mathbf{k}} = \langle \phi_{s\mathbf{k}} | \gamma(\mathbf{r}) | \phi_{s\mathbf{k}} \rangle$ is identical for each partner of the set of degenerate states $\epsilon_{s\mathbf{k}} = \epsilon_{n\mathbf{k}}$, we can apply Eq. (6.10) and thus get

$$\mathbf{j}_{nm}(\mathbf{k} + \mathbf{h}) = 2\gamma_{n\mathbf{k}}\delta_{nm}\mathbf{h} + \mathcal{O}(h^2) + \sum_{s,t} c_{n\mathbf{k}}^{s*}(\mathbf{h}) \langle \phi_{s\mathbf{k}} | \hat{\mathbf{j}} | \phi_{t\mathbf{k}} \rangle c_{m\mathbf{k}}^t(\mathbf{h}). \quad (6.13)$$

By taking the derivative with respect to \mathbf{h} of the $\mathbf{k} \cdot \mathbf{p}$ equation (6.11), one can readily deduce that

$$\begin{aligned} \sum_{s,t} c_{n\mathbf{k}}^{s*}(\mathbf{h}) \langle \phi_{s\mathbf{k}} | \hat{\mathbf{j}} | \phi_{t\mathbf{k}} \rangle c_{m\mathbf{k}}^t(\mathbf{h}) = \\ [\nabla_{\mathbf{h}} \epsilon_{n\mathbf{k}+\mathbf{h}} - 2\gamma_{n\mathbf{k}}\mathbf{h}] \delta_{nm} + [\epsilon_{n\mathbf{k}+\mathbf{h}} - \epsilon_{m\mathbf{k}+\mathbf{h}}] \sum_s c_{n\mathbf{k}}^{s*}(\mathbf{h}) \nabla_{\mathbf{h}} c_{m\mathbf{k}}^s(\mathbf{h}). \end{aligned} \quad (6.14)$$

In the limit $h \rightarrow 0$ we thus get for the diagonal terms $n = m$

$$\nabla_{\mathbf{k}} \epsilon_{n\mathbf{k}} = \sum_{s,t} c_{n\mathbf{k}}^{s*}(\mathbf{0}) \langle \phi_{s\mathbf{k}} | \hat{\mathbf{j}} | \phi_{t\mathbf{k}} \rangle c_{n\mathbf{k}}^t(\mathbf{0}) = \langle \psi_{n\mathbf{k}} | \hat{\mathbf{j}} | \psi_{n\mathbf{k}} \rangle, \quad (6.15)$$

a well-known result. In this particular case, i.e., for the critical states $\epsilon_{s\mathbf{k}} = \epsilon_{t\mathbf{k}} = \epsilon_{\text{Fermi}}$ at $\mathbf{k} = \Gamma$, all diagonal $\hat{\mathbf{j}}$ -matrix elements vanish due to symmetry, so that we get a quadratic energy dispersion relation $\epsilon_{n\mathbf{k}} - \epsilon_{n\mathbf{0}} \propto k^2$. The leading order terms are then given by

$$\mathbf{j}_{nm}(\mathbf{k}) \approx \mathcal{O}(k)\delta_{nm} + \mathcal{O}(k^2), \quad (6.16)$$

so we get a quadratic leading order in the off-diagonal $\hat{\mathbf{j}}$ -matrix elements in the case of $\epsilon_{n\mathbf{k}} = \epsilon_{m\mathbf{k}} = \epsilon_{\text{Fermi}}$ with $n \neq m$.

In the subsequent analysis we can neglect any anisotropy in the energy dispersion, as well as the angular dependence of the $\hat{\mathbf{j}}$ -matrix elements, without invalidating the arguments. In the evaluation of the small frequency behaviour of the critical contributions to the various response kernels $\chi_{ab}(\omega)$, we encounter integrals of the following general form:

$$\Delta\chi_{ab}(\omega) \propto \int_{\Omega} \frac{(a_n(\mathbf{k}) + (-1)^n a_n^*(\mathbf{k})) k^{2n}}{k^2 - \omega + i\eta} d\mathbf{k} + c.c.(-\omega), \quad (6.17)$$

where Ω is a small sphere surrounding Γ and n is the number of times the off-diagonal $\hat{\mathbf{j}}$ -matrix elements appear in the numerator, i.e., $n=0$ for $\chi_{\rho\rho}(\omega)$, $n=1$ for $\chi_{\rho\mathbf{j}}, \chi_{\mathbf{j}\rho}(\omega)$, and $n=2$ for $\chi_{\mathbf{j}\mathbf{j}}(\omega)$. Note that the diagonal elements do not contribute at all. The functions $a_n(\mathbf{k}) \approx a_n(\mathbf{0}) + \mathcal{O}(k)$ are regular functions of \mathbf{k} . The contributions of $\psi_{n\mathbf{k}}$ and $\psi_{n-\mathbf{k}} = \psi_{n\mathbf{k}}^*$ are related due to time-reversal symmetry, which has been made explicit in the combination of $a_n(\mathbf{k})$ and $a_n^*(\mathbf{k})$ in the numerator. These integrals can be evaluated directly, with a general structure given by

$$\Delta\chi_{ab}(\omega) \propto p_n(\omega) + \omega^n \sqrt{|\omega|} \cdot [q(\omega) - 2i\pi^2\theta(\omega)] + \mathcal{O}(h^{n+2}), \quad (6.18)$$

in which the polynomial part $p_n(\omega)$ of order n contains only even(odd) powers of ω for even(odd) n , just like the regular contributions to the response functions which result from

the nondegenerate bands. The additional terms [in which $\theta(\omega)$ is the unit stepfunction and $q(\omega)$ a regular function of ω] scale like $\omega^n \sqrt{|\omega|}$ which is just one-half an order higher. We can conclude that the absence of a band gap does not lead to irregular contributions to the response functions, and that we can expect a small frequency behaviour of $\chi_e(\omega) \approx \chi_e(0) + \mathcal{O}(\sqrt{\omega})$.

Chapter 7

A polarization dependent functional

P. L. de Boeij, F. Kootstra, J. A. Berger, R. van Leeuwen, and J. G. Snijders, "*Current density functional theory for optical spectra, a polarization functional*", J. Chem. Phys. **115**, 1995-1999 (2001).

7.1 Abstract

We present a new approach to calculate optical spectra, which for the first time uses a polarization dependent functional within current density functional theory (CDFT), which was proposed by Vignale and Kohn [108]. This polarization dependent functional includes exchange-correlation (xc) contributions in the effective macroscopic electric field. This functional is used to calculate the optical absorption spectrum of several common semiconductors. We achieved in all cases good agreement with experiment.

7.2 Introduction

Time-dependent density functional theory (TDDFT), as formulated by Runge and Gross [4], makes it *in principle* possible to study the dynamical properties of interacting many-particle systems. The formulation of a local *dynamical* approximation for the xc potential turns out to be extremely difficult, because such an xc potential in TDDFT is an intrinsically nonlocal functional of the density (i.e., there does not exist a gradient expansion for the frequency-dependent xc potential in terms of the density alone). Vignale and Kohn [108] were the first who formulated a local gradient expansion in terms of the *current density*. In a time-dependent current density functional approach to linear response theory, they derived an expression for the linearized xc vector potential $\mathbf{a}_{xc}(\mathbf{r}, \omega)$ for a system of slowly varying density, subject to a spatially slowly varying external potential at a finite frequency ω .

7.3 Theory

Let us first recall our definitions for the macroscopic electric field and polarization, before we derive an expression in which the macroscopic xc potential contributions of Vignale and Kohn [108] are incorporated. If we apply a time-dependent electric field of frequency ω , we will induce a macroscopic polarization $\mathbf{P}_{\text{mac}}(\omega)$ which will be proportional to the macroscopic field $\mathbf{E}_{\text{mac}}(\omega)$, i.e., the applied field plus the average electric field caused by induced charges in the solid. The constant of proportionality is known as the electric susceptibility and is a material property,

$$\mathbf{P}_{\text{mac}}(\omega) = \chi(\omega) \cdot \mathbf{E}_{\text{mac}}(\omega). \quad (7.1)$$

The macroscopic polarization is defined by the induced current density,

$$\mathbf{P}_{\text{mac}}(\omega) = \frac{i}{\omega V} \int_V \delta \mathbf{j}(\mathbf{r}, \omega) d\mathbf{r}. \quad (7.2)$$

We see that if we want to calculate the susceptibility and the related dielectric function we need to calculate the induced current. The induced current $\delta \mathbf{j}$ and induced density $\delta \rho$ can, in principle, be calculated from the current-current and density-current response functions of the solid in the following way, where we use a shortened notation which implies integration over spatial coordinates [63]:

$$\delta \mathbf{j} = \frac{i}{\omega} \chi_{\mathbf{j}\mathbf{j}} \cdot \mathbf{E}_{\text{mac}}, \quad (7.3)$$

$$\delta \rho = \frac{i}{\omega} \chi_{\rho\mathbf{j}} \cdot \mathbf{E}_{\text{mac}}. \quad (7.4)$$

This requires, however, knowledge of the exact response functions of the system. Within a Kohn-Sham formulation the exact density and current response are calculated as the response of an auxiliary noninteracting system to an effective electric field and potential,

$$\delta \mathbf{j} = \frac{i}{\omega} \chi_{\mathbf{j}\mathbf{j}}^s \cdot \mathbf{E}_{\text{eff}} + \chi_{\mathbf{j}\rho}^s \delta v_{\text{eff}}, \quad (7.5)$$

$$\delta \rho = \frac{i}{\omega} \chi_{\rho\mathbf{j}}^s \cdot \mathbf{E}_{\text{eff}} + \chi_{\rho\rho}^s \delta v_{\text{eff}}, \quad (7.6)$$

where the superscript s indicates that we are dealing with the response functions of the noninteracting Kohn-Sham system. The equations above are our basic equations of time-dependent current-density functional theory (TDCDFT). The effective fields have the property that they produce the exact density and current when applied to the Kohn-Sham system. Hence they are functionals of $\delta \mathbf{j}$ and $\delta \rho$, and have to be obtained self consistently. If we neglect the microscopic contributions to the transverse components, we can split up these fields as follows

$$\mathbf{E}_{\text{eff}}(\omega) = \mathbf{E}_{\text{mac}}(\omega) + \mathbf{E}_{\text{xc,mac}}(\omega), \quad (7.7)$$

$$\delta v_{\text{eff}}(\mathbf{r}, \omega) = \delta v_{\text{mic}}(\mathbf{r}, \omega) + \delta v_{\text{xc,mic}}(\mathbf{r}, \omega), \quad (7.8)$$

where v_{mic} is the microscopic part of the Hartree potential and $v_{\text{xc,mic}}$ is the microscopic part of the exchange-correlation potential. The term $\mathbf{E}_{\text{xc,mac}}$ denotes the macroscopic xc-electric field. The gauge is chosen in such a way that the microscopic parts of the external field are included in the scalar potential and the macroscopic part of the fields are included in the vector potential. Our goal is to derive an expression for $\mathbf{E}_{\text{xc,mac}}$. Let us first look at the consequences of such a term. With Kohn-Sham theory the macroscopic polarizability is proportional to the effective field \mathbf{E}_{eff} . This defines a Kohn-Sham susceptibility $\tilde{\chi}$ by the equation,

$$\mathbf{P}_{\text{mac}}(\omega) = \tilde{\chi}(\omega) \cdot \mathbf{E}_{\text{eff}}(\omega). \quad (7.9)$$

We are, however, interested in the actual susceptibility χ . With the Eqs. 7.1, 7.7, and 7.9 we obtain

$$(\tilde{\chi}^{-1}(\omega) - \chi^{-1}(\omega)) \cdot \mathbf{P}_{\text{mac}}(\omega) = \mathbf{E}_{\text{xc,mac}}(\omega). \quad (7.10)$$

We see that we can calculate the susceptibility χ once we know how to calculate $\mathbf{E}_{\text{xc,mac}}$. In previous calculations [63, 94], $\mathbf{E}_{\text{xc,mac}}$ was simply put to zero, which yields the approximation $\chi = \tilde{\chi}$. Here we want to improve upon this approximation and derive an explicit expression for $\mathbf{E}_{\text{xc,mac}}$. The starting point is the current-density functional derived by Vignale and Kohn [108, 109] which we write in the compact form derived by Vignale, Ullrich and Conti [$\mathbf{E}_{\text{xc1}}(\mathbf{r}, \omega) \equiv \frac{i\omega}{c} \mathbf{a}_{\text{xc}}(\mathbf{r}, \omega)$] [110],

$$-E_{\text{xc1},i}(\mathbf{r}, \omega) = -\partial_i v_{\text{xc1}}^{\text{ALDA}} + \frac{1}{\rho_0(\mathbf{r})} \sum_j \partial_j \sigma_{\text{xc},ij}(\mathbf{r}, \omega). \quad (7.11)$$

Here $E_{\text{xc1},i}$ is the induced xc-electric field in linear response and $v_{\text{xc1}}^{\text{ALDA}}$ is the first order change in the xc-potential in the adiabatic local density approximation (ALDA). The last term contains the ground state density ρ_0 of the system and the viscoelastic stress tensor,

$$\sigma_{\text{xc},ij} = \tilde{\eta}_{\text{xc}} \left(\partial_j u_i + \partial_i u_j - \frac{2}{3} \delta_{ij} \left(\sum_k \partial_k u_k \right) \right) + \tilde{\zeta}_{\text{xc}} \delta_{ij} \left(\sum_k \partial_k u_k \right). \quad (7.12)$$

Here $\mathbf{u}(\mathbf{r}, \omega) = \delta \mathbf{j}(\mathbf{r}, \omega) / \rho_0(\mathbf{r})$ is the induced velocity field and the constants $\tilde{\eta}_{\text{xc}}(\rho_0, \omega)$ and $\tilde{\zeta}_{\text{xc}}(\rho_0, \omega)$ are coefficients, which can be expressed in terms of the transverse and longitudinal xc-kernels of the electron gas [110]. In order to isolate the macroscopic component of the xc-electric field we take the average over a unit cell of the solid and obtain

$$\mathbf{E}_{\text{xc,mac}}(\omega) = \frac{i}{\omega} \sum_k \frac{1}{\Omega} \int_{\Omega} d\mathbf{r} y_{ik}(\mathbf{r}, \omega) \delta j_k(\mathbf{r}, \omega), \quad (7.13)$$

where Ω denotes the unit cell volume and we defined the matrix

$$y_{ik}(\mathbf{r}, \omega) = -\delta_{ik} \frac{\nabla \cdot (f_{\text{xcT}} \nabla \rho_0)}{\rho_0} - \frac{\partial_k (h_{\text{xc}} \partial_i \rho_0)}{\rho_0}. \quad (7.14)$$

Here $f_{\text{xcT}}(\rho_0, \omega)$ is the transverse xc-kernel of the electron gas and $h_{\text{xc}}(\rho_0, \omega)$ is given as

$$h_{\text{xc}}(\rho_0, \omega) = f_{\text{xcL}}(\rho_0, \omega) - f_{\text{xcT}}(\rho_0, \omega) - \frac{d^2 e_{\text{xc}}}{d\rho_0^2}. \quad (7.15)$$

Here $f_{xcL}(\rho_0, \omega)$ is the longitudinal part of the electron gas xc-kernel and e_{xc} the xc-energy per volume unit of the electron gas. The equation for the macroscopic part of the xc-electric field can be simplified if we replace $\delta\mathbf{j}$ by its macroscopic value, i.e., its average over the unit cell. In that case we obtain

$$\mathbf{E}_{xc,mac}(\omega) = \frac{i}{\omega} \mathbf{Y}([\rho_0], \omega) \cdot \delta\mathbf{j}(\omega) = \mathbf{Y}([\rho_0], \omega) \cdot \mathbf{P}_{mac}(\omega). \quad (7.16)$$

Here the tensor \mathbf{Y} is given by

$$\mathbf{Y}([\rho_0], \omega) = \frac{1}{\Omega} \int_{\Omega} d\mathbf{r} \frac{(\nabla\rho_0)^2}{\rho_0^2} f_{xcT}(\rho_0, \omega) + \frac{1}{\Omega} \int_{\Omega} d\mathbf{r} \frac{\nabla\rho_0 \otimes \nabla\rho_0}{\rho_0^2} h_{xc}(\rho_0, \omega). \quad (7.17)$$

Equation (7.16) represents the first explicit example of the often discussed density-polarization functional [27, 111, 112]. With this functional and the Eqs. 7.1, 7.7, and 7.9, we see that the susceptibility becomes equal to

$$\chi(\omega) = (1 - \tilde{\chi}(\omega) \mathbf{Y}([\rho_0], \omega))^{-1} \tilde{\chi}(\omega). \quad (7.18)$$

This equation clearly displays the influence of the macroscopic xc-electric field on the susceptibility. It remains to find an appropriate approximation for the functions f_{xcT} and f_{xcL} . These functions have been investigated in detail for the electron gas [113, 114, 115, 116]. In these works it has been shown that they are smooth functions of the frequency, except at twice the plasma frequency. For the optical spectra we are, however, interested in much smaller frequencies. In the limit $\omega \rightarrow 0$ the function $h_{xc}(\rho_0, \omega)$ becomes equal to $f_{xcT}(\rho_0, 0)/3$ [110]. In that limit the tensor $\mathbf{Y}([\rho_0], 0)$ is completely determined by $f_{xcT}(\rho_0, 0)$.

7.4 Calculations

We have tested this new functional for silicon as an example of a group IV semiconductor in the diamond structure. We used Eq. 19 (and the values of μ_{xc} in Table I) of Ref. [115], to obtain values for $f_{xcT}(\rho_0, 0)$ at arbitrary ρ_0 , thereby using a cubic spline interpolation in the range 0-5 for the r_s values, in which we take into account the exactly known small r_s behavior [116]. The macroscopic dielectric function $\epsilon(\omega)$ can be obtained directly from the electric susceptibility $\chi(\omega)$ through $\epsilon(\omega) = 1 + 4\pi\chi(\omega)$. The optical absorption spectrum ϵ_2 for Si, shows two major peaks in the range from 3-6 eV [45, 46]. The first peak (E_1) is attributed to an M_0 - or M_1 -type critical point transition, and the second (E_2) one to an M_2 type [56, 93]. All previous "one-electron" approximations, ranging from the early pseudopotential approaches in the 1970s [118, 119], to the *ab initio* DFT-LDA of the end 1990s [120], showed the same features for ϵ_2 . However, the E_1 peak is usually underestimated, and appears just as a shoulder, whereas the E_2 is overestimated and appears at too high energies compared to experiment [45, 46]. The underestimation of the E_1 peak was attributed to excitonic effects (the attractive interaction between the

virtual hole and the *excited* electron). In the recent calculations [121], these excitations are explicitly taken into account by solving the Bethe-Salpeter equation (BSE) for the coupled electron-hole excitations, and in these spectra the E_1 peak is clearly resolved and in good agreement with experiment [45, 46]. The ratio of the E_1 - E_2 peak heights in the ϵ_2 of Si proved to be rather sensitive to the numerical value of $\mathbf{Y}([\rho_0], 0)$. However, it turned out that the theoretical value that we list in Table 7.1, is too high by about a factor of 2. In view of the uncertainty in the published values of $f_{xcT}(\rho_0, 0)$ [116], we introduce a prefactor of 0.4 in front of the matrix $\mathbf{Y}([\rho_0], 0)$ in Eq. 7.18, which was determined in order to get an optimal agreement with experiment for the ratio of the E_1 - E_2 peak heights. This prefactor is used in all the subsequent cases.

7.5 Results

7.5.1 Silicon

In Fig. 7.1, we show the effect of this polarization functional on the $\epsilon(\omega)$ of Si in comparison with experiment [45, 46]. In order to facilitate the comparison with experiment, the spectra have been shifted to higher energies, see Table 7.1.

Table 7.1: The calculated values for $\mathbf{Y}([\rho_0], 0)$, and the applied energy shifts to the dielectric functions, for the crystals in the Figs. 7.1 - 7.5.

Solid	$\mathbf{Y}([\rho_0], 0)$ (a.u.)	Applied shift (eV.) ^a	
		Without $\mathbf{Y}([\rho_0], 0)$	With $\mathbf{Y}([\rho_0], 0)$
C	0.367	0.60	0.70
Si	0.355	0.40	0.58
GaP	0.409	0.50	0.60
GaAs	0.416	0.45	0.50
ZnS	0.489	0.90	0.90

^aSpectra have been shifted such that the calculated and experimental zero-crossings of ϵ_1 coincide.

It is clear that without the $\mathbf{E}_{xc,mac}$ contributions, the E_1 peak appears as a shoulder and is underestimated in amplitude, the E_2 peak is too sharp, and therefore overestimated in magnitude. When including the macroscopic xc-contributions, the E_1 peak is now clearly resolved. As can be seen in Fig. 7.1, for both the real and imaginary part of $\epsilon(\omega)$, the whole dielectric function is improved considerably. Therefore it should be concluded that it is necessary to include the $\mathbf{E}_{xc,mac}$ contributions to get the E_1 peak in the ϵ_2 of Si in good agreement with experiment [45, 46]. In addition, we have calculated the optical absorption spectra ϵ_2 for C, also a group IV element, GaP and GaAs (III-V), and ZnS (II-VI) using the same polarization functional. We checked that the used prefactor led to uniformly improved spectra, and hence we have obtained a new polarization functional that in all cases improves our previous ALDA results [94].

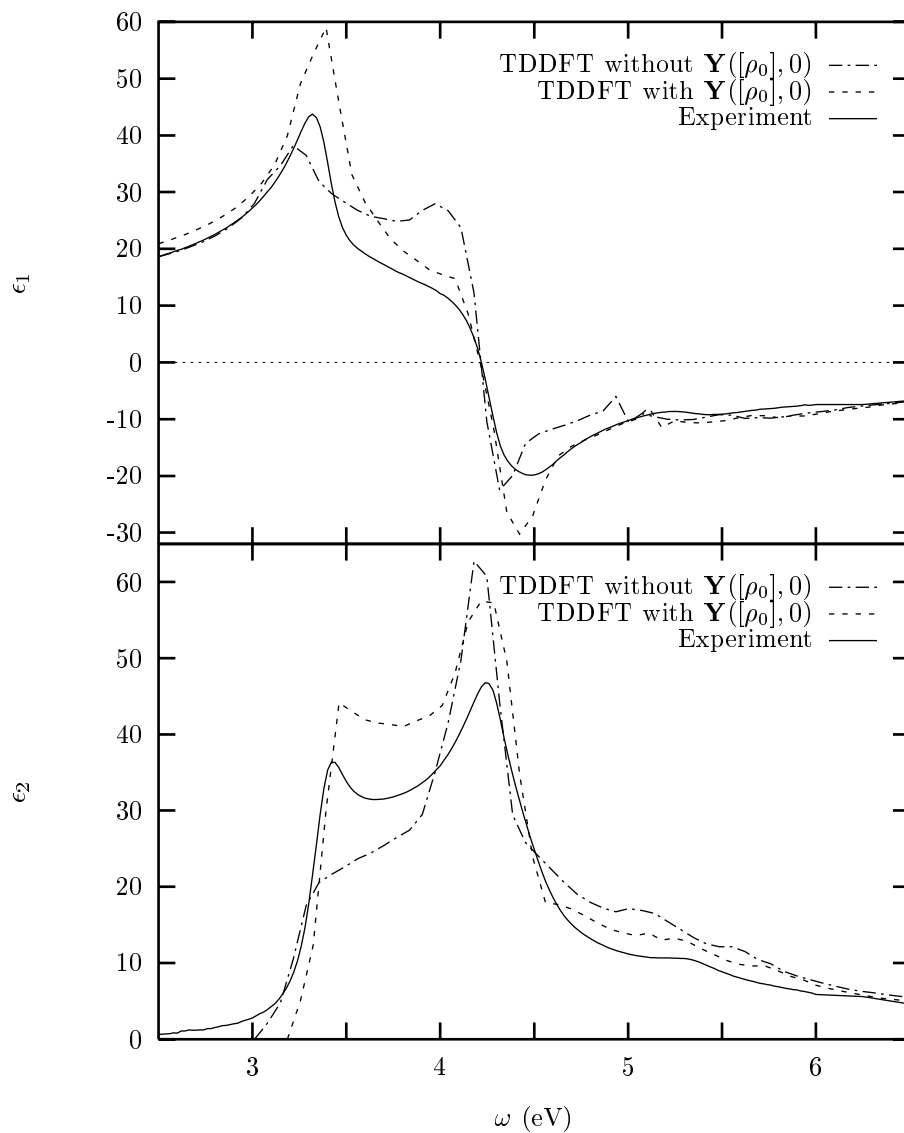


Figure 7.1: The dielectric function for Silicon (Si), with and without the inclusion of the polarization dependent functional, in comparison with the experimental data [45, 46]. The applied energy shifts to the TDDFT calculated dielectric function were 0.60 eV without, and 0.70 eV with the inclusion of $\mathbf{Y}([\rho_0], 0)$.

7.5.2 Diamond

The experimental [46] absorption spectrum ϵ_2 for diamond shows an E_2 peak around 12 eV. In all previous calculations of ϵ_2 for C this E_2 peak is overestimated, just like in our recently performed time-dependent DFT calculations [63, 94], as well as in the BSE calculations [117], which include *in detail* the electron-hole interactions. In Fig. 7.2 we show the effect of including the polarization functional on the ϵ_2 of diamond, in comparison with experiment [46]. Clearly there is a very small effect on ϵ_2 when using the polarization functional. Therefore it can be concluded that the xc-contributions to the effective macroscopic electric field in diamond are negligible.

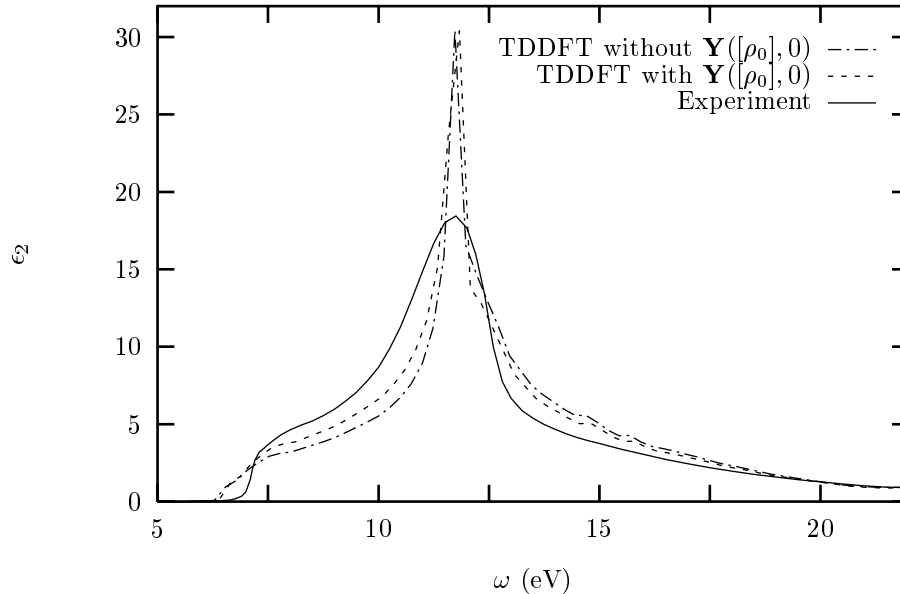


Figure 7.2: The optical absorption spectrum for Diamond (C), with and without the inclusion of the polarization dependent functional, in comparison with the experimental data [46]. The applied energy shifts to the TDDFT calculated dielectric function were 0.40 eV without, and 0.58 eV with the inclusion of $\mathbf{Y}([\rho_0], 0)$.

7.5.3 Gallium phosphide

The experimental [46] absorption spectrum ϵ_2 of GaP in the zincblende structure, also shows a double peak structure in the range from 3 to 6 eV, just like Si. In Fig. 7.3, the effect of the polarization functional on the ϵ_2 of GaP is shown and compared with experiment [46]. Upon inclusion of the scaled $\mathbf{Y}([\rho_0], 0)$ term, the originally underestimated E_1 peak is now found in full agreement with experiment [46], but the E_2 peak is still overestimated and too sharp.

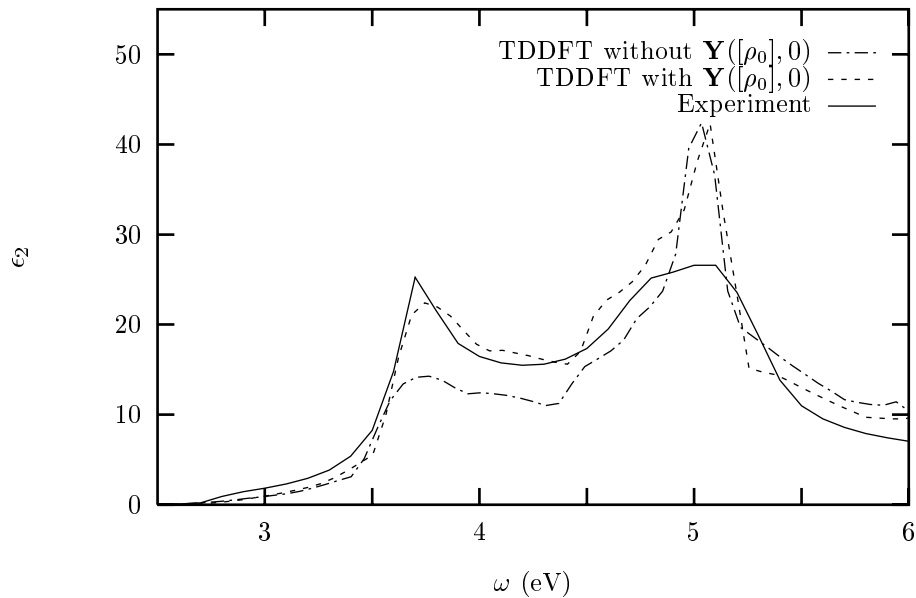


Figure 7.3: The optical absorption spectrum for Gallium Phosphide (GaP), with and without the inclusion of the polarization dependent functional, in comparison with the experimental data [46]. The applied energy shifts to the TDDFT calculated dielectric function were 0.50 eV without, and 0.60 eV with the inclusion of $\mathbf{Y}([\rho_0], 0)$.

7.5.4 Gallium arsenide

The experimental absorption spectrum for GaAs (Ref. [46]) shows the same features as for GaP. In Fig. 7.4 the effect of the polarization functional is shown on the ϵ_2 of GaAs. Including $\mathbf{Y}([\rho_0], 0)$ gives an increase in the oscillator strength for the E_1 peak, just like in GaP, and it is now also in good agreement with experiment [46].

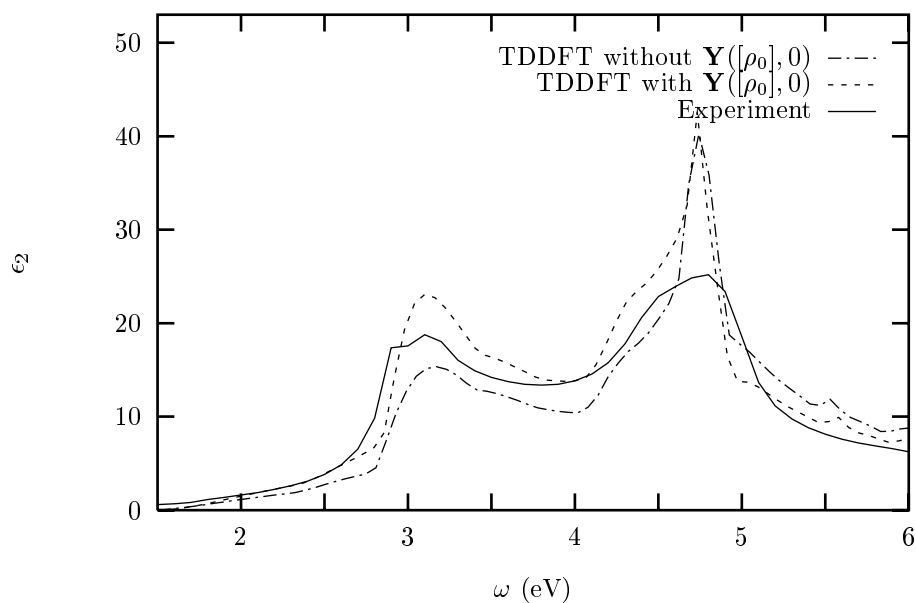


Figure 7.4: The optical absorption spectrum for Gallium Arsenide (GaAs), with and without the inclusion of the polarization dependent functional, in comparison with the experimental data [46]. The applied energy shifts to the TDDFT calculated dielectric function were 0.45 eV without, and 0.50 eV with the inclusion of $\mathbf{Y}([\rho_0], 0)$.

7.5.5 Zinc sulfide

In the II-VI semiconductor ZnS the E_1 peak is also underestimated in our previous calculations [94], compared to experiment [90]. In Fig. 7.5, it can be seen that also for ZnS the oscillator strength for the E_1 peak increases after inclusion of the $\mathbf{Y}([\rho_0], 0)$ term, and is now in better agreement with experiment [90].

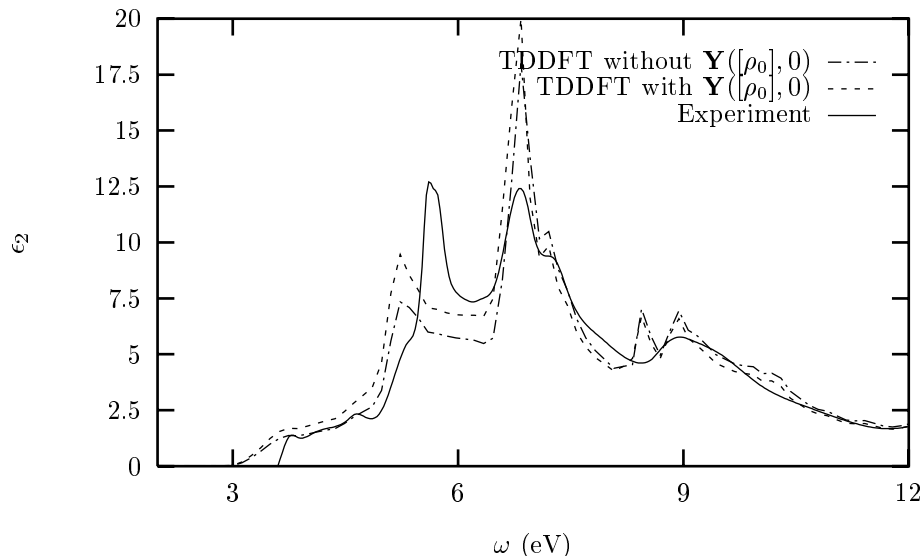


Figure 7.5: The optical absorption spectrum for Zinc Sulfide (ZnS), with and without the inclusion of the polarization dependent functional, in comparison with the experimental data [90]. The applied energy shifts to the TDDFT calculated dielectric function were 0.90 eV without and with the inclusion of $\mathbf{Y}([\rho_0], 0)$.

7.6 Conclusions

In conclusion, we presented the first successful computational approach of a polarization dependent functional within current density functional theory, as it was suggested in 1996 by Vignale and Kohn [108]. The calculated optical absorption spectra of several semiconductors clearly improved considerably with the inclusion of the exchange-correlation contributions to the effective macroscopic electric field.

Chapter 8

Excitons in crystalline insulators, described by TDDFT

F. Kootstra, P. L. de Boeij, and J. G. Snijders, *J. Chem. Phys.* to be submitted.

8.1 Abstract

In this chapter we demonstrate that time-dependent density-functional theory (TDDFT), within the adiabatic local density approximation (ALDA), describes the excitonic effects for the insulators CaF_2 , SiO_2 , and GaN correctly. Results for the electronic band structure, the density of states (DOS) and the optical spectra (ϵ_2) are reported for these wide band gap insulators. The optical spectra calculated by TDDFT are compared directly with experimental measurements, and with the ϵ_2 's as calculated by a Green's function approach (DFT/GW/BSE). In DFT/GW/BSE, these excitons are explicitly taken into account by evaluating the two-body Green's function G_2 . The features in the optical absorption spectra, that are attributed to excitonic effects according to the DFT/GW/BSE results, are also found in the TDDFT calculations. This contradicts the common assumption that TDDFT is not able to describe these excitonic effects properly.

8.2 Introduction

When a solid in its ground state is perturbed by an electromagnetic field, an electron can be promoted from the valence band to the conduction band, thereby leaving a hole behind. In the case of a Coulombic interaction between this excited electron and the remaining hole, a bound state is formed. Such bound states of electron-hole pairs are called excitons [8]. The optical excitations, e.g., in semiconductors, can be described in terms of very weakly bound electron-hole pairs. On average, the electron-hole distance is large in comparison with the lattice constant of the corresponding semiconductor. Such excitons are called Mott-Wannier excitons. Excitons are called Frenkel excitons, when the correlation between the electron and the hole is strong. In these excitations, the electrons

are always found very close to the holes. Recently, in several groups [122, 123, 124, 125], it has been claimed that the description of optical electron-hole excitations requires an effective two-body approach, which goes beyond the single-particle picture. In the rest of this chapter the single-particle Green's function approach will be abbreviated as the GW approach¹, in which G stands for the one-particle Green's function G_1 and the W for the screened Coulomb interaction. In the past, the GW approach has been shown to be highly successful for the prediction of quasiparticle spectra [25, 133]. In the effective two-body approach² the coupled electron-hole excitations are calculated by solving the Bethe-Salpeter equation (BSE), which enables the evaluation of the optical absorption spectra. The effect of such a two-body approach becomes directly clear when comparing the corresponding optical spectra, 'GW' vs. 'BSE'. The differences between these spectra are defined, in the DFT/GW/BSE theory, as features of excitonic nature. The explicit inclusion of these electron-hole excitations can be quite substantial, e.g., a large influence is observed in the optical absorption of α -quartz. The question arises to what extent excitonic effects are also included in time-dependent density-functional theory. Therefore it is interesting to investigate if these excitonic features in the optical absorption spectra are also found in a TDDFT calculation.

In this chapter we investigate three wide band gap insulators: CaF_2 , SiO_2 , and GaN . In these insulators, the optical spectra were all substantially improved upon the inclusion of the electron-hole excitations (i.e., after solving the Bethe-Salpeter equation). In those calculations, the spectra are found in excellent agreement with the experimentally measured spectra. The rest of this chapter is arranged in the following way. In the theory section, we briefly outline the DFT/GW/BSE theory, and we show the similarity between the DFT/GW/BSE equations and the TDDFT equations. In the subsequent section we give the results and analyses for the three wide band gap insulators.

8.3 Theory

8.3.1 Green's function approach

The following outline of the Green's function approach is based upon the Refs. [125, 126]. The key concept of the Green's function approach is to describe the excitations of the electronic system by the corresponding one- and two-particle Green's function. The formalism is fully described and discussed in the Refs. [127, 128, 129, 130, 131, 132]. In practice three computational techniques are combined: (1) The ground state of the electronic system is described by density-functional theory (DFT) within the local density approximation (LDA), (2) The quasiparticle (QP) excitation spectrum of the electrons and holes is obtained within the GW approximation to the electron self-energy operator, (3) The coupled electron-hole excitations are calculated by solving the Bethe-Salpeter equation (BSE), to evaluate the optical spectrum.

¹'GW' in the Figures

²'BSE' in the Figures

Quasiparticle excitation spectrum

The process of removing and adding an electron to the N -particle system is described by the one-electron Green's function

$$G_1(1, 2) = -i\langle N, 0 | T[\psi(1)\psi^\dagger(2)] | N, 0 \rangle , \quad (8.1)$$

in which we have used the abbreviated notation $(i) = (\mathbf{r}_i, t_i)$. The ground state configuration of the N electron system is given by $|N, 0\rangle$, and in second quantization notation, $\psi^\dagger(i)$ and $\psi(i)$ are the creation and annihilation operators. In Eq. 8.1, T is Wick's time-ordering operator, which is given by:

$$T[\psi(1)\psi^\dagger(2)] = \begin{cases} \psi(1)\psi^\dagger(2) & \text{if } t_1 > t_2, \\ -\psi^\dagger(2)\psi(1) & \text{if } t_1 < t_2. \end{cases} \quad (8.2)$$

For an interacting N -electron system the Hamiltonian is given by,

$$\hat{H} = \hat{T} + \hat{V} + \hat{U} , \quad (8.3)$$

in which \hat{T} is the kinetic term, \hat{V} the interaction with the external field, and \hat{U} the Coulomb interaction between the electrons: $1/|\mathbf{r} - \mathbf{r}'|$. Similarly, for a fictitious non-interacting system the Hamiltonian is given by,

$$\hat{H}_0 = \hat{T} + \hat{V}_0 , \quad (8.4)$$

in which \hat{V}_0 is an external potential, which, in addition to the interaction with the external field, also takes into account the electron-electron interaction in an effective way. Therefore this \hat{V}_0 is often denoted by \hat{V}_{eff} , which includes in addition to the external potential \hat{V} also the electrostatic electron-electron interaction and the exchange-correlation potential.

The equation of motion for the one-particle Green's function $G(1, 2)$ can be derived by using the following commutation rules in second quantization

$$[\psi^\dagger(\mathbf{r}, t), \psi^\dagger(\mathbf{r}', t)]_+ = [\psi(\mathbf{r}, t), \psi(\mathbf{r}', t)]_+ = 0 , \quad (8.5)$$

$$[\psi(\mathbf{r}, t), \psi^\dagger(\mathbf{r}', t)]_+ = \delta(\mathbf{r} - \mathbf{r}') , \quad (8.6)$$

and the Heisenberg equations of motion

$$i\frac{\partial\psi(\mathbf{r}, t)}{\partial t} = [\psi(\mathbf{r}, t), \hat{H}] , \quad (8.7)$$

$$-i\frac{\partial\psi^\dagger(\mathbf{r}, t)}{\partial t} = [\psi^\dagger(\mathbf{r}, t), \hat{H}] . \quad (8.8)$$

For the non-interacting system this results in:

$$\left[i\frac{\partial}{\partial t_1} + \frac{1}{2}\nabla_1^2 - V_{\text{eff}}(1) \right] G_0(1, 2) = \delta(1, 2) . \quad (8.9)$$

In a similar way, for the interacting N -electron system, one can derive the equation of motion for interacting Green's function $G(1, 2)$

$$\left[i \frac{\partial}{\partial t_1} + \frac{1}{2} \nabla_1^2 - V_{\text{eff}}(1) \right] G(1, 2) - \int d3 \Sigma(1, 3) G(3, 2) = \delta(1, 2) , \quad (8.10)$$

which defines the self-energy operator $\Sigma(1, 3)$ by

$$\int d3 \Sigma(1, 3) G(3, 2) = \langle N, 0 | T \left[[\psi^\dagger(1), \hat{U} + \hat{V} - \hat{V}_{\text{eff}}] \psi^\dagger(2) \right] | N, 0 \rangle . \quad (8.11)$$

One now arrives at the Dyson's equation by combining the Eqs. 8.9 and 8.10

$$G(1, 2) = G_0(1, 2) + \int d3d4 G_0(1, 3) \Sigma(3, 4) G(4, 2) , \quad (8.12)$$

which can be written symbolically as: $G = G_0 + G_0 \Sigma G$.

In principle the self-energy operator Σ should be calculated self-consistently. This is most easily done by solving the Hedin equations [127] using linear response theory. The Hedin equations are a set of four coupled integral equations, for the self-energy Σ , the screened interaction W , the polarizability P , and the vertex function Γ .

In the GW approximation the vertex function $\Gamma(1, 2, 3)$ is approximated by $\delta(1, 2)\delta(1, 3)$, leading to the following reduced set of equations:

$$P(1, 2) = -2iG(1, 2)G(2, 1^+) , \quad (8.13)$$

$$W(1, 2) = v(1, 2) + \int d3d4 v(1^+, 3)P(3, 4)W(4, 2) , \quad (8.14)$$

$$\Sigma(1, 2) = iG(1, 2)W(1^+, 2) . \quad (8.15)$$

Starting from the zeroth-order approximation: $\Sigma = 0$ and $G = G_0$, where G_0 can be calculated using DFT-LDA, one first obtains the polarizability P as the response of the system to a change in the effective potential. From P , the interaction between the quasiparticles W is calculated, and finally the self-energy operator Σ is obtained.

The quasiparticle energies are then calculated by inserting this self-energy operator Σ in the quasiparticle equation (i.e., the Dyson's equation 8.12 in disguise)

$$\left[-\frac{\nabla^2}{2} + V_{\text{eff}}(\mathbf{r}) \right] \phi_{nk}(\mathbf{r}) + \int d\mathbf{r}' \Sigma(\mathbf{r}, \mathbf{r}', E_{nk}) \phi_{nk}(\mathbf{r}') = E_{nk} \phi_{nk}(\mathbf{r}) . \quad (8.16)$$

In practice, only one GW iteration is performed to update the DFT-LDA eigenvalues. In this way many band structures and electronic spectra have been calculated within the GW approximation [127, 128]. The GW spectrum, of the individual electron and hole states, serves as input for the Bethe-Salpeter equation, which results in the *coupled* electron-hole

excitations and the optical absorption spectrum, $\epsilon_2(\omega)$ (Eq. 8.25).

From the GW spectrum one can also directly calculate the optical absorption spectrum ('one-electron' spectrum, $\epsilon_2^{(0)}(\omega)$). This spectrum does not include the electron-hole interaction, and in this case the excitations are calculated by the vertical transitions between the *independent* electron and hole states, according to

$$\epsilon_2^{(0)}(\omega) = \frac{16\pi^2}{\omega^2} \sum_{c\nu\mathbf{k}} \left| \langle c\mathbf{k} | \hat{\mathbf{j}} \cdot \hat{\mathbf{e}} | \nu\mathbf{k} \rangle \right|^2 \delta(\omega - (E_{c\mathbf{k}} - E_{\nu\mathbf{k}})) , \quad (8.17)$$

in which $\hat{\mathbf{j}}$ and $\hat{\mathbf{e}}$ are the current operator and the polarization unit vector of the electric field respectively.

Electron-hole excitations

The two-particle Green's function can be defined, in analogy with the one-electron Green's function of Eq. 8.1, as

$$G_2(1, 2, 1', 2') = -\langle N, 0 | T[\psi(1)\psi(2)\psi^\dagger(2')\psi^\dagger(1')] | N, 0 \rangle . \quad (8.18)$$

The two-particle correlation function is introduced as

$$\begin{aligned} L(1, 2, 1', 2') &= G_1(1, 2')G_1(2, 1') - G_2(1, 2, 1', 2') , \\ &= L_0(1, 2, 2', 1') - G_2(1, 2, 1', 2') , \end{aligned} \quad (8.19)$$

in which L_0 is the propagator for the free electron-hole pair.

The Bethe-Salpeter equation is found as the equation of motion for $L(1, 2, 1', 2')$. The derivation is similar to the one for the Dyson's equation 8.12, as the equation of motion for $G(1, 2)$.

$$L(1, 2, 1', 2') = L_0(1, 2, 2', 1') + \int d3d4d5d6 L_0(1, 4, 1', 3)K(3, 5, 4, 6)L(6, 2, 5, 2') , \quad (8.20)$$

where the effective two-particle interaction kernel K is given by

$$K(3, 5, 4, 6) = \frac{\delta\Sigma(3, 4)}{\delta G_1(6, 5)} . \quad (8.21)$$

If again the GW approximation is used for the self-energy operator Σ , and if we further neglect the derivative of the screened interaction W with respect to the one-particle Green function G_1 , one obtains:

$$\begin{aligned} K(3, 5, 4, 6) &= -i\delta(3, 4)\delta(5, 6)v(3, 6) + i\delta(3, 6)\delta(4, 5)W(3, 4) , \\ &= K^x(3, 5, 4, 6) + K^d(3, 5, 4, 6) . \end{aligned} \quad (8.22)$$

The term K^x contains the bare Coulomb interaction v , and is called the *exchange* term, while K^d results from the screened Coulomb interaction W , and has the form of a so-called

direct term. It is the K^x term which is responsible for the attractive nature of the electron-hole interaction and the formation of bound electron-hole states.

The BSE (Eq. 8.20) can be transformed into a generalized eigenvalue problem, if we expand L_0 and L in the quasiparticle functions and energies. This results in

$$(E_{c\mathbf{k}} - E_{v\mathbf{k}})A_{c\mathbf{k}}^S + \sum_{c'v'\mathbf{k}'} K_{c\mathbf{k}c'\mathbf{k}'}^{c'v'\mathbf{k}'}(\Omega_S)A_{c'\mathbf{k}'}^S = \Omega_S A_{c\mathbf{k}}^S. \quad (8.23)$$

The indices c , v and \mathbf{k} denote the conduction bands, valence bands and the \mathbf{k} -vectors of the quasiparticle states. The electron-hole amplitudes $A_{c\mathbf{k}}^S$, contain information about the electron-hole correlation and the spatial nature of the excited states $|S\rangle$, having excitation energies Ω_S . $K_{c\mathbf{k}c'\mathbf{k}'}^{c'v'\mathbf{k}'}(\Omega_S)$ is the electron-hole interaction kernel. The evaluation of $K_{c\mathbf{k}c'\mathbf{k}'}^{c'v'\mathbf{k}'}(\Omega_S)$ forms the bottleneck in the BSE calculation, because the screened interaction part K^d contains an energy convolution, depending on the excitation energy Ω_S .

After solving the Bethe-Salpeter equation (Eq. 8.23), the electron-hole amplitudes $A_{c\mathbf{k}}^S$ and the coupled electron-hole excitation energies Ω_S can be used to calculate the excitonic wave functions $\Psi_S(\mathbf{r}_e, \mathbf{r}_h)$, belonging to the excitations $|S\rangle$.

$$\Psi_S(\mathbf{r}_e, \mathbf{r}_h) = \sum_{c\mathbf{k}} A_{c\mathbf{k}}^S \phi_{c\mathbf{k}}(\mathbf{r}_e) \phi_{v\mathbf{k}}^*(\mathbf{r}_h). \quad (8.24)$$

The optical absorption spectrum $\epsilon_2(\omega)$ now follows from:

$$\epsilon_2(\omega) = \frac{16\pi^2}{\omega^2} \sum_S \left| \sum_{c\mathbf{k}} A_{c\mathbf{k}}^S \langle c\mathbf{k} | \hat{\mathbf{j}} \cdot \hat{e} | v\mathbf{k} \rangle \right|^2 \delta(\omega - \Omega_S). \quad (8.25)$$

8.3.2 TDDFT approach

In this section we focus on the similarity between the DFT/GW/BSE equations of the previous section and the corresponding TDDFT equations. A full description of this real-space formulation to time-dependent density-functional theory can be found in Ref. [63], and results for the dielectric function for a large number of nonmetallic crystals in Ref. [94, 102, 136].

For simplicity we will only consider isotropic systems. The key quantity is the induced density

$$\delta\rho(\mathbf{r}, \omega) = 2 \sum_{c\mathbf{k}} \psi_{v\mathbf{k}}^*(\mathbf{r}) \psi_{c\mathbf{k}}(\mathbf{r}) \frac{\int_V d\mathbf{r}' \psi_{c\mathbf{k}}^*(\mathbf{r}') (\hat{\mathbf{j}} \cdot \hat{e} + \delta v_{eff}(\mathbf{r}', \omega)) \psi_{v\mathbf{k}}(\mathbf{r}')}{(\epsilon_{v\mathbf{k}} - \epsilon_{c\mathbf{k}}) + \omega + i\eta} + c.c.(-\omega), \quad (8.26)$$

in which \hat{e} is the direction of the electric field, $\mathbf{E}(\omega) = -i\omega \cdot \hat{e}$, the summation is over the conduction (c) and valence (v) states, the (paramagnetic) current operator is given by $\hat{\mathbf{j}} = -i(\nabla - \nabla^\dagger)/2$, and the effective potential $\delta v_{eff}(\mathbf{r}', \omega)$ is the result of the microscopic

Coulomb potential and the exchange-correlation contribution.

The similarity between the DFT/GW/BSE and TDDFT equations becomes evident if we introduce the density matrix $P_{c\mathbf{v}\mathbf{k}}(\omega)$ and write the induced density $\delta\rho(\mathbf{r}, \omega)$ in Eq. 8.26 as

$$\delta\rho(\mathbf{r}, \omega) = 2 \sum_{c\mathbf{v}\mathbf{k}} \psi_{v\mathbf{k}}^*(\mathbf{r}) \psi_{c\mathbf{k}}(\mathbf{r}) P_{c\mathbf{v}\mathbf{k}}(\omega) + c.c.(-\omega) . \quad (8.27)$$

From the Eqs. 8.26 and 8.27, we see that $P_{c\mathbf{v}\mathbf{k}}(\omega)$ has to satisfy the following inhomogeneous eigenvalue equation

$$\begin{aligned} [(\epsilon_{c\mathbf{k}} - \epsilon_{v\mathbf{k}}) - \omega] P_{c\mathbf{v}\mathbf{k}}(\omega) + \sum_{c'\mathbf{v}'\mathbf{k}'} \mathcal{K}_{c'\mathbf{v}'\mathbf{k}'}^{c\mathbf{v}\mathbf{k}}(\omega) P_{c'\mathbf{v}'\mathbf{k}'}(\omega) \\ = -2 \int_V d\mathbf{r} \left(\psi_{c\mathbf{k}}^*(\mathbf{r}) [\hat{\mathbf{j}} \cdot \hat{e}] \psi_{v\mathbf{k}}(\mathbf{r}) \right) , \end{aligned} \quad (8.28)$$

in which the couplings matrix $\mathcal{K}_{c'\mathbf{v}'\mathbf{k}'}^{c\mathbf{v}\mathbf{k}}(\omega)$ is given by

$$\begin{aligned} \mathcal{K}_{c'\mathbf{v}'\mathbf{k}'}^{c\mathbf{v}\mathbf{k}}(\omega) = 2 \int_V d\mathbf{r} \int_V d\mathbf{r}' \times \\ \left(\psi_{c\mathbf{k}}^*(\mathbf{r}) \psi_{v\mathbf{k}}(\mathbf{r}) \left[\frac{1}{|\mathbf{r} - \mathbf{r}'|} + f_{xc}(\mathbf{r}, \mathbf{r}', \omega) \right] \psi_{v'\mathbf{k}'}^*(\mathbf{r}') \psi_{c'\mathbf{k}'}(\mathbf{r}') \right) . \end{aligned} \quad (8.29)$$

Let us first look for the eigenvalues Ω_S and eigenstates $P_{c\mathbf{v}\mathbf{k}}^S(\omega)$ of the following eigenvalue equation, i.e., the homogeneous part of Eq. 8.28:

$$[(\epsilon_{c\mathbf{k}} - \epsilon_{v\mathbf{k}})] P_{c\mathbf{v}\mathbf{k}}^S + \sum_{c'\mathbf{v}'\mathbf{k}'} \mathcal{K}_{c'\mathbf{v}'\mathbf{k}'}^{c\mathbf{v}\mathbf{k}}(\omega) P_{c'\mathbf{v}'\mathbf{k}'}^S = \Omega_S P_{c\mathbf{v}\mathbf{k}}^S . \quad (8.30)$$

The solution of the inhomogeneous equation (Eq. 8.28) can be expressed in terms of these eigenvalues and eigenstates, in the following way

$$P_{c\mathbf{v}\mathbf{k}}(\omega) = -2 \sum_S \frac{P_{c\mathbf{v}\mathbf{k}}^{S*} \langle \psi_{c\mathbf{k}} | \hat{\mathbf{j}} \cdot \hat{e} | \psi_{v\mathbf{k}} \rangle}{\Omega_S - \omega - i\eta} P_{c\mathbf{v}\mathbf{k}}^S . \quad (8.31)$$

We can now get the induced macroscopic current according to the expressions in the Eqs. 4.58 ff., which is very similar to the induced density of Eq. 8.27

$$\delta\mathbf{j}(\omega) \cdot \hat{e} = 2 \sum_{c\mathbf{v}\mathbf{k}} \langle \psi_{v\mathbf{k}} | \hat{\mathbf{j}} \cdot \hat{e} | \psi_{c\mathbf{k}} \rangle P_{c\mathbf{v}\mathbf{k}}(\omega) + c.c.(-\omega) . \quad (8.32)$$

For isotropic systems, we now get the imaginary part of the electric susceptibility and dielectric function, $\epsilon_2(\omega)$, according to

$$\epsilon_2(\omega) = 4\pi \text{Im} \chi_e(\omega) = \frac{16\pi^2}{\omega^2} \sum_S \left| \sum_{c\mathbf{v}\mathbf{k}} P_{c\mathbf{v}\mathbf{k}}^S \langle \psi_{c\mathbf{k}} | \hat{\mathbf{j}} \cdot \hat{e} | \psi_{v\mathbf{k}} \rangle \right|^2 \delta(\omega - \Omega_S) . \quad (8.33)$$

When we neglect the Coulomb and exchange-correlation interactions in the TDDFT calculations, by setting the couplings matrix $\mathcal{K}_{c'v'\mathbf{k}'}^{cv\mathbf{k}}(\omega)$ to zero, it immediately becomes clear from Eq. 8.30, that the Ω_S reduce to the Kohn-Sham energy differences ($\Omega_S = \epsilon_{c\mathbf{k}} - \epsilon_{v\mathbf{k}}$), and that the $P_{cv\mathbf{k}}^S$ become the unit vectors. The optical absorption spectrum is then obtained according to

$$\epsilon_2^{(0)}(\omega) = \frac{16\pi^2}{\omega^2} \sum_{cv\mathbf{k}} \left| \langle \psi_{c\mathbf{k}} | \hat{\mathbf{j}} \cdot \hat{\mathbf{e}} | \psi_{v\mathbf{k}} \rangle \right|^2 \delta(\omega - (\epsilon_{c\mathbf{k}} - \epsilon_{v\mathbf{k}})). \quad (8.34)$$

This is completely equivalent to Eq. 8.17, with the obvious difference that there the Ω_S are the quasiparticle energy differences ($\Omega_S = E_{c\mathbf{k}} - E_{v\mathbf{k}}$).

Now the similarities have become evident. If we identify the density matrix elements $P_{cv\mathbf{k}}^S$ with the electron-hole amplitudes $A_{cv\mathbf{k}}^S$, then Eq. 8.30 can be interpreted as the Bethe-Salpeter equation (Eq. 8.23), with the quasiparticle eigenvalues replaced by the Kohn-Sham eigenvalues (and a different coupling matrix, in which the self-energy operator, Σ has been replaced by the exchange-correlation kernel, f_{xc}). With the same identification, the resulting expression for the electric susceptibility (Eq. 8.33) yields exactly the same expression for the optical absorption spectrum $\epsilon_2(\omega)$ as was obtained in the BSE derivation (Eq. 8.25).

8.4 Calculations on insulators

8.4.1 Calcium fluoride

CaF₂ is a highly ionic (wide band gap) insulator, which has been examined extensively for many years as well experimentally [83, 84, 137, 138, 139, 140] as theoretically [64, 70, 122, 141, 142]. The CaF₂ crystal has the fluoride structure with a lattice constant $a=5.46 \text{ \AA}$ [64].

Bandstructure

The calculated band structure for CaF₂ is shown in Fig. 8.1.

The bottom of the conduction-band (CB) is found at Γ , whereas the top of the valence-band (VB) is found at X . Therefore we get an indirect band gap of 6.93 eV, which is an underestimation by LDA of 43% compared to the experimental value of 12.1 eV found by Rubloff [139]. Other theoretical bandstructures are given in the Refs. [70, 141, 142]. Albert [141] used the tight-binding method for the VB and a pseudopotential method for the CB. The experimental band gap was reproduced by using a Slater exchange parameter of $\alpha=0.795$ in their overlapping-atomic-potential model. Heaton [142] used the self-consistent linear combination of atomic orbitals (LCAO) method, for as well the CB as the VB, and found, when using the full exchange parameter ($\alpha=1$), an indirect band gap of 9.8 eV in their overlapping-atomic-charge model. Gan [70] found an indirect band gap of 6.53 eV,

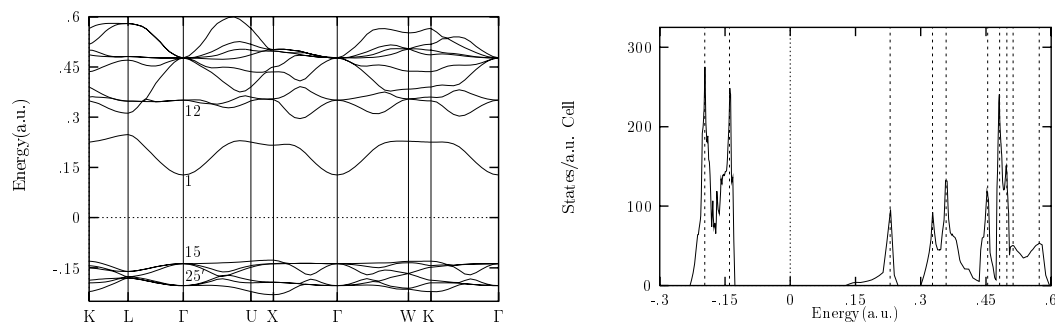


Figure 8.1: The bandstructure and the density of states (DOS) of CaF_2

when using their self-consistent orthogonalised LCAO method in the LDA approximation. Looking at the complete bandstructures of Refs. [70, 141, 142], we see a clear resemblance of our structure and that of Albert [141], which is, however, different (for example at the point L in the Brillouin zone) from the structures found by Gan [70] and Heaton [142].

Density of states

The Density of States (DOS) for CaF_2 , as calculated from the bandstructure, is also depicted in Fig. 8.1. We find for the upper VB two peaks at -5.35 and -3.80 eV respectively (zero energy is centered between VB and CB). The same two peak structure in the DOS for the VB was found by others [70, 142]. The total width of this upper VB is 2.84 eV, which is in good agreement with the experimental value of 3.0 eV by Pool [140]. Others calculated the width of the VB to be 3.1 [70], 2.7 [141], and 2.0 eV [142] respectively. The DOS for the CB is rather complicated, and shows peaks at 6.25 , 8.90 , 9.75 , 12.35 , 13.10 , 13.55 , 13.95 and 15.58 eV (as indicated in Fig. 8.1.). A very similar structure for the DOS for the CB was found by Gan [70], which was rather different from the one found by Heaton [142].

Optical spectrum

The earliest experimental reflectance and optical spectra of CaF_2 [84, 137, 138, 139, 140] showed interesting and substantial differences from the most recent one by Barth [83]. The early measurements (photographic photometry, ultraviolet photoelectron spectroscopy (UPS) and x-ray photoelectron spectroscopy (XPS)) all revealed the presence of an exciton peak around 11 eV. In the most recent spectroscopic ellipsometric synchrotron measurements of ϵ_1 and ϵ_2 however, this exciton could not be resolved clearly, because the peak is in the energy range that is contaminated by second-order diffracted light. Furthermore, the intensity of the ϵ_2 of the early measurements [84, 137, 138, 139, 140] differed by a factor of 2 from the one measured by Barth [83]. Despite the fact that Barth claimed to be convinced that their spectroscopic ellipsometry measurements are significantly more accurate than all the previous ones [84, 137, 138, 139, 140], from a simple Kramers-Kronig (KK)

transformation of their directly measured ϵ_1 and ϵ_2 , it can be seen that these components do not form a KK-couple.

The first calculated optical spectra of CaF_2 by Gan *et al.* [64, 70], were obtained using uncoupled response calculations, i.e., without the inclusion of Coulomb and exchange-correlation contributions in the response calculation. Therefore these spectra can not show the exciton peak, and the overall comparison with the experimental data available [83, 84, 137, 138, 139, 140], was very poor. Recently this exciton peak was calculated by explicitly including the electron-hole interaction in the Green's function (DFT/GW/BSE) approach by Benedict [122].

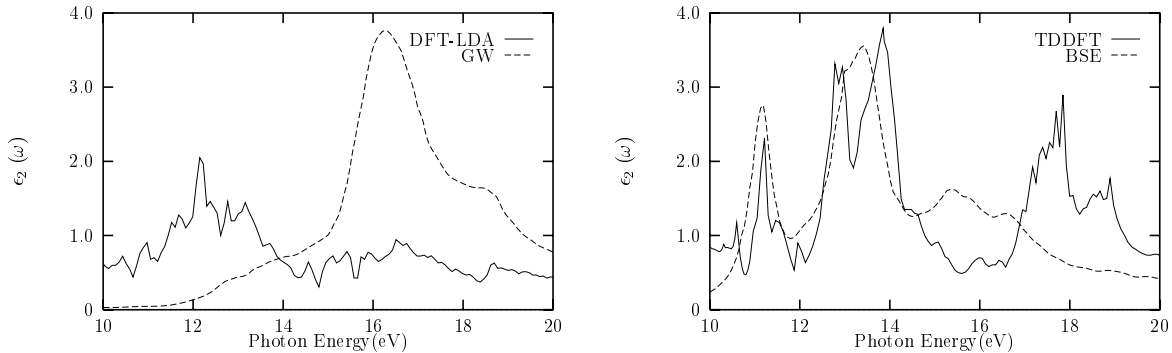


Figure 8.2: Comparison of the calculated $\epsilon_2(\omega)$ for CaF_2 ; DFT-LDA vs. GW (left), and TDDFT vs. BSE (right).

In Fig. 8.2, the GW and BSE results of Benedict [122] are compared with the DFT-LDA and TDDFT results respectively. By comparing the GW vs. BSE results, and the DFT-LDA vs. TDDFT results in Fig. 8.2, it is clear that the electron-hole interaction in CaF_2 is very strong. The calculated BSE spectrum, which does include the electron-hole interaction, were obtained by evaluating Eq. 8.25. The GW spectrum, which does not include the electron-hole interaction, were obtained by evaluating Eq. 8.17. In GW the excitations are calculated using only the vertical transitions between the independent hole and electron states. The DFT-LDA spectrum was calculated by setting the couplings matrix $\mathcal{K}_{c'v'\mathbf{k}'}^{cv\mathbf{k}}(\omega)$ in Eq. 8.28 to zero. Therefore it should give 'in principle' the same result as the GW spectrum as calculated by Eq. 8.17, apart from a shift to lower energies, which accounts for the differences in energies (~ 4 eV) between the GW and DFT-LDA wavefunctions. This shift between the DFT-LDA and GW spectra is exactly found, as can be seen in Fig. 8.2. The $\epsilon_2^{\text{TDDFT}}$ clearly resembles ϵ_2^{BSE} in Fig. 8.2, in particular in the region from 10-15 eV, and thus it should be concluded that the excitonic effects, that are obtained in CaF_2 using the BSE, are also properly handled in the TDDFT calculation, already within the ALDA. In the region above 15 eV, $\epsilon_2^{\text{TDDFT}}$ still differs from ϵ_2^{BSE} , because there the correct description of the higher conduction bands becomes important and depends heavily on the method and accuracy of the calculation.

In Fig. 8.3 the $\epsilon_2^{\text{TDDFT}}$ is compared with several experiments [83, 84, 137]. The double

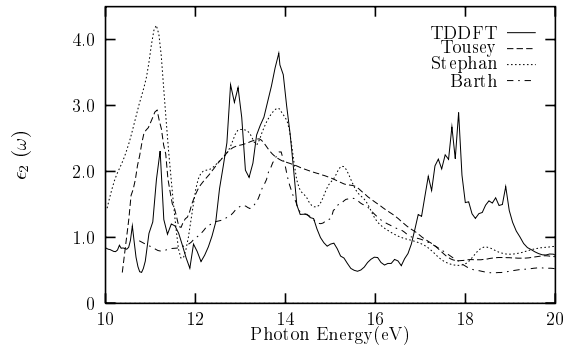


Figure 8.3: Comparison of the TDDFT calculated $\epsilon_2(\omega)$ for CaF_2 with experimentally measured $\epsilon_2(\omega)$ by Tousey (Ref. [137]), Stephan (Ref. [84]), and Barth (Ref. [83])

peak structure around 13-14 eV, which was not found in the ϵ_2^{BSE} , agrees well with the experimental findings of Stephan *et al.* [84].

8.4.2 α -Quartz

α -quartz has a hexagonal structure with the lattice constants $a=4.9134$ and $c=5.4052$ Å. The basisfunctions used in the SiO_2 calculation, are a combination of numerical atomic and Slater type orbitals. The $3Z2P$ NAO/STO basis (basis V in the ADF-BAND program [37, 38]) consists of a triple zeta set augmented with two polarization functions. For the integration in reciprocal space, only 4 symmetry unique \mathbf{k} points (kspace 2 in the BAND program) were used, which was sufficient due to the large unit cell size, and consequently the small Irreducible Brillouin Zone (IBZ), and hence very small energy dispersion.

Bandstructure

The bandstructure for α -quartz, as obtained in our DFT-LDA calculation, is shown in Fig. 8.4. The indirect band gap, as found in our LDA calculation, is $E_g^{\text{LDA}}=5.92$ eV ($A \rightarrow \Gamma$). This is considered to be an LDA underestimation, because the GW correction opens up the band gap to $E_g^{\text{GW}}=10.1$ eV [143]. In the current literature available the experimental band gap of SiO_2 is reported to be 9.0 eV [145, 146, 147], 8.9 eV [148]. The question of the exact experimental band gap of SiO_2 is still an issue which is not fully agreed on. The reason for this is that the optical absorption spectrum (ϵ_2) is still not completely understood for several reasons. First of all, SiO_2 is a structurally quite complex material, it appears in many polycrystalline forms under different thermodynamical conditions (α -quartz, β -quartz, β -tridymite, α -cristobalite, β -cristobalite, keatite, coesite, and stishovite). Therefore it is experimentally hard to grow specific crystals. Secondly, SiO_2 has an excitonic resonance peak in the absorption spectrum very close to the absorption edge, which consequently makes the determination of the absorption edge very hard from experimental measurements. The absorption edge of SiO_2 is further influenced by

low absorption levels near the absorption threshold originating from direct transitions near Γ , which are formally symmetry forbidden [144].

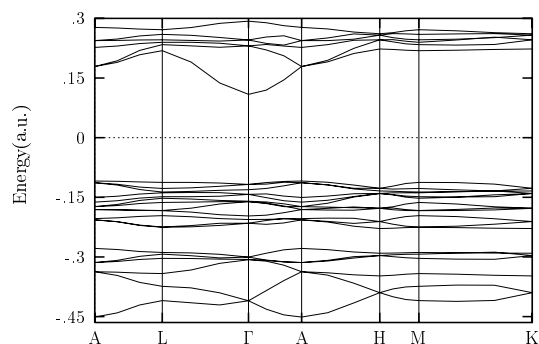


Figure 8.4: The bandstructure of SiO_2

Density of states

The experimental DOS for the valence bands obtained using ultraviolet-photoemission spectroscopy (UPS) and x-ray photoemission spectroscopy (XPS) can be found in the Refs. [147] and [149]. The complete DOS, as measured by x-ray emission spectroscopy, is given in Ref. [150]. The density of states resulting from our DFT calculation (Fig. 8.5) showed a similar structure as was found in the self-consistent pseudopotential calculation of Chelikowsky [151].

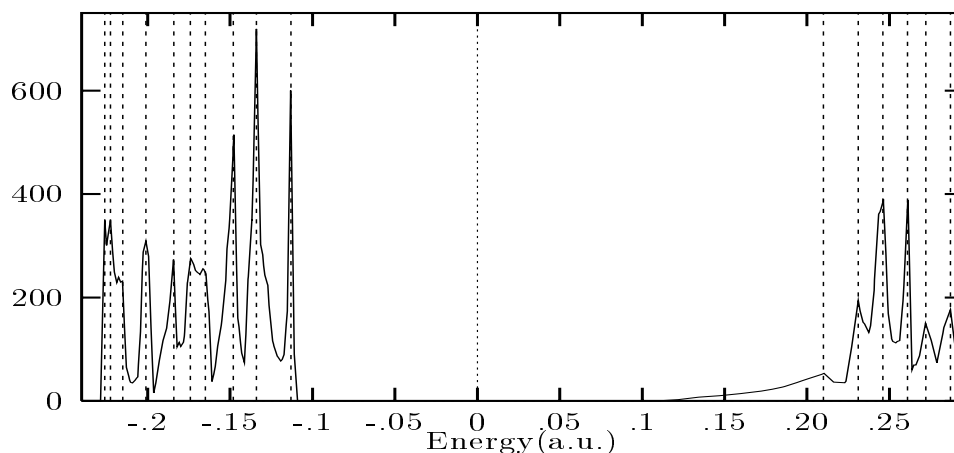


Figure 8.5: Density of States (DOS) of SiO_2

The features in the region $-0.81 \leftrightarrow -0.72$ a.u. (not shown in the Figs. 8.4 and 8.5) originate from the oxygen ($2s$) nonbonding state. The contributions in the energy region

$-0.45 \leftrightarrow -0.28$ (shown in Fig. 8.4, but not in Fig. 8.5) result from bonding states between the oxygen ($2p$) and silicon ($3s, 3p$) atomic orbitals. The nonbonding states on the oxygen ($2p$) are found in the energy region $-0.23 \leftrightarrow -0.11$ (as shown in the Figs. 8.4 and 8.5). The DOS for the conduction bands [the energy range starting from 0.11 a.u and higher] (as shown in Fig. 8.5) consisted of bonding states between the oxygen and the silicon atomic orbitals. These DFT results for the DOS of α -quartz were very similar to the self-consistent pseudopotential results as calculated by Chelikowsky [151], and in good agreement with the experimentally found UPS and XPS [147, 149] results.

Optical spectrum

The static dielectric constant for electric fields with a polarization direction within the hexagonal plane, is determined in experiment, and found to be $\epsilon_{\infty}^{\text{Exp}}=2.38$ [135]. In our TDDFT calculation we found $\epsilon_{\infty}^{\text{TDDFT}}=2.03$, the same value which was found by Chang *et al.* [143] in their RPA calculation, where they took local field effects into account. This value of $\epsilon_{\infty}^{\text{RPA}}=2.0$, was greatly enhanced, after taking the electron-hole interactions (the excitons) into account, to $\epsilon_{\infty}^{\text{BSE}}=2.44$. The experimental optical spectrum [146] of α -quartz shows four peaks, located at 10.3, 11.7, 14.0 and 17.3 eV. The first two are, according to the BSE calculations of Chang [143] clearly excitonic in nature, and are consequently only found in the BSE calculation. The TDDFT ϵ_2 for α -quartz is shown in Fig. 8.6 up to ~ 10.5 eV (because of convergence problems in the SCF procedure at higher photon energies), together with the GW and BSE results of Chang [143].

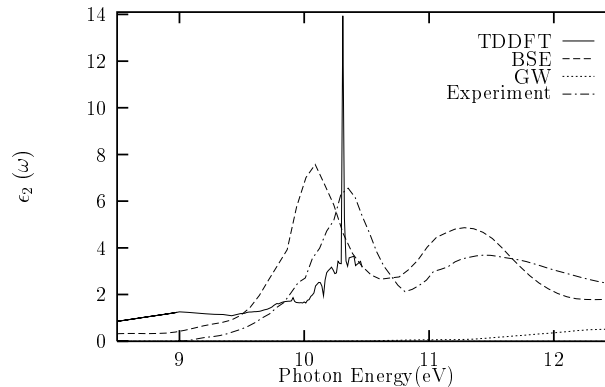


Figure 8.6: Comparison of the calculated $\epsilon_2(\omega)$ for SiO_2 within TDDFT (solid line), BSE (dashed line), the GW theory (dotted line) and Experiment (dash-dotted line).

As can be seen from Fig. 8.6, by comparing the GW with the BSE results, the first two peaks in the ϵ_2 for α -quartz are excitonic in nature, although they appear to be shifted a little to lower energy when compared to experiment. It is also clear that, looking at the TDDFT results, the first excitonic peak in the absorption spectrum is found exactly at the experimental value of 10.3 eV, although much sharper and overestimated compared to experiment [146].

8.4.3 Gallium nitride

In the last few years also many theoretical [67, 68, 69, 122, 152, 153, 154, 155] and experimental [152, 154, 155, 156, 157] studies have been performed on GaN. This nitride occurs in the wurtzite (WZ) as well as in the zincblende (ZB) structure, and is a very interesting and challenging compound. First of all, it has a high ionicity like CaF_2 and short bond lengths. GaN may therefore find application in the blue-light-emitting diodes and lasers which operate in the blue and ultraviolet regime, or in high temperature transistors. Measurements of the optical properties of GaN have always been difficult, in reflectivity measurements, as well as in spectroscopic ellipsometry performed with synchrotron radiation. In the reflectivity measurements [155] there is an ambiguity in the Kramers-Kronig transformation between ϵ_1 and ϵ_2 , and in the spectroscopic ellipsometry measurements [156, 157] the synchrotron light is contaminated by second-order radiation in certain energy regions. Furthermore, it is extremely difficult to grow high-quality GaN crystals, and due to the surface roughness the intensity is decreased in reflectivity and ellipsometry measurements. We used the experimental lattice constants in the calculations, which, for the WZ structure are: $a = 3.19$, $c = 5.189$ and $u = 0.375\text{\AA}$ [66], while for the ZB structure the parameter is: $a = 4.54\text{\AA}$ [159].

Bandstructure

The LDA band structures for GaN are depicted in Fig. 8.7 for in the WZ and the ZB structure. They have direct ($\Gamma_{1v} \rightarrow \Gamma_{1c}$) band gaps of $E_g^{\text{LDA}}=2.24$ and 1.89 eV respectively, which is an underestimation of the experimental values, respectively $E_g^{\text{Exp}}(\text{WZ})=3.5$ [49] and $E_g^{\text{Exp}}(\text{ZB})=3.2$ [158] / 3.3 [159] eV.

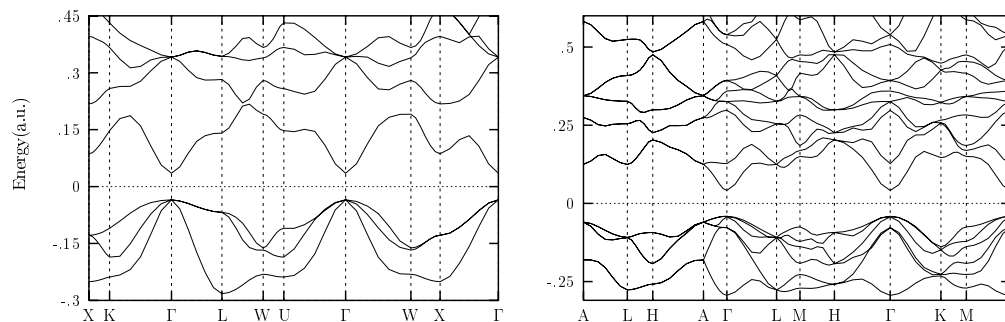


Figure 8.7: The bandstructures of GaN in the ZB (left) and the WZ structure (right).

The bandstructures for both structures resembled those found in other calculations [68, 152, 153, 154, 155] apart from the LDA band gap mismatch.

Density of states

The DOS for GaN in the ZB and WZ structure are depicted in Fig. 8.8. The similarity between both DOS spectra is high.

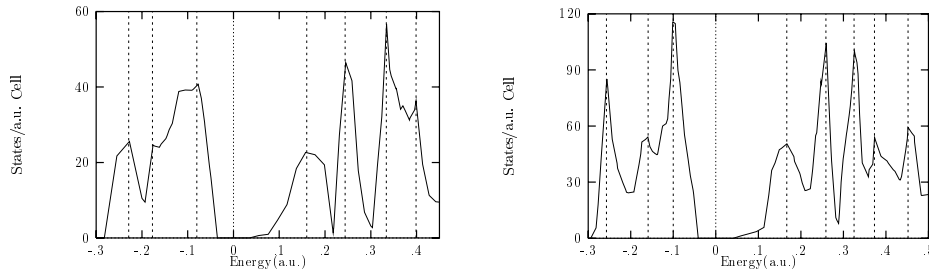


Figure 8.8: Density of States for GaN in the ZB (left) and the WZ (right) structure.

Optical spectrum

The static dielectric constants ϵ_∞ for GaN calculated for both structures have been collected in Table 8.1, together with the lattice constants [66, 159], the experimental values [49, 87, 88] for ϵ_∞ and other theoretical results [66, 67, 68, 69]. Our result for the ϵ_∞ of GaN in the wurzite structure is found in better agreement with experiment than other theoretical calculations. For the zincblende structure, our calculated ϵ_∞ matches exactly the experimental value.

The dielectric function of GaN in the WZ structure can be resolved into two components, with the polarization field either parallel to the z direction (c axis) [$\mathbf{E}\parallel c$], or perpendicular to the z direction [$\mathbf{E}\perp c$].

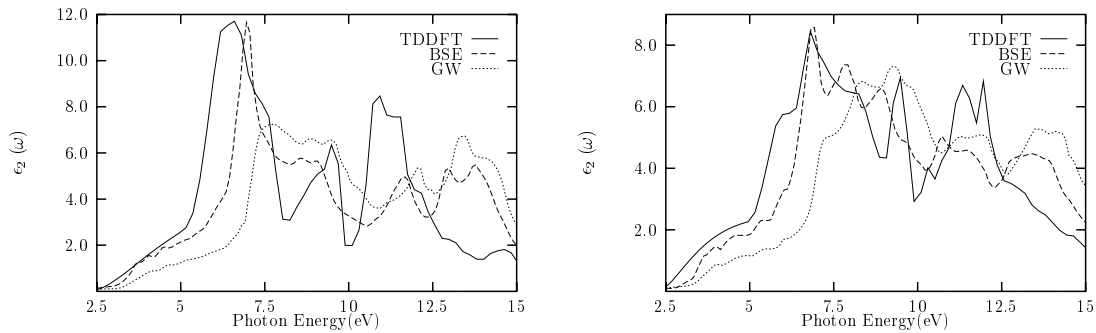


Figure 8.9: Comparison of the calculated $\epsilon_2(\omega)$ for GaN in the WZ structure [$\mathbf{E}\parallel c$ (left) and $\mathbf{E}\perp c$ (right)]. TDDFT (solid line), BSE (dashed line) and the GW theory (dotted line).

In Fig. 8.9, the TDDFT results for $\mathbf{E}\parallel c$ are compared to the BSE and GW results of

Table 8.1: Optical dielectric constants for GaN in the wurtzite and the zincblende lattice structure

GaN	Lattice (Å)	This work		Exp.	Error	Other theory		Method
Structure	a	ϵ_∞^a	$\Delta\epsilon_\infty^b$	ϵ_∞	%	ϵ_∞	$\Delta\epsilon_\infty$	c,d,e,f
Wurtzite	3.190 ^g (c=5.189) (u=0.375)	5.31	0.30	5.2 ^h	2	9.53	2.44 ^g	UR,FP,LCAO
				5.7 ⁱ	7	5.56	0.06 ^j	UR,PP,PW,LF
						4.68	0.09 ^k	UR,ASA,LMTO
						5.47	0.22 ^l	UR,PP
Zincblende	4.54 ^m	5.51		5.5 ⁿ	0	5.74 ^j		UR,PP,PW,LF
						4.78 ^k		UR,ASA,LMTO
						5.16 ^l		UR,PP

^aIn case of the wurtzite structure: $\epsilon_\infty = \bar{\epsilon}_\infty = \frac{1}{3}(\epsilon_{xx} + \epsilon_{yy} + \epsilon_{zz})$

^b $\Delta\epsilon_\infty = \epsilon_{zz} - \frac{1}{2}(\epsilon_{xx} + \epsilon_{yy})$

^cUR: uncoupled response.

^dFP: full potential; PP: pseudopotential; ASA: atomic-sphere approximation.

^ePW: plane wave; LMTO: linearized muffin-tin orbitals; LCAO: linear combination of atomic orbitals.

^fLF: local-field effects.

^gRef. [66] ^hRef. [87] ⁱRef. [88] ^jRef. [67] ^kRef. [68] ^lRef. [69] ^mRef. [159] ⁿRef. [49]

Benedict [122]. The same comparisons are made in Fig. 8.10 for the ϵ_2 of GaN in the ZB structure. Inspection of the Figs. 8.9 and 8.10 reveals the three major peaks in the absorption spectra for both structures of GaN. It can be seen from the absorption spectra, that the TDDFT results are more similar to the BSE results [122] than the GW results [68, 122, 155]. In particular the intensity and position of the first absorption peak fully agrees with the BSE results for both components ($\mathbf{E} \perp c$ and $\mathbf{E} \parallel c$) of the WZ structure. So, again, we find that the excitonic effects, for both structures of GaN, are also obtained in the TDDFT calculations.

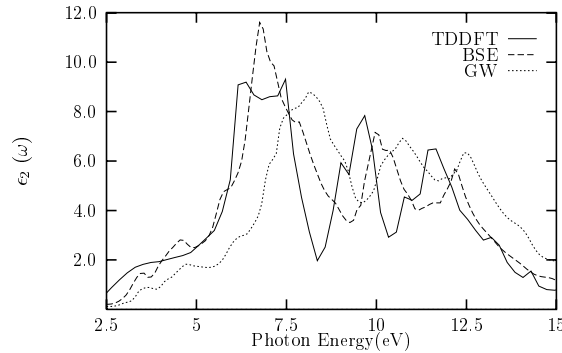


Figure 8.10: Comparison of the calculated $\epsilon_2(\omega)$ for GaN in the ZB structure. TDDFT (solid line), BSE (dashed line) and the GW theory (dotted line).

8.5 Conclusions

In this chapter we investigated to what extent excitonic effects are included in time-dependent density-functional theory (TDDFT) within the adiabatic local density approximation (ALDA). First we briefly outlined the Green's function approach (DFT/GW/BSE), and we showed the similarity between the Bethe-Salpeter equation and the corresponding TDDFT equations. Three wide band gap insulators, CaF_2 , SiO_2 and GaN , were examined. We compared the calculated TDDFT optical spectra for these insulators with the experimental measurements, and also with the $\epsilon_2(\omega)$'s as calculated by DFT/GW/BSE. The optical absorption spectra calculated using TDDFT showed all the excitonic features that were obtained using BSE, and agreed very well with experiment. In conclusion we can say that, contrary to the the general assumption, TDDFT is quite capable of describing these excitonic effects, at least in the systems investigated here.

Chapter 9

Infinite conjugated polymeric chains

F. Kootstra, P. L. de Boeij, R. van Leeuwen, and J. G. Snijders, to be submitted.

9.1 Abstract

The linear optical polarizability of several infinite conjugated polymers is examined within the time-dependent density functional theory approach, by making use of the periodicity in these systems. The polymeric chains studied were the model system polyhydrogen (H), polyacetylene (PA), polydiacetylene (PDA), polybutatriene (PBT), polythiophene (PT), polysilane (PSi) and polymethineimine (PMI). The results for the longitudinal polarizability, i.e., along the polymeric backbone α_{zz} , were highly overestimated by TDDFT in comparison with the more traditional calculation methods (like e.g., Hartree-Fock and coupled cluster) for all the considered polymeric chains. The overestimation is most likely due to the incorrect description of the macroscopic exchange-correlation (xc) electric field contribution by the LDA and GGA approximation for the xc-functional. An estimate for this macroscopic exchange-correlation contribution $E_{xc,mac}$, is given for the polymeric chains considered.

9.2 Introduction

There is currently a lot of interest in the linear and nonlinear optical (NLO) properties of large polymeric systems due to the application of these systems in optical and photonic devices. The polarizability component along the backbone of the polymeric chains, and in general also the big NLO response, increases with the chain length and with the degree of π -conjugation, which are well known phenomena caused by the electron delocalization along the backbone in these polymeric chains. The calculations of several properties of these π -conjugated chains, requires the inclusion of electron correlation effects to achieve accurate results. The correlation effects are known to be large in these systems with multiple and single bonds. Over the years many techniques have been developed, which are able to deal successfully with the electron correlation effects like, Møller-Plesset (MP),

configuration interaction (CI), coupled cluster (CC) and multiconfiguration self-consistent field (MCSCF). These approaches become too time consuming when considering the more interesting (longer) systems in material science, because of their high and unfavourable computational needs. Another method, which scales much more favourable in computational costs than the more conventional methods is density functional theory (DFT), which, in principle, also handles the electron correlation effects correctly. Therefore the methods based on DFT have gained much in popularity in *ab initio* quantum chemistry over the last years [13, 14]. As mentioned before, the NLO properties are currently under intense study, and, when using DFT, calculations are now feasible on the more interesting longer conjugated polymeric systems as well. In such systems the polarizability grows non-linearly with increasing chain length. The polarizability per unit cell, increases rapidly for the shortest chain lengths, then saturates and becomes near-constant for the longest chains.

For the determination of the asymptotic polarizability per unit cell, two different approaches can be followed. In the first one, one repeats the calculations to determine the characteristics and properties of the polymeric systems of varying length. The calculated polymers thereby consist of an increasing number of the same monomeric units. The infinite polymeric chain limit is obtained by extrapolating these results. This approach has the disadvantage that the onset of the saturation can be slow in the more conjugated and more interesting systems, and that the asymptotic values for the polarizability are often highly sensitive to the extrapolation model, which is always needed in this approach (See Section 9.4).

The alternative approach is to apply the methods of polymer quantum chemistry which make use of the periodicity in these polymeric systems, and perform a band structure calculation. In recent years only uncoupled and coupled Hartree-Fock (UHF/CHF) methods have been developed to calculate the polarizabilities per unit cell of the infinite polymeric chains.

In this chapter we apply the second approach and investigate the suitability of the first approach for determining the polarizability of several π -conjugated systems by employing conventional DFT schemes, while using different exchange-correlation functionals. The pioneering work in this area by others [160, 161], resulted in a number of conclusions considering DFT; (i) the correlation correction obtained in such systems is either much too small or even in the wrong direction, causing α to be overestimated; (ii) the chain length dependence is excessively large, in particular for the more alternating systems. These failures by DFT were attributed to the short-sightedness of the xc potentials, causing them to be insensitive to the polarization charge at the ends of the polymeric chain. After some further analysing [162], the failure was traced back to originate from an incorrect electric field dependence of the 'response part' of the xc potential in both the local, and the gradient corrected density approximations. The xc-approximations do not correctly predict a linear term counteracting the applied electric field.

We compare in this chapter the above (overestimated) DFT results (first approach) for the asymptotic longitudinal polarizability of the π -conjugated polymeric chains with the ones as obtained directly by our recently implemented periodic band structure TDDFT approach (second approach) [63, 94].

9.3 DFT versus other calculation methods

Nowadays several methods exist for calculating the polarizabilities of molecular systems. Some of these methods include correlation effects, others do not. In general, when a centrosymmetric molecule is placed in a static homogeneous electric field F^0 , the energy E of the molecule is stabilized according to

$$E = E_0 - \frac{1}{2!}\alpha_{ij}F_i^0F_j^0 - \frac{1}{4!}\gamma_{ijkl}F_i^0F_j^0F_k^0F_l^0 - \dots, \quad (9.1)$$

in which the summation over repeated indices is implied, α , and γ are the polarizability, and second hyperpolarizability tensors, and E_0 is the energy of the free molecule. The i -th component of the dipole moment of the molecule, which is induced by this electric field, is given by

$$\mu_i = \alpha_{ij}F_j^0 + \frac{1}{3!}\gamma_{ijkl}F_j^0F_k^0F_l^0 + \dots. \quad (9.2)$$

Among the available calculation methods the molecular polarizability is obtained in different ways. The polarizability is defined, either as the linear response of the dipole moment to an external electric field, or as the second-order derivative in the perturbation expansion of the electronic energy with respect to the electric field. These definitions are equivalent due to the Hellmann-Feymann theorem, and we can write

$$\alpha = - \left(\frac{\partial^2 E}{\partial F^2} \right)_{F=F^0} = \left(\frac{\partial \mu}{\partial F} \right)_{F=F^0}. \quad (9.3)$$

Therefore, by using these techniques one needs to know the wave functions and energies of the system in the presence of the perturbation by the electric field, or equivalently, the derivatives of the wave functions and energies with respect to this electric field. These methods, which take the field-induced electron reorganization effects into account in a self consistent way, are said to be *coupled* methods. Examples are the coupled Hartree-Fock (CHF), the Møller-Plesset (MP), and the Configuration Cluster (CC) methods. In other *uncoupled* methods, which do not include field-induced electron reorganization effects, like e.g. uncoupled Hartree-Fock (UCHF), the polarizability tensor is obtained by a summation over states (SOS) procedure:

$$\alpha = 2 \sum_{n \neq 0} \frac{|\langle \psi_0 | \mathbf{r} | \psi_n \rangle|^2}{E_n - E_0}, \quad (9.4)$$

in which the sum runs over all the excited states of the system. Here ψ_0 and ψ_n are the ground- and the excited state wave functions with corresponding energies E_0 and E_n , respectively.

In Density Functional Theory (DFT), the electron density $\rho(\mathbf{r})$ is the central quantity which determines all the properties of the system [13, 14]. The density $\rho(\mathbf{r})$ is evaluated self-consistently by solving the Kohn-Sham equation [3] which involves the evaluation of the exchange and correlation terms. The calculated results, depend on the particular approximations for the exchange-correlation functional. Several studies have already

demonstrated how accurate and useful DFT calculations can be, e.g., for the prediction of ground state geometries, atomization energies, vibrational frequencies and the energies of reactions. The results are of comparable quality as MP2 calculations, but at much lower computational costs.

9.4 Extrapolation procedures

As was already mentioned in the introduction of this chapter, the calculations to determine the characteristics and properties of the infinite polymeric chains consisted of studying the asymptotic behaviour of oligomers increasing in length, i.e., by successive addition of the same monomer unit. The extrapolations of these results to the infinite polymeric chain limit, which is necessary to determine the asymptotic longitudinal polarizability per unit cell, are often highly sensitive to the extrapolation model used, and an extrapolation scheme always has the disadvantage that the onset of the saturation can be very slow in the more conjugated and interesting systems. For the CHF, MP4, and CCSD results, given in the Tables 9.1 and 9.2, one of the following extrapolation procedures was used.

For evaluating and finding the variation in the longitudinal polarizability between consecutive oligomers, the first (most simple and fundamental) formula is

$$\Delta\alpha_{zz}(N) = \alpha_{zz}(N)/N , \quad (9.5)$$

in which N is the unit cell number. Comparing Eq. 9.5 with the differential approach

$$\Delta\alpha_{zz}(N) = \alpha_{zz}(N) - \alpha_{zz}(N - 1) , \quad (9.6)$$

shows that Eq. 9.6 has the advantage that it eliminates, the chain-end effects of the oligomer in the polarizability increase.

In addition to the above two extrapolation formulas, there are several ad-hoc model functions used, for finding the asymptotic value of the polarizability [174] of the polymer. Namely,

$$\Delta\alpha_{zz}(N) = a + \frac{b}{N} + \frac{c}{N^2} , \quad (9.7)$$

$$\Delta\alpha_{zz}(N) = a + be^{-cN} , \quad (9.8)$$

$$\Delta\alpha_{zz}(N) = \frac{a}{1 + be^{-cN}} . \quad (9.9)$$

The advantage of the function in Eq. 9.7 is, that it can be systematically improved by adding higher terms in $1/N$. The model function in Eq. 9.8 has been used to predict the polymeric $\Delta\alpha_{zz}(N)$ of polyacetylene chains (Ref. [172]), and the last one (Eq. 9.9) is called the logistic equation.

Until now there is no reason to prefer one of the above model functions, since the correct analytic form of the equation which describes the evolution of $\Delta\alpha_{zz}(N)$ with chain length is not known. A complete discussion on extrapolation techniques can be found in the Refs. [163] and [164].

9.5 Theory

When a system is perturbed by applying a time-dependent external electric field $\mathbf{E}_{ext}(\mathbf{r}, t)$, the density will become time-dependent and currents will be induced, so the system will become polarized. In the time-dependent (TD) version of density functional theory (DFT), one adds time-dependent vector and scalar contributions to the effective ground state potential. These additional potentials, respectively $\mathbf{A}_{eff}(\mathbf{r}, t)$ and $\delta v_{eff}(\mathbf{r}, t)$, have the property that they produce the exact time-dependent density and current of the true system, when applied to the Kohn-Sham system of non-interacting particles. According to the Runge-Gross theorem [4], the time-dependent extension of the Hohenberg-Kohn theory [2, 3], these potentials are, apart from the usual freedom of choice for the gauge, functionals of the density and the current, and should therefore be obtained self-consistently. The time-dependent Kohn-Sham system is now obtained by replacing both the ground state momentum operator by

$$\mathbf{p} \rightarrow -i\nabla + 1/c \mathbf{A}_{eff}(\mathbf{r}, t) , \quad (9.10)$$

and the effective scalar potential by the time-dependent version

$$v_{eff}(\mathbf{r}) \rightarrow v_{eff,0}(\mathbf{r}) + \delta v_{eff}(\mathbf{r}, t) . \quad (9.11)$$

When one neglects the small microscopic contributions to the transverse vector potential (such as the Breit term [40]), we can make a special choice for the gauge, which we will call the microscopic Coulomb gauge [63]. In this gauge both the scalar and vector potential are lattice periodic, and have the property that all microscopic components are included in the scalar potential, whereas all macroscopic components are described by the vector potential. The perturbing potentials can be given in this gauge as,

$$\mathbf{A}_{eff}(\mathbf{r}, t) = \mathbf{A}(\mathbf{r}, t) = -c \int^t dt' \mathbf{E}_{mac}(\mathbf{r}, t') , \quad (9.12)$$

$$\delta v_{eff}(\mathbf{r}, t) = \delta v_{mic}(\mathbf{r}, t) + \int d\mathbf{r}' \left. \frac{\partial v_{xc}[\rho](\mathbf{r})}{\partial \rho(\mathbf{r}')} \right|_{\rho_0} \delta \rho(\mathbf{r}', t) . \quad (9.13)$$

Here $\delta v_{mic}(\mathbf{r}, t)$ is the microscopic part of the Hartree potential of the induced density $\delta \rho(\mathbf{r}, t)$. In these relations we have neglected any macroscopic contributions of the exchange-correlation (xc) in the vector potential [108], and we used the adiabatic local density approximation (ALDA) for the first order xc-contribution to the scalar potential. The macroscopic electric field $\mathbf{E}_{mac}(\mathbf{r}, t)$ is the average field in a region around \mathbf{r} inside the solid, and hence it comprises both the externally applied field $\mathbf{E}_{ext}(\mathbf{r}, t)$ plus the macroscopic part of the induced field. This latter field is in addition to the induced charge density also due to the induced current density $\delta \mathbf{j}(\mathbf{r}, t)$. We will treat this macroscopic field as the perturbing field. The quantity of interest (written in the frequency domain) is the induced macroscopic polarization $\mathbf{P}_{mac}(\omega)$, which will be proportional to the macroscopic electric field $\mathbf{E}_{mac}(\mathbf{r}, t)$, and also to the average induced current density $\delta \mathbf{j}(\mathbf{r}, \omega)$, according to,

$$\mathbf{P}_{mac}(\omega) = \chi_e(\omega) \cdot \mathbf{E}_{mac}(\omega) = \frac{i}{\omega V} \int_V d\mathbf{r} \delta \mathbf{j}(\mathbf{r}, \omega) . \quad (9.14)$$

Within time-dependent linear response theory, we obtain the following relation for the induced density,

$$\delta\rho(\mathbf{r}, \omega) = \int \left(\frac{i}{\omega} \chi_{\rho\mathbf{j}}(\mathbf{r}, \mathbf{r}', \omega) \cdot \mathbf{E}_{mac}(\omega) + \chi_{\rho\rho}(\mathbf{r}, \mathbf{r}', \omega) \delta v_{eff}(\mathbf{r}', \omega) \right) d\mathbf{r}'. \quad (9.15)$$

The various Kohn-Sham response functions can be obtained from the occupied (*i*) and virtual (*a*) states of the ground-state system. They can be evaluated using the general form,

$$\chi_{ab}(\mathbf{r}, \mathbf{r}', \omega) = \frac{V}{4\pi^3} \sum_{i,a} \int d\mathbf{k} \frac{\mathbf{a}_{iak}(\mathbf{r}) \mathbf{b}_{iak}^*(\mathbf{r}')}{\epsilon_{i\mathbf{k}} - \epsilon_{a\mathbf{k}} + \omega + i\eta} + c.c.(-\omega), \quad (9.16)$$

by substituting for $\mathbf{a}_{iak}(\mathbf{r})$ and $\mathbf{b}_{iak}(\mathbf{r})$ either the transition density,

$$\rho_{iak}(\mathbf{r}) = \psi_{i\mathbf{k}}^*(\mathbf{r}) \psi_{a\mathbf{k}}(\mathbf{r}), \quad (9.17)$$

or the transition current,

$$\mathbf{j}_{iak}(\mathbf{r}) = \psi_{i\mathbf{k}}^*(\mathbf{r}) \nabla \psi_{a\mathbf{k}}(\mathbf{r}) - (\nabla \psi_{i\mathbf{k}}^*(\mathbf{r})) \psi_{a\mathbf{k}}(\mathbf{r}). \quad (9.18)$$

The Brillouin zone integrations in Eq. 9.16 are evaluated numerically, by including the energy denominator in the integration weights. The way these integration weights are obtained is subject of the Appendix (See Section 9.9).

Now, by keeping the macroscopic field fixed, and noting that within the ALDA the effective potential is a functional of the density alone, we can solve the set of response equations, Eqns. 9.13 and 9.15, self-consistently. With the perturbing effective potentials now fully determined, the induced paramagnetic current density $\delta\mathbf{j}_p(\mathbf{r}, \omega)$ follows from

$$\delta\mathbf{j}_p(\mathbf{r}, \omega) = \int \left(\frac{i}{\omega} \chi_{\mathbf{j}\mathbf{j}}(\mathbf{r}, \mathbf{r}', \omega) \cdot \mathbf{E}_{mac}(\omega) + \chi_{\mathbf{j}\rho}(\mathbf{r}, \mathbf{r}', \omega) \delta v_{eff}(\mathbf{r}', \omega) \right) d\mathbf{r}'. \quad (9.19)$$

The total induced current contains, apart from this paramagnetic term, also the diamagnetic contribution,

$$\delta\mathbf{j}_d(\mathbf{r}, \omega) = \frac{1}{c} \rho_0(\mathbf{r}) \mathbf{A}(\mathbf{r}, \omega). \quad (9.20)$$

In the special case in which we choose the macroscopic field along one of the Cartesian directions *j*, and with a frequency dependence according to $\mathbf{E}_{mac}(\omega) = -i\omega\mathbf{e}_j$, the diamagnetic contribution to the current density reduces to $\delta\mathbf{j}_d(\mathbf{r}, \omega) = -\delta\mathbf{j}_p(\mathbf{r}, 0)$, i.e. to minus the static paramagnetic value [63]. The paramagnetic and diamagnetic components together form the total current, of which the average value yields the macroscopic polarization. The Cartesian components of the susceptibility follow from the Eq. 9.14,

$$[\chi_\epsilon(\omega)]_{ij} = \left\{ \frac{-1}{V\omega^2} \int_V [\delta\mathbf{j}_p(\mathbf{r}, \omega) - \delta\mathbf{j}_p(\mathbf{r}, 0)]_i d\mathbf{r} \right\}_{\mathbf{E}_{mac}(\omega) = -i\omega\mathbf{e}_j}. \quad (9.21)$$

Under the assumption that in linear polymeric chains there is no macroscopic screening, i.e., the induced electric field in the chains is not of macroscopic nature, the macroscopic

electric field equals the externally applied electric field ($\mathbf{E}_{mac} \equiv \mathbf{E}_{ext}$). The longitudinal polarizability, along the backbone of the polymer α_{zz} , can be obtained as the integrated susceptibility $\chi_e(\mathbf{r}, \omega)$ over the unit cell

$$\mu = \int \mathbf{P}(\mathbf{r}, \omega) d\mathbf{r} = \underbrace{\left(\int \chi_e(\mathbf{r}, \omega) d\mathbf{r} \right)}_{\alpha} \cdot \mathbf{E}_{ext}(\omega) = \alpha \cdot \mathbf{E}_{ext}(\omega) . \quad (9.22)$$

9.6 Basis sets and parameters in the calculations

For the time-dependent density functional theory (TDDFT) calculations, we used the Amsterdam Density Functional (ADF) program [38] for the *molecular* calculations, and the *periodic* band structure calculations were performed with the Amsterdam Density Functional BAND-structure program (ADF-BAND) [37]. The basis sets in the molecular ADF and the periodic ADF-BAND calculations were triple zeta s, p Slater-type basisfunctions (STO's) plus a polarization function, which we denote as 3Z2P*. For the integration in the 1-dimensional reciprocal space we used 7 symmetry unique \mathbf{k} -points for all oligomers. The geometries for all the polymeric chains examined are depicted in Fig. 9.4, as they were found in the Refs. [161, 167, 168, 169, 170, 171, 172, 173, 174, 176].

9.7 Results

9.7.1 The model system polyhydrogen

The infinite molecular hydrogen chain model $(\text{H}_2)_n$ has been studied extensively by Champagne and co-workers [165, 166]. The main objectives of these studies were to determine the electron-electron interaction and the size of atomic basis set needed to correctly estimate the asymptotic static longitudinal polarizability per unit cell of a polymeric system. Their results already pointed out the importance of developing direct techniques, which are able to deal with the periodicity in such systems to get the asymptotic values for the polarizability directly.

We extended our time-dependent periodic band structure DFT approach [63], which had already proven to be very successful for crystals [94, 102, 136, 180], to handle also systems which possess only periodicity in one dimension. This periodic TDDFT approach is used to get the asymptotic values for the longitudinal polarizability directly for the polymeric chains without the use of an extrapolation model, as is always necessary in the molecular programs.

The periodic implementation was first used for calculations on the model system polyhydrogen. We considered chains in which the unit cell length (a) (See Fig. 9.4) was varied from 4.5 to 22.0 a.u. and the intramolecular distance (H-H) was fixed at 2.0 a.u. Resulting in a bond length alternation (BLA) from 0.5 to 18.0 a.u. (See Table. 9.1)

In Table. 9.1, the asymptotic longitudinal polarizabilities (α_{zz}) per unit cell (containing one H_2 -unit) of different alternating model hydrogen chains are given. The polarizabilities were

calculated by using several different calculation methods, all with different (comparable) basissets. The basis used in the coupled Hartree-Fock (CHF), the Møller-Plesset (MP4) and coupled cluster (CCSD(T)) calculations [165] and in the G92/DMol calculations [160] were Gaussian triple- ζ plus polarization (6)-311G(*)* atomic basis sets. Basis sets, which are comparable to the STO 3Z2P* used in the TDDFT calculations by the ADF [38] and the BAND [37] program.

Table 9.1: Asymptotic longitudinal polarizabilities (α_{zz}) per H_2 unit of the model system polyhydrogen with different bond length alternation, as calculated at the CHF, MP4 and CCSD(T) level in comparison with several TDDFT (ADF/BAND/G92/DMol) calculations (all values in atomic units).

BLA	CHF ^a	MP4 ^a	CCSD(T) ^a	ADF ^b	BAND	G92/DMol ^c
0.5	55.079	53.564	50.632	162.00	121.9	139.087
1.0	28.602	26.508	25.666	47.02	46.2	48.338
2.0	17.682	15.826	15.511	22.14	22.2	21.753
6.0				12.57	12.4	
10.0				12.06	11.7	
14.0				11.94	11.6	
18.0				11.92	11.6	
∞				11.84		

^aRef. [165] ^bRef. [38] ^cRef. [160]

The results in Table 9.1, for the asymptotic longitudinal polarizabilities of the model system polyhydrogen with different BLA, are also depicted in Fig. 9.1.

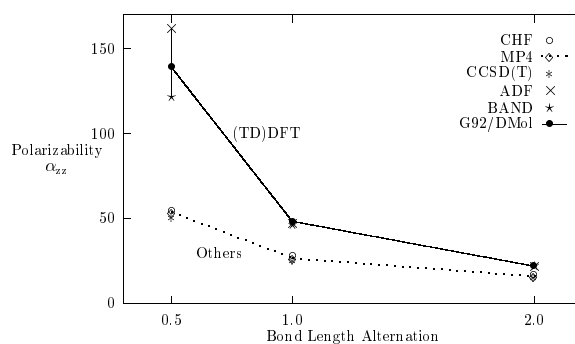


Figure 9.1: Comparison of the asymptotic longitudinal polarizabilities α_{zz} of the model $(H_2)_n$ -chains with different BLA. The TDDFT based methods in comparison with others, as given in Table 9.1 (all values in atomic units).

As can be seen from Fig 9.1, the shorter the BLA in the model hydrogen chain the higher the overestimation of the polarizability in the TDDFT based methods in comparison to the other methods. Further we see from Table 9.1 that the molecular based ADF program

and the periodic BAND implementation gave approximately the same overestimated results, which converged in the chains with the longest BLA to the polarizability of a single H_2 -molecule. The different extrapolation procedures used in the *molecular* programs for evaluating the asymptotic value of the longitudinal polarizability are plotted in Fig. 9.2, for the model system polyhydrogen $(\text{H}_2)_n$ with a BLA of 0.5 \AA . This was done by repeating the polarizability calculations of successive polyhydrogen chains, by increasing the length of the chain through the addition of more monomeric H_2 -units. The extrapolation procedures used, are given in Eqs. 9.5 and 9.6, respectively. The polarizability values α_{zz} are plotted against the number of H_2 -units (Fig. 9.2).

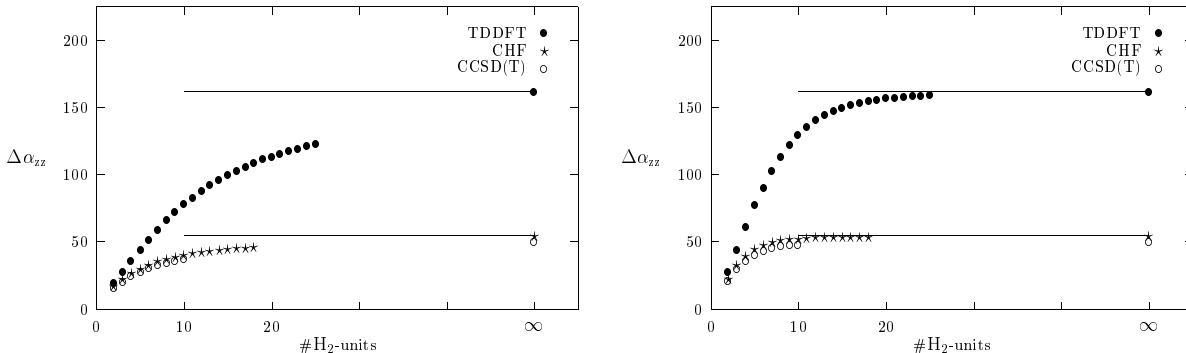


Figure 9.2: Evaluation of the asymptotic longitudinal polarizability $\Delta\alpha_{zz}$ per H_2 -unit for the model hydrogen chain $(\text{H}_2)_n$, with a bond length alternation of 0.5 \AA , and as calculated by TDDFT, CHF, and CCSD(T). The extrapolation procedures used are given in Eq. 9.5 [left], and to Eq. 9.6 [right]. These values were plotted against the number of H_2 -units.

As can be seen in Fig. 9.2, the value for the by TDDFT calculated value of the longitudinal polarizability of an infinite model $(\text{H}_2)_n$ -chain with a BLA of 0.5 \AA , as found directly by our *periodic* ADF-BAND implementation, is consistent with the extrapolated asymptotic *molecular* ADF result. The use of the periodic ADF-BAND implementation is therefore much more convenient, because 1. the polarizability value is found in a single calculation, 2. the extrapolation step, for finding α_{zz} , is not necessary, and 3. no choice for a particular extrapolation model is needed. Looking at Fig. 9.2, it should also be concluded, that the extrapolation models as given by Eq. 9.5 and 9.6 are reasonably reliable, but that the differential approach (Eq. 9.6), which eliminates the chain-end effects in the oligomers, converges much faster.

Earlier, van Gisbergen et al.[162] attributed the overestimation of the longitudinal polarizability in the model system polyhydrogen $(\text{H}_2)_n$ -chain to an incorrect electric field dependence of the xc-potential. The LDA potential lacks a linear term, which is counteracting the externally applied electric field. From Fig. 2 in Ref. [162] it can be deduced that, when an externally applied electric field with a strength of 10^{-3} a.u. ($\mathbf{E}_{ext} = 0.001$ a.u.) is applied to a model $(\text{H}_2)_n$ -chain with a BLA of ~ 3 a.u., the strength of the counteracting field of which LDA lacks has a strength of 10^{-4} a.u. In Chapter 7, we introduced an

approximate xc-functional for the macroscopic xc-electric field. We can now estimate the value for the \mathbf{Y} -functional needed to correct the differences between the HF and TDDFT results. Using the expression

$$\mathbf{P} = \tilde{\chi} (\mathbf{E}_{ext} - \mathbf{Y} \cdot \mathbf{P}) , \quad (9.23)$$

and requiring the corrected longitudinal polarizability per H_2 unit to be equal to the HF value for the model $(\text{H}_2)_n$ -chain with a BLA of ~ 3 a.u., as it was deduced from the HF results in Table 9.1. We find an \mathbf{Y} -value of 0.01. This value of 10^{-2} for \mathbf{Y} is also found in the periodic ADF-BAND calculations. Current density functional theory gives an explicit expression for \mathbf{Y} (See Chapter 7), and we are currently investigating if this functional indeed reproduces this value of 10^{-2} for \mathbf{Y} .

9.7.2 Other polymeric chains

After using the periodic TDDFT approach to get the asymptotic values for the longitudinal polarizability for the *model* system polyhydrogen $(\text{H}_2)_n$, we also calculated the α_{zz} for several *real* polymeric systems, and compared our TDDFT results to the (extrapolated) CHF results. The investigated polymeric chains were polyynes (PY, C_{2n}H_2), polyacetylene (PA, $\text{C}_{2n}\text{H}_{2n+2}$), polydiacetylene (PDA, $\text{C}_{4n}\text{H}_{2n+2}$), polybutatriene (PBT, $\text{C}_{4n}\text{H}_{2n+2}$), polythiophene (PT, $\text{C}_{8n}\text{S}_{2n}\text{H}_{4n+2}$), polysilane (PSi, $\text{Si}_{2n}\text{H}_{4n+2}$), and polymethineimine (PMI, $\text{C}_n\text{N}_n\text{H}_{n+2}$, trans-transoid). The structures and geometries of the polymers examined are depicted in Fig. 9.4. The results for the longitudinal polarizability have been collected in Table 9.2, for the polymers examined, as calculated by CHF and by our periodic TDDFT implementation (BAND). From the ratio's of the BAND and CHF values listed in Table 9.2, it can be seen that TDDFT in the ALDA gives longitudinal polarizability for these polymers, which are overestimated by a factor of 2 to 5 compared to the CHF results. The overestimation by TDDFT is also depicted in Fig. 9.3.

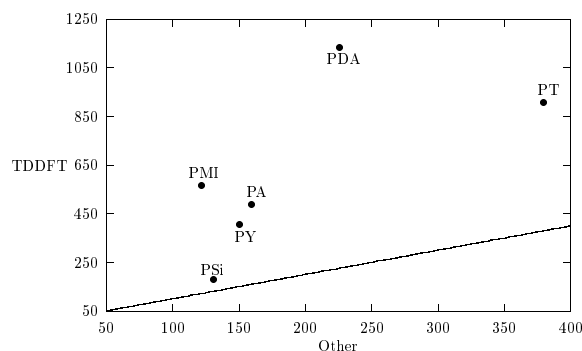


Figure 9.3: TDDFT versus CHF results for the asymptotic longitudinal polarizability of the polymers: PY, PA, PDA, PT, PSi, and PMI.

As was already discussed in Section 9.7.1 for the model system polyhydrogen $(\text{H}_2)_n$, the overestimation of α_{zz} by TDDFT is due to an incorrect electric field dependence of the xc-potential, which lacks a linear term counteracting this externally applied electric field.

In the same way as was done for the $(\text{H}_2)_n$ -chains, we can calculate and give a numerical value of this linear counteracting term, which is given in Table 9.2 for the investigated polymeric chains, showing that an \mathbf{Y} -value in the order of 10^{-3} is needed. This value of \mathbf{Y} , for the *real* polymeric systems, is in the same order as found for the *model* system polyhydrogen, but again it remains to be seen if this value can be reproduced by current density functional theory.

Table 9.2: Comparison of the asymptotic longitudinal polarizabilities of polyynes (PY), polyactelene (PA), polydiacetylene (PDA), polybutatriene (PBT), polythiophene (PT), polysilane (PSi) and polymethineimine (PMI), as calculated by CHF and TDDFT (all values in atomic units).

Polymer	Geometry unit cell	BLA (Å)	TDDFT		Ratio BAND/CHF	\mathbf{Y}
			CHF	BAND		
PY	$-\text{[C}_{2n}\text{]}-$	0.166 ^j	151±2 ^j	412.2	2.73	0.004
		0.220 ^a	113.5±1.5 ⁱ			
PA	$-\text{[C}_{2n}\text{H}_{2n}\text{]}-$	0.112 ^{b,n}	160.5±1.5 ^k	493.9	3.08	0.004
		0.082 ^c	220.7 ^f			
PDA	$-\text{[C}_{4n}\text{H}_{2n}\text{]}-$	0.225;0.088 ^e	226±2 ^e	1138.2	5.04	0.004
		0.230;0.100 ^d	203±4 ^l			
PBT	$-\text{[C}_{4n}\text{H}_{2n}\text{]}-$	0.194;0.128 ^e	1060±14 ^e	2498.6	2.36	0.001
PT	$-\text{[C}_{8n}\text{S}_{2n}\text{H}_{4n}\text{]}-$	0.064 ^f	380.0 ^f	914.8	2.41	0.002
PSi	$-\text{[Si}_{2n}\text{H}_{4n}\text{]}-$	0.0 ^g	131.4±0.2 ^m	182.1	1.39	0.002
PMI	$-\text{[C}_n\text{N}_n\text{H}_n\text{]}-$	0.100 ^h	122.6±0.9 ^h	572.3	4.67	0.006

^aRef. [167] ^bRef. [168] ^cRef. [169] ^dRef. [170] ^eRef. [171] ^fRef. [172] ^gRef. [173] ^hRef. [174] ⁱRef. [175]
^jRef. [176] ^kRef. [177] ^lRef. [178] ^mRef. [179] ⁿRef. [161]

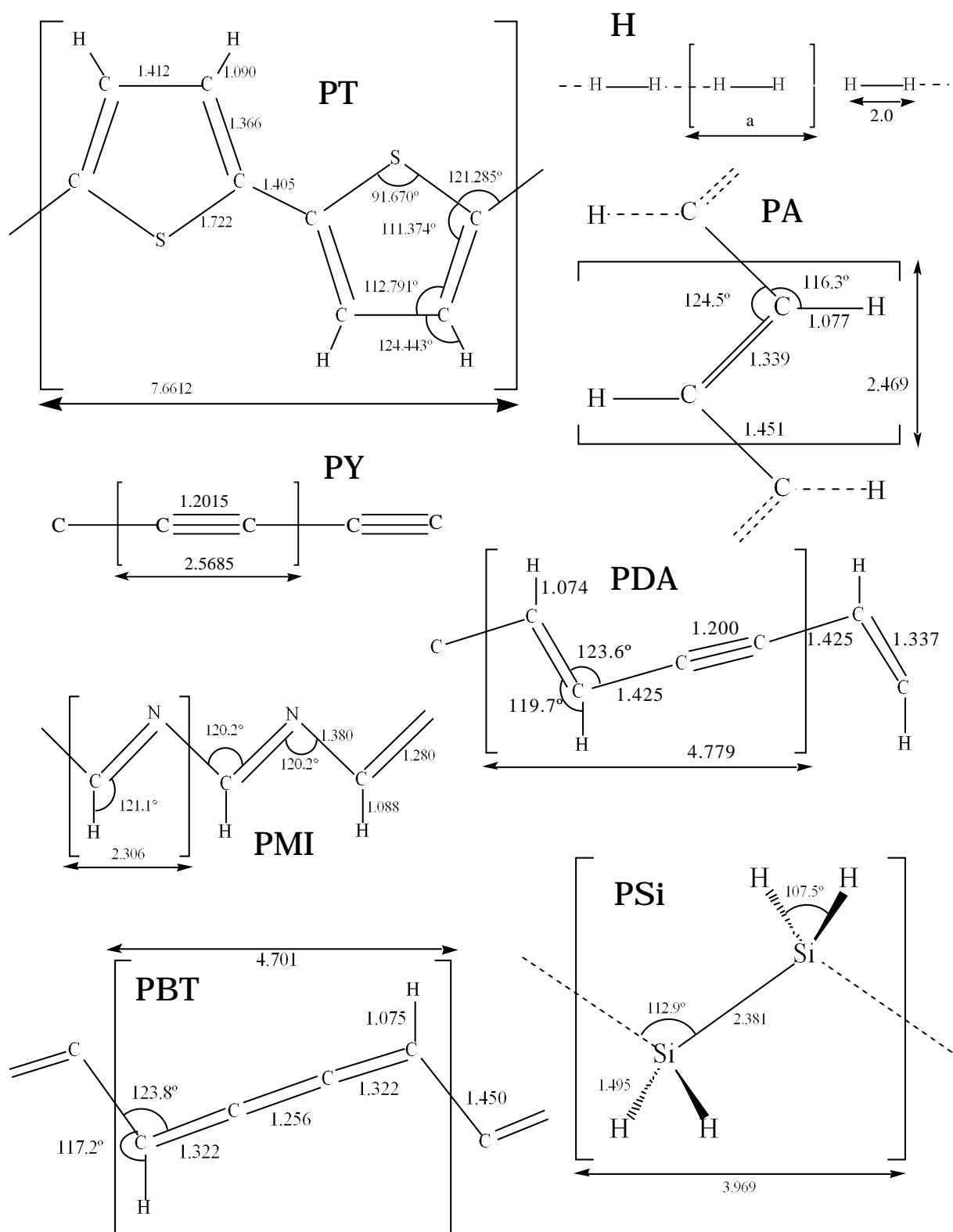


Figure 9.4: Polymers. The bond lengths are given in a.u., the bond angles in deg.

9.8 Conclusions

In this chapter we investigated the longitudinal polarizability of several infinite conjugated polymers, as calculated by time-dependent density functional theory. Our TDDFT implementation makes direct use of the periodicity in these systems. The TDDFT polarizabilities for the model H₂-chains, as found by our periodic BAND implementation, were close to the molecular ADF results, found after extrapolation. Both, BAND as well as ADF, overestimated the α_{zz} in the model system polyhydrogen, and the overestimation is largest for the smallest BLA. The extrapolation procedures which are used in the molecular programs for calculating the static longitudinal polarizability are reasonably reliable, but it is much more convenient to do a periodic BAND calculation, in which the extrapolation step is superfluous. The same polarizability overestimation was also found for all the polymeric chains considered. This overestimation is caused by an incorrect electric field dependence of the xc potential. The LDA and GGA potentials lack a linear term, the macroscopic exchange-correlation electric field, which counteracts the externally applied electric field. The macroscopic exchange-correlation contribution $E_{xc,mac}$ is estimated by the value of the polarization functional \mathbf{Y} . The \mathbf{Y} -value is found to be in the order of $10^{-2}/10^{-3}$ a.u. for the model system polyhydrogen and for the other polymeric chains.

9.9 Appendix: Periodic implementation

Our successful implementation of TDDFT for solids can be found in Chapter 4. The benchmarking results of this method for a large range of nonmetallic crystals, together with the incorporation, and results, of relativistic effects in TDDFT are compiled in the Chapters 5-8. Here we very briefly reconsider the the integration over the Irreducible wedge of the Brillouin zone (IBZ), to which the intergration can be reduced because the wedges are related by symmetry, and in particular consider the implications for polymers, e.g., periodic systems with periodicity in one dimension.

9.9.1 Quadrature for the response kernels

The Kohn-Sham response functions, as given in Eq. 9.16, involve integrations over the irreducible Brillouin zone, in which the denominator can become singular. The energy dependent part is therefore separated from the rest according to

$$I_{ia}(\omega) = \int_{V_{IBZ}} \frac{g_{ia}(\mathbf{k})}{\omega - (\epsilon_{a\mathbf{k}} - \epsilon_{i\mathbf{k}}) + i\eta} d\mathbf{k} = \int_{\epsilon_0}^{\epsilon_1} \frac{g_{ia}(\epsilon)}{\omega - \epsilon + i\eta} d\epsilon, \quad (9.24)$$

in which $g_{ia}(\epsilon) = \int d\mathbf{k} g_{ia}(\mathbf{k}) \delta(\epsilon - (\epsilon_{a\mathbf{k}} - \epsilon_{i\mathbf{k}}))$, and ϵ_0, ϵ_1 are the minimum and maximum value of $\epsilon(\mathbf{k})$ occurring in V_{IBZ} . For the integration in Eq. 9.24 accurate quadrature schemes exist (Ref. [48]) which give us the weights $\tilde{w}_{ia\mathbf{k}_j}(\epsilon)$, such that

$$g_{ia}(\epsilon) = \sum_j \tilde{w}_{ia\mathbf{k}_j}(\epsilon) g_{ia}(\mathbf{k}_j). \quad (9.25)$$

In the linear tetrahedron scheme these weights are piecewise cubic polynomials in ϵ . For the quadrature of Eqn. 9.24 we can write

$$I_{ia}(\omega) = \int_{\epsilon_0}^{\epsilon_1} \frac{g_{ia}(\epsilon)}{\omega - \epsilon + i\eta} d\epsilon = \sum_j w_{ia\mathbf{k}_j}(\omega) g_{ia}(\mathbf{k}_j). \quad (9.26)$$

We only have to integrate the weights $\tilde{w}_{ia\mathbf{k}_j}(\epsilon)$ in the following way to obtain the new weights $w_{ia\mathbf{k}_j}(\omega)$ as functions of ω ,

$$w_{ia\mathbf{k}_j}(\omega) = \int_{\epsilon_0}^{\epsilon_1} \frac{\tilde{w}_{ia\mathbf{k}_j}(\epsilon)}{\omega - \epsilon + i\eta} d\epsilon = \mathcal{P} \int_{\epsilon_0}^{\epsilon_1} \frac{\tilde{w}_{ia\mathbf{k}_j}(\epsilon)}{\omega - \epsilon} d\epsilon + i\pi \tilde{w}_{ia\mathbf{k}_j}(\omega). \quad (9.27)$$

The real and imaginary parts of this weight can thus be obtained separately using the Cauchy principle value and residual parts.

9.9.2 Integrations in the IBZ

Two algorithms are generally used (depending on the energy dispersion in the energybands) for the calculation of the integration weights, $w_{ia\mathbf{k}_j}(\omega)$, as given in Eqn. 9.27.

1. Energybands with dispersion

For the integration of Eq. 9.26, the parameterization inside the tetrahedrons (3D) or triangles (2D), in which the IBZ is divided, is the same as given in Ref. [48]. In the general (3D case), $g_{ia}(\mathbf{k})$ is found by linear interpolation inside the tetrahedron by

$$g_{ia}(\mathbf{k}) = g_{ia}(k_x, k_y, k_z) = g_1 + g_2 k_x + g_3 k_y + g_4 k_z. \quad (9.28)$$

Thus the contributions from a simplex S become

$$\int_S \frac{g_{ia}(\mathbf{k})}{\omega - \epsilon + i\eta} d\mathbf{k} = \sum_{i=1}^4 g_i I_i, \quad (9.29)$$

in which the coördinate transformation from Cartesian (k_x, k_y, k_z) to internal coördinates, parametrizing the constant energy surface, (e, u, v) is made, and when writing $\mu_i = 1, k_x, k_y, k_z$ and $e = \omega - \epsilon$; I_i in Eqn. 9.29. is calculated from

$$I_i = \int_{\epsilon_0}^{\epsilon_1} de \int_0^1 du \int_0^{1-u} dv \left[\frac{\mu_i}{e + i\eta} \cdot \frac{\delta(k_x, k_y, k_z)}{\delta(e, u, v)} \right]. \quad (9.30)$$

The numerical integration weights $w_{ia\mathbf{k}_j}(\omega)$ are than directly calculated from I_i as described in Appendix 2. from Ref. [48].

2. Energybands without dispersion

The term

$$\frac{1}{\omega - (\epsilon_{a\mathbf{k}} - \epsilon_{i\mathbf{k}}) + i\eta} , \quad (9.31)$$

in Eqn. 9.24. becomes \mathbf{k} independent, and can be placed outside the integral over \mathbf{k} . When writing $\Delta = \omega - (\epsilon_{a\mathbf{k}} - \epsilon_{i\mathbf{k}})$ as the average value in the tetrahedron, the integral of Eqn. 9.29. takes the form

$$\frac{1}{\Delta + i\eta} \int_S g_{ia}(\mathbf{k}) d\mathbf{k} . \quad (9.32)$$

Also using linear interpolation for $g_{ia}(\mathbf{k})$ in this case, but now making the coördinate transformation $\delta(k_x, k_y, k_z)/\delta(k_x, u, v)$ (in the 3D case again). Results for the integrals I_i of Eqn. 9.29 in

$$I_i = \frac{1}{\Delta + i\eta} \int_{k_{xmin}}^{k_{xmax}} dk_x \int_0^1 du \int_0^{1-u} dv \left[\mu_i \frac{\delta(k_x, k_y, k_z)}{\delta(k_x, u, v)} \right] \quad (9.33)$$

9.9.3 Crystals, surfaces, and polymers

The irreducible Brillouin zone is subdivided into tetrahedrons in the three dimensional case (crystals). The tetrahedrons are indentified by 4 \mathbf{k} -points in the reciprocal space. For the two dimensional case (surfaces), the IBZ reduces to triangles which can be indentified by 3 \mathbf{k} -points. For polymers, the one dimensional case, the IBZ is subdivided into lines. The lines are indentified by 2 \mathbf{k} -points in the reciprocal space. In these 2 \mathbf{k} -points, the x-coördinates and also the energy $\epsilon_{n\mathbf{k}}$ of the n energy bands are known from the DFT groundstate calculation. The integral in Eq. 9.30, in case the energybands show dispersion, reduces in the one dimension case to

$$I_i = \int_{e_0}^{e_1} de \left[\frac{\mu_i}{e + i\eta} \cdot \frac{\partial k_x}{\partial e} \right] , \quad (9.34)$$

in which $e_1 = \omega - (\epsilon_{a\mathbf{k}_1} - \epsilon_{i\mathbf{k}_1})$ for that specific occupied (i), virtual (a) combination in \mathbf{k}_1 . The \mathbf{k} -points have been ordered on the values of e . Only one case needs to be considered in which $e_1 < e < e_2$. The intersection of e with the line is just a point for which

$$\mathbf{k} = \mathbf{k}_1 + \frac{e - e_1}{e_2 - e_1} (\mathbf{k}_2 - \mathbf{k}_1) , \quad (9.35)$$

and

$$\frac{\partial k_x}{\partial e} = \frac{1}{(e_2 - e_1)} [k_{2x} - k_{1x}] . \quad (9.36)$$

At most, this parameterization for evaluating the integrals I_i in Eq. 9.34 gives us a linear term in e . In case the energybands show no dispersion the intergral in Eq. 9.33 reduces to

$$I_i = \frac{1}{\Delta + i\eta} \int_{k_{xmin}}^{k_{xmax}} dk_x [\mu_i] \quad (9.37)$$

The integration over ϵ is not necessary, and is just over the x-coördinate of the \mathbf{k} -points. These integrals become extremely simple, as can be seen directly from Eqn. 9.37.

Summary

In this thesis the time-dependent version of density functional theory is described, which has been developed for crystalline non-metallic systems with periodicity in one to three dimensions. The application of this theory to the calculation of the optical response properties of a wide range of materials proved to be very successful.

The description of an interacting many-particle system is, in general, very complicated and approximations need to be made. Many methods in quantum chemistry try to describe the motion of the electrons in such systems by the electronic wavefunction, the solution of the time-dependent Schrödinger equation. The computational effort involved in these methods, for the evaluation of the electronic wavefunction, is very high, contrary to density functional theory (DFT), in which the computational costs are much lower. In DFT, not the electronic wavefunction is evaluated for a full description of the interacting many-particle system, but it is sufficient to look at the electron density. The fundamental theorems for this theory were first formulated in the early 1960s by Hohenberg and Kohn, and, for practical use, incorporated, shortly after, in a one-electron self-consistent field calculation scheme by Kohn and Sham. In this Kohn-Sham approach to density functional theory, the interacting many-particle system is modelled in terms of an effective non-interacting particle system, called the Kohn-Sham system. The effective external field, to which this Kohn-Sham system is subjected, incorporates the true external field and, in an effective way, the interparticle interactions. The modelling of the effective potential, which is called the Kohn-Sham potential, is done in such a way that the electron density of the non-interacting Kohn-Sham system exactly reproduces the electron density of the true interacting many-particle system. The Kohn-Sham potential is thus a functional of the electron density, however, this density can only be obtained if this Kohn-Sham potential is known. Both the electron density and the Kohn-Sham potential can be obtained in a self-consistent field scheme in which self-consistency is achieved for the electron density. The electron density and the Kohn-Sham potential are hereby updated in an iterative way. In the time-dependent extension of DFT, the external potential varies in time, and consequently also the electron density and effective potential become time-dependent.

After a brief and short introduction of the concepts behind time-dependent density functional theory in Chapter 2, we discuss in Chapter 3 the polarization of a dielectric medium. We show that, when polarization in such a dielectric medium is introduced as the dynamic response of the system to an externally applied electric field, the definition of polarization in terms of the induced current flowing through the system provides an elegant way

to avoid the problems as faced in the description of polarization in terms of the electron density. Such definitions of polarization are always ill-defined, because they depend on the particular choice of partitioning the system into separate elements. When the concept of polarization in a dielectricum is defined in terms of the induced current flowing through the system, these problems are circumvented. The definition in terms of the induced current is also more attractive because in this way it is not necessary to consider the surface of the system explicitly. The charge that piles up at the surface of the system is after all directly related to the induced current flowing through the interior of the system.

Our approach to time-dependent density functional theory (TDDFT) for the description of the dielectric properties of crystalline solids is described in Chapter 4. The solids, modelled as ideal lattice periodic systems, are treated in the presence of time-dependent electromagnetic fields. This description requires the combination of uniform electric fields with lattice periodic effective potentials. A perturbative approach to the time-dependent self-consistent field scheme is used, involving both the density and the current density in a real space description, in contrast with many other approaches that use a description in reciprocal space. Advantage is the high spatial resolution achieved, and the flexibility to use various potentially very complicated functionals of the density and the current density. The electric susceptibility can then be obtained if the macroscopic polarization is derived from the induced current density. The elegant and efficient iterative calculation scheme, as implemented in the state of the art full-potential periodic version of the Amsterdam Density Functional (ADF-BAND) code, is described. Some features of the implementation are, the use of a linear combination of atomic orbitals as a basis and linear response theory in which Coulomb interactions and exchange-correlation effects are included. Further, the explicit evaluation of the Kohn-Sham response kernels is avoided by treating these kernels analytically and the Coulomb integrals are evaluated by the use of auxiliary fitfunctions, and also a screening technique is used to evaluate the lattice sums.

The success of our TDDFT approach, as introduced in Chapter 4, becomes clear when looking at the results presented in Chapter 5. There the dielectric constants and functions for a variety of elemental and binary crystals are presented. Already within the adiabatic local density approximation for the exchange-correlation functional, we get good agreement with experiment. The accuracy of the dielectric constants is about 5%, and the spectral features in the dielectric functions are well reproduced, but appear at energies that are rigidly shifted towards lower energies.

The only exceptions, however, were found for InSb and HgSe in the zincblende structure. Their static dielectric constants were underestimated by about 40% when compared with experiment. A further analysis, presented in Chapter 6, showed that these deviations are caused by relativistic effects. We demonstrated that our TDDFT approach can also be applied successfully for the description of these zincblende materials when relativistic effects are included in TDDFT within the so-called zeroth order regular approximation (ZORA). Thereby drastic effects on the dielectric properties for these materials were observed. The materials InSb and HgSe turn into semimetals due to relativistic effects, because, within the local density approximation, their bandstructures were inverted. Now, with the inclusion of scalar relativistic effects, the same order of accuracy of about 5% relative to

experiment was achieved for the static dielectric constants. The dielectric functions were greatly improved, and are now also found in good agreement with experiment.

In a first attempt to go beyond the adiabatic local density approximation we investigated in Chapter 7 a polarization functional. The effects on the absorption spectra of various semiconductors are presented. This polarization functional, as derived by Vignale and Kohn, includes the exchange-correlation contributions in the effective macroscopic electric field. For all the semiconductors for which we tested this polarization functional, the optical absorption spectra showed a better agreement with experiment than when the spectra were calculated within the adiabatic local density approximation.

In Chapter 8 we demonstrate that TDDFT describes the excitonic effects correctly in some solids. Perturbing a solid by an electromagnetic field can cause the formation of bound electron-hole pairs which are called excitons. Such an exciton is usually understood as an additional two-particle interaction in the effective one-particle picture, namely as the Coulombic interaction between an excited electron in the conduction band, and the hole which this electron leaves behind in the valence band. For the investigated systems: CaF_2 , SiO_2 and GaN , it is shown that TDDFT, in the adiabatic local density approximation, is already capable to describe such excitonic effects, within an effective one-particle picture, contrary to common belief. For being able to describe the optical electron-hole excitations one invariably assumes that an effective two-body approach is required, and therefore, in principle, TDDFT should not be able to resolve the excitonic features in the calculated optical absorption spectra.

In the last chapter, the longitudinal polarizability of several infinite conjugated polymers is investigated using the periodicity of these systems. The results as calculated by our TDDFT implementation overestimated the polarizability for all the polymers considered, when compared to the results as found by more traditional calculation methods. The overestimation is caused by an incorrect description of the macroscopic exchange-correlation electric field contribution in the local density approximation for the exchange-correlation functional. An estimate for the value of this counteracting macroscopic exchange-correlation contribution is given for all the considered polymers. This contribution is calculated in the form of a polarization functional, as was introduced in Chapter 7. It remains to be demonstrated whether such a polarization functional exists, which is indeed able to reproduce correctly these values.

Samenvatting

In dit proefschrift is de tijdsafhankelijke versie van dichtheidsfunctionaaltheorie beschreven die ontwikkeld is voor kristallijne niet-metallische systemen met periodiciteit in één tot drie dimensies. De toepassing van deze theorie voor de berekening van de optische responseeigenenschappen voor een grote reeks van materialen is erg succesvol gebleken.

De beschrijving van een wisselwerkend veel-deeltjes systeem is, in het algemeen, erg ingewikkeld, waardoor het maken van benaderingen nodig is. Veel methodes in de quantumchemie proberen de beweging van de elektronen in zulke systemen te beschrijven met behulp van de elektronengolffunctie: de oplossing van de tijdsafhankelijke Schrödinger vergelijking. De inspanning qua computertijd die gepaard gaat met de rekenmethoden voor de berekening van deze elektronengolffunctie zijn erg hoog, in tegenstelling tot dichtheidsfunctionaaltheorie (DFT) waarin de kosten in termen van computertijd veel lager zijn. In DFT wordt de elektronengolffunctie namelijk niet berekend voor de volledige beschrijving van het wisselwerkende veel-deeltjes systeem, maar is het voldoende om slechts de elektronendichtheid te bekijken. De fundamentele theorema's voor deze theorie werden beginjaren '60 voor het eerst geformuleerd door Hohenberg en Kohn. Kort daarna is deze theorie door Kohn en Sham voor praktisch gebruik gevat in een één-deeltjes zelfconsistente berekeningsmethode. In die Kohn-Sham aanpak van dichtheidsfunctionaaltheorie wordt het wisselwerkende veel-deeltjes systeem gemodelleerd met behulp van een niet-wisselwerkend veel-deeltjes systeem, het zogenaamde Kohn-Sham systeem. Het effectieve externe veld, waaraan dit Kohn-Sham systeem is blootgesteld, bevat het ware externe veld en, op een effectieve wijze, de wisselwerking tussen de deeltjes. De modellering van de effectieve potentiaal, de zogenaamde Kohn-Sham potentiaal, is op dusdanige wijze gedaan, dat de elektronendichtheid van het niet-wisselwerkende systeem precies de elektronendichtheid van het ware wisselwerkende veel-deeltjes systeem oplevert. De Kohn-Sham potentiaal is dus een functionaal van de elektronendichtheid. Deze dichtheid kan echter alleen worden verkregen als de Kohn-Sham potentiaal reeds bekend is. Zowel de elektronendichtheid als de Kohn-Sham potentiaal kunnen worden verkregen op zelfconsistente wijze, waarbij de elektronendichtheid wordt berekend die met zichzelf in overeenstemming is. De elektronendichtheid en de Kohn-Sham potentiaal worden daarbij op iteratieve wijze aangepast. In de tijdsafhankelijke uitbreiding van DFT varieert de externe potentiaal in de loop van de tijd, met als gevolg dat ook de elektronendichtheid en de effectieve potentiaal tijdsafhankelijk worden.

Na een kort en bondige introductie van de ideeën achter tijdsafhankelijke dichtheidsfunc-

tionaaltheorie in Hoofdstuk 2, bediscussiëren we in Hoofdstuk 3 het verschijnsel van polarisatie in een dielektrisch medium. Polarisation in zo'n dielektrisch medium wordt geïntroduceerd als de dynamische respons van het systeem op een extern aangelegd elektrisch veld. We laten zien dat de definitie van polarisatie in termen van de geïnduceerde stroom die door het systeem stroomt, een elegante oplossing biedt om de problemen te omzeilen die altijd optreden bij de beschrijving in termen van de elektronendichtheid. Zulke definities van polarisatie zijn onhoudbaar, omdat ze afhankelijk zijn van de specifieke keuze van de opdeling van het systeem in afzonderlijke elementen. Als polarisatie in een dielektricum wordt gedefinieerd in termen van de geïnduceerde stroom binnenin het systeem, dan worden deze problemen omzeild. De definitie met behulp van de geïnduceerde stroom is ook aantrekkelijker, want op deze wijze is het niet nodig om het oppervlak van het systeem expliciet te beschouwen. De lading die zich ophoopt aan het oppervlak van het systeem is immers direct gerelateerd aan de geïnduceerde lading die door het binnenste van het systeem is gestroomd.

Onze aanpak van tijdsafhankelijke dichtheidsfunctionaaltheorie (TDDFT) voor de beschrijving van de dielektrische eigenschappen van kristallijne (vaste) stoffen is beschreven in Hoofdstuk 4. De vaste stoffen, gemodelleerd als ideale roosterperiodieke systemen, worden beschouwd in de aanwezigheid van tijdsafhankelijke elektromagnetische velden. Deze beschrijving vereist de combinatie van uniforme elektrische velden met roosterperiodieke (effectieve) potentialen. Een aangepaste aanpak voor de tijdsafhankelijke zelfconsistente berekeningswijze wordt gebruikt, waarin zowel de dichtheid als de stroomdichtheid betrokken zijn. We gebruiken een beschrijving in de directe ruimte, in tegenstelling tot vele andere aanpakken die een beschrijving in de reciproke ruimte gebruiken. Voordeel hiervan is de hoge ruimtelijke resolutie die bereikt wordt en de flexibiliteit om verschillende, mogelijke erg gecompliceerde, functionalen van de dichtheid en de stroomdichtheid te gebruiken. De elektrische susceptibiliteit kan dan worden verkregen zodra de macroscopische polarisatie is afgeleid van de geïnduceerde stroomdichtheid. De efficiënte iteratieve berekeningswijze wordt beschreven zoals die is geïmplementeerd in de moderne 'volledige potentiaal' periodieke versie van de Amsterdam Density Functional (ADF-BAND) computercode. Enkele kenmerken van de implementatie zijn het gebruik van een lineaire combinatie van atomaire orbitalen als basis en de lineaire respons theorie waarin Coulomb interacties en de zogenaamde exchange-correlatie effecten inbegrepen zijn. Verder is de expliciete berekening van de Kohn-Sham respons kernen omzeild door deze kernen analytisch te behandelen, worden de Coulomb integralen berekend met behulp van fitfuncties en wordt voor de berekening van de roostersommaties van een afschermingstechniek gebruik gemaakt.

Het succes van onze TDDFT aanpak, zoals geïntroduceerd in Hoofdstuk 4, wordt duidelijk als naar de resultaten zoals gepresenteerd in Hoofdstuk 5 gekeken wordt. Daar worden de dielektrische constanten en functies voor allerlei elementaire en binaire vaste stoffen gepresenteerd. Reeds in de adiabatische lokale dichtheidsbenadering voor de exchange-correlatie functionaal krijgen we goede overeenstemming tussen theorie en experiment. De nauwkeurigheid van de berekende dielektrische constanten is ongeveer 5%, terwijl de spectrale kenmerken in de dielektrische functies goed worden gereproduceerd. Wel zijn de dielektrische functies daarbij verschoven over een vaste afstand naar lagere energieën.

De enige uitzonderingen hierop werden gevonden voor de InSb en HgSe kristallen in de zinkblende structuur. Hun statische diëlektrische constanten werden ongeveer 40% onderschat in vergelijking met de experimentele waarden. Analyse, zoals gepresenteerd in Hoofdstuk 6, laat zien dat deze afwijkingen veroorzaakt worden door relativistische effecten. We hebben gedemonstreerd dat onze TDDFT aanpak ook succesvol kan worden toegepast voor de beschrijving van deze zinkblende materialen wanneer relativistische effecten meegenomen worden in de zogenaamde 'zeroth order regular approximation' (ZORA) binnen TDDFT. Daarbij worden drastische effecten waargenomen op de berekende diëlektrische eigenschappen voor deze materialen. De materialen InSb en HgSe veranderen in halfmetalen ten gevolge van relativistische effecten, want in de lokale dichtheidsbenadering worden hun bandenstructuren geïnverteerd. Met de scalaire relativistische effecten meegenomen wordt de gebruikelijke nauwkeurigheid bereikt voor de statische diëlektrische constanten. De diëlektrische functies worden enorm verbeterd en zijn nu ook in goede overeenstemming met experiment.

In een eerste poging om verder te gaan dan de adiabatische lokale dichtheidsbenadering, hebben we in Hoofdstuk 7 een polarisatiefunctionaal onderzocht. De effecten op de absorptiespectra van verscheidene halfgeleiders worden in dit hoofdstuk getoond. Deze polarisatiefunctionaal, zoals afgeleid door Vignale en Kohn, neemt de exchange-correlatie bijdragen in het effectieve macroscopische elektrische veld mee. De optische absorptiespectra van alle halfgeleiders waarvoor we deze polarisatiefunctionaal getest hebben, vertoonden een betere overeenstemming met experiment dan wanneer de spectra werden berekend in de adiabatische lokale dichtheidsbenadering.

In Hoofdstuk 8 hebben we aangetoond dat TDDFT voor sommige vaste stoffen de exciton effecten correct beschrijft. Verstoring van een vaste stof door een elektromagnetisch veld kan de vorming van gebonden 'elektron-gat' paren veroorzaken, welke excitonen worden genoemd. Zo'n exciton wordt normaal gesproken begrepen als een extra twee-deeltjes interactie in een effectief één-deeltjes beeld, namelijk als de Coulomb interactie tussen een geëxciteerd elektron in de geleidingsband en het gat dat dit elektron achterlaat in de valentie band. Voor de onderzochte systemen: CaF₂, SiO₂ en GaN, is aangetoond dat TDDFT binnen de adiabatische lokale dichtheidsbenadering reeds in staat is om zulke exciton effecten te beschrijven binnen het effectieve één-deeltjes beeld, in tegenstelling tot datgene dat gewoonlijk wordt verondersteld. Om in staat te zijn de optische elektron-gat excitaties te beschrijven, neemt men steeds aan dat een effectieve twee-deeltjes aanpak nodig is, en dus TDDFT in principe niet in staat zou moeten zijn om de exciton kenmerken in de berekende optische absorptie spectra te vinden.

In het laatste hoofdstuk is de polariseerbaarheid langs de lengterichting van verscheidene oneindig geconjugeerde polymeren onderzocht, waarbij gebruik gemaakt is van de periodiciteit in deze systemen. De resultaten zoals die berekend zijn met onze TDDFT implementatie, overschatten de polariseerbaarheid voor alle beschouwde polymeren in vergelijking met de resultaten zoals die worden gevonden door meer traditionele berekeningsmethoden. De overschatting wordt veroorzaakt door een incorrecte beschrijving van de exchange-correlatie bijdrage aan het macroscopische elektrische veld in de lokale dichtheidsbenadering voor de exchange-correlatie functionaal. Een schatting voor de waarde van deze tegen-

werkende macroscopische exchange-correlatie bijdrage wordt gegeven voor alle beschouwde polymeren. Deze bijdrage is berekend in de vorm van een polarisatie functionaal, zoals geïntroduceerd in Hoofdstuk 7. Het moet nog aangetoond worden of zo'n polarisatie functionaal, die in staat is om deze waarden correct te reproduceren, inderdaad bestaat.

Bibliography

- [1] P. Fulde, *Electron Correlations in Molecules and Solids*, 2nd ed. (Springer-Verlag, Berlin Heidelberg, 1993) ISBN 0-387-56376-8.
- [2] P. Hohenberg and W. Kohn, Phys. Rev. B **136**, 864 (1964).
- [3] W. Kohn and L. J. Sham, Phys. Rev. A **140**, 1133 (1965).
- [4] E. Runge and E. K. U. Gross, Phys. Rev. Lett. **52**, 997 (1984).
- [5] E. K. U. Gross, J. F. Dobson, and M. Petersilka, in: *Topics in Current Chemistry*, Vol. 181 (Springer-Verlag, Berlin Heidelberg, 1996).
- [6] R. van Leeuwen, Int. J. Mod. Phys. B **15**, 1969 (2001).
- [7] N. W. Ashcroft and N. D. Mermin, *Solid State Physics*, (Holt, Rinehart, and Winston, New York, 1976), ISBN 0-03-049346-3.
- [8] C. Kittel, *Introduction to solid state physics*, 6th ed. (Wiley, New York, 1986) ISBN 0-03-083993-9.
- [9] M. Born and E. Wolf, *Principles of optics*, 6th ed. (Academic, Cambridge, 1980), ISBN 0-521-63921-2.
- [10] J. D. Jackson, *Classical Electrodynamics*, 2nd ed. (Wiley, New York, 1975).
- [11] R. O. Jones and O. Gunnarsson, Rev. Mod. Phys. **61**, 689 (1989).
- [12] E. J. Baerends, D. E. Ellis, and P. Ros, Chem. Phys. **2**, 41 (1973).
- [13] R. M. Dreizler and E. K. U. Gross, *Density Functional Theory; An Approach to the Quantum Many-Body Problem* (Springer-Verlag, Berlin, 1990).
- [14] R. G. Parr and W. Yang, *Density Functional Theory of Atoms and Molecules*, (Oxford University Press, Oxford, 1990).
- [15] S. Baroni and R. Resta, Phys. Rev. B **33**, 7017 (1986).
- [16] Z. H. Levine and D. C. Allan, Phys. Rev. B **43**, 4187 (1991); **44**, 12781 (1991); Phys. Rev. Lett. **63**, 1719 (1989); **66**, 41 (1991).

- [17] A. Zangwill and P. Soven, *Phys. Rev. A* **21**, 1561 (1980).
- [18] R. van Leeuwen and E. J. Baerends, *Phys. Rev. A* **49**, 2421 (1994).
- [19] S. J. A. van Gisbergen, V. P. Osinga, O. V. Gritsenko, R. van Leeuwen, J. G. Snijders, and E. J. Baerends, *J. Chem. Phys.* **105**, 3142 (1996).
- [20] M. S. Hybertsen and S. G. Louie, *Phys. Rev. B* **30**, 5777 (1984).
- [21] A. Dal Corso, S. Baroni, and R. Resta, *Phys. Rev. B* **49**, 5323 (1994).
- [22] L. J. Sham and M. Schlüter, *Phys. Rev. Lett.* **51**, 1888 (1983); *Phys. Rev. B* **32**, 3883 (1965).
- [23] J. P. Perdew and M. Levy, *Phys. Rev. Lett.* **51**, 1884 (1983).
- [24] M. S. Hybertsen and S. G. Louie, *Phys. Rev. B* **34**, 5390 (1986).
- [25] R. W. Godby, M. Schlüter, and L. J. Sham, *Phys. Rev. Lett.* **56**, 2415 (1986); *Phys. Rev. B* **37** 10159 (1988).
- [26] J. Chen, Z. H. Levine, and J. W. Wilkins, *Phys. Rev. B* **50**, 11514 (1994).
- [27] X. Gonze, P. Ghosez, and R. W. Godby, *Phys. Rev. Lett.* **74**, 4035 (1995).
- [28] G. D. Mahan and K. R. Subbaswami, *Local Density Theory of Polarizability* (Plenum Press, New York, 1990).
- [29] E. K. U. Gross, C. A. Ullrich, and U. J. Gossmann, in *Density Functional Theory*, edited by E. K. U. Gross and R. M. Dreizler, (Plenum Press, New York, 1995), p. 149ff.
- [30] S. J. A. van Gisbergen, J. G. Snijders, and E. J. Baerends, *J. Chem. Phys.* **103**, 9347 (1995); *Comput. Phys. Commun.* **118**, 119 (1999).
- [31] A. K. Dhara and S. K. Ghosh, *Phys. Rev. A* **35**, 442 (1987).
- [32] S. K. Ghosh and A. K. Dhara, *Phys. Rev. A* **38**, 1149 (1988).
- [33] S. L. Adler, *Phys. Rev.* **126**, 413 (1962).
- [34] N. Wisser, *Phys. Rev.* **129**, 62 (1963).
- [35] M. S. Hybertsen and S. G. Louie, *Phys. Rev. B* **35**, 5585 (1987); **35**, 5602 (1987).
- [36] S. Baroni, P. Giannozzi, and A. Testa, *Phys. Rev. Lett.* **58**, 1861 (1987).
- [37] G. te Velde and E. J. Baerends, *Phys. Rev. B* **44**, 7888 (1991); *J. Comput. Phys.* **99**, 84 (1992).

- [38] C. Fonseca Guerra, O. Visser, J. G. Snijders, G. te Velde, and E. J. Baerends, in *Methods and Techniques in Computational Chemistry*, edited by E. Clementi and G. Corongiu, (STEF, Cagliari, 1995), p. 305; G. te Velde, F. M. Bickelhaupt, E. J. Baerends, C. Fonseca Guerra, S. J. A. van Gisbergen, J. G. Snijders, and T. Ziegler, *J. Comput. Chem.* **22**, 931 (2001).
- [39] O. L. Brill and B. Goodman, *Am. J. Phys.* **35**, 832 (1967).
- [40] G. Breit, *Phys. Rev.* **34**, 553 (1929); **39**, 616 (1932).
- [41] S. H. Vosko, L. Wilk, and M. Nusair, *Can. J. Phys.* **58**, 1200 (1980).
- [42] P. Pulay, *Chem. Phys. Lett.* **73**, 393 (1980); *J. Comput. Chem.* **3**, 556 (1982).
- [43] F. Herman and S. Skillman, *Atomic Structure Calculations*, (Prentice-Hall, Englewood Cliffs NJ, 1963).
- [44] P. M. Boerrigter, G. te Velde, and E. J. Baerends, *Int. J. Quantum Chem.* **33**, 87 (1988).
- [45] *Handbook of optical constants of solids*, edited by E. D. Palik, (Academic Press, New York, 1985).
- [46] P. E. Aspnes and A. A. Studna, *Phys. Rev. B* **27**, 985 (1983).
- [47] G. Lehmann and M. Taut, *Phys. Status. Solidi. B* **54**, 469 (1972).
- [48] G. Wiesenekker and E. J. Baerends, *J. Phys.: Condens. Matter* **3**, 6721 (1991); G. Wiesenekker, G. te Velde, and E. J. Baerends, *J. Phys. C* **21**, 4263 (1988).
- [49] *Numerical Data and Functional Relationships in Science and Technology*, edited by O. Madelung, (Springer-Verlag, New York, 1982), Landolt-Börnstein, New Series, Group III, Vol. 17, Pt. A.
- [50] M. Rohlfing, P. Krüger, and J. Pollmann, *Phys. Rev. B* **48**, 17791 (1993).
- [51] M. Z. Huang and W. Y. Ching, *Phys. Rev. B* **47**, 9449 (1993).
- [52] D. J. Moss, E. Ghahramani, J. E. Sipe, and H. M. van Driel, *Phys. Rev. B* **34**, 8758 (1986).
- [53] H. H. Li, *J. Chem. Phys. Ref. Data* **9**, 561 (1980).
- [54] P. Giannozzi, S. de Gironcoli, P. Pavone, and S. Baroni, *Phys. Rev. B* **43**, 7231 (1991).
- [55] M. Alouani and J. Wills, *Phys. Rev. B* **54**, 2480 (1996).
- [56] C. S. Wang and B. M. Klein, *Phys. Rev. B* **24**, 3417 (1981).

- [57] K. B. Kahen and J. P. Leburton, *Phys. Rev. B* **32**, 5177 (1985).
- [58] O. Pulci, G. Onida, A. I. Shkrebtii, R. Del Sole, and B. Adolph, *Phys. Rev. B* **55**, 6685 (1997).
- [59] S. J. A. van Gisbergen, F. Kootstra, P. R. T. Schipper, O. V. Gritsenko, J. G. Snijders, and E. J. Baerends, *Phys. Rev. A* **57**, 2556 (1998).
- [60] O. Gunnarsson and R. O. Jones, *Phys. Scr.* **21**, 394 (1980).
- [61] Z. H. Levine and S. G. Louie, *Phys. Rev. B* **25**, 6310 (1982).
- [62] Y. T. Shen, D. M. Bylander, and L. Kleinman, *Phys. Rev. B* **36**, 3465 (1987).
- [63] F. Kootstra, P. L. de Boeij, and J. G. Snijders, *J. Chem. Phys.* **112**, 6517 (2000).
- [64] W. Y. Ching, F. Gan, and M. Z. Huang, *Phys. Rev. B* **52**, 1596 (1995).
- [65] J. Li, C. Duan, Z. Gu, and D. Wang, *Phys. Rev. B* **57**, 2222 (1998).
- [66] Y. N. Xu and W. Y. Ching, *Phys. Rev. B* **48**, 4335 (1993).
- [67] J. Chen, Z. H. Levine, and J. W. Wilkins, *Appl. Phys. Lett.* **66**, 1129 (1995).
- [68] N. E. Christensen and I. Gorczyca, *Phys. Rev. B* **50**, 4397 (1994).
- [69] R. Wang, P. P. Ruden, J. Kolnik, I. Oguzman, and K. F. Brennan, *J. Phys. Chem. Solids* **58**, 913 (1997).
- [70] F. Gan, Y. Xu, M. Huang, W. Y. Ching, and J. G. Harrison, *Phys. Rev. B* **45**, 8248 (1992).
- [71] M. Cardona, N. E. Christensen, and G. Fasol, *Phys. Rev. B* **38**, 1806 (1988).
- [72] G. Y. Guo, J. Crain, P. Blaha, and W. M. Temmerman, *Phys. Rev. B* **47**, 4841 (1993).
- [73] M. E. Lines, *Phys. Rev. B* **41**, 3372 (1990).
- [74] N. A. Goryunova, in *Chemistry of Diamond-like Semiconductors* (Chapman and Hall, London, 1965), p. 115.
- [75] As listed in W. A. Harrison, *Electronic Structure and the Properties of Solids*, (Freeman, San Francisco, 1980).
- [76] R. E. Fern and A. Onton, *J. Appl. Phys.* **42**, 3499 (1971).
- [77] E. Burstein, H. Brodsky, and G. Lucousky, *Int. J. Quantum Chem.* **1**, 756 (1967).
- [78] A. S. Barker, Jr. , *Phys. Rev.* **165**, 917 (1968).

- [79] S. J. Czyzak, W. M. Barker, R. C. Crane, and J. B. Howe, *J. Opt. Soc. Am.* **47**, 240 (1957).
- [80] A. Manabe, A. Mitsuishi, and H. Yoshinaga, *Jpn. J. Appl. Phys.* **6**, 593 (1967).
- [81] D. T. F. Marple, *J. Appl. Phys.* **35**, 539 (1964).
- [82] T. M. Bieniewski and S. J. Czyzak, *J. Opt. Soc. Am.* **53**, 496 (1963).
- [83] J. Barth, R. L. Johnson, M. Cardona, D. Fuchs, and A. M. Bradshaw, *Phys. Rev. B* **41**, 3291 (1990).
- [84] G. Stephan, Y. le Calvez, J. C. Lemonier, and S. Robin, *J. Phys. Chem. Solids* **30**, 601 (1969).
- [85] A. T. Collins, E. C. Lightowers, and P. J. Dean, *Phys. Rev.* **158**, 833 (1967).
- [86] L. Akasaki and M. Hashimoto, *Solid State Commun.* **5**, 851 (1967).
- [87] E. Ejder, *Phys. Status Solidi A* **5**, 445 (1971).
- [88] P. Perlin, I. Gorczyca, N. E. Christensen, I. Grzegory, H. Teisseyre and T. Suski, *Phys. Rev. B* **45**, 13 307 (1992); P. Perlin, I. Gorczyca, S. Porowski, T. Suski, N. E. Christensen and A. Polian, *Jpn. J. Appl. Phys.* , Part 1 **32**, 334 (1993).
- [89] J. Misek and F. Srobar, *Elektrotech. Cas.* **30**, 690 (1979).
- [90] J. L. Freelouf, *Phys. Rev. B* **7**, 3810 (1973).
- [91] G. te Velde, Ph.D. thesis, Free University, Amsterdam,1990.
- [92] *CRC Handbook of Chemistry and Physics*, 80th Edition (CRC Press, Boca Raton, 1999).
- [93] cf. nomenclature, e.g., M. Cardona, *Modulation Spectroscopy* (Academic, New York, 1969).
- [94] F. Kootstra, P. L. de Boeij, and J. G. Snijders, *Phys. Rev. B* **62**, 7071 (2000).
- [95] E. van Lenthe, E. J. Baerends, and J. G. Snijders, *J. Chem. Phys.* **101**, 9783 (1994).
- [96] E. van Lenthe, R. van Leeuwen, E. J. Baerends, and J. G. Snijders, *Int. J. Quantum Chem.* **57**, 281 (1996).
- [97] P. H. T. Philipsen, E. van Lenthe, J. G. Snijders, and E. J. Baerends, *Phys. Rev. B* **56**, 13556 (1997).
- [98] F. Bassani and G. Pastori Parravicini, *Electronic states and optical properties of solids*, edited by R. A. Ballinger (Pergamon Press, Oxford, 1975).

- [99] R. K. Willardson and A. C. Beer, *Semiconductors and semimetals* (Academic, New York, 1966).
- [100] A. Svane and E. Antoncik, *J. Phys. C* **20**, 2683 (1987).
- [101] L. Leij. R. A. Pollak, F. R. McFeely, S. P. Kowalczyk, and D. A. Shirley, *Phys. Rev. B* **9**, 600 (1974).
- [102] F. Kootstra, P. L. de Boeij, H. Aissa, and J. G. Snijders, *J. Chem. Phys.* **114**, 1860 (2001).
- [103] K. U. Gawlik, L. Kipp, M. Skibowski, N. Orlowski, and R. Manzke, *Phys. Rev. Lett.* **78**, 3165 (1997); T. Dietl *et al.* *Phys. Rev. Lett.* **81**, 1535 (1998); K. U. Gawlik *et al.* *Phys. Rev. Lett.* **81**, 1536 (1998).
- [104] S. Einfeldt, F. Goschenhofer, C. R. Becker, and G. Landwehr, *Phys. Rev. B* **51**, 4915 (1995).
- [105] M. Rohlfing and S. G. Louie, *Phys. Rev. B* **57**, R9392 (1998).
- [106] K. Kumazaki, L. Viña, C. Umbach, and M. Cardona, *Solid State Commun.* **68**, 591 (1988).
- [107] Ch. Jung and P. R. Bressler, *J. Electr. Spectr. Rel. Phen.* **78**, 503 (1996).
- [108] G. Vignale and W. Kohn, *Phys. Rev. Lett.* **77**, 2037 (1996).
- [109] G. Vignale and W. Kohn, in *Electronic Density Functional Theory: Recent Progress and New Directions*, edited by Dobson *et al.* (Plenum Press, New York, 1998).
- [110] G. Vignale, C. A. Ullrich, and S. Conti, *Phys. Rev. Lett.* **79**, 4878 (1997).
- [111] X. Gonze, P. Ghosez, and R. Godby, *Phys. Rev. Lett.* **78**, 294 (1997).
- [112] R. M. Martin and G. Ortiz, *Phys. Rev. B* **56**, 1124 (1997).
- [113] H. M. Böhm, S. Conti, and M. P. Tosi, *J. Phys. Cond. Matter* **8**, 781 (1996).
- [114] S. Conti, R. Nifosi, and M. P. Tosi, *J. Phys. Cond. Matter* **9**, L475 (1997).
- [115] R. Nifosi, S. Conti, and M. P. Tosi, *Phys. Rev. B* **58**, 12758 (1998).
- [116] S. Conti and G. Vignale, *Phys. Rev. B* **60**, 7966 (1999).
- [117] L. X. Benedict, E. L. Shirley, and R. B. Bohn, *Phys. Rev. B* **57**, R9385 (1998).
- [118] D. J. Stukel, R. N. Euwema, T. C. Collins, F. Herman, and R. L. Kortum, *Phys. Rev.* **179**, 740 (1969).

- [119] J. P. Walter, M. L. Cohen, Y. Petroff, and M. Balkanski, *Phys. Rev. B* **1**, 2661 (1970).
- [120] V. I. Gravilenko and F. Bechstedt, *Phys. Rev. B* **54**, 13416 (1996).
- [121] S. Albrecht, L. Reining, R. Del Sole, and G. Onida, *Phys. Rev. Lett.* **80**, 4510 (1998).
- [122] L. X. Benedict and E. L. Shirley, *Phys. Rev. B* **59**, 5441 (1999).
- [123] J.-W. van der Horst, P. A. Bobbert, M. A. J. Michels, G. Brocks, and P. J. Kelly, *Phys. Rev. Lett.* **83**, 4413 (1999).
- [124] J.-W. van der Horst, P. A. Bobbert, P. H. L. de Jong, M. A. J. Michels, G. Brocks, and P. J. Kelly, *Phys. Rev. B* **61**, 15817 (2000).
- [125] M. Rohlfing and S. G. Louie, *Phys. Rev. B* **62**, 4927 (2000).
- [126] J.-W. van der Horst, Ph.D. thesis, Technische Universiteit Eindhoven, Eindhoven, 2001.
- [127] L. Hedin, *Phys. Rev.* **139**, A796 (1965).
- [128] L. Hedin and S. Lundqvist, in *Solid State Physics, Advances in Research and Application*, edited by F. Seitz, D. Turnbull, and H. Ehrenreich (Academic, New York, 1969), Vol. 23, p. 1.
- [129] L. J. Sham and T. M. Rice, *Phys. Rev.* **144**, 708 (1966).
- [130] G. Strinati, *Phys. Rev. Lett.* **49**, 1519 (1982); *Phys. Rev. B* **29**, 5718 (1984); *Riv. Nuovo Cimento* **11**, 1 (1988).
- [131] W. Hanke and L. J. Sham, *Phys. Rev. Lett.* **43**, 387 (1979); *Phys. Rev. B* **21**, 4656 (1980).
- [132] R. Del Sole and E. Fiorino, *Phys. Rev. B* **29**, 4631 (1984).
- [133] M. Rohlfing, P. Krüger, and J. Pollmann, *Phys. Rev. B* **52**, 1905 (1995).
- [134] G. B. Bachelet, D. R. Hamann, and M. Schlüter, *Phys. Rev. B* **26**, 4199 (1982).
- [135] A. L. Fetter and J. D. Walecka, *Quantum Theory of Many-Particle Systems* (McGraw-Hill, San Francisco, 1971).
- [136] P. L. de Boeij, F. Kootstra, and J. G. Snijders, *Int. J. Quantum Chem.* accepted.
- [137] R. Tousey, *Phys. Rev.* **50**, 1057 (1936).
- [138] T. Tomiki and T. Miyata, *J. Phys. Soc. Jpn.* **27**, 658 (1969).
- [139] G. W. Rubloff, *Phys. Rev. B*, **5**, 662 (1972).

- [140] R. T. Poole, J. Szajman, R. C. G. Leckey, J. G. Jenkin, and J. Liesegang, Phys. Rev. B, **12**, 5872 (1975).
- [141] J. P. Albert, C. Jouanin, and C. Gout, Phys. Rev. B **16**, 925 (1977); **16**, 4619 (1977).
- [142] R. A. Heaton and C. C. Lin, Phys. Rev. B **22**, 3629 (1980).
- [143] E. K. Chang, M. Rohlfing, and S. G. Louie, Phys. Rev. Lett. **85**, 2613 (2000).
- [144] *Structure and bonding in noncrystalline solids*, edited by G. E. Walrafen and A. G. Reverzy (Plenum, New York, 1986).
- [145] E. Loh, Solid State Commun. **2**, 269 (1964).
- [146] H. R. Philipp, Solid State Commun. **4**, 73 (1966).
- [147] T. H. DiStefano and D. E. Eastman, Phys. Rev. Lett. **27**, 1560 (1971).
- [148] R. B. Laughlin, Phys. Rev. B **22**, 3021 (1980).
- [149] H. Ibach and J. E. Rowe, Phys. Rev. B **10**, 710 (1974).
- [150] V. Jeyasingh Nithianandam and S. E. Schnatterly, Phys. Rev. B **38**, 5547 (1988).
- [151] J. R. Chelikowsky and M. Schlüter, Phys. Rev. B **15**, 4020 (1977).
- [152] J. Petalas, S. Logothetidis, S. Bouladakis, M. Alouani, and J. M. Wills, Phys. Rev. B **52**, 8082 (1995).
- [153] A. Rubio, J. L. Corkill, M. L. Cohen, E. S. Shirley, and S. G. Louie, Phys. Rev. B **48**, 11810 (1993).
- [154] L. X. Benedict, T. Wethkamp, K. Wilmers, C. Cobet, N. Esser, E. L. Shirley, W. Richter, and M. Cardona, Solid State Commun. **112**, 129 (1999).
- [155] W. R. L. Lambrecht, B. Segall, J. Rife, W. R. Hunter, and D. K. Wickenden, Phys. Rev. B **51**, 13516 (1995).
- [156] S. Logothetidis, J. Petalas, M. Cardona, and T. D. Moustakas, Phys. Rev. B **50**, 18017 (1994).
- [157] T. Wethkamp, K. Wilmers, W. Richter, O. Ambacher, H. Angerer, G. Jungk, R. L. Johnson, and M. Cardona, Thin Solid Films **313-314**, 745 (1998).
- [158] T. Lei, T. D. Moustakas, R. J. Graham, Y. He, and S. J. Berkowitz, J. Appl. Phys. **71**, 4933 (1992); T. Lei, M. Fanciulli, R. J. Molnar, T. D. Moustakas, R. J. Graham, and J. Scanlon, Appl. Phys. Lett. **59**, 944 (1992); C. R. Eddy, T. D. Moustakas, and J. Scanlon, J. Appl. Phys. **73**, 448 (1993).

- [159] M. J. Paisley, Z. Sitar, J. B. Posthill, and R. F. Davis, *J. Vac. Sci. Technol. A* **7**, 701 (1989); Z. Sitar *et al.*, *J. Mater. Sci. Lett.* **11**, 261 (1992).
- [160] D. H. Mosley, B. Champagne, and J.-M. André, *Int. J. Quantum Chem.* **29**, 117 (1995).
- [161] B. Champagne, E. A. Perpète, S. J. A. van Gisbergen, E. J. Baerends, J. G. Snijders, C. Soubra-Ghaoui, K. A. Robins, and B. Kirtman, *J. Chem. Phys.* **109**, 10489 (1998), *ibid.* **110**, 11664 (1999).
- [162] S. J. A. van Gisbergen, P. R. T. Schipper, O. V. Gritsenko, E. J. Baerends, J. G. Snijders, B. Champagne, and B. Kirtman, *Phys. Rev. Lett.* **83**, 694 (1999).
- [163] B. Kirtman, J. L. Toto, K. A. Robins, and M. Hasan, *J. Chem. Phys.* **102**, 5350 (1995).
- [164] B. Champagne, D. Jacquemin, J.-M. André, and B. Kirtman, *J. Phys. Chem. A* **101**, 3158 (1997).
- [165] B. Champagne, D. H. Mosley, M. Vračko, and J.-M. André, *Phys. Rev. A* **52**, 178 (1995), *ibid.* **52**, 1039 (1995).
- [166] B. Champagne, J.-M. André, and Y. Öhrn, *Int. J. Quantum Chem.* **57**, 811 (1996).
- [167] P. Chopra, L. Carlacci, H. F. King, and P. N. Prasad, *J. Phys. Chem.* **93**, 7920 (1989).
- [168] H. O. Villar, M. Dupuis, J. D. Watts, G. J. B. Hurst, and E. Clementi, *J. Chem. Phys.* **88**, 1003 (1988).
- [169] S. Suhai, *Int. J. Quantum Chem.* **42**, 193 (1992).
- [170] A. Karpfen, *J. Phys. C* **13**, 5673 (1980).
- [171] E. A. Perpète, B. Champagne, and B. Kirtman, *J. Chem. Phys.* **107**, 2463 (1997).
- [172] B. Champagne, D. H. Mosley, and J.-M. André, *J. Chem. Phys.* **100**, 2034 (1994).
- [173] H. Teramae and T. Takeda, *J. Am. Chem. Soc.* **111**, 1281 (1989).
- [174] D. Jacquemin, B. Champagne, and B. Kirtman, *J. Chem. Phys.* **107**, 5076 (1997).
- [175] E. F. Archibong and A. J. Thakker, *J. Chem. Phys.* **98**, 8324 (1993).
- [176] J. L. Toto, T. T. Toto, C. P. de Melo, B. Kirtman, and K. Robins, *J. Chem. Phys.* **104**, 8586 (1996).
- [177] G. J. B. Hurst, M. Dupuis, and E. Clementi, *J. Chem. Phys.* **89**, 385 (1988).

- [178] B. Kirtman, *Int. J. Quantum Chem.* **36**, 119 (1989); B. Kirtman and M. Hasan, *Chem. Phys. Lett.* **157**, 123 (1989).
- [179] B. Kirtman and M. Hasan, *J. Chem. Phys.* **96**, 470 (1992).
- [180] P. L. de Boeij, F. Kootstra, J. A. Berger, R. van Leeuwen, and J. G. Snijders, *J. Chem. Phys.* **115**, 1995 (2001).

List of publications

F. Kootstra, P. L. de Boeij, R. van Leeuwen, and J. G. Snijders, Festschrift in honour of R. G. Parr, Editor K. D. Sen, accepted, *Time-dependent (current) density functional theory of solids*, Chapters 4,5,6,7.

F. Kootstra, P. L. de Boeij, and J. G. Snijders, J. Chem. Phys. **112**, 6517-6531 (2000), *Efficient real-space approach to time-dependent density functional theory for the dielectric response of nonmetallic crystals*, Chapter 4.

F. Kootstra, P. L. de Boeij, and J. G. Snijders, Phys. Rev. B **62**, 7071-7083 (2000), *Application of time-dependent density-functional theory to the dielectric function of various nonmetallic crystals*, Chapter 5.

F. Kootstra, P. L. de Boeij, H. Aissa, and J. G. Snijders, J. Chem. Phys. **114**, 1860-1865 (2001), *Relativistic effects on the optical response of InSb by time-dependent density-functional theory*, Chapter 6.

P. L. de Boeij, F. Kootstra, and J. G. Snijders, Int. J. Quantum Chem. accepted, *Relativistic effects in the optical response of HgSe by time-dependent density-functional theory*, Chapter 6.

P. L. de Boeij, F. Kootstra, J. A. Berger, R. van Leeuwen, and J. G. Snijders, J. Chem. Phys. **115**, 1995-1999 (2001), *Current density functional theory for optical spectra, a polarization functional*, Chapter 7.

F. Kootstra, P. L. de Boeij, and J. G. Snijders, J. Chem. Phys. to be submitted, Chapter 8.

F. Kootstra, P. L. de Boeij, R. van Leeuwen, and J. G. Snijders, to be submitted, Chapter 9.

Dankwoord

Het proefschrift dat voor u ligt, is het resultaat van bijna vier jaar werk binnen de Basiseenheid Theoretische Chemie (TC) van de Faculteit der Wis- en Natuurwetenschappen (FWN) aan de Rijksuniversiteit Groningen (RuG). Deze periode is het beste te omschrijven als: *fijn, aangenaam en onvergetelijk*. Ik wil dan ook op deze plaats veel mensen bedanken voor de geweldige tijd in Groningen, vooral de mensen die op directe wijze hebben bijgedragen aan het tot stand komen van dit proefschrift.

Allereerst wil ik natuurlijk mijn promotor Jaap Sniijders heel hartelijk danken. Hij was het die me de mogelijkheid gaf om mijn promotieonderzoek in Groningen te doen. Het onderzoeksvorstel lag direct in het verlengde van mijn afstudeeropdracht en vormde dus een mooie aansluiting daarop. Deze promotieplaats impliceerde ook dat we beiden vertrokken uit de Vakgroep Theoretische Chemie van de Vrije Universteit (VU) te Amsterdam; de gezamenlijke autorit naar het sollicitatiegesprek in Groningen zal me zeker nog lang blijven en heugen. Jaap, je gaf me veel vrijheid tijdens het onderzoek en je was altijd bereid te discussiëren, samen met Paul, mij en later ook Robert, over nieuwe ideeën en opvattingen. Telkens weer wist je me te verrassen met je enorm brede kennis over de meest uiteenlopende onderwerpen binnen de quantumchemie.

Verder wil ik natuurlijk mijn referent Paul de Boeij bedanken. Paultje, na je komst als post-doc in februari 1998 te Groningen is het onderzoek in een grote stroomversnelling terechtgekomen, wat de laatste tijd zeker zijn vruchten heeft afgeworpen. Maar bovenal is onze persoonlijke vriendschap me dierbaar. Ik kon altijd met alle zinnige en meestal onzinnige dingen bij je terecht. Veel van die dingen zullen me eeuwig heugen. Het is te veel om hier nu op te noemen, maar de laatste vakantie in Sicilië was erg mooi. Paultje, bedankt voor alles en blij uitkijken voor al die -met name Duitse- vrouwen hè :-)

Prof. dr. E. J. Baerends, prof. dr. K. Duppen en prof. dr. J. Knoester wil ik danken voor het zitting nemen in de leescommissie, en het bestuderen van het manuscript.

Van de vaste staf binnen de Basiseenheid Theoretische Chemie wil ik de volgende mensen bedanken: Ria Broer, Piet van Duijnen, Johan Heijnen, Robert van Leeuwen en Alex de Vries. Alle aio's en oio's in de groep dank ik voor de goede sfeer: Marcel Swart, Thomas la Cour Jansen, Rosanna Telesca, Liviu Hozoi, Meta van Faassen en Lasse Jensen.

De studenten, Hedi Aissa en Arjan Berger, die ervoor kozen om af te studeren bij de Basiseenheid Theoretische Chemie, wil ik hartelijk danken voor de vruchtbare samenwerking en hun bijdrage aan dit proefschrift. De resultaten van jullie afstudeeropdrachten over relativistische effecten en polarisatiefunctionalen binnen de tijdsafhankelijke dichtheidsfunc-

tionaaltheorie zijn gedeeltelijk opgenomen in de hoofdstukken 6 en 7 van dit proefschrift, en al in publicaties tot uitdrukking gekomen.

Ook de studente Nienke Boeijenga wil ik bedanken voor de gezellige sfeer die ze altijd bij Paul en mij, direct bij binnenkomst, op de kamer bracht.

I would also like to thank several foreign guests, who visited our Theoretical Chemistry group in Groningen: Mrinalini Puranik, Markus Pernpointer and Kechen Wu. Thanks for all the funny moments and especially the stories about the customs in their homelands India, Germany and China.

De (ex-)bestuursleden van het Groninger Aio Overleg (Gaioo): Joanneke Prenger, Radboud van Trigt, Peter Ebbes, Laura Sabourin, Paul van Zomeren, Bart van der Aa, Heidi Stiegelis, Jolanda Smit, Gerhard Sjobbema en Anne Keirse, bedank ik voor de vele gezellige (eet-)vergaderingen waarin we -naast veel lol- zeer nuttige en waardevolle dingen hebben bereikt voor, met name, de Groningse promovendi.

Ook mogen de beide Hennie's, Henriette van Ingen en Henriette van Mil-Boddeveld, niet ongenoemd blijven. Bedankt voor alle nuttige secretaressewerkzaamheden in de afgelopen vier jaren. Jullie brede glimlach leverde altijd een gezellig praatje op, met veel gelach in de wandelgang.

Op deze plaats wil ik ook graag al mijn zeer dierbare vriend(inn)en in het Groningse bedanken. Zonder daarbij volledig te kunnen zijn wil ik er nog enkele noemen die ik hierboven nog niet ergens heb bedankt: Diana Alfons, Fenna Marinus, Jaap Oudman, Linda Geritsen, Anthony Hams, Gerard Smeenk, Marjolein Prenger, Jeroen Blomesath en Maaïke Pulles. Bedankt voor de vele leuke dingen die we samen hebben gedaan en ondernomen, van het vliegeren op Schier tot de gezellige spelletjesavonden, en natuurlijk niet te vergeten voor het genieten van de stad Groningen zelf met al zijn gezellig eet- en drinkgelegenheden. Ook wil ik nog twee mensen uit mijn Amsterdamse studententijd noemen: Vincent Osinga en Anouk Rijs. Vinnie, het samen bestuderen van TC-tentamens en de vele voetbalavonden hebben die tijd overgetelijk gemaakt. Anouk, ondanks alles wat er is gebeurd en misgegaan, toch bedankt.

In het bijzonder wil ik alvast mijn 'zussie' Saskia en 'buurvrouw' Rosie bedanken. Zij zullen me als paranimfen bijstaan tijdens de verdediging van mijn proefschrift.

En Jenny Ros, zo plots als je in mijn leven bent gekomen. Het geweldige gevoel dat je me in de afgelopen maanden hebt gegeven is zo mooi en werkelijk onbeschrijfelijk. Ik hoop echt nog heel lang zo met je door te kunnen gaan.

Tenslotte wil ik mijn ouders Jurjen en Gezina en mijn zusje Saskia bedanken voor het feit dat ze, ondanks alles in de afgelopen jaren, altijd in me zijn blijven geloven. Bedankt voor alle hulp en steun die jullie me altijd weer gegeven.

Freddie Kootstra, september 2001

Curriculum vitae

29 mei 1974 Geboren te Hengelo(o).

1986 - 1992 Vooropleiding:
Atheneum B,
Ichthus College,
Enschede.

1992 - 1997 Academische opleiding:
Scheikunde,
Vrije Universiteit Amsterdam,
Amsterdam.

1997 - 2001 Promotie onderzoek:
Theoretische Chemie,
Rijksuniversiteit Groningen,
Groningen.

STELLINGEN

behorend bij het proefschrift

Time-dependent density functional theory for periodic systems

Freddie Kootstra

1. Voor de complete beschrijving van zowel de grondtoestand als de response-eigenschappen van periodieke systemen moet niet slechts de periodieke dichtheid als onafhankelijk vrijheidsgraad worden beschouwd, maar tevens de macroscopische polarisatie.

X. Gonze, Ph. Ghosez, and R. W. Godby, *Phys. Rev. Lett.* **74**, 4035 (1995).

2. De formulering van dichtheidsfunctionaaltheorie voor periodieke systemen die op natuurlijke wijze macroscopische polarisatie bevat, heeft niet de deeltjesdichtheid maar de stroomdichtheid als kerngrootheid.

3. Voor niet-metallische kristallen in de zinkblende structuur is er geen directe relatie tussen de onderschatting van de bandgap door DFT-LDA en de uniforme verschuiving naar lagere energieën van de met TDDFT-ALDA berekende diëlektrische functies.

4a. De bewering van Rohlfing and Louie dat exciton effecten alleen kunnen worden beschreven binnen een twee-deeltjes model is uitsluitend het gevolg van hun definitie van excitonen.

M. Rohlfing and S. G. Louie, *Phys. Rev. B* **62**, 4927 (2000).

4b. Bovenstaande exciton effecten kunnen niet alleen in theorie maar ook in praktijk worden beschreven met behulp van het één-deeltjes formalisme van TDDFT.

5. De conclusie van Kirtman dat "berekeningen aan eindige oligomeren het effectiefst zijn voor de beschrijving van lokale eigenschappen, terwijl de berekeningen aan oneindige polymeren het beste zijn voor de gedelokaliseerde eigenschappen" en dat "deze twee berekeningswijzen in nauwkeurigheid competitief en derhalve als complementair kunnen worden beschouwd" is onjuist.

B. Kirtman, *Int. J. Quant. Chem.* **43**, 147 (1992).

6. De discussie over de aard van het materiaal HgSe in de zinkblende structuur, of het een halfgeleider met een kleine gap of een halfmetaal is, kan worden beëindigd. HgSe is een halfmetaal.

K. U. Gawlik, L. Kipp, M. Skibowski, N. Orlowski, and R. Manzke, *Phys. Rev. Lett.* **78**, 3165 (1997).

K. U. Gawlik *et al.*, *Phys. Rev. Lett.* **81**, 1536 (1998).

M. von Truchseß, A. Pfeuffer-Jeschke, C. R. Becker, G. Landwehr, and E. Barke, *Phys. Rev. B* **61**, 1666 (2000).

S. Einfeldt, F. Goschenhofer, C. R. Becker, and G. Landwehr, *Phys. Rev. B* **51**, 4915 (1995).

M. Rohlfing and S. G. Louie, *Phys. Rev. B* **57**, R9392 (1998).

7. Zij die een belangrijke bijdrage leveren aan de begeleiding van promotieonderzoek zouden daarvoor meer krediet moeten krijgen, ook in materiële vorm, zodat het niet blijft bij de vermelding als referent of co-promotor in een proefschrift.

D. F. J. Bosscher, *Rector Magnificus Rijksuniversiteit Groningen, De Groninger Gezinsbode, 06-09-2000.*

8. Een uitdaging ter uitdaging is een uitdaging om te weerstaan.

9. Theoretici hebben het grote voordeel dat iedere vorm van normaal gedrag als bonus wordt beschouwd.